Numerical Studies of Colloidal Systems

- Dissertation -

zur Erlangung des Grades
"Doktor der Naturwissenschaften"
am Fachbereich Physik,
Mathematik und Informatik der
Johannes Gutenberg-Universität in Mainz

Roman Schmitz
geboren in Trier

Max Planck-Institut für Polymerforschung
Mainz, Juli 2011

Tag der mündlichen Prüfung: 21. September 2011

Zusammenfassung

Das Wechselspiel zwischen elektrostatischen und hydrodynamischen Kräften spielt eine wichtige Rolle beim Verständnis kolloidaler Systeme. Im Mittelpunkt einer theoretischen Betrachtung findet sich häufig das *Standard elektrokinetische Modell*. Dieser Mean-Field-Ansatz setzt sich aus der Stokes-Gleichung für die Hydrodynamik, der Poisson Gleichung für die Elektrostatik und einer Kontinuitätsgleichung zur Beschreibung der Ionenkonzentrationen zusammen. Ein neuer Gitteralgorithmus zur effizienten Lösung dieses nichtlinearen Gleichungssytems im Falle einer ladungsstabilisierten Kolloiddispersion unter Einfluss eines elektrischen Feldes wird im ersten Teil dieser Arbeit präsentiert. Die Untersuchung konzentriert sich hierbei hauptsächlich auf die Berechnung der *elektrophoretischen Mobilität*. Da dieser Transportkoeffizient nur für schwache Felder von diesen unabhängig ist, basiert der Algorithmus auf einer Linearisierung der Gleichungen. Die nullte Ordnung besteht dabei aus der wohlbekannten *Poisson-Boltzmann*-Theorie, während die erste Ordnung aus einem linearen Gleichungssystem besteht. Dieses Gesamtsystem wird dann in einzelne Teilprobleme gegliedert. Nacheinander werden spezialisierte Lösungen für jedes Teilproblem entwickelt und verschiedene Tests sowie Anwendungsmöglichkeiten für die einzelnen Methoden diskutiert. Letztendlich werden die Teilprogramme in einer iterativen Prozedur verknüpft. Diese wird angewendet, um einigen interessanten Fragestellungen nachzugehen, wie der Effekt unterschiedlicher Abschirmungsmechanismen auf die elektrophoretische Mobilität oder die Ladungsabhängigkeit der induzierten Dipolmomente und Ionenwolken um ein schwach geladenes Kolloid.
Im zweiten Teil dieser Dissertation wird eine Methode zur quantitativen Datenanalyse einer neuen experimentellen Methode entwickelt, die unter dem Namen "Total Internal Reflection Fluorescence Cross-Correlation Spectroscopy" (TIR-FCCS) bekannt ist. TIR-FCCS beschreibt eine optische Messmethode, in der fluoreszierende Kolloide verwendet werden um das Strömungsfeld nahe einer fest-flüssig-Grenzfläche zu verfolgen. Die Interpretation der experimentellen Ergebnisse bedarf dabei eines theoretischen Modells, das i.A. durch die Lösung einer Konvektions-Diffusions-Gleichung gegeben ist. Da aufgrund des Geschwindigkeitsfeldes und der Randbedingungen eine analytische Lösung unzugänglich ist, wird alternativ ein Lösungsweg auf der Basis von "Brownian Dynamics" und Monte-Carlo-Methoden entwickelt. Schlussendlich werden experimentelle Daten zu Messungen mit hydrophiler Oberfläche mithilfe dieser numerischen Methode analysiert.

Abstract

The interplay of hydrodynamic and electrostatic forces is of great importance for the understanding of colloidal dispersions. Theoretical descriptions are often based on the so called *standard electrokinetic model*. This Mean Field approach combines the Stokes equation for the hydrodynamic flow field, the Poisson equation for electrostatics and a continuity equation describing the evolution of the ion concentration fields.
In the first part of this thesis a new lattice method is presented in order to efficiently solve the set of non-linear equations for a charge-stabilized colloidal dispersion in the presence of an external electric field. Within this framework, the research is mainly focused on the calculation of the *electrophoretic mobility*. Since this transport coefficient is independent of the electric field only for small driving, the algorithm is based upon a linearization of the governing equations. The zeroth order is the well known *Poisson-Boltzmann* theory and the first order is a coupled set of linear equations. Furthermore, this set of equations is divided into several subproblems. A specialized solver for each subproblem is developed, and various tests and applications are discussed for every particular method. Finally, all solvers are combined in an iterative procedure and applied to several interesting questions, for example, the effect of the screening mechanism on the electrophoretic mobility or the charge dependence of the field-induced dipole moment and ion clouds surrounding a weakly charged sphere.

In the second part a quantitative data analysis method is developed for a new experimental approach, known as Total Internal Reflection Fluorescence Cross-Correlation Spectroscopy (TIR-FCCS). The TIR-FCCS setup is an optical method using fluorescent colloidal particles to analyze the flow field close to a solid-fluid interface. The interpretation of the experimental results requires a theoretical model, which is usually the solution of a convection-diffusion equation. Since an analytic solution is not available due to the form of the flow field and the boundary conditions, an alternative numerical approach is presented. It is based on stochastic methods, i. e. a combination of a Brownian Dynamics algorithm and Monte Carlo techniques. Finally, experimental measurements for a hydrophilic surface are analyzed using this new numerical approach.

Contents

Introduction

The understanding of colloidal systems is one of the most important topics in the field of soft matter research. However, the first question we have to clarify is, how to define *colloidal system*. In the Britannica Online Encyclopedia [1] we find:

> *"***colloid***, any substance consisting of particles substantially larger than atoms or ordinary molecules but too small to be visible to the unaided eye; more broadly, any substance, including thin films and fibres, having at least one dimension in this general size range, which encompasses about* 10^{-7} *to* 10^{-3} *cm. Colloidal systems may exist as dispersions of one substance in another–for example, smoke particles in air–or as single materials, such as rubber or the membrane of a biological cell."*

Colloidal dispersions can be found everywhere in everyday life and are of high importance for biological, chemical and physical systems. Therefore it is not surprising that the field of colloid science has a long tradition. Although an article of Thomas Graham in 1861 [2] is viewed as the official "hour of birth" of this scientific field, colloids have already been observed and studied since the seventeenth century [3]. Nevertheless, up to date we are far away from a full understanding of colloidal phenomena. The interplay between a wide range of chemical and physical mechanisms, e. g. electrostatics and thermodynamics, hydrodynamics and rheological effects, and moreover, the separation of length and time scales, on which the dynamics of colloidal particles and the surrounding medium takes place, induce a high degree of complexity. A closed analytical theory is certainly not feasible and also the theoretical predictions available make use of rather crude approximations. Fortunately, a third pillar in scientific research besides experiment and theory has grown in the last decades, namely the use of computers for simulations and expensive calculations. The benefit of computer calculations in science starts with the treatment of a huge amount of experimental data and their analysis. Simulations offer the opportunity of studying physical systems under well defined conditions and testing theoretical predictions by comparison with the experiments. Furthermore, very complex systems can be solved by

means of numerical calculations, where analytical solutions are not available or only using rough approximations. Thus computational methods became an important and helpful tool in science, moreover, are often cheaper than designing experiments, and thus, are of high interest for industry and life science. However, the physical resources are limited, either by computational power or memory. Therefore special care has to be taken on the actual problems and specialized computational methods must be developed for those problems. For example, trying to solve the flow field in a micro channel on a quantum mechanical or even on an atomistic level of the fluid particles would be senseless. In other words, real physical systems contain a huge number of degrees of freedom. In practice, a lot of them are of minor interest, and thus, their explicit treatment would be wasted computer time. One approach for this problem is the well known Mean–Field ansatz. The physical system is treated on a rather coarse level, where cross correlations are neglected.

This thesis is located in the field of method development.
In the first and major part, a colloidal system is studied on such a Mean–Field level. A charged colloidal sphere is dissolved in an ambient fluid, containing counterions and additional ionic species, and a constant external electric field is applied. This results in an electro–hydrodynamic phenomenon, known as *electrophoresis*. In the Mean–Field approximation, the ionic species and the fluid are not treated explicitly, rather by means of concentration and velocity fields. The governing equations consist in the Navier–Stokes equation for the treatment of hydrodynamics, a convection–diffusion equation coupling the ionic concentrations to the ambient fluid and the Poisson equation accounting for electrostatics. A detailed description of the Mean–Field approach and the underlying ideas for a computational treatment of these equations is presented in chapter 1. The strategy lies in dividing the complex system into smaller sub–problems, which could be handled much easier. In chapter 2 to 4 specialized solvers for those sub–problems are developed and tested. The combined algorithm is a rather efficient tool for studying electrophoresis of colloidal particles. The advantage is that the method offers the opportunity of varying several parameters independently, for example the charge of the macro particles, the fraction of the amount of counterions to all ions in the system and the diffusion constant of micro ions. In chapter 5 numerical results for the combined method are presented. In addition to some "classical" questions, e. g. the dependency of the electrophoretic mobility on κR or the ζ-potential (these concepts will be discussed later in detail), we focus on the dependency of the mobility on the screening mechanism. And indeed we could observe a difference in the mobility of salt screened and counterion dominated systems. Furthermore, a very interesting phenomenon in weakly charged colloidal systems is studied. If an external field is applied to a system of an uncharged colloidal sphere in a solution of negative and positive ions, electro–osmotic

flow occurs and since the ions cannot penetrate the solid sphere, the ion fluxes are reflected. This results in an accumulation of negative charges at one side of the particle, and positive ions on the other side, as recently shown by K. Kang and J.K.G. Dhont [4]. Using our numerical approach we could indeed observe this effect. Furthermore, upon increasing the charge of the colloidal sphere, we find a reversal of the ion clouds and the pertaining dipole moment.

In chapter 6 we leave the field of electrokinetics and study a rather different topic. From a collaboration with S. Yordanov and K. Koynov (AK Butt, MPIP Mainz) aroused the question if it is possible to find a theoretical prediction for their experimental results in order to develop a method for a quantitative analysis. In their new experimental approach, known as *Total Internal Reflection Fluorescence Cross–Correlation Spectroscopy* (TIR–FCCS), fluorescent colloidal particles are used for tracking a flow field close to an solid–fluid interface [5]. The dynamics of the tracer particles can be theoretically described via a convection–diffusion equation. However, the flow field and the boundary conditions at the channel wall complicate the search for an analytical solution of the problem. Therefore a new computational approach is presented in chapter 6, based on stochastic methods, i. e. Brownian Dynamics combined with Monte Carlo techniques, and some experimental results are analyzed using this new approach.

1. Theoretical Background

In almost all situations where two phases are brought in contact, a difference in the electric potential is produced. For example, if a solid is brought in contact with a liquid, charges are dissociated or associated at the surface; or if the liquid is polar, its molecules will tend to orient at the interface and hence a difference in the potential is caused [6]. Furthermore, if we think about water as a solvent, its self–dissociation always produces a small amount of negative and positive ions. Thus the interplay between electrostatics and hydrodynamics is of high importance for the understanding of a wide range of biological, chemical and physical systems. Moreover, electro–hydrodynamic phenomena also offer a great opportunity for the development of new applications in science and industry, e. g. electro–hydrodynamic pumps offer the advantage that electric forces act on a fluid over the whole pumping volume and do not require any moving parts as in the case of mechanical pumps [7, 8]; or pressure–driven flows through microchannels can be used to develop electrokinetic batteries [9]. One of the most important applications of electro–hydrodynamic effects in science are in separation techniques based on electrophoresis, used e. g. for the analysis of DNA [10].

Charged solid colloidal spheres in suspension in an aqueous solution containing counterions and salt ions will be surrounded by a cloud of oppositely charged ions. This cloud, typically called the *electric double layer*, is responsible for screening the electrostatic potential. If an external electric field is acting on the system, the charged spheres start to migrate in the direction of the oppositely charged electrode and the surrounding cloud will be deformed and becomes anisotropic due to the electric field and also to the friction between the ions and the fluid. This effect is called *electrophoresis* and the characterizing transport coefficient is the *electrophoretic mobility*, determined by the balance of electric driving and hydrodynamic frictional force acting on the sphere. The electrophoretic mobility μ is defined as the proportionality constant between the constant velocity $\boldsymbol{u}$ of the particle and the external driving field $\boldsymbol{E}_{ext}$ in the linear regime, i. e. for small driving fields,

$$\boldsymbol{u} = \mu \boldsymbol{E}_{ext} \,. \tag{1.1}$$

Efforts have been made to study the phenomena of electrophoresis by experimental methods [11–15] as well as by analytical and numerical calculations over the decades [16–33]. Due to the complexity of the field and the complicated

many–body nature of the problem, a quantitative theoretical understanding of the electrophoresis is still incomplete today. Only limiting cases are well understood.
One of the first and simplest analytical models for the electrophoretic mobility was introduced by Hückel in 1924 [17]. In the salt-free case and vanishing colloidal volume fraction, the mobility of a single sphere of charge Ze with radius R, in the presence of a constant electric field is given by the well known Stokes formula

$$6\pi\eta R\boldsymbol{u} = Ze\boldsymbol{E} \tag{1.2}$$

and hence

$$\mu_H = \frac{Ze}{6\pi\eta R}\,. \tag{1.3}$$

Here, η is the viscosity of the ambient fluid.
Conversely, some years earlier, Smoluchowski developed an analytic solution in the case of very high salt concentration [16], essentially given by

$$\mu_S = \frac{3}{2}\mu_H\,, \tag{1.4}$$

if the ζ potential, i. e. the electrostatic potential at the surface of the particle, remains the same. In both cases, rough simplifications have been applied for the form of the electric field close to the particle. While Smulochowski assumed the field to be constant and at every point parallel to the object surface, Hückel disregarded the deformation of the electric field completely [6]. Both cases are, however, well-defined and rigorous limits for the extreme cases of infinitely thick ($\kappa R \to 0$) or thin ($\kappa R \to \infty$) diffusive layers. In 1931, Henry published an approximate method which takes the field deformation into account [18]. He found that the mobility could be written as

$$\mu = \mu_H\, f(\kappa R)\,. \tag{1.5}$$

Here, κ is the Debye screening parameter, which will be discussed later on in detail. f is a function with limiting values $f \to 1$ for $\kappa R \ll 1$ (Hückel limit) and $f \to 3/2$ if $\kappa R \gg 1$ (Smulochowski limit). In the following decades alternative solutions have been investigated, which differ from the function f given by Henry (see for example [19–22]). However, all of them interpolate from the Hückel to the Smoluchowski limit.
In recent years, various sophisticated numerical and simulation methods for the treatment of hydrodynamics in colloidal systems have been developed, e. g. multiparticle–collision dynamics[34–36] or lattice Boltzmann simulations [37–40]. Former studies done in our group are based on the so called “raspberry model”, which is a hybrid simulation method. In this model the ions and the colloidal particle, which is represented by a two dimensional bead–spring network, wrapped around a solid sphere, are treated by explicit molecular

dynamics simulations and coupled to a lattice Boltzmann background for the treatment of fluid dynamics [41]. This kind of simulation is computationally expensive, and furthermore, can cause some undesired effects, since the explicit ionic particles are unrealistically large and hence packing effects could occur. Later studies, based on a Mean–Field approach and the use of a commercial finite elements package (COMSOL), were limited due to an enormous demand of memory. This thesis resumes the former Mean–Field approach, such that its main focus is the development of an efficient computational method for solving the Mean–Field equations numerically.
In the current chapter the basic equations and underlying ideas will be presented. In the subsequent chapters the development of the computational method will be investigated successively. Throughout, we assume a finite system with periodic boundary conditions.

1.1. The Mean-Field Approach – The Electrokinetic Equations

The effect of electrophoresis is balanced by electrostatic and hydrodynamic effects. In the case of a Mean–Field picture the system is described in terms of ion concentration fields c_i, electrostatic potential ψ and the flow velocity field $\boldsymbol{v}$. Cross–correlations between salt ions and thermal fluctuations are neglected. In this regime, the system is described by the Poisson equation, mass conservation equations and the Navier–Stokes equation. First of all, the Poisson equation couples the concentration fields to the electrostatic potential ψ

$$-\nabla^2\psi = \frac{1}{\varepsilon} e \sum_i z_i c_i \,. \tag{1.6}$$

Here, ε is the dielectric constant, e denotes the elementary charge and z_i is the valence of the ionic species, where the subscript i indicates the different ionic species in the system. Counterions, which assure the charge neutrality of the system, are denoted by the index $i = 0$. The charged colloids are taken into account via boundary conditions.
The mass conservation condition for all ion concentration fields is described by a continuity equation,

$$\partial_t c_i + \nabla \cdot \boldsymbol{j}_i = 0 \,. \tag{1.7}$$

The current density consists of three different parts. Firstly, a diffusive current

$$\boldsymbol{j}_i^{(diff)} = -D_i \nabla c_i \,, \tag{1.8}$$

where D_i is the diffusion constant of species i. Furthermore, the external driving field acts on the ions, and thus this electric force gives rise to a second current density

$$\boldsymbol{j}_i^{(el)} = -e z_i (\nabla\psi) \mu_i c_i \,. \tag{1.9}$$

The mobility μ_i of species i is related to the diffusion constant via Einstein's relation,

$$\mu_i = \frac{D_i}{k_B T}\,, \tag{1.10}$$

with T the temperature and k_B is the the Boltzmann constant, and hence, one may write

$$\boldsymbol{j}_i^{(el)} = -ez_i \frac{D_i}{k_B T}(\nabla\psi)c_i\,. \tag{1.11}$$

Furthermore, the ions will move with the ambient fluid, such that the fluid velocity field $\boldsymbol{v}$ causes a convective current,

$$\boldsymbol{j}_i^{(con)} = \boldsymbol{v}c_i\,. \tag{1.12}$$

Summing up all contributions and including them in the continuity equation results in a convection–diffusion equation, known as *Nernst–Planck* equation,

$$\begin{aligned} 0 &= \partial_t c_i + \nabla\cdot(\boldsymbol{j}_i^{(el)} + \boldsymbol{j}_i^{(diff)} + \boldsymbol{j}_i^{(con)}) \\ &= \partial_t c_i + \nabla\cdot\left(-D_i\nabla c_i - \frac{D_i}{k_B T}ez_i(\nabla\psi)c_i + \boldsymbol{v}c_i\right)\,. \end{aligned} \tag{1.13}$$

Electric forces and hydrodynamic viscous forces are balanced in the Navier–Stokes equation

$$\rho\partial_t\boldsymbol{v} = -\nabla p + \eta\nabla^2\boldsymbol{v} - e(\nabla\psi)\sum_i z_i c_i\,, \tag{1.14}$$

where ρ is the mass density of the fluid. In this formulation, known as *Stokes* equation, the Reynolds number is set to zero. As we will see later, the pressure p has the function of a Lagrange multiplier, enforcing the constraint of incompressibility

$$\nabla\cdot\boldsymbol{v} = 0\,. \tag{1.15}$$

At a certain velocity of the sphere the friction forces balance the driving electric force. Then, these equations will reach a stationary limit, and the whole system of equations we will study is given by [3]

$$0 = \nabla^2\psi + \frac{1}{\varepsilon}e\sum_i z_i c_i\,, \tag{1.16a}$$

$$0 = \nabla\cdot\left(D_i\nabla c_i + \frac{D_i}{k_B T}ez_i(\nabla\psi)c_i - \boldsymbol{v}c_i\right)\,, \tag{1.16b}$$

$$0 = -\nabla p + \eta\nabla^2\boldsymbol{v} - e(\nabla\psi)\sum_i z_i c_i\,, \tag{1.16c}$$

$$0 = \nabla\cdot\boldsymbol{v}\,. \tag{1.16d}$$

Notice that the stationary formulation is not manifestly Galilean invariant, but rather selects one particular frame of reference, in which it is valid. If a colloidal sphere would move relative to the chosen inertial frame, the local ionic concentration would change with time, and hence, a stationary solution cannot exist. The only exception is the frame in which all colloids are at rest. This means that the requirement of vanishing time derivatives fixes the system to the rest frame of the colloidal spheres. The particle velocity, which determines the mobility, is the relative velocity of the particles to the center of mass of the system. Another important observation is therefore that the requirement of a stationary solution either confines the theory to single-colloid studies, or imposes an unphysical "rigid-body" constraint between the colloidal spheres.

1.2. Dimensionless Formulation

The electrokinetic equations may be reformulated in terms of dimensionless quantities. This means that we introduce reduced units, consistent with the intrinsic scales of the system.
First of all, we define a very natural unit for the electrophoretic mobility via the combination of the "Hückel" mobility, Eq. (1.3), with an intrinsic length scale of the system. Such a length could be defined by the balance between electrostatic and thermal energy

$$l_B = \frac{e^2}{4\pi\varepsilon k_B T}\,, \tag{1.17}$$

which is called *Bjerrum length*. Inserting this into Eq. (1.3), the natural unit of the mobility reads

$$\mu_0 := \frac{e}{6\pi\eta l_B}\,, \tag{1.18}$$

and a dimensionless *reduced electrophoretic mobility* is defined as

$$\mu_{red} := \frac{\mu}{\mu_0}\,. \tag{1.19}$$

The most natural energy scale is the thermal energy $k_B T$. In combination with the elementary charge e, we define the dimensionless potential as

$$\tilde{\psi} = \psi \frac{e}{k_B T}\,, \tag{1.20}$$

i. e. the reduced potential is the electrostatic energy of an elementary charge in units of thermal energy. Inserting this into the Poisson equation leads to

$$\nabla^2 \tilde{\psi} + 4\pi l_B \sum_i z_i c_i = 0\,. \tag{1.21}$$

parameter	physical units	dimensionless formulation
Bjerrum length	$l_B = \frac{e^2}{4\pi\varepsilon k_B T}$	
screening parameter	$\kappa^2 = 4\pi l_B \sum_i z_i^2 \frac{N_i}{V}$	
electrophoretic mobility	μ	$\mu_{red} = \frac{6\pi\eta l_B}{e}\mu$
spatial position	$\boldsymbol{r}$	$\tilde{\boldsymbol{r}} = \kappa\boldsymbol{r}$
spatial derivative	∇	$\tilde{\nabla} = \frac{1}{\kappa}\nabla$
electrostatic potential	ψ	$\tilde{\psi} = \frac{e}{k_B T}\psi$
electric field	$\boldsymbol{E}$	$\tilde{\boldsymbol{E}} = \frac{e}{\kappa k_B T}\boldsymbol{E}$
ion concentration	c_i	$\tilde{c}_i = \frac{4\pi l_B}{\kappa^2}c_i$
colloid charge	Ze	$\tilde{Z} = 4\pi l_B \kappa Z$
number of ions	N_i	$\tilde{N}_i = 4\pi l_B \kappa N_i$
flow velocity	$\boldsymbol{v}$	$\tilde{\boldsymbol{v}} = \frac{6\pi l_B \eta}{\kappa k_B T}\boldsymbol{v}$
pressure	p	$\tilde{p} = \frac{4\pi l_B}{\kappa^2 k_B T}p$
diffusion constant	D_i	$\tilde{D}_i = \frac{6\pi l_B \eta}{k_B T}D_i$

Table 1.1.: Summary of all parameters in physical units and their reduced counterparts.

Introducing an arbitrary parameter κ^{-1} as a characteristic length scale, the gradient is rescaled via

$$\tilde{\nabla} = \frac{1}{\kappa}\nabla\,. \tag{1.22}$$

This allows us to write Eq. (1.21) in a dimensionless form,

$$\tilde{\nabla}^2\tilde{\psi} + \sum_i z_i\tilde{c}_i = 0\,, \tag{1.23}$$

where

$$\tilde{c}_i := \frac{4\pi l_B}{\kappa^2}c_i \tag{1.24}$$

is the concentration field in reduced units. The mass normalization condition for the counterions then reads

$$\int d^3\tilde{r}\tilde{c}_0 = \frac{\tilde{Z}}{z_0}\,. \tag{1.25}$$

where

$$\tilde{Z} = 4\pi l_B\kappa Z\,. \tag{1.26}$$

Consequently, this yields also a reformulation of the number of ions in the system

$$\tilde{N}_i = 4\pi l_B\kappa N_i\,. \tag{1.27}$$

The reduced electric field is simply defined by its connection to the electrostatic potential

$$\tilde{\boldsymbol{E}} = -\tilde{\nabla}\tilde{\psi} = \frac{e}{\kappa\, k_B T}\boldsymbol{E}\,. \tag{1.28}$$

Combining this with the definition of the reduced electrophoretic mobility, Eq. (1.1) and Eq. (1.18), gives rise to a natural formulation of a reduced velocity

$$\begin{aligned}\tilde{\boldsymbol{v}} &= \mu_{red}\tilde{\boldsymbol{E}}\\ &= \frac{6\pi\eta l_B}{e}\frac{e}{\kappa k_B T}\mu\boldsymbol{E}\\ &= \frac{6\pi l_B\eta}{\kappa k_B T}\boldsymbol{v}\,.\end{aligned} \tag{1.29}$$

This allows us to write the Stokes equation in its dimensionless form

$$0 = \tilde{\nabla}\cdot\tilde{\boldsymbol{v}}\,, \tag{1.30}$$

$$0 = -\tilde{\nabla}\tilde{p} + \frac{2}{3}\tilde{\nabla}^2\tilde{\boldsymbol{v}} - (\tilde{\nabla}\tilde{\psi})\sum_i z_i\tilde{c}_i\,, \tag{1.31}$$

with the reduced pressure

$$\tilde{p} := \frac{4\pi l_B}{\kappa^2 k_B T}p\,. \tag{1.32}$$

Finally, reformulation of the diffusion constants via

$$\tilde{D}_i := \frac{6\pi l_B \eta}{k_B T} D_i \tag{1.33}$$

and replacing all other quantities by their rescaled counterpart, results in a dimensionless formulation of the Nernst-Planck equation,

$$\tilde{\nabla} \cdot \left\{ \tilde{D}_i \tilde{\nabla} \tilde{c}_i + \tilde{D}_i z_i (\tilde{\nabla} \tilde{\psi}) \tilde{c}_i - \tilde{\boldsymbol{v}} \tilde{c}_i \right\} = 0 \quad . \tag{1.34}$$

The choice of the scaling parameter κ is completely immaterial for the mathematical formulation of the problem. It is only important to map the numerical results back onto a physical system, and it is therefore a matter of convention. A choice for this length scale, convenient for many applications, can be motivated by the linearized *Debye-Hückel* theory. For vanishing driving field $\mathbf{E}_{ext} = 0$ the last term of Eq. (1.34) disappears, and in this equilibrium formulation, i. e. $\boldsymbol{j}_i = 0$, the electrokinetic theory reduces to the *Poisson-Boltzmann* equation

$$-\tilde{\nabla}^2 \tilde{\psi} = \sum_i z_i \tilde{c}_i \,, \tag{1.35a}$$

$$\tilde{\nabla} \ln \tilde{c}_i + z_i (\tilde{\nabla} \tilde{\psi}) = 0 \,. \tag{1.35b}$$

It is useful to reformulate these equations in terms of an electric field $\tilde{\boldsymbol{E}} = -\tilde{\nabla}\tilde{\psi}$, such that

$$\tilde{\nabla} \cdot \tilde{\boldsymbol{E}} - \sum_i z_i \tilde{c}_i = 0 \,, \tag{1.36}$$

$$\tilde{\nabla} \ln \tilde{c}_i - z_i \tilde{\boldsymbol{E}} = 0 \,, \tag{1.37}$$

$$\tilde{\nabla} \times \tilde{\boldsymbol{E}} = 0 \,. \tag{1.38}$$

For the linearized formulation of this equations, one may assume that the concentration profiles can be written as the constant equilibrium value plus some small perturbation

$$\tilde{c}_i \equiv \frac{\tilde{N}_i}{\tilde{V}} (1 + \varphi_i) \tag{1.39}$$

with $\varphi_i \ll 1$. Thus, we get

$$\tilde{\nabla} \cdot \tilde{\boldsymbol{E}} - \sum_i z_i \frac{\tilde{N}_i}{\tilde{V}} (1 + \varphi_i) = 0 \,, \tag{1.40}$$

$$\tilde{\nabla} \ln(1 + \varphi_i) - z_i \tilde{\boldsymbol{E}} = 0 \,. \tag{1.41}$$

Expansion of the logarithm up to linear order in φ_i leads to

$$\tilde{\nabla}\varphi_i = z_i\tilde{\boldsymbol{E}}\,. \tag{1.42}$$

Inserting this into Eq. (1.40) and taking the gradient of this equation results in

$$\begin{aligned}\tilde{\nabla}\left(\tilde{\nabla}\cdot\tilde{\boldsymbol{E}}\right) &= \sum_i z_i\frac{\tilde{N}_i}{\tilde{V}}(\tilde{\nabla}\varphi_i)\\ &= \sum_i z_i^2\frac{\tilde{N}_i}{\tilde{V}}\tilde{\boldsymbol{E}}\,,\end{aligned} \tag{1.43}$$

and applying the identity

$$0 = \tilde{\nabla}\times(\tilde{\nabla}\times\tilde{\boldsymbol{E}}) = \tilde{\nabla}(\tilde{\nabla}\cdot\tilde{\boldsymbol{E}}) - \tilde{\nabla}^2\tilde{\boldsymbol{E}} \tag{1.44}$$

results in

$$\left(\tilde{\nabla}^2 - \sum_i z_i^2\frac{\tilde{N}_i}{\tilde{V}}\right)\tilde{\boldsymbol{E}} = 0\,. \tag{1.45}$$

The freedom to choose κ arbitrarily allows us to write Eq. (1.45) in the simple form

$$\left(\tilde{\nabla}^2 - 1\right)\tilde{\boldsymbol{E}} = 0\,, \tag{1.46}$$

with

$$1 = \sum_i z_i^2\frac{\tilde{N}_i}{\tilde{V}} = \sum_i z_i^2\frac{4\pi l_B}{\kappa^2}\frac{N_i}{V}\,, \tag{1.47}$$

and hence

$$\kappa^2 = 4\pi l_B\sum_i z_i^2\frac{N_i}{V}\,. \tag{1.48}$$

This is the natural Debye screening parameter in the finite–volume version of the linearized Poisson–Boltzmann theory.

All together, the dimensionless formulation of the electrokinetic equations, Eq. (1.16), reads

$$0 = \tilde{\nabla}^2\tilde{\psi} + \sum_i z_i\tilde{c}_i\,, \tag{1.49a}$$

$$0 = \tilde{\nabla}\cdot\left(\tilde{D}_i\tilde{\nabla}\tilde{c}_i + \tilde{D}_i z_i(\tilde{\nabla}\tilde{\psi})\tilde{c}_i - \tilde{\boldsymbol{v}}\tilde{c}_i\right)\,, \tag{1.49b}$$

$$0 = -\tilde{\nabla}\tilde{p} + \frac{2}{3}\tilde{\nabla}^2\tilde{\boldsymbol{v}} - (\tilde{\nabla}\tilde{\psi})\sum_i z_i\tilde{c}_i\,, \tag{1.49c}$$

$$0 = \tilde{\nabla}\cdot\tilde{\boldsymbol{v}}\,. \tag{1.49d}$$

In the following, for practical reasons the tildes are omitted, with the understanding that *all* parameters, including N_i and Z, are given in reduced units.

1.3. Linearization of the Electrokinetic Equations

The high non-linearity of the Mean–Field equations causes two problems. First of all, it is very difficult, and at least computational expensive, to solve a coupled system of nonlinear differential equations. Furthermore, the quantity we are mainly interested in, namely the electrophoretic mobility, is well defined (i. e. independent of the driving field) only in the linear regime. Consequently, if a fully nonlinear solution of the equations is obtained, an extrapolation to zero driving field is required. The second problem can be avoided completely, and the first one at least reduced, by a linearization of the equations in terms of the driving field [3]. This can be done by a formal expansion with respect to a small parameter ϵ, corresponding to the external field. We assume that all fields in the system have a regular expansion in ϵ, and hence we write

$$
\begin{aligned}
c_i &\equiv c_i^{(0)} + \epsilon c_i^{(1)} + \mathcal{O}(\epsilon^2)\,, && \text{(1.50a)}\\
\psi &\equiv \psi^{(0)} + \epsilon \psi^{(1)} + \mathcal{O}(\epsilon^2)\,, && \text{(1.50b)}\\
\boldsymbol{v} &\equiv \epsilon \boldsymbol{v}^{(1)} + \mathcal{O}(\epsilon^2)\,, && \text{(1.50c)}\\
p &\equiv p^{(0)} + \epsilon p^{(1)} + \mathcal{O}(\epsilon^2)\,. && \text{(1.50d)}
\end{aligned}
$$

The reduced electrophoretic mobility is then given by

$$
\mu_{red} = \frac{\boldsymbol{u}^{(1)}}{\boldsymbol{E}_{ext}}\,, \tag{1.51}
$$

where $\boldsymbol{u}^{(1)}$ is the constant velocity of the colloid in the system's center-of-mass reference frame, i. e. the value of the flow velocity field at the surface of the colloidal sphere

$$
\boldsymbol{u}^{(1)} := \boldsymbol{v}^{(1)}(R)\,, \tag{1.52}
$$

with R the radius of the particle. This mobility is strictly independent of the strength of the external driving force.

By applying the expansion, Eq. (1.50), to the electrokinetic equations and making use of the requirement that each order must be satisfied independently, we get:

- Zeroth Order

$$
\begin{aligned}
0 &= \nabla\left(z_i\psi^{(0)} + \ln c_i^{(0)}\right)\,, && \text{(1.53a)}\\
0 &= \nabla^2\psi^{(0)} + \sum_i z_i c_i^{(0)}\,, && \text{(1.53b)}\\
0 &= -\nabla p^{(0)} - (\nabla\psi^{(0)})\sum_i z_i c_i^{(0)}\,. && \text{(1.53c)}
\end{aligned}
$$

- First Order

$$
\begin{aligned}
0 &= \nabla\cdot\Big\{D_i\nabla c_i^{(1)} + D_i z_i(\nabla\psi^{(1)})c_i^{(0)} \\
&\quad + D_i z_i(\nabla\psi^{(0)})c_i^{(1)} - \boldsymbol{v}^{(1)}c_i^{(0)}\Big\}\,, && \text{(1.54a)}\\
0 &= -\nabla p^{(1)} + \frac{2}{3}\nabla^2\boldsymbol{v}^{(1)} \\
&\quad -(\nabla\psi^{(1)})\sum_i z_i c_i^{(0)} - (\nabla\psi^{(0)})\sum_i z_i c_i^{(1)}\,, && \text{(1.54b)}\\
0 &= \nabla\cdot\boldsymbol{v}^{(1)}\,, && \text{(1.54c)}\\
0 &= \nabla^2\psi^{(1)} + \sum_i z_i c_i^{(1)}\,. && \text{(1.54d)}
\end{aligned}
$$

The first order consists of a coupled set of *linear* equations. The zeroth order equations are still nonlinear, but of much simpler structure than the full set of equations, Eq. (1.49). Note that the last equation of zeroth order, Eq. (1.53c), containing the pressure field is irrelevant for the future development. However, the remaining two equations are the standard electrokinetic equations in the equilibrium system without any external driving force, known as *Poisson–Boltzmann* theory.
Integrating Eq. (1.53a), one obtains

$$c_i^{(0)} = A_i \exp\left(-z_i\psi^{(0)}\right), \tag{1.55}$$

where the integration constant A_i must have, for normalization reasons, the value

$$A_i = \frac{N_i}{\int_V \exp\left(-z_i\psi^{(0)}\right) dV}. \tag{1.56}$$

Inserting this result into Eq. (1.53b), one can write the zeroth order as the more compact Poisson–Boltzmann equation

$$\nabla^2\psi^{(0)} + \sum_i z_i A_i \exp\left(-z_i\psi^{(0)}\right) = 0\,. \tag{1.57}$$

In the first order equations, the external field is taken into account by decomposing the potential $\psi^{(1)}$ into a periodic part and one part corresponding to the constant electric field

$$\psi^{(1)} \equiv \psi'^{(1)} + \psi''^{(1)}\,, \tag{1.58}$$

such that

$$\nabla^2\psi'^{(1)} = -\sum_i z_i c_i^{(1)}\,, \tag{1.59}$$

$$\nabla^2\psi''^{(1)} = 0\,, \tag{1.60}$$

$$\nabla\psi''^{(1)} = -\boldsymbol{E}_{ext}\,. \tag{1.61}$$

Thus, we write the first order equations in the form

$$\begin{aligned} 0 &= \nabla\cdot\Big\{D_i\nabla c_i^{(1)} + D_i z_i(\nabla\psi'^{(1)})c_i^{(0)} - D_i z_i \boldsymbol{E}_{ext} c_i^{(0)} \\ &\quad + D_i z_i(\nabla\psi^{(0)})c_i^{(1)} - \boldsymbol{v}^{(1)}c_i^{(0)}\Big\}\,, \end{aligned} \tag{1.62a}$$

$$\begin{aligned} 0 &= -\nabla p^{(1)} + \frac{2}{3}\nabla^2\boldsymbol{v}^{(1)} - (\nabla\psi'^{(1)})\sum_i z_i c_i^{(0)} \\ &\quad + \boldsymbol{E}_{ext}\sum_i z_i c_i^{(0)} - (\nabla\psi^{(0)})\sum_i z_i c_i^{(1)}\,, \end{aligned} \tag{1.62b}$$

$$0 = \nabla\cdot\boldsymbol{v}^{(1)}\,, \tag{1.62c}$$

$$0 = \nabla^2\psi'^{(1)} + \sum_i z_i c_i^{(1)}\,. \tag{1.62d}$$

1.4. Iterative Procedure

The linearization of the problem divides the challenge of solving the electrokinetic equations into two different subproblems. For the zeroth order, a solution of the fully non-linear Poisson–Boltzmann equation must be found. The first order consists in a set of linear equations, while the fields of zeroth order only occur as prefactors. A logical way for solving these first order equations consists on using finite–difference or finite–element methods. However, this can get very challenging, due to the high complexity of the problem, i. e. handling the conservation laws in this kind of methods is not easy. We decided to use a different strategy for solving the first order equations. Since the set of equations is constructed by three different kinds of equations, we divide the first order into three different subproblems, the Poisson equation, the Nernst–Planck equation and the incompressible Stokes equation. Each particular problem is solved by a specialized numerical method. Using this ansatz offers the opportunity to choose methods, which will intrinsically satisfy all conservation laws up to inevitable round–off errors. All methods are then connected via an iterative method as sketched by Fig. 1.1

It should be noted that the Stokes equation is solved in the center-of-mass reference frame, while the Nernst–Planck equation is solved in the colloid's

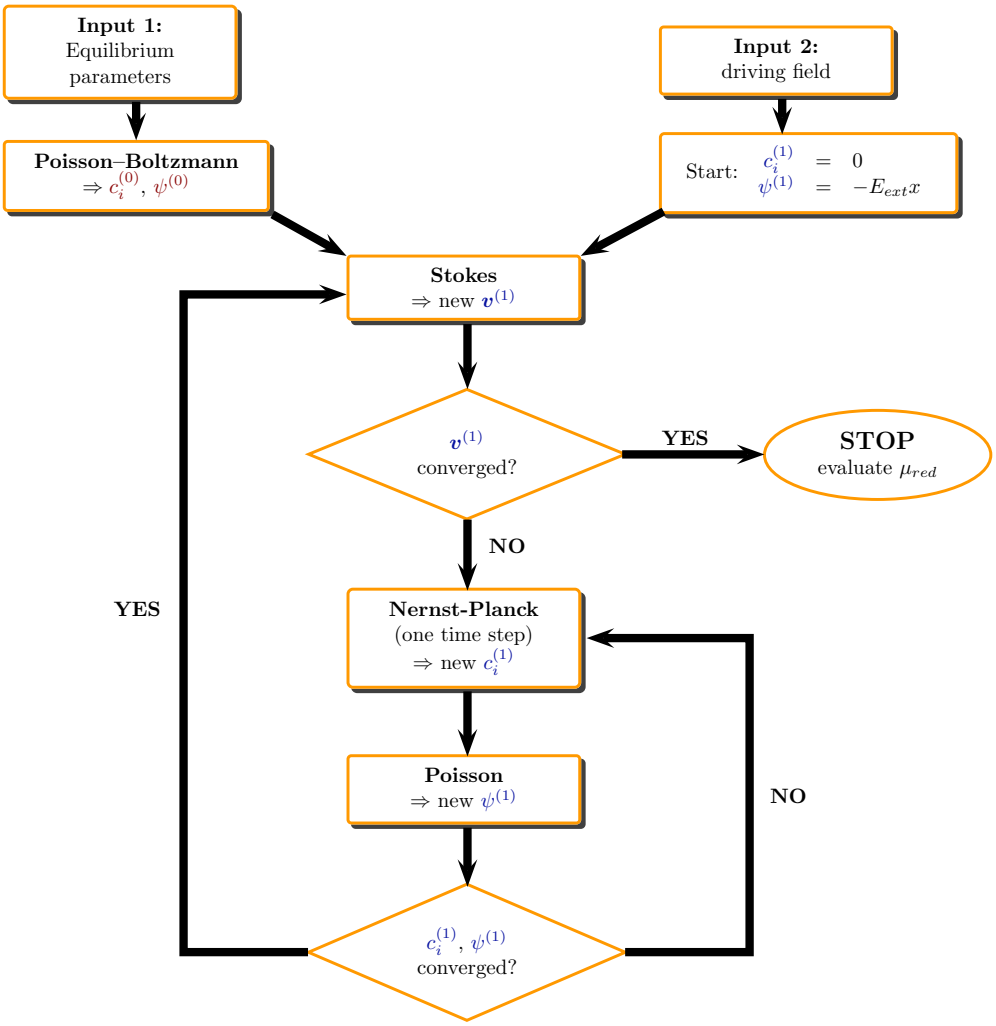

Figure 1.1.: Schematic description of the algorithm for solving the electrokinetic equations

rest frame. Therefore, the velocity flow field must first be subjected to a Galilei transform before feeding the data into the Nernst–Planck equation.

Every solver is a kind of finite–difference algorithm, discretized on a regular lattice with periodic boundary conditions.

In contrast to the other equations, which will be discussed in detail in the following chapters, the Poisson equation for a given charge density can be solved efficiently by a simple standard method. The evaluation of differential operators becomes very easy in Fourier space, and thus the potential and the

charge density are expanded in terms of Fourier series via

$$\psi(\boldsymbol{r}) \;=\; \sum_{\boldsymbol{k}} \hat{\psi}(\boldsymbol{k}) \exp[-i\boldsymbol{k}\boldsymbol{r}]\,, \tag{1.63}$$

$$\rho(\boldsymbol{r}) \;=\; \sum_{\boldsymbol{k}} \hat{\rho}(\boldsymbol{k}) \exp[-i\boldsymbol{k}\boldsymbol{r}]\,, \tag{1.64}$$

with

$$\boldsymbol{k} = 2\pi \begin{pmatrix} k/L_x \\ l/L_y \\ m/L_z \end{pmatrix}\,, \quad k,l,m \in \mathbb{Z}\,. \tag{1.65}$$

Here, $L_x \times L_y \times L_z$ is the dimension of the computational domain.
The solution of the Poisson equation in Fourier space is then given by

$$\hat{\psi} = \frac{1}{\boldsymbol{k}^2}\hat{\rho}. \tag{1.66}$$

Hence, this equation can be solved by only three steps:

1. Fast Fourier transformation (FFT) of the discretized charge density,
2. Solving the Poisson equation in Fourier space via Eq. (1.66),
3. Backtransformation (IFFT) of the electrostatic potential.

Note that for consistency reasons, a discretized version, i. e. a lattice Green's function, is used instead of the continuum Green's function.
A derivation for a *finite–difference* version of this Green's function can for example be found in Ref. [42].
Consider a one-dimensional periodic function g with periodicity L_x, i. e.

$$g(x) \;=\; g(x + L_x)\,. \tag{1.67}$$

The function is discretized on a cubic lattice with lattice spacing a and N_x lattice sites, such that

$$L_x = N_x a\,, \tag{1.68}$$

and hence the periodicity is given by

$$g(n_x a) \;=\; g((n_x + N_x)a)\,, \tag{1.69}$$

where $n_x \in \mathbb{Z}$ adresses the discrete grid point. Writing $g(x)$ as Fourier transformed function of $\hat{g}(k)$, one obtains

$$g(n_x a) \;=\; \sum_{k=0}^{N_x-1} \hat{g}(k)\, e^{-2\pi i \frac{k n_x}{N_x}}\,. \tag{1.70}$$

and

$$\hat{g}(k) \;=\; \frac{1}{N_x}\sum_{n_x=0}^{N_x-1} g(n_x a)\, e^{2\pi i \frac{k n_x}{N_x}}\,. \tag{1.71}$$

In one dimension the midstep finite–difference version of the second derivative of g is given by

$$\frac{d^2}{dx^2}g(x) \simeq \frac{1}{a^2}\left\{g((n_x+1)a) + g((n_x-1)a) - 2g(n_x a)\right\}\,. \tag{1.72}$$

Making use of Eq. (1.70), this finite–difference scheme can also be re–formulated in terms of a Fourier series,

$$\begin{aligned}
\frac{d^2}{dx^2}g(x) \;&\simeq\; \sum_{k=0}^{N_x-1}\frac{\hat{g}(k)}{a^2}\left\{e^{-2\pi i\frac{k(n_x+1)}{N_x}} + e^{-2\pi i\frac{k(n_x-1)}{N_x}} - 2e^{-2\pi i\frac{k n_x}{N_x}}\right\}\\
&=\; \sum_{k=0}^{N_x-1}\frac{\hat{g}(k)}{a^2}\left\{e^{-2\pi i\frac{k}{N_x}} + e^{2\pi i\frac{k}{N_x}} - 2\right\}e^{-2\pi i\frac{k n_x}{N_x}}\\
&=\; \sum_{k=0}^{N_x-1}\frac{\hat{g}(k)}{a^2}2\left\{\cos\left(2\pi\frac{k}{N_x}\right) - 1\right\}e^{-2\pi i\frac{k n_x}{N_x}}\,.
\end{aligned} \tag{1.73}$$

If we now substitute this expression to the three dimensional version of the Poisson equation in a periodic box with $N_x \times N_y \times N_z$ lattice sites, we get

$$\begin{aligned}
&\sum_{k=0}^{N_x-1}\sum_{l=0}^{N_y-1}\sum_{m=0}^{N_z-1}\frac{2}{a^2}\hat{\psi}(k,l,m)e^{-2\pi i\left(\frac{k n_x}{N_x}+\frac{l n_y}{N_y}+\frac{m n_z}{N_z}\right)}\\
&\cdot\left\{\cos\left(2\pi\frac{k}{N_x}\right) + \cos\left(2\pi\frac{l}{N_y}\right) + \cos\left(2\pi\frac{m}{N_z}\right) - 3\right\}\\
=\;&\sum_{k=0}^{N_x-1}\sum_{l=0}^{N_y-1}\sum_{m=0}^{N_z-1}\hat{\rho}(k,l,m)e^{-2\pi i\left(\frac{k n_x}{N_x}+\frac{l n_y}{N_y}+\frac{m n_z}{N_z}\right)}\,.
\end{aligned} \tag{1.74}$$

Thus, the discretized counterpart to Eq. (1.66) reads

$$\hat{\psi}(k,l,m) = \frac{a^2}{2}\frac{\hat{\rho}(k,l,m)}{\cos\left(2\pi\frac{k}{N_x}\right) + \cos\left(2\pi\frac{l}{N_y}\right) + \cos\left(2\pi\frac{m}{N_z}\right) - 3}\,. \tag{1.75}$$

Backtransformation finally yields the desired electrostatic potential in real space.

1.5. The Work of O'Brien and White

The idea of linearizing the electrokinetic equations and of solving these linearized equations using a numerical method is not new. In 1978 Richard W. O'Brien and Lee R. White developed this method in their famous and frequently cited publication, Ref. [23]. The aim of their work was to calculate the electrophoretic mobility of a colloidal particle as function of the ζ-potential under the influence of a constant external electric field. The difference to our method is that they assume only a single sphere dissolved in an electrolyte solution and set into an infinite domain, which consequently omits the influence of counterions. However, our method can be understood as a generalization of the method of O'Brien and White for a finite-sized system. In the limit of zero volume fraction the screening of the colloidal sphere is mainly dominated by the salt ions and the results of our method should recover the results of O'Brien and White. This is indeed the case, as we will see in Chap. 5. The numerical results of O'Brien and White are shown in Fig. 1.2.

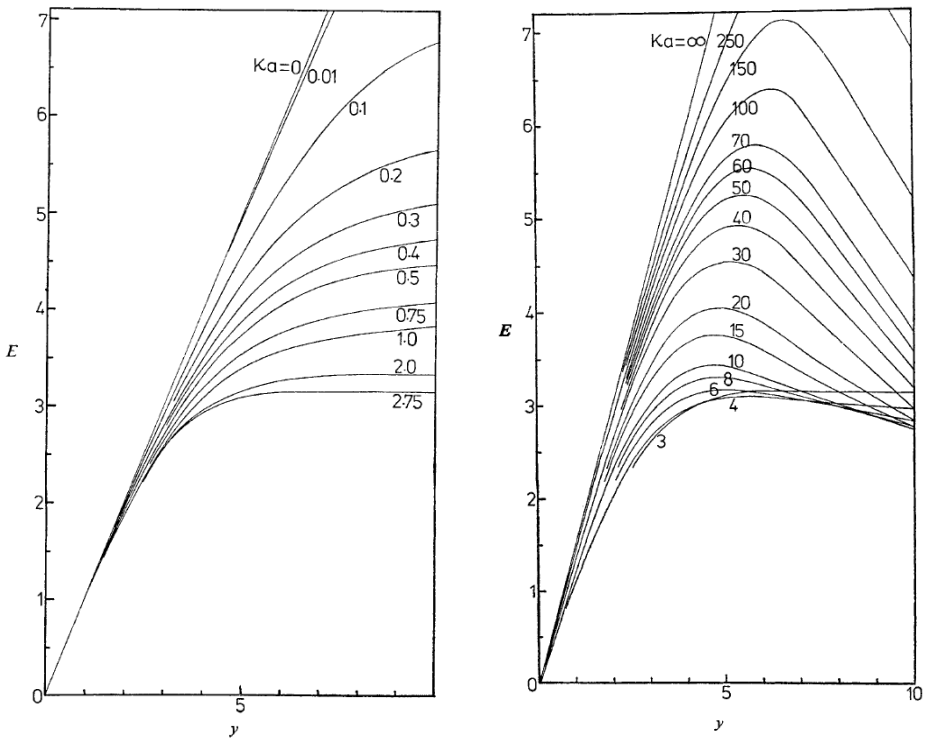

Figure 1.2.: Reduced mobility $E = 6\pi\eta e\mu/\varepsilon k_B T$ as function of the reduced zeta potential $y = e\zeta/k_B T$. These images are taken from Ref. [23] (Fig. 3 and 4).

2. Solving the Poisson-Boltzmann Equation

The zeroth order of the electrokinetic equations consists of the well known Poisson-Boltzmann equation, Eq. (1.57), which is a highly non-linear partial differential equation. Analytical work in this field is often restricted to a linearized version of this equation, known as *Debye-Hückel theory*. However, this linearization is only valid for weakly charged colloidal spheres, and therefore insufficient for our purposes. In recent years, new numerical methods have been developed for solving the fully non-linear Poisson-Boltzmann equation [43, 44].

In the current chapter, a fairly new numerical approach is presented in order to construct an unconditionally stable lattice algorithm for solving the Poisson-Boltzmann equation. This approach is based on ideas of A. C. Maggs and coworkers [27, 45–49] who investigated a completely new approach for the treatment of electrostatics in soft–matter systems. The advantage of Maggs' ideas is the completely local character of his lattice algorithm. Maggs formulates the electrostatic equations in terms of a variational problem where the functional depends on the electric field $\boldsymbol{E}$[1] and charge density ρ. Gauss' law $\nabla \cdot \boldsymbol{E} = \rho$ is viewed as a constraint. While a field which initially satisfies the Gauss' law can be easily constructed on a lattice, the transversal degree of freedom must be removed, $\nabla \times \boldsymbol{E} = 0$. This can be either integrated out by Monte Carlo [45–47] or Molecular Dynamics [27, 48, 49] techniques, or, as it is presented in the current chapter, by performing local relaxation moves.

These ideas can be applied to the Mean-Field equations. The Poisson-Boltzmann equation can be formulated in terms of a constrained variational problem, where Gauss' law and the mass normalization condition span a constraint surface. In a first step ionic concentrations and the electric field are initialized within this constraint surface and then local updates of both density and electric field are performed simultaneously such that the constraint surface is never left.

The basic idea and the method itself was mainly developed by M. Baptista and B. Dünweg, and is already published in Ref. [50]. Recently, this method was extended for non-uniform size effects of ionic concentrations by B. Li et al. [51]. The contribution of this thesis mainly consists of practical aspects (implementation, computational speedups, parallelization ...) and the appli-

[1] *not* on the electrostatic potential

cations. The present chapter outlines these developments in a self-contained way, and adds further results that have not yet been published.

2.1. Variational Approach

One way for solving the Poisson–Boltzmann equation (1.57) is to re-formulate it as a constrained variational problem. In this formulation a free energy functional is minimized, which is constructed such that its Euler–Lagrange equations reproduce Eq. (1.53). In the early 1970's Brenner and McQuarrie [52] constructed such a functional in the Debye–Hückel approximation for polyions of cylindrical shape and Brenner and Roberts [53] studied a similar variational principle to determine the electrostatic potential surrounding a spherical colloid. Since the 1990's several publications dealing with a free energy formulation and variational techniques for the fully non-linear Poisson–Boltzmann equation can be found (see e.g. [54–58]).
The functional is typically of the form

$$\mathcal{F} = \int_V f \, dV, \tag{2.1}$$

with

$$f = -\frac{1}{2}(\nabla\psi)^2 + \sum_i c_i \ln c_i + \psi \sum_i z_i c_i - \sum_i \mu_i (c_i - \frac{N_i}{V}). \tag{2.2}$$

Here, the first term corresponds to the electrostatic energy and the second term to the entropy. The μ_i are the chemical potentials of the species i, and furthermore Lagrange multipliers accounting for the mass normalization condition such that variation with respect to μ_i results in the constraint equation

$$\int_V c_i \, dV = N_i \, . \tag{2.3}$$

The Euler–Lagrange equation with respect to the electrostatic potential ψ recovers the Poisson equation (1.53b), and by extremizing the functional with respect to c_i, one obtains

$$\ln c_i + 1 + z_i\psi - \mu_i = 0. \tag{2.4}$$

Taking the gradient of this equation recovers Eq. (1.53a). Note that the equilibrium concentrations and potential do not minimize the functional but rather form a saddle point. This can be observed by decomposing the electrostatic potential and the concentrations into the solution plus a small deviation,

$$\psi = \psi^{(0)} + \delta\psi, \tag{2.5a}$$

$$c_i = c_i^{(0)} + \delta c_i, \tag{2.5b}$$

where δc_i must satisfy the mass normalization

$$\int_V \delta c_i \, dV = 0. \tag{2.6}$$

From this, one obtains

$$\mathcal{F} = \int_V (f_0 + f_2) dV + \mathcal{O}(\delta c^3), \tag{2.7}$$

with

$$\begin{aligned} f_0 &= -\frac{1}{2}(\nabla\psi^{(0)})^2 + \sum_i c_i^{(0)} \ln c_i^{(0)} \\ &\quad + \psi^{(0)} \sum_i z_i c_i^{(0)}, \end{aligned} \tag{2.8}$$

$$\begin{aligned} f_2 &= -\frac{1}{2}(\nabla\delta\psi^{(0)})^2 + \frac{1}{2}\sum_i \frac{\delta c_i^2}{c_i^{(0)}} \\ &\quad + \delta\psi \sum_i z_i \delta c_i. \end{aligned} \tag{2.9}$$

Thus, the quadratic form of the deviations is *not* positive–definite and this lack of positive–definiteness can cause various numerical difficulties in terms of stability.

Following the ideas of Maggs and Rosetto [45] and re–formulating the equations in terms of the electric field instead of the electrostatic potential, a variational formulation is constructed where this built-in lack of stability is intrinsically absent. In terms of the electric field $\boldsymbol{E} = -\nabla\psi$, Eq. (1.53) reads

$$\nabla \ln c_i = z_i \boldsymbol{E}, \tag{2.10a}$$

$$\nabla \cdot \boldsymbol{E} = \sum_i z_i c_i, \tag{2.10b}$$

$$\nabla \times \boldsymbol{E} = 0. \tag{2.10c}$$

These equations are recovered as the Euler–Lagrange equations of a constrained free energy functional of the form

$$\mathcal{F} = \int_V f \, dV, \tag{2.11}$$

$$\begin{aligned} f &= \frac{1}{2}\boldsymbol{E}^2 + \sum_i c_i \ln c_i - \psi(\nabla \cdot \boldsymbol{E} - \sum_i z_i c_i) \\ &\quad - \sum_i \mu_i (c_i - \frac{N_i}{V}). \end{aligned} \tag{2.12}$$

In this formulation, ψ is not a degree of freedom but rather a Langrange multiplier, accounting for Gauss' law which is considered as a constraint. The variation with respect to μ_i and ψ recovers the constraint conditions (2.3) and (2.10b). Minimization with respect to c_i again results in

$$\ln c_i + 1 + z_i\psi - \mu_i = 0, \tag{2.13}$$

while variation with respect to $\boldsymbol{E}$ yields

$$\boldsymbol{E} = -\nabla\psi. \tag{2.14}$$

Taking the gradient of Eq. (2.13), one obtains

$$\nabla \ln c_i + z_i\nabla\psi = 0, \tag{2.15}$$

and inserting Eq. (2.14) leads to

$$\nabla \ln c_i = z_i\boldsymbol{E}. \tag{2.16}$$

The curl of Eq. (2.14) finally recovers Eq. (2.10c).
To show that the solution of the variational problem is indeed a local minimum, one may rewrite again the concentration and the electric field as a small perturbation around the solution

$$c_i = c_i^{(0)} + \delta c_i, \tag{2.17a}$$
$$\boldsymbol{E} = \boldsymbol{E}^{(0)} + \delta\boldsymbol{E}. \tag{2.17b}$$

The deviations must satisfy Gauss' law and the mass normalization condition

$$\nabla\cdot\delta\boldsymbol{E} = \sum_i z_i\delta c_i, \tag{2.18}$$

$$\int_V \delta c_i\, dV = 0. \tag{2.19}$$

Inserting Eq. (2.17) into the functional, we get

$$\begin{aligned}\mathcal{F} = &\int_V \left\{\frac{1}{2}\boldsymbol{E}^{(0)2} + \sum_i c_i^{(0)}\ln c_i^{(0)}\right\} dV \\ &+ \int_V \left\{\frac{1}{2}\delta\boldsymbol{E}^2 + \frac{1}{2}\sum_i \frac{\delta c_i^2}{c_i^{(0)}}\right\} dV + \mathcal{O}(\delta c^3),\end{aligned} \tag{2.20}$$

i. e. small deviations from the solution will *always* increase the functional. Furthermore it has been proven that the Poisson–Boltzmann equation has one unique solution [59–61]. This guarantees that the functional has one and only

one minimum, which corresponds to the solution of the Poisson–Boltzmann equation.
To find this minimum we follow again the ideas of Maggs [46], who investigated a local algorithm for determining Coulombic interactions. The idea is to use an iterative procedure that relaxes all degrees of freedom of the functional such that it is systematically decreased, while staying strictly on the constraint surface. Such a procedure will ultimately run into the one and only minimum of the free energy landscape.
The system is initialized such that all constraints are satisfied, and the procedure treats them such that the system *always* stays on the constraint surface. Therefore, the Lagrange multiplier terms in the functional can be omitted, and hence it simplifies to

$$\mathcal{F} = \int_V \left\{ \frac{1}{2}\boldsymbol{E}^2 + \sum_i c_i \ln c_i \right\} dV \,. \tag{2.21}$$

2.2. Discretization

Before investigating the iterative procedure, we define a discretization scheme as follows. The computational domain is a rectangular box of size $l_1 \times l_2 \times l_3$ with periodic boundary conditions and is discretized by a regular orthorhombic lattice with lattice spacings Δx_α, $\alpha = 1, 2, 3$. Thus the volume of a unit cell is $\Delta V = \prod_{\alpha=1}^{3} \Delta x_\alpha$. The lattice sites are denoted by $\mathbf{r}_0$.
Following the ideas of Yee [62], scalar fields are set as variables on the nodes, while vector fields should be associated with the links and pseudo-vector fields are located at the centers of the plaquettes, i. e. the faces of the rectangular unit cells. Hence, the positions of the concentration fields are the vectors

$$\mathbf{r}_0(\mathbf{n}) = (\Delta x_1 n_1, \Delta x_2 n_2, \Delta x_3 n_3), \tag{2.22}$$

where n_α are integers. The x_1 component of the electric field E_1 is located at

$$\mathbf{r}_1(\mathbf{n}) = (\Delta x_1 (n_1 + 1/2), \Delta x_2 n_2, \Delta x_3 n_3), \tag{2.23}$$

and respectively the positions for the other two components E_2 and E_3 are given by

$$\mathbf{r}_2(\mathbf{n}) = (\Delta x_1 n_1, \Delta x_2 (n_2 + 1/2), \Delta x_3 n_3), \tag{2.24}$$
$$\mathbf{r}_3(\mathbf{n}) = (\Delta x_1 n_1, \Delta x_2 n_2, \Delta x_3 (n_3 + 1/2)). \tag{2.25}$$

Furthermore, it is useful to define

$$\mathbf{r}'_1(\mathbf{n}) = (\Delta x_1 (n_1 - 1/2), \Delta x_2 n_2, \Delta x_3 n_3), \tag{2.26}$$
$$\mathbf{r}'_2(\mathbf{n}) = (\Delta x_1 n_1, \Delta x_2 (n_2 - 1/2), \Delta x_3 n_3), \tag{2.27}$$
$$\mathbf{r}'_3(\mathbf{n}) = (\Delta x_1 n_1, \Delta x_2 n_2, \Delta x_3 (n_3 - 1/2)), \tag{2.28}$$

to keep the notations as simple as possible.
Replacing the integral over space by a sum with respect to all lattice nodes and using the definitions above, a discretized approximation of the functional is formulated as

$$\frac{\mathcal{F}}{\Delta V} = \frac{1}{2}\sum_{\mathbf{n}}\sum_{\alpha=1}^{3} E_\alpha^2(\mathbf{r}_\alpha(\mathbf{n})) + \sum_i \sum_{\mathbf{n}} c_i(\mathbf{r}_0(\mathbf{n}))\ln c_i(\mathbf{r}_0(\mathbf{n})). \tag{2.29}$$

Discretizing the divergence operator by a midstep finite–difference scheme

$$(\nabla\cdot\mathbf{E})(\mathbf{r}_0(\mathbf{n})) = \sum_{\alpha=1}^{3}\frac{1}{\Delta x_\alpha}\big(E_\alpha(\mathbf{r}_\alpha(\mathbf{n})) - E_\alpha(\mathbf{r}'_\alpha(\mathbf{n}))\big), \tag{2.30}$$

Gauss' law is written as

$$\sum_{\alpha=1}^{3}\frac{1}{\Delta x_\alpha}\big(E_\alpha(\mathbf{r}_\alpha(\mathbf{n}) - E_\alpha(\mathbf{r}'_\alpha(\mathbf{n})\big) = \sum_i z_i c_i(\mathbf{r}_0(\mathbf{n}))\,. \tag{2.31}$$

Similarly the normalization condition for the amount of ionic species i is discretized as

$$\sum_{\mathbf{n}} c_i(\mathbf{r}_0(\mathbf{n})) = \frac{N_i}{\Delta V}. \tag{2.32}$$

Since the orthorhombic lattice is not necessarily cubic, i. e. $\Delta x_1 \neq \Delta x_2 \neq \Delta x_3$ is possible, it is useful to re–formulate Gauss' law in terms of fluxes,

$$\phi_1 = E_1\Delta x_2\Delta x_3, \tag{2.33}$$
$$\phi_2 = E_2\Delta x_3\Delta x_1, \tag{2.34}$$
$$\phi_3 = E_3\Delta x_1\Delta x_2, \tag{2.35}$$

and

$$\sum_{\alpha=1}^{3}\big(\phi_\alpha(\mathbf{r}_\alpha(\mathbf{n}) - \phi_\alpha(\mathbf{r}'_\alpha(\mathbf{n})\big) = \Delta V\sum_i z_i c_i(\mathbf{r}_\alpha(\mathbf{n}))\,. \tag{2.36}$$

The advantage of this formulation is the simplification in the relaxation steps of the electric field, discussed in Sec. 2.3.2.

2.3. Algorithm

As mentioned previously, the numerical minimization procedure consists of the iterative relaxation of the degrees of freedom of the free energy functional, namely the concentration fields and the electric fields. The procedure starts from an arbitrary initial configuration of the discretized fields, only restricted by the requirement that this configuration satisfies the constraints. The iterative procedure then performs successive local changes in the electric fields and the concentrations such that the constraints are rigorously conserved. These moves can be performed in such a way that the functional decreases in every time step, and does that in an optimal fashion. As already shown in Sec. 2.1, the free energy landscape has a simple structure, and hence this procedure will run always into the global minimum. The algorithm is schematically illustrated by Fig. 2.1 and discussed in detail in the following sections.

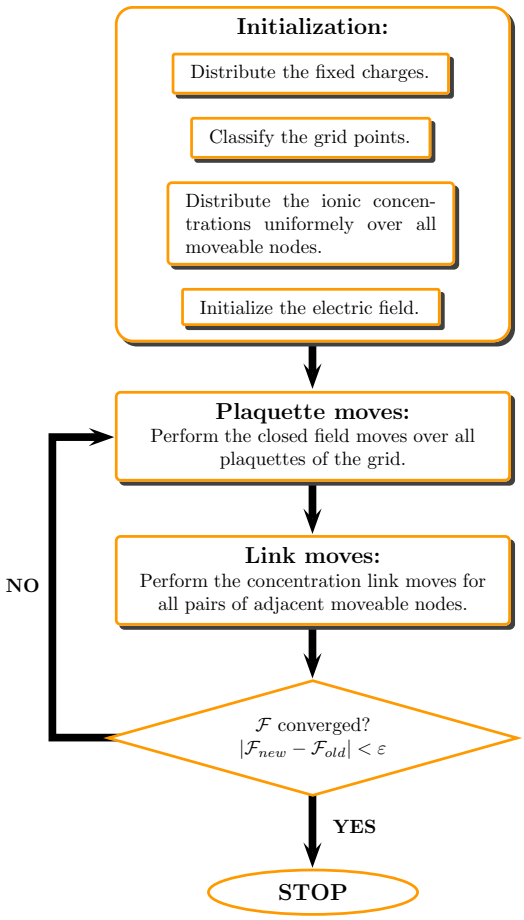

Figure 2.1.: Illustration of the iterative Poisson–Boltzmann equation solver.

2.3.1. Initialization

In the beginning, ionic species and fixed charges have to be distributed over the grid. Usually fixed charges are associated with surfaces (here this is the surface charge density of a colloidal sphere), and hence elements of the surface charge density have to be mapped to volume elements and can therefore be associated with some nodes. One way for distributing these charges to the nodes is to divide the surface charge density into small "partial charges", located at nodes near the surface.

In a second step, the grid points should be classified in *"movable"* and *"fixed"* nodes, i. e. those grid points associated with fixed charges or embedded in a compact region of a closed surface are marked as "fixed", all other grid points representing the volume where ions can move are classified as "movable".

Initially, each ionic species is uniformly distributed over those "movable" nodes. The amount of counterions is determined by the amount of fixed charges and the charge neutrality condition.

When all charges are distributed and the charge neutrality condition is satisfied, the electric field must be initialized. It is important that this is done such that Gauss' law will be fulfilled. In one dimension this can be easily done by summation of the charge density of all preceding grid nodes. Consider a charge density satisfying the charge neutrality condition, discretized on a one-dimensional chain of grid nodes located at $n\Delta x$, and closed via periodic boundary conditions. Consistent with the Yee discretization the electric fields should be located at $(n+1/2)\Delta x$. Now, starting with $E(-0.5\Delta x)$ and setting

$$E(-0.5\Delta x) = 0\,, \tag{2.37}$$

and summing subsequently

$$E((n+0.5)\Delta x) = E((n-0.5)\Delta x) + \Delta x\,\rho(n\Delta x)\,, \tag{2.38}$$

results in a one dimensional solution of Gauss' law. The combination of charge neutrality and periodic boundary conditions ensures a consistent closure of the loop. This method can be generalized to three spatial dimensions by means of a recursion over all dimensions [27].
First the lattice is decomposed into a set of planes perpendicular to the x_1–axis and it is required that E_1 takes the same identical value for all links with identical x_1–coordinate. Replacing the charge density by a plane average charge density $\langle\rho\rangle(n_1\Delta x_1)$ the iterative method above can be performed. Then each plane is decomposed into a sequence of lines, perpendicular to the x_1– and the x_2–axis, and the same procedure is again applied to obtain the field

in x_2–direction. The charges which occur here are the line averages, where the plane averages have been subtracted (the latter have already been taken into account via E_1). Finally, the lines are decomposed into sites, and E_3 is determined from the remaining charges where both line and plane averages have been subtracted.
Although Gauss' law is satisfied, this configuration violates Eq. (2.10c). However, since the iterative procedure runs into the one and only minimum this curl is removed by the relaxation method. Alternatively the Poisson equation can be solved once numerically for initialization.

2.3.2. Plaquette Moves

For the changes of the transversal component of the electric field, closed loops on the faces of the unit cells are considered. For a rectangular lattice, these plaquettes are spanned by four lattice sites and their associated links. The loops are designed such that the flux on each of the corresponding links is changed by the same amount. Since the net flux entering and leaving each node remains unchanged, Gauss' law is still satisfied.

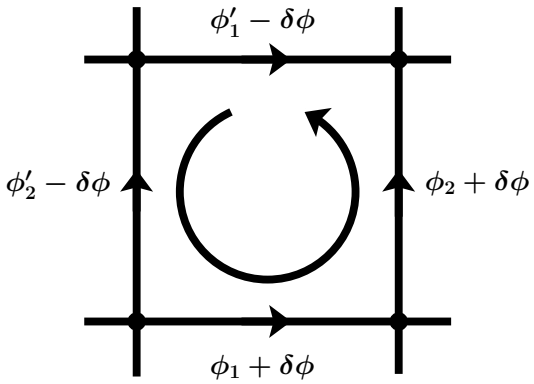

Figure 2.2.: Rotational moves for field updates on all plaquettes.

Such a rotational move is sketched by Fig. 2.2. Consider for example a loop with a sequence of fields E_1, E_2, E_1', E_2' and corresponding fluxes ϕ_1, ϕ_2, ϕ_1', ϕ_2' perpendicular to the 3-axis. The fields are positive when aligned with the corresponding link direction. The field updates are given by

$$E_1 \rightarrow E_1 + \delta E_1, \tag{2.39}$$
$$E_2 \rightarrow E_2 + \delta E_2, \tag{2.40}$$
$$E_1' \rightarrow E_1' + \delta E_1', \tag{2.41}$$
$$E_2' \rightarrow E_2' + \delta E_2'. \tag{2.42}$$

Since the flux changes entering a node also have to leave it, these field changes have to satisfy the condition

$$\begin{aligned} \delta\phi_1 &= \Delta x_2 \Delta x_3 \delta E_1 = \delta\phi, && (2.43)\\ \delta\phi_2 &= \Delta x_1 \Delta x_3 \delta E_2 = \delta\phi, && (2.44)\\ \delta\phi_1' &= \Delta x_2 \Delta x_3 \delta E_1' = -\delta\phi, && (2.45)\\ \delta\phi_2' &= \Delta x_1 \Delta x_3 \delta E_2' = -\delta\phi. && (2.46) \end{aligned}$$

Apart from that, $\delta\phi$ can be chosen arbitrarily without violating the Gauss' law. The rotational move results in a change of the functional by

$$\begin{aligned} \delta\mathcal{F}\,\Delta V &= \frac{1}{2}\Delta x_1^2 \left[(\phi_1+\delta\phi)^2 - \phi_1^2 + (\phi_1'-\delta\phi)^2 - \phi_1'^2\right] && (2.47)\\ &+ \frac{1}{2}\Delta x_2^2 \left[(\phi_2+\delta\phi)^2 - \phi_2^2 + (\phi_2'-\delta\phi)^2 - \phi_2'^2\right] \\ &= (\Delta x_1^2 + \Delta x_2^2)\delta\phi^2 + \left[\Delta x_1^2(\phi_1-\phi_1') + \Delta x_2^2(\phi_2-\phi_2')\right]\delta\phi \\ &= (\Delta x_1^2 + \Delta x_2^2)\delta\phi^2 + \Delta V\left[\Delta x_1(E_1-E_1') + \Delta x_2(E_2-E_2')\right]\delta\phi\,. \end{aligned}$$

Minimizing this functional change, one obtains an optimal value for the change in the fluxes[2]

$$\delta\phi = \frac{1}{2}\frac{\Delta V}{\Delta x_1^2 + \Delta x_2^2}\left[\Delta x_1(E_1'-E_1) + \Delta x_2(E_2'-E_2)\right]\,. \qquad (2.48)$$

2.3.3. Link Moves

Local concentration moves are performed between two nodes connected by a single link, as sketched in Fig. 2.3.

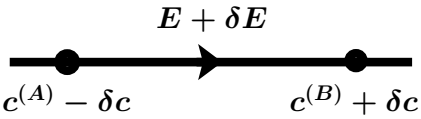

Figure 2.3.: Concentration moves for all adjacent movable nodes.

A certain amount of the concentration of an ionic species with valence z is moved from one lattice site $\mathbf{r}_0^{(A)}$ to its neighbor $\mathbf{r}_0^{(B)}$,

$$\begin{aligned} c^{(A)} &\rightarrow c^{(A)} - \delta c, && (2.49)\\ c^{(B)} &\rightarrow c^{(B)} + \delta c. && (2.50) \end{aligned}$$

[2]Note that in our paper [50] a small error occurred at this point, i. e. the sign within the bracket must be a '+'.

This update conserves the charge neutrality and the mass conservation condition, and since the amount of concentration on a node must have a positive value, δc must satisfy the condition

$$-c^{(B)} \leq \delta c \leq c^{(A)}. \tag{2.51}$$

By updating the electric flux accordingly, Gauss' law is kept conserved. Suppose E is the electric field located on the link connecting $\mathbf{r}_0^{(A)}$ with $\mathbf{r}_0^{(B)}$ and Δl is the length of this link. The electric flux ϕ according to E is given by

$$\phi = \frac{\Delta V}{\Delta l} E. \tag{2.52}$$

From Gauss' law one obtains

$$\delta\phi = -\Delta V \, z \, \delta c \,, \tag{2.53}$$

or

$$\delta E = -\Delta l \, z \, \delta c \,. \tag{2.54}$$

This results in a change of the functional value of

$$\begin{aligned} \frac{\delta \mathcal{F}}{\Delta V} &= \frac{1}{2}\left\{(E+\delta E)^2 - E^2\right\} \\ &+ \left(c^{(A)} - \delta c\right) \ln\left(c^{(A)} - \delta c\right) - c^{(A)} \ln c^{(A)} \\ &+ \left(c^{(B)} + \delta c\right) \ln\left(c^{(B)} + \delta c\right) - c^{(B)} \ln c^{(B)} \\ &= \left(E + \frac{1}{2}\delta E\right) \delta E - \delta c \ln\left(\frac{c^{(A)} - \delta c}{c^{(B)} + \delta c}\right) \\ &+ c^{(A)} \ln\left(1 - \frac{\delta c}{c^{(A)}}\right) + c^{(B)} \ln\left(1 + \frac{\delta c}{c^{(B)}}\right) . \end{aligned} \tag{2.55}$$

An optimal value for the change in the concentrations is obtained again from the minimization of the functional change. This extremization results in a nonlinear equation,

$$\delta c = \frac{c^{(A)} - c^{(B)} \exp[-z \, \Delta l \, (E - z \, \Delta l \, \delta c)]}{1 - \exp[-z \, \Delta l \, (E - z \, \Delta l \, \delta c)]} \,, \tag{2.56}$$

which must be solved numerically. This can be either done by a simple bisection or secant method, or computationally more efficient, by a Newton method. Therefore one may introduce

$$c_+ = \frac{1}{2}\left(c^{(A)} + c^{(B)}\right), \tag{2.57}$$

$$c_- = \frac{1}{2}\left(c^{(A)} - c^{(B)}\right), \tag{2.58}$$

$$\xi = \frac{1}{2} z \, \Delta l \, (z \, \Delta l \, \delta c - E). \tag{2.59}$$

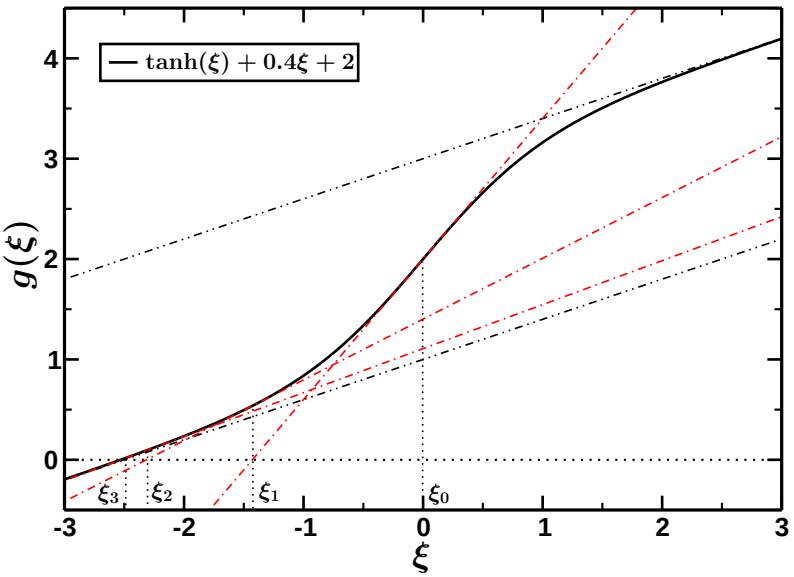

Figure 2.4.: Graphical illustration of the Newton method.

Using these variables, Eq. (2.56) is transformed to

$$g(\xi) = 0, \tag{2.60}$$

with

$$g(\xi) = \tanh \xi + \frac{2\xi}{(z\,\Delta l)^2\, c_+} + \frac{E}{z\,\Delta l\, c_+} - \frac{c_-}{c_+}\,. \tag{2.61}$$

The derivative of $g(\xi)$ is given by

$$g'(\xi) \equiv \frac{\partial g(\xi)}{\partial \xi} = \frac{1}{\cosh^2(\xi)} + \frac{2}{(z\,\Delta l)^2\, c_+}, \tag{2.62}$$

which shows that $g(\xi)$ is a monotonous function, and hence Eq. (2.60) has exactly one unique solution. Since $-1 < \tanh \xi < 1$, the solution will satisfy the condition

$$-1 < -\frac{2}{(z\,\Delta l)^2\, c_+}\xi - \frac{E}{z\,\Delta l\, c_+} + \frac{c_-}{c_+} < 1, \tag{2.63}$$

which is equivalent to the condition (2.51). The Newton method

$$\xi^{(n+1)} = \xi^{(n)} - \frac{g(\xi^{(n)})}{g'(\xi^{(n)})}, \tag{2.64}$$

starting at

$$\xi^{(0)} = 0\,, \tag{2.65}$$

will always converge due to the shape of $g(\xi)$, as sketched in Fig. 2.4.

2.4. Numerical Results

In this section, the method is demonstrated and tested for two numerical examples. In a first test system the fixed charges are distributed in two infinite parallel plates. If only one ionic species occur, an analytical solution for this problem can be calculated. We compare the numerical results with this analytical expression. The second system is a single charged colloidal sphere in the center of a cubic box. The choice of parameters is inspired by previous studies on electrokinetics done in our group [30–32] and are therefore quoted here in unscaled "physical" units, where λ_0 denotes the elementary length scale (this length scale coincides the Lennard–Jones diameter in the simulations). All numerical runs below are done with a Bjerrum length of $l_B = 1.3\lambda_0$. The fixed charge distribution consists in positive charges only, and only one ionic species, the monovalent counterions with valence $z = -1$, is distributed in the system. The numerical results are also given in "physical units".
Furthermore, possible speedups of the code, based on the full solution of the Poisson equation and on preconditioning of the concentration fields are discussed.
In a last subsection, we discuss briefly the possibility of calculating the radial distribution function of multi–colloidal systems, with fully non-linear Poisson–Boltzmann interaction.

2.4.1. Double Plane

Consider the fixed charges to be distributed in two infinite parallel plates, perpendicular to the x_1-axis, located at $x_1 = -d$ and $x_1 = +d$. The surface charge density in each plate is given by σ and only one ionic species with concentration $c(\boldsymbol{r})$ and valence $z = -1$ is distributed in the spatial region between the two plates. Charge neutrality is given by

$$\int_S d\Omega\, \sigma + z \int_V dV\, c(\boldsymbol{r}) = 0\,. \tag{2.66}$$

This problem is effectively one–dimensional and its analytic solution is well–known [63]. In reduced units, the one–dimensional Poisson–Boltzmann equation is

$$\begin{aligned} \frac{d^2\psi}{dx_1^2} &= -Az\exp(-z\psi) \\ &= -\frac{d}{d\psi}\big(-A\exp(-z\psi)\big)\,, \end{aligned} \tag{2.67}$$

which is isomorphic to Newton's equation of motion of a particle with unit mass, spatial coordinate ψ and where x_1 corresponds to the time. Hence, the

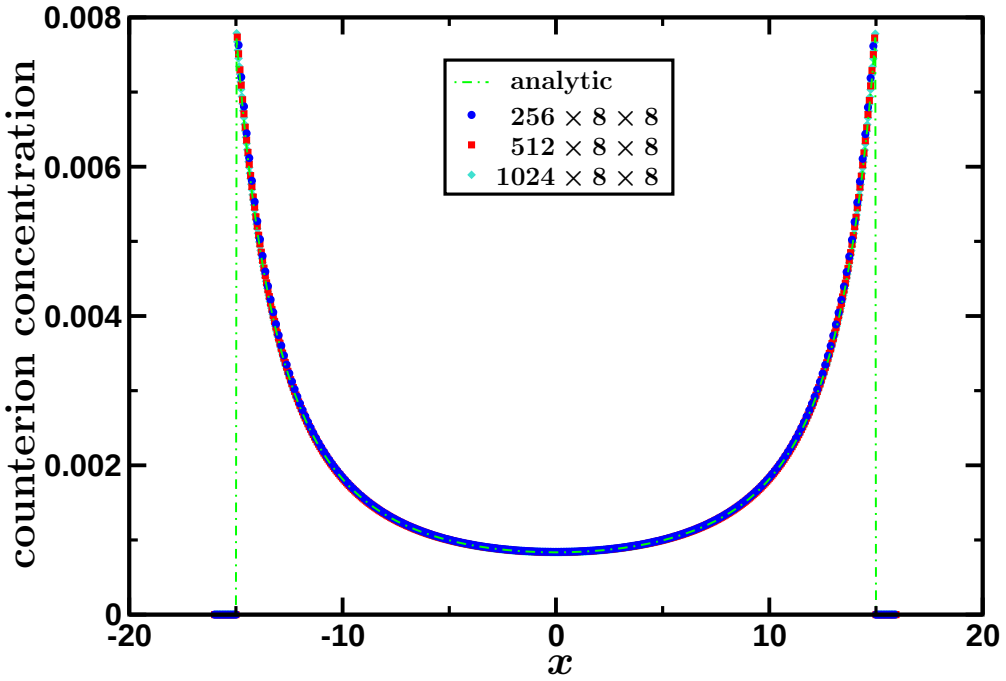

Figure 2.5.: Counterion concentration profiles for the charged double plane for various grid resolutions and the analytic expression, Eq. (2.73).

corresponding energy conservation is given by

$$\frac{1}{2}\left(\frac{d\psi}{dx_1}\right)^2 - A\exp(-z\psi) = K\,, \tag{2.68}$$

with integration constant K. Symmetry dictates $d\psi/dx_1|_{x_1=0} = 0$ and, combining this with the energy conservation plus the normalization $\psi(0) = 0$, results in $K = -A$. Thus one obtains

$$\frac{d\psi}{dx_1} = \pm\sqrt{2A\big(\exp(-z\psi) - 1\big)}\,. \tag{2.69}$$

Focusing on the branch where $d\psi/dx_1 > 0$, this equation is integrated by separation of variables,

$$\begin{aligned} x_1 &= \frac{1}{\sqrt{2A}}\int_0^{\psi(x_1)} \frac{d\psi}{\sqrt{\exp(-z\psi) - 1}} \\ &= -\sqrt{\frac{2}{Az^2}}\arctan\sqrt{\exp(-z\psi) - 1}\,, \end{aligned} \tag{2.70}$$

$$\psi = \frac{2}{z}\ln\cos\left(z\sqrt{\frac{A}{2}}x_1\right)\,. \tag{2.71}$$

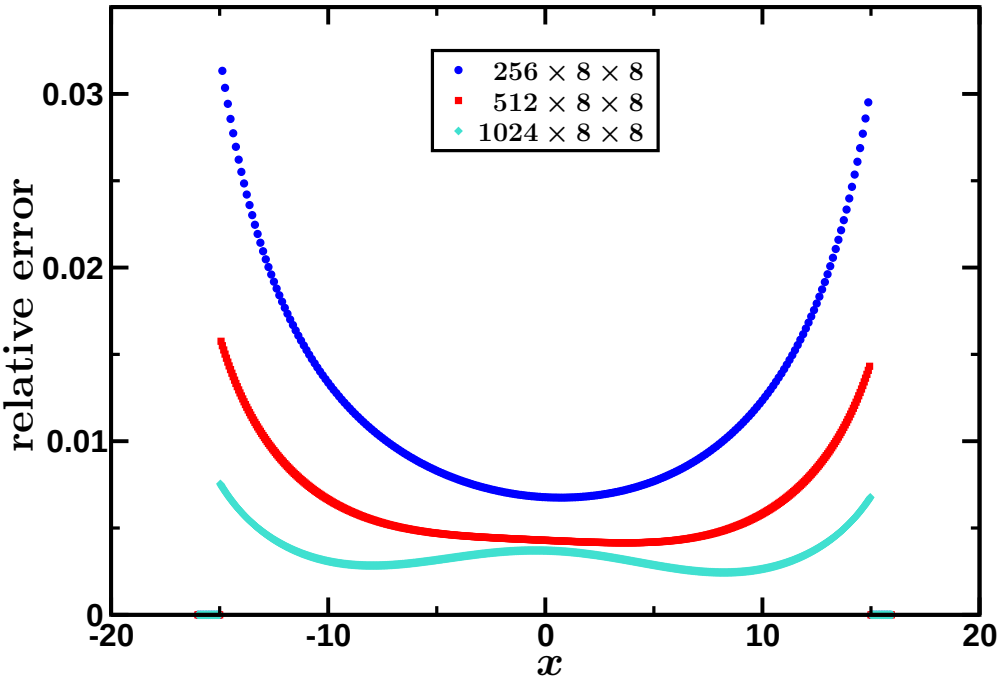

Figure 2.6.: Relative errors of the counterion concentration profiles for different grid resolutions as indicated by the legend.

Replacing A by a more suitable parameter $s := \sqrt{A/2}\, zd$, Eq. (2.71) is written as

$$\psi \;=\; \frac{2}{z} \ln \cos\left(s \frac{x_1}{d}\right) \,, \tag{2.72}$$

and the counterion concentration is obtained by differentiating twice,

$$c(x) = \frac{2}{z^2} \frac{s^2}{d^2} \cos^{-2}\left(s \frac{x_1}{d}\right) \,. \tag{2.73}$$

Finally, an expression for the parameter s is obtained from the electrostatic boundary condition

$$\sigma \;=\; \left.\frac{d\psi}{dx_1}\right|_{x_1=d} \;=\; -\frac{2}{z}\frac{s}{d} \tan s \,. \tag{2.74}$$

This, however, must be solved numerically.
For the numerical solution the amount of fixed charges, Ze, is distributed homogeneously in two planes, located in a periodic box of size $l_1 \times l_2 \times l_3$, at $x_1 = \pm d$. The surface charge density is then given by $\sigma = Ze/(2l_2l_3)$. Note that the dimension of the box in x_1 direction must be somewhat larger than $2d$, in order to be able to apply the periodic boundary conditions. The corresponding amount of counterions is initially distributed homogeneously between the two plates. Since periodic boundary conditions are applied in x_2 and x_3 direction, the system is translationally invariant, and hence the solution is effectively

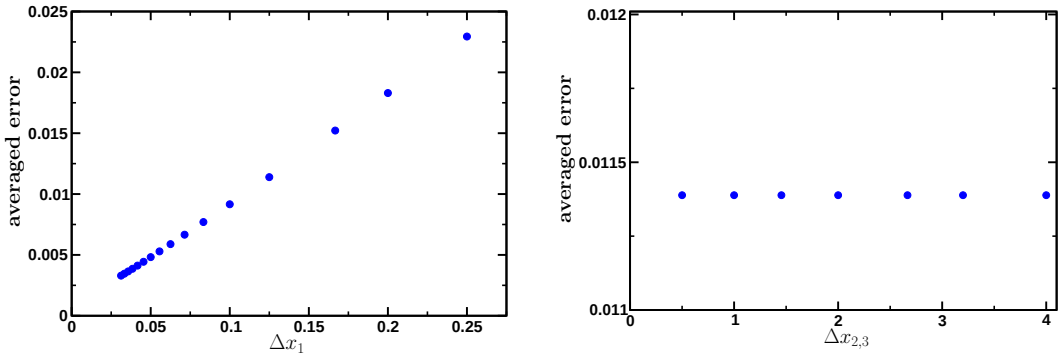

Figure 2.7.: Averaged error of the counterion concentration as function of the lattice spacing in x_1–direction Δx_1 (left) and in $x_{2,3}$–direction (right).

one–dimensional. The calculations were performed for $l_1 = l_2 = l_3 = 32\lambda_0$, $2d = 30\lambda_0$, $Z = 60$ and different lattice spacings. A quite good agreement between the numerical and the analytic solution can be observed, as shown in Fig. 2.5. This agreement increases with the grid resolution in x_1–direction, which is observed from the relative error,

$$\text{relative error} = \left| \frac{c_{ana}(x_1) - c_{num}(x_1)}{c_{ana}(x_1)} \right| . \tag{2.75}$$

Here, c_{ana} denotes the analytic expression for the counterion concentration and c_{num} the numerical results. Fig. 2.6 shows the relative error for three different grid resolutions, namely $256 \times 8 \times 8$, $512 \times 8 \times 8$ and $1024 \times 8 \times 8$ lattice sites. More systematically, the first image of Fig. 2.7 shows the averaged error as function of the lattice spacing in x_1–direction, showing linear behavior, i. e. first order accuracy. Increasing the resolution in the orthogonal directions has no effect, as expected (see Fig. 2.7, right image).

2.4.2. Colloidal Sphere in a Box

The second numerical example, and for our purposes the more important one, is the case of a single colloidal charged sphere of radius R, located in the center of a periodic box of size $l_1 \times l_2 \times l_3$. The sphere has a total charge of Ze, uniformly distributed over its surface. In the computational model, the fixed charge has to be interpolated onto the nodes of the grid. The simplest way is to generate $M \gg 1$ random points distributed uniformly over the surface of the particle, and a volume charge density $Ze/(M\Delta V)$ is added for each point to its closest grid node. These nodes as well as all nodes embedded in the particle region are marked as fixed. The calculations were performed for a cubic box of size $l_1 = l_2 = l_3 = 30\lambda_0$. A colloidal sphere with radius $R = 3\lambda_0$

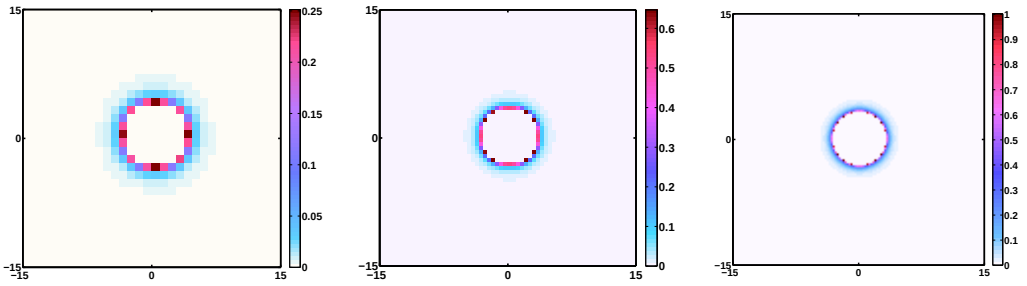

Figure 2.8.: Counterion concentration for a charged colloidal sphere for grid resolutions 32^3, 64^3 and 128^3 lattice sites.

and valence $Z = 60$ was placed at the center of the box, and the counterions were initially distributed uniformly over the outer space. Tab. 2.1 summarizes performance results for an implementation of the present algorithm in its basic formulation, written in C, compared to an implementation in C++, written by M. Baptista[64]. In both cases the exit condition for the iterative procedure was given by a change in the functional of less than 10^{-8}. The runs were performed on an Intel Core 2 Duo E6600 FSB 1022 2x2.4 Ghz with 4GB RAM.

Fig. 2.8 shows two–dimensional cuts of the counterion concentration profile in a plane perpendicular to the x_3–axis for different grid resolutions. In Fig. 2.9 one–dimensional cuts along the x_1–direction of the computational box are presented. We see that close to the surface of the sphere discretization effects due to the cubic box are quite large; nevertheless the data for 256^3 grid points seem reasonable well converged to the continuum limit. The concentration profiles in (100)–direction and along the (111)–diagonal are very close (see Fig. 2.10). Hence, one should expect that the solution is essentially identical to one obtained with strict spherical symmetry. This is indeed the case, as comparison with the solution of the isotropic Poisson–Boltzmann cell model shows (see Fig. 2.9). In the latter, the cubic simulation cell is replaced by a spherical cell of the same volume, and the Poisson–Boltzmann equation is solved for the radial coordinate. The numerical method we used was implemented by B. Dünweg and is described in detail in the appendix.

The profile determined by the cell model agrees quite well with the one obtained from the present algorithm for the finest resolution.

Nevertheless, the solution for the cubic geometry does exhibit some anisotropy that, by construction, is absent in the cell model. This is essentially not visible in the concentration profile, but clearly observable in the profile of the electric field, as shown in Fig. 2.11, where the decays in (100) and (111)–direction are compared.

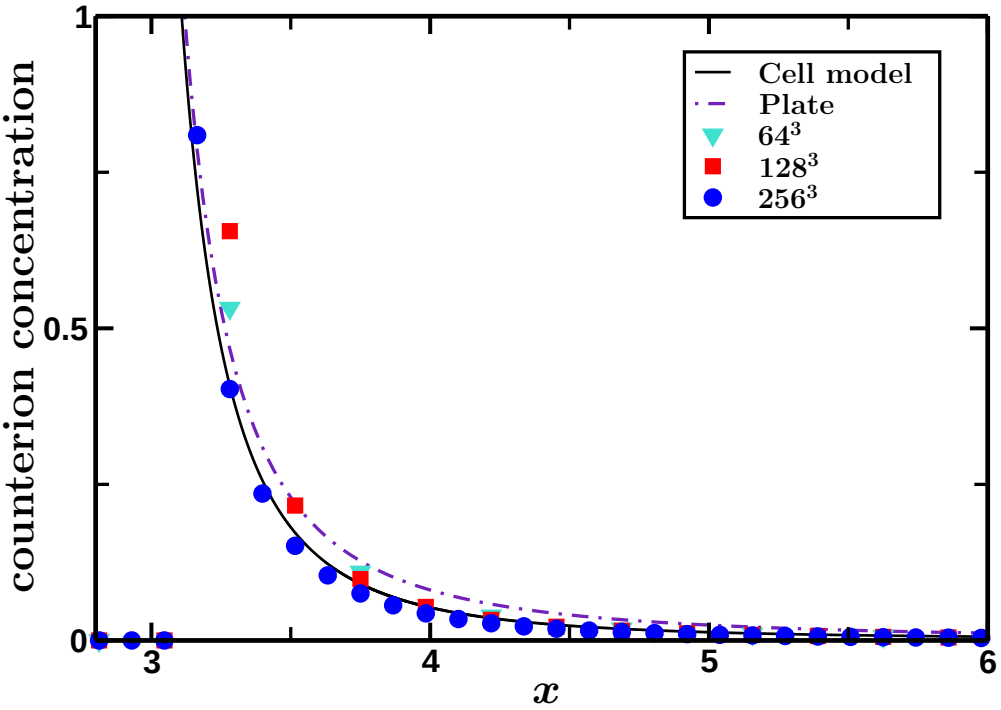

Figure 2.9.: Counterion concentration profile of a colloidal sphere along the x_1–axis for various grid resolutions. The solid line is the solution of the one–dimensional isotropic cell model. The dash–dotted line shows the counterion concentration for a two–dimensional charged plate with the same surface charge density as the colloidal sphere.

	C++ - Version		C - Version	
Grid Resolution	Time (s)	Memory (%)	Time (s)	Memory (%)
$32 \times 32 \times 32$	30	0.2	30	0.1
$64 \times 64 \times 64$	836	0.5	844	0.5
$128 \times 128 \times 128$	20701	2.9	20574	3.6
$256 \times 256 \times 256$	381371	22.5	389030	24.4
	Iterations	Functional	Iterations	Functional
$32 \times 32 \times 32$	642	1114.83	634	1113.88
$64 \times 64 \times 64$	2265	1024.14	2226	1024.19
$128 \times 128 \times 128$	7206	957.63	7038	957.63
$256 \times 256 \times 256$	20323	923.85	19711	924.70

Table 2.1.: Performance data for the basic C implementation compared to the C++ code of M. Baptista[64].

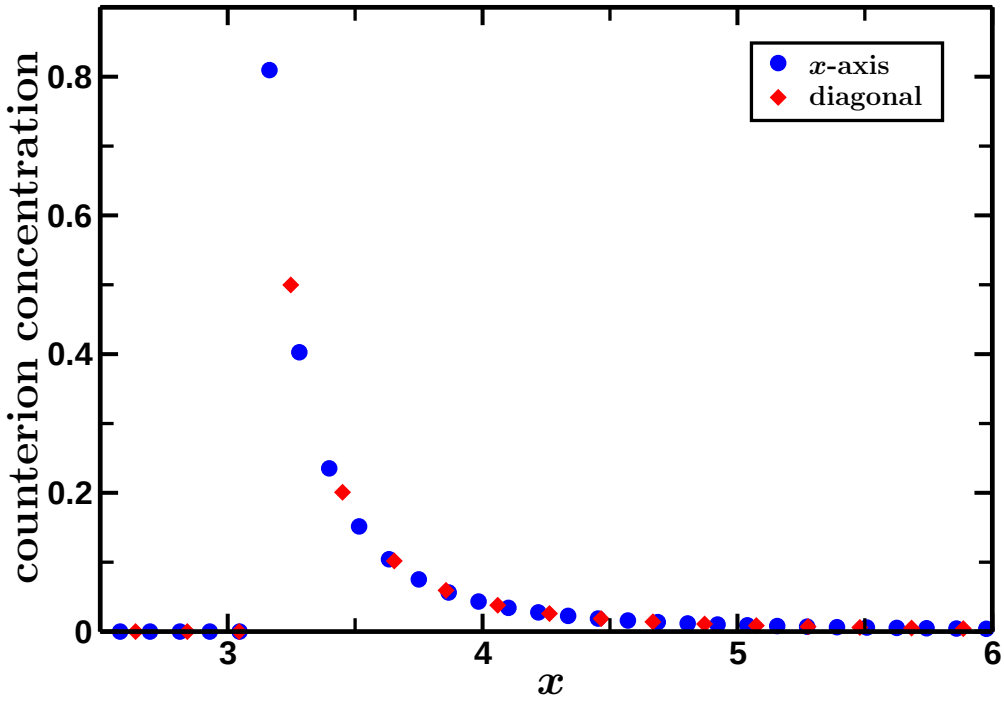

Figure 2.10.: Counterion concentration profile of a colloidal sphere along the x_1–axis and along the (111)–diagonal for a grid resolution of 256^3.

If the curvature of the sphere is not too strong, one may view the geometry as effectively planar in the immediate vicinity of the colloidal surface. For the planar surface, the solution is characterized by the so–called Gouy–Chapman length λ_{GC}[65]. The planar solution is also shown in Fig. 2.9 (dash–dotted line) and it also agrees reasonably well with the profiles from our algorithm. In our reduced units, the planar solution is given by

$$c(x) \;=\; \frac{2}{z^2}\frac{1}{(x+\lambda_{GC})^2}\,, \tag{2.76}$$

where

$$\lambda_{GC} = -\frac{2}{\sigma z} \tag{2.77}$$

is the Gouy–Chapman length (see Appendix A.2).
In the example above, this length has the value $\lambda_{GC} = 0.044$. This should be compared to the colloid radius (~ 0.5728 in reduced units) and the lattice spacing ($\sim$ 0.022 for the 256^3 grid). Altogether, the data indicate that a lattice spacing of roughly half a Gouy–Chapman length is small enough to yield a reasonably well converged solution.

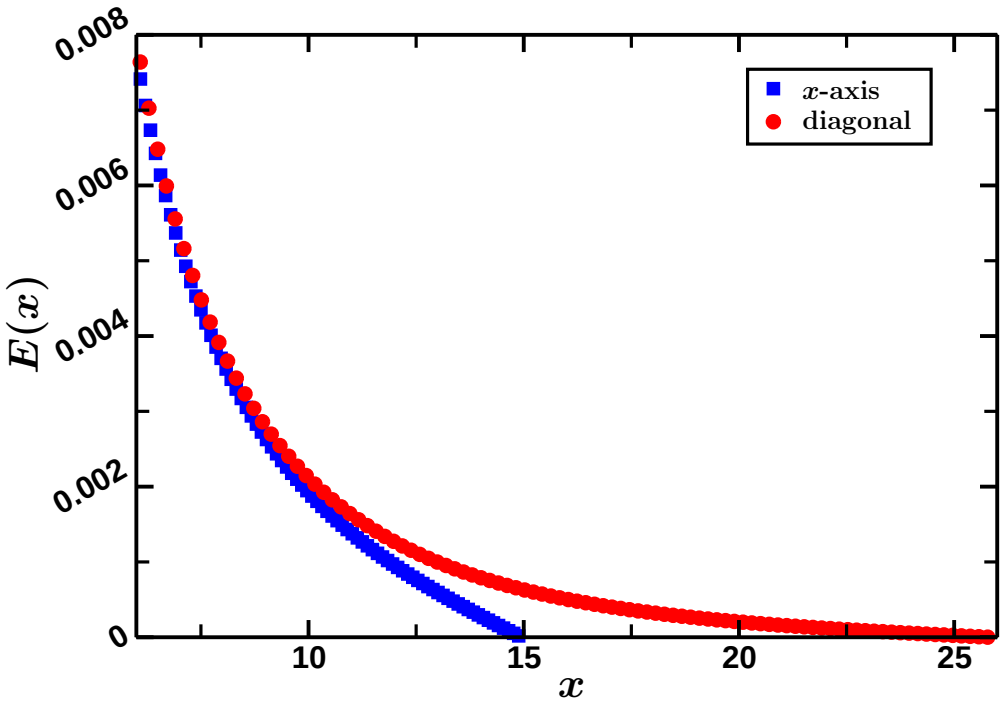

Figure 2.11.: Electric field E along x_1–axis and along the (111)–diagonal for a grid resolution of 256^3 lattice sites.

2.4.3. Speedups

Before describing modifications of the procedure to gain a speedup, one observation should be noticed for practical reasons, which we have made during testing and comparing the two implementations (C and C++). While implementing the code, one should take care of the order of operations, namely the order of computing the concentration moves in connection with the way of walking over the lattice. It is important to perform the link move first in that direction of the link which will be updated next; otherwise one would "shovel" concentration out of the way of the walker. The data presented in Tab. 2.1 gained by implementations, which follow this principle, i. e. the moves are first performed in x_1–direction, then in x_2 and finally in x_3–direction, while the order of updating the single links is given in the same way. For example, a change in the order of the directions from (x_1, x_2, x_3) to (x_3, x_2, x_1) but still keeping the way of walking through the grid, results in increasing the numbers of iterations to 1416 instead of 634 for the 32^3 grid.

Apart from that, one sees from Tab. 2.1 that the number of necessary iterations and the amount of CPU time is quite large. In the following some strategies to speed up the procedure without sacrificing the basic formulation that provides

	Pure FFT	
Grid Resolution	Time (s)	Number of iterations
$32 \times 32 \times 32$	14	297
$64 \times 64 \times 64$	409	1150
$128 \times 128 \times 128$	12180	4427
$256 \times 256 \times 256$	354783	16766
	FFT + pre–conditioner	
Grid Resolution	Time (s)	Number of iterations
$32 \times 32 \times 32$	11	242
$64 \times 64 \times 64$	331	888
$128 \times 128 \times 128$	9744	3421
$256 \times 256 \times 256$	273538	12430

Table 2.2.: Performance data for our two speeded–up implementations. Note that the data for the runs with pre–conditioner mean (i) CPU time for the overall procedure, and (ii) number of iterations in the final run with the finest resolution.

intrinsic stability will be discussed.

One possibility is to remove the rotational component of the electric field *not* by means of plaquette moves but rather by solving the Poisson equation. This can be efficiently done by the FFT–based method (see Sec. 1.4). The advantage is that, in contrast to the plaquette moves, a single lattice sweep does not only reduce the rotational component of the electric field, but rather eliminates it completely. Therefore the FFT promises to increase the convergence speed. It should be noted that the link moves, which update concentrations and the fields simultaneously, remain unchanged, such that the procedure still stays strictly on the constraint surface.

In a first implementation, we eliminated all plaquette moves and replaced them with FFT sweeps done during initialization and subsequently after every 25th link sweep. As seen from Tab. 2.2, this improves the efficiency roughly by a factor of $1.1 \ldots 2$. These results were obtained on the same computer as those of Tab. 2.1.

Furthermore, we can tackle the slowdown that comes from the fact that the ions have to be moved by site–by–site hops throughout the system ("hydrodynamic slowing down"). To this end, we first run the calculation on a rather coarse grid (in practice, we started with $8 \times 8 \times 8$), such that most of the necessary "mass transport" is already done in that preliminary run. Starting from there, we go to a finer grid (in practice, we reduced the lattice spacing in all three directions by a factor of two) and linearly interpolate the output of the previous run onto that grid. Then the free energy is relaxed again; the output of that

run is interpolated onto a yet finer grid, and so on. Obviously, this can be done rather easily by a straightforward recursion, until the desired grid resolution is reached. The runs before the finest resolution may then be viewed as a "pre–conditioner". This optimization yields another speedup by roughly 25%, as seen from Tab. 2.2.
These two rather simple optimizations do not interfere with the basic data structure of the simple Cartesian grid. We expect that further optimizations which are however much more complicated such as more sophisticated multi-grid methods, adaptive mesh refinement or the discretization in terms of finite-element-type unstructured grids will yield further substantial speedups. However, this was not attempted here, and is rather mentioned as a suggestion for future projects.

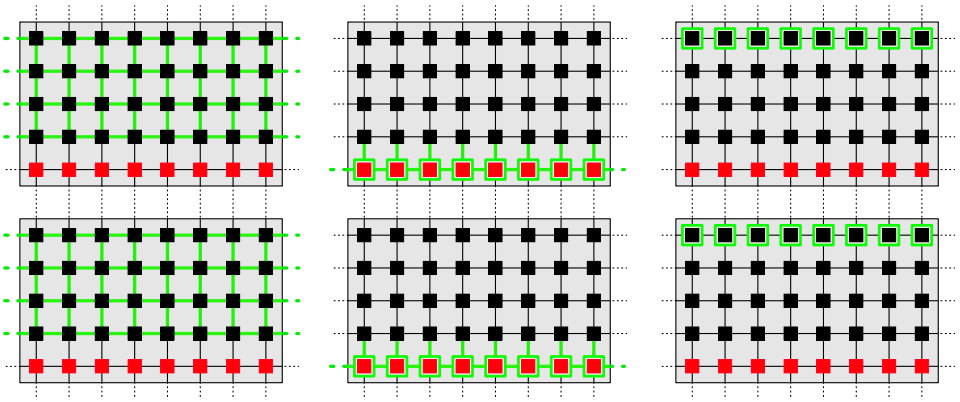

Figure 2.12.: Illustration of the decomposition and the updates for the parallel version of the PB solver.

Furthermore, the simple structure of the orthorhombic lattice in combination with the highly local structure of the algorithm, enables the opportunity of a simple parallelization of the code. In practice, the computational domain is decomposed in equal slices in direction of the slowly varying index (in our case the x_3–direction). Each slice is taken care of by an individual processor. Since the updates are done along links, an artificial halo layer is added at the bottom of every slice. Every halo layer is a copy of the top layer of the next slice. For one update of the whole grid, two inter-processor communication steps have do be done. One iteration then consists in a first update of the inner links of each slice. Subsequently the concentrations of the top boundary nodes are copied to their equivalent counterpart in the halo regions. After the link updates between the bottom boundary nodes and the connected halo, the concentrations located in the halo are copied to the equivalent nodes at the top boundary of each slice. Thus, the total number of link updates remains the same as in the single–processor implementation, the communication between

the several processes is quite small and the total amount of memory increases moderate.

2.4.4. A Monte Carlo Algorithm for Computing Radial Distribution Functions

In the following a possible application of this method is sketched, namely the possibility to simulate radial distribution functions (rdf) of charge stabilized colloidal suspensions with fully non-linear Poisson–Boltzmann interaction. The current implementation of this part is not parallelized yet, and since the algorithm is still computationally expensive when running on a single processor, the few examples shown in the end of this subsection were only computed with low accuracy and at low volume fraction to gain reasonable statistics.

For the purpose of simulations, the interaction between macro-ions in an ambient fluid containing micro-ions is usually replaced by an effective pair potential V^{eff} of the Yukawa form, i. e. a screened Coulombic interaction. One of the simplest and most used potential is the DLVO (Derjaguin–Landau–Verwey–Overbeek) potential [66, 67],

$$V^{eff}(r) = \begin{cases} \infty & r < 2R \\ \frac{1}{(4\pi)^2 l_B \kappa} \frac{Z^2}{(1+R)^2} \frac{e^{-(r-2R)}}{r} & r \geq 2R \end{cases} . \tag{2.78}$$

This expression has been determined by using the Debye–Hückel approximation.
Conversely, our method offers the possibility to take the fully non-linear Poisson–Boltzmann equation into account, and to do that not only for pairs of two macro-ions, but rather to account for the full interaction arising from the Mean–Field theory. The idea is to use the free energy functional (2.11) for an importance sampling Monte Carlo algorithm [68]. First a certain number of colloidal spheres N with charge Ze and radius R is distributed randomly in a box of size $l_1 \times l_2 \times l_3$. The centers of the spheres are located at $\boldsymbol{r}^{(i)}$, $i = 1, \ldots, N$. The box is discretized by a regular grid with lattice spacings Δx_1, Δx_2, Δx_3 and the gridpoints are classified as described in Sec. 2.2. The counterion concentration is initially distributed uniformly over the outer space, and the Poisson–Boltzmann equation is solved initially by the iterative method and the value of the functional $\mathcal{F}$ is stored in memory.
After that we pick randomly a colloid k and move it by a small step $\Delta\boldsymbol{r}$ in a random direction. This one sphere is then again discretized on the lattice. Since now some lattice sites are marked as "fixed" which have been classified as "movable" before, and vice versa, the ion concentration around the moved sphere has also to be re-distributed, such that no concentration is left on

a "fixed" node. Then the Poisson–Boltzmann equation is solved again and a Metropolis step is applied [68], where $\mathcal{F}$ is viewed as Hamiltonian of the system of colloids. Note also that in our reduced units $k_B T = 1$.

An advantage of our formulation of the Poisson–Boltzmann solution is that we already know the local electric field, and thus we are able to calculate the total force $\boldsymbol{F}$ acting on the surface of the sphere, which should be moved. This allows us to do the Monte–Carlo moves using a standard *force-biasing* scheme. Instead of choosing a random direction and a random step size for the displacement of the colloid, we apply a Langevin step via

$$\boldsymbol{r}'^{(i\neq k)} = \boldsymbol{r}^{(i\neq k)}\,, \tag{2.79a}$$

$$\boldsymbol{r}'^{(k)} = \boldsymbol{r}^{(k)} + \tau \boldsymbol{F}(\boldsymbol{r}^{(k)}) + \sqrt{2\tau}\boldsymbol{\xi}\,. \tag{2.79b}$$

Here, τ is a small step size and $\boldsymbol{\xi}$ is a random variable with mean $\langle \xi_i \rangle = 0$ and variance $\langle \xi_i \xi_j \rangle = \delta_{ij}$. Thus, the sphere will move most probably to the "right" direction. But if this force bias is applied, one also has to take care of the Metropolis criterion, such that the condition of *detailed balance* is still satisfied.

The transition probability distribution $T(\boldsymbol{r}'|\boldsymbol{r})$, of making a move from position $\boldsymbol{r}$ to $\boldsymbol{r}'$, is a combination of the probability $A(\boldsymbol{r}'|\boldsymbol{r})$ that the move is accepted and a conditional probability distribution function $\Pi(\boldsymbol{r}'|\boldsymbol{r})$ for choosing a new position $\boldsymbol{r}'$, given an old position $\boldsymbol{r}$,

$$T(\boldsymbol{r}'|\boldsymbol{r}) = \Pi(\boldsymbol{r}'|\boldsymbol{r}) A(\boldsymbol{r}'|\boldsymbol{r})\,. \tag{2.80}$$

The condition of detailed balance then dictates

$$a(\boldsymbol{r}'|\boldsymbol{r}) := \frac{A(\boldsymbol{r}'|\boldsymbol{r})}{A(\boldsymbol{r}|\boldsymbol{r}')} = \frac{\Pi(\boldsymbol{r}|\boldsymbol{r}')P(\boldsymbol{r}')}{\Pi(\boldsymbol{r}'|\boldsymbol{r})P(\boldsymbol{r})}\,, \tag{2.81}$$

where $P(\boldsymbol{r})$ is the Boltzmann distribution. In the Metropolis step a uniform random number in the range of $\rho \in [0, 1)$ is generated and the new position of the particle is accepted if $\rho < \min(1, a(\boldsymbol{r}'|\boldsymbol{r}))$. Since no point is preferred within a given range, the *a priori* probability Π is constant in the case of an unbiased MC update. However, this changes in the case of force bias. Solving Eq. (2.79b) for $\boldsymbol{\xi}$, one obtains

$$\boldsymbol{\xi} = \frac{1}{\sqrt{2\tau}}(\boldsymbol{r}'^{(k)} - \boldsymbol{r}^{(k)} - \tau \boldsymbol{F}(\boldsymbol{r}^{(k)}))\,. \tag{2.82}$$

Knowing that ξ_i are independent Gaussian random numbers with mean 0 and

variance 1, the conditional probability distribution is written as

$$\begin{aligned} & \Pi(\boldsymbol{r}'^{(k)}|\boldsymbol{r}^{(k)}) \qquad (2.83) \\ = \; & \mathcal{N} \exp\Big[-\frac{1}{4\tau}(\boldsymbol{r}'^{(k)} - \boldsymbol{r}^{(k)} - \tau \boldsymbol{F}(\boldsymbol{r}^{(k)}))^2\Big], \end{aligned}$$

$$\begin{aligned} & \Pi(\boldsymbol{r}^{(k)}, \boldsymbol{r}'^{(k)}) \qquad (2.84) \\ = \; & \mathcal{N} \exp\Big[-\frac{1}{4\tau}(\boldsymbol{r}^{(k)} - \boldsymbol{r}'^{(k)} - \tau \boldsymbol{F}(\boldsymbol{r}'^{(k)}))^2\Big]. \end{aligned}$$

Calculating the ratio of the probability functions, the acceptance rate for the force bias MC is given by

$$\begin{aligned} a(\boldsymbol{r}'^{(k)}|\boldsymbol{r}^{(k)}) \; = \; & \exp\Big[-\big\{\mathcal{F}(\{\boldsymbol{r}'\}) - \mathcal{F}(\{\boldsymbol{r}\})\big\} \qquad (2.85) \\ & - \frac{\tau}{4}\big\{\boldsymbol{F}^2(\boldsymbol{r}'^{(k)}) - \boldsymbol{F}^2(\boldsymbol{r}^{(k)})\big\} \\ & - \frac{1}{2}\big\{\boldsymbol{F}(\boldsymbol{r}'^{(k)}) + \boldsymbol{F}(\boldsymbol{r}^{(k)})\big\} \cdot \big\{\boldsymbol{r}^{(k)} - \boldsymbol{r}'^{(k)}\big\}\Big]. \end{aligned}$$

Two radial distribution functions $g(r)$ determined by this "*PB/MC*" method

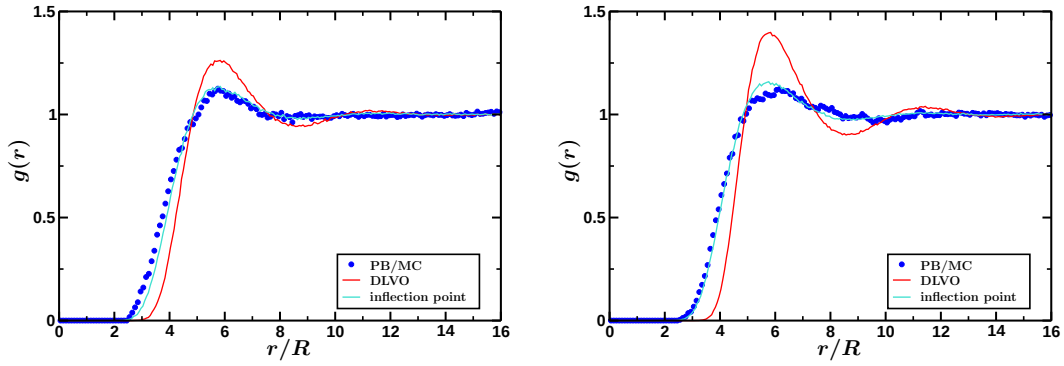

Figure 2.13.: Radial distribution functions for dispersions of colloidal spheres with charge $Z = 20$ (left) and $Z = 30$ (right). The blue circles are results from the MC method described here. The solid lines are results from molecular dynamic simulations based on effective pair potentials (DLVO (red), inflection point criterion (turquoise)).

are presented in Fig. 2.13. We simulated a system of 40 spheres in a cubic box of size $l_1 = l_2 = l_3 = 60\lambda_0$ with periodic boundary conditions. The radius of the spheres were set to $R = 3\lambda_0$ and the Bjerrum length was chosen as $l_B = 1\lambda_0$. The box was discretized by 128^3 lattice sites. The charge of the colloidal spheres was $Z = 20$ for the first image and $Z = 30$ for the

second one. These distribution functions are compared to molecular dynamics results[3] of two systems with different effective pair potentials. The red line was computed for a DLVO interaction (see Eq. (2.78)). These DLVO simulations overestimate the structure of the system. This is not surprising, since the charge in the DLVO potential does not account for ion condensation at the surface of the colloidal sphere, and thus is only valid for extremely low charges [69]. Furthermore we calculated the rdf for a screened potential of the Yukawa form. Here the charge is replaced by an effective charge, determined by the so called inflection point criterion, based on the spherical cell model [69, 70]. In this simple charge renormalization model the nonlinear Poisson-Boltzmann equation is solved in a spherical cell and the accumulated charge curves are analyzed as function of the radial distance. These curves typically show an inflection point and the effective charge is determined by means of this point. This procedure is supposed to mimic the effect of charge condensation at the colloid surface. The radial distribution function obtained by this potential agrees reasonably well with the results of our method. Although the examples shown here are taken only for low accuracy and small systems with low volume fraction, we assume that an optimized version of the method would lead to a rather helpful tool for the quantitative understanding of structural effects in charge stabilized colloidal dispersions (as far as they can be described within Mean–Field theory).

2.5. Electro-Osmotic Flow in a Slit Channel

Most materials associate or dissociate ions, when brought in contact with a liquid, and consequently get charged. Hence, the walls of microchannels typically attract a layer of counterions, compensating this effect. In the following, the simple model of fluid flow in a slit channel, i. e. two infinite plates with distance $2d$ in x_1-direction and homogeneous surface charge density σ, is considered. Additional ions with charge $z_{ion}e$ are dissolved in the fluid. Charge neutrality is satisfied by the presence of counterions with charge $z_{ci}e$. Furthermore, also salt ions can be taken into account.
A constant external electric field, acting parallel to the walls in x_2-direction, causes a net fluid flow, due to the movement of the ions, corresponding to their charges, and friction forces, coupling the ions to the fluid. This net flow is called *electro–osmotic flow*.
The aim of this section is the application of our Poisson–Boltzmann solver to the calculation of the electro–osmotic flow field for unsymmetric[4] ionic solutions.

[3] Thanks to Victor Rühle.

[4] The valence of every ionic species is independent of each other. Charge neutrality of the system is the only restriction on the charges and the concentrations.

The development of this application was originally motivated by the experiments of Jinyu Zhao (AK Butt, MPIP Mainz), who observed electro-osmotic flow of a colloidal suspension in confined geometries when an electric field is acting along the channel direction [71]. Unfortunately, the conditions in the experiments are not ideal. For example, the colloids in the suspension are sedimenting to the bottom of the channel. Friction with the channel wall then results in a rather slow motion of the colloids, and hence to very low electro-osmotic mobilities. Furthermore the parameters of the system are not known precisely, e. g. the ζ-potentials of the channel walls and the colloidal particles. Thus, we were not able to compare the experimental results of J. Zhao with our numerical predictions.

The system is again described in terms of electrostatic potential ψ, ion concentrations c_i, pressure p and flow velocity $\boldsymbol{v}$ and the analysis starts with the electrokinetic equations in the stationary regime and thermal equilibrium as given by Eq. (1.16):

$$\begin{aligned} 0 &= \sum_i z_i c_i + \nabla^2 \psi, && \text{(2.86a)} \\ 0 &= \nabla \cdot \{-D_i \nabla c_i - D_i z_i (\nabla \psi) c_i + \boldsymbol{v} c_i\}, && \text{(2.86b)} \\ 0 &= \nabla \cdot \boldsymbol{v}, && \text{(2.86c)} \\ 0 &= -\nabla p + \frac{2}{3} \nabla^2 \boldsymbol{v} - (\nabla \psi) \sum_i z_i c_i. && \text{(2.86d)} \end{aligned}$$

Symmetry dictates

$$\begin{aligned} v_1 &= 0, && \text{(2.87)} \\ \frac{\partial}{\partial x_2} c_i &= 0, && \text{(2.88)} \\ \frac{\partial^2}{\partial x_2^2} \psi &= 0, && \text{(2.89)} \end{aligned}$$

such that the Poisson equation and the Nernst-Planck equation simplify to

$$\begin{aligned} 0 &= \sum_i z_i c_i + \frac{\partial^2}{\partial x_1^2} \psi, && \text{(2.90)} \\ 0 &= \frac{\partial}{\partial x_1} \left\{ -D_i \frac{\partial}{\partial x_1} c_i - D_i z_i (\frac{\partial}{\partial x_1} \psi) c_i \right\}. && \text{(2.91)} \end{aligned}$$

This implies a one dimensional Poisson-Boltzmann equation perpendicular to the channel walls

$$\frac{\partial^2}{\partial x_1^2} \psi + \sum_i z_i A_i exp\left(-z_i \psi\right) = 0. \qquad \text{(2.92)}$$

The Stokes equation then yields the velocity profile. Due to symmetry, we can write

$$\frac{\partial}{\partial x_2} v_2 = 0 \tag{2.93}$$

and

$$\frac{2}{3}\frac{\partial^2}{\partial x_1^2} v_2 = -E_2 \sum_i z_i c_i. \tag{2.94}$$

It should be noted that we assume that no external pressure is applied ($\nabla p = 0$). Inserting the Poisson equation results in

$$\frac{\partial^2}{\partial x_1^2} v_2 = \frac{3}{2} E_2 \frac{\partial^2}{\partial x_1^2} \psi. \tag{2.95}$$

Integrating this equation twice and applying the symmetry $\frac{\partial}{\partial x_1} v_2 \Big|_{x_1=0} = 0$ and *no–slip* boundary conditions

$$v_2 \Big|_{x_1=\pm d} = 0, \tag{2.96}$$

one finally obtains

$$v_2(x_1) = \frac{3}{2} E_2 (\psi(x_1) - \psi(\pm d)). \tag{2.97}$$

Consequently, one can obtain the ion concentrations and the electro–osmotic flow velocity profile for this simple geometry from the solution of a one dimensional Poisson–Boltzmann equation. In the special case that only one ionic species occurs, this problem can be solved analytically (see J. Smiatek et al. [72, 73]). Furthermore, this case is identical to the problem of Sec. 2.4.1. However, the restriction to one ionic species is not required, rather any set of asymmetric ion concentrations can be solved easily and, since only a *one* dimensional Poisson–Boltzmann equation has to be solved, computationally very efficiently.
The implementation is simplified substantially, since only concentration updates occur. The plaquette moves for the electric field updates or a FFT-based solution of the Poisson equation are obviously not necessary in the one dimensional case. For the initialization the electric field can be calculated by a simple integration in one direction. Furthermore, the solution must be invariant under inversion at $x_1 = 0$,

$$c_i(-x_1) = c_i(x_1)\,, \tag{2.98a}$$
$$v_2(-x_1) = v_2(x_1)\,, \tag{2.98b}$$

thus, the computational efficiency can be increased by a factor of 2. Therefore the computational domain does not include the full width of the channel,

rather the problem is solved at one half of the channel. However, this requires a slight modification of the periodic boundary conditions. Therefore we adjust the lattice spacing such that $2d = (2N-1)\Delta x_1$. Thus each of the walls is located at a lattice site, and the center of the channel is located on a link. The positions of the grid nodes are then given by $r = (n+1/2)\Delta x_1$, $n = -N-1, \ldots, N$. Note that we added one further site beyond each plate in order to apply periodic boundary conditions. The channel walls are then located at $r_- = (-N+1/2)\Delta x_1$ and $r_+ = (N-1/2)\Delta x_1$. Application of the invariance condition and modifying the boundary conditions as

$$c_i\left(-\frac{1}{2}\Delta x_1\right) = c_i\left(\frac{1}{2}\Delta x_1\right), \tag{2.99a}$$

$$c_i\left((N+\frac{1}{2}+1)\Delta x_1\right) = c_i\left((N+\frac{1}{2})\Delta x_1\right), \tag{2.99b}$$

we may replace the computational domain of $2N+2$ lattice sites by one with only $N+1$ grid nodes. This modification is illustrated in Fig. 2.14.

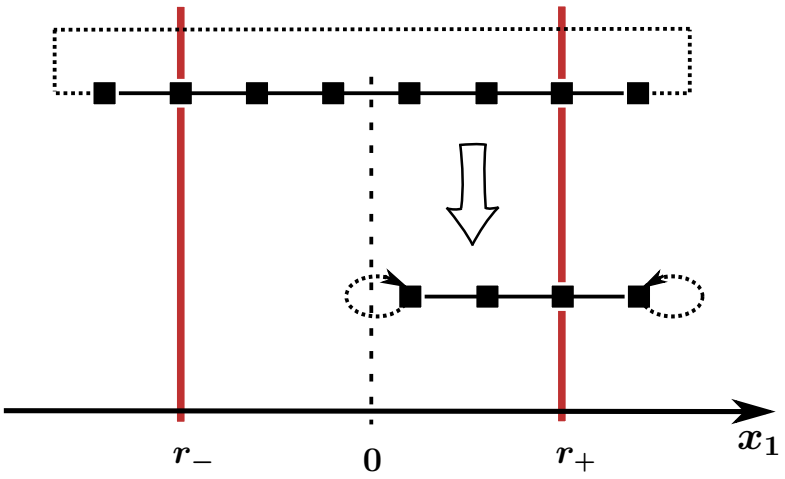

Figure 2.14.: Illustration of the computational domain.

This method was tested for the salt-free case without any additional ions. In accordance with Sec. 2.4, we quote the results here also in unscaled "physical" units, with λ_0 as elementary length scale. All numerical results are given for a slit channel of width $2d = 30\lambda_0$ with surface charge density $\sigma = -0.03e\lambda_0^{-2}$. The Bjerrum length is again set to $l_B = 1.3\lambda_0$. The counterion valence is $z_{ci} = 1$. Fig. 2.15 shows the averaged deviation of the counterion concentration gained by our numerical method to the analytic solution, Eq. (2.73), as function of the lattice spacing Δx_1. As expected this is in accordance with

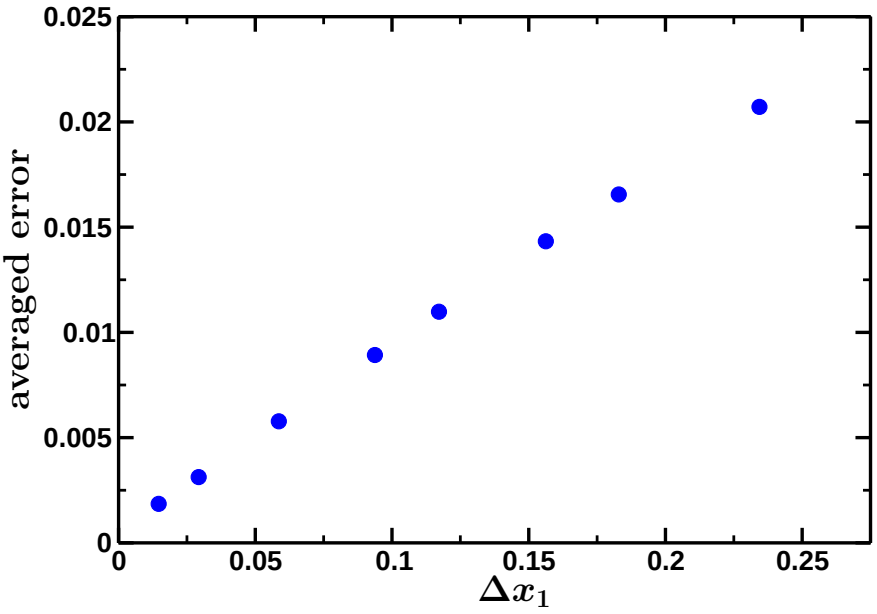

Figure 2.15.: Averaged error in the counterion concentration as function of the lattice spacing Δx_1 for a slit channel without additional ions or salt.

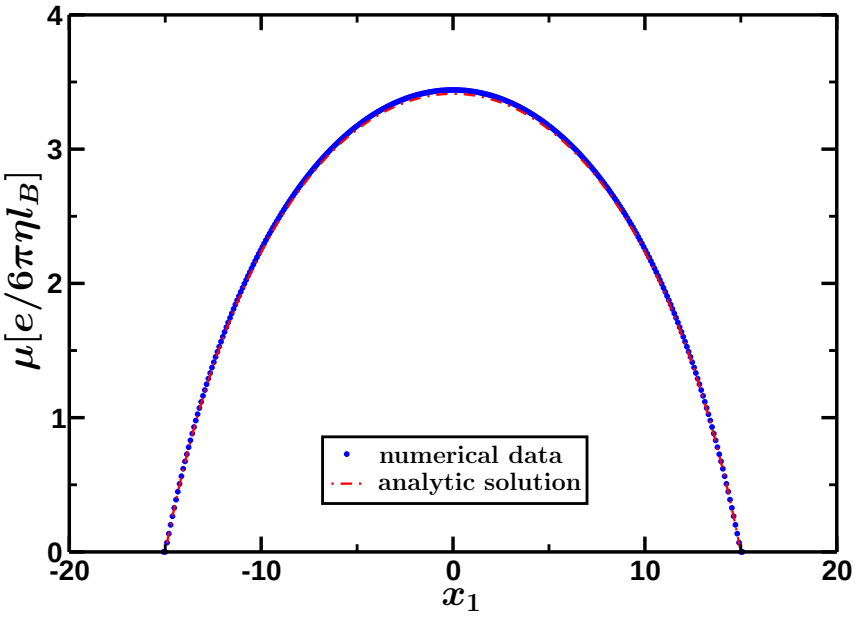

Figure 2.16.: Electro–osmotic mobility for a slit channel without additional ions or salt.

the results of Sec. 2.4.1. Additionally, Fig. 2.16 shows the electro–osmotic mobility profile, according to

$$\mu(x_1) = \frac{v_2(x_1)}{E_2} = \frac{3}{2}(\psi(x_1) - \psi(\pm d))\,. \tag{2.100}$$

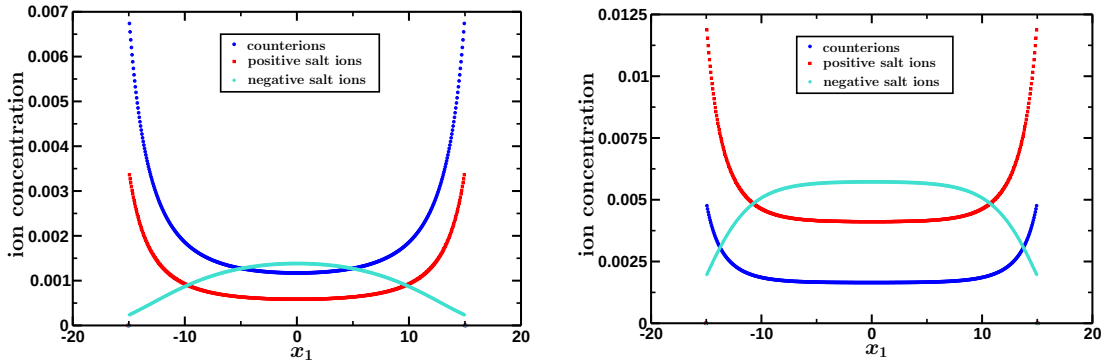

Figure 2.17.: Counterion and salt ion concentration profiles for a system with $10^{-3}\lambda_0^{-3}$ (left) and $5 \cdot 10^{-3}\lambda_0^{-3}$ (right) monovalent salt ions added.

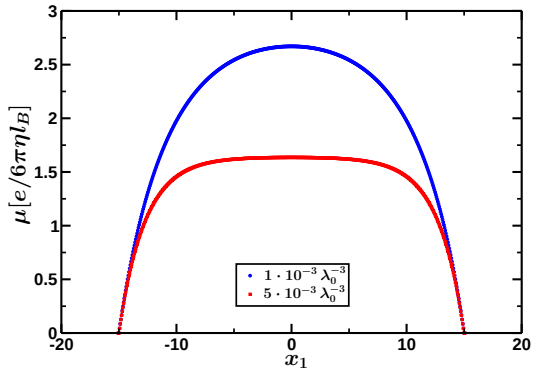

Figure 2.18.: Electro–osmotic mobility for a slit channel with additional monovalent salt ions ($10^{-3}\lambda_0^{-3}$ and $5 \cdot 10^{-3}\lambda_0^{-3}$).

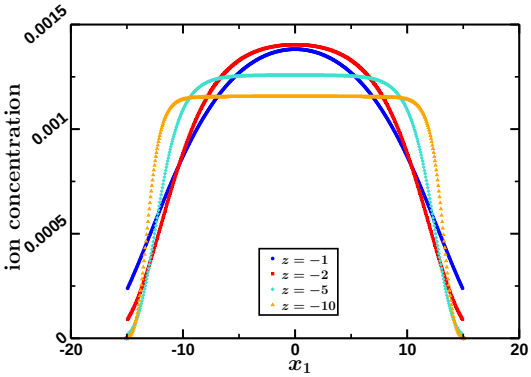

Figure 2.19.: Concentration profile of systems with additional ionic species of various valences ($10^{-3}\lambda_0^{-3}$ added).

In Fig. 2.17 the counterion and salt ion concentrations for systems with added salt are shown, while Fig. 2.18 shows the corresponding mobility profiles. In Fig. 2.19 and 2.20 the effect of adding an ionic species with valence z_{ion} is presented and Fig. 2.21 shows the ion concentration if a certain amount of

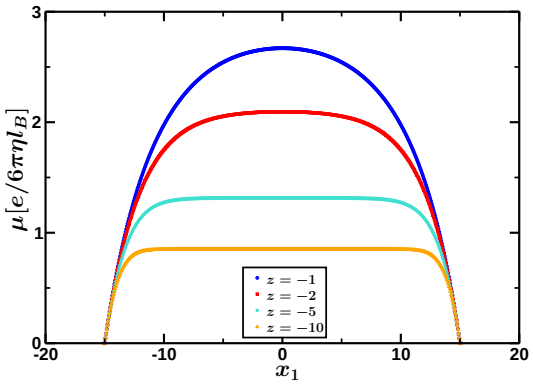

Figure 2.20.: Mobility profile of slit channels with additional ionic species of various valences ($10^{-3}\lambda_0^{-3}$ added).

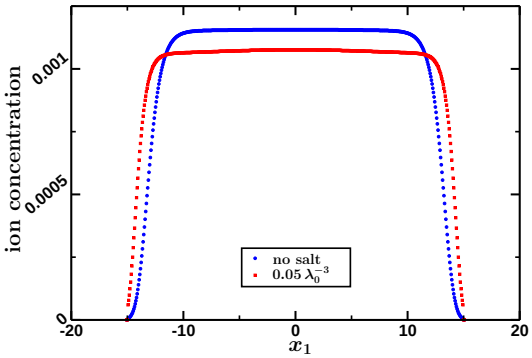

Figure 2.21.: Concentration profiles for ionic species of valence $z_{ion} = -10$ ($\langle c_{ion}\rangle = 10^{-3}\lambda_0^{-3}$) for a system with and without additional monovalent salt ions.

salt is added. Note that in all systems the amount of counterions is calculated by charge neutrality conditions, which means that it also compensates the effect of an additional ionic species, and hence can vary. Furthermore, adding a certain concentration of additional ions of valence $z_{ion} = -1$ does not differ from adding the same amount of monovalent salt. However, it seems that screening has a similar effect in all systems. The mobility profiles flatten and decrease for increasing screening, i. e. decreasing screening length κ^{-1}. Thus, one may ask if the mobility is just an effect of screening length, regardless of the exact screening mechanism. We performed computational runs for a counterion screened system, salt screened system and systems without monovalent salt, but with an additional species of ions with valence $z_{ion} = -5$ and $z_{ion} = -10$. We varied the initial concentration of added ions and calculated the screening parameter. The averaged mobility as function of κ^{-1} is presented in Fig. 2.22. From this, we find that the mobility does not only depend on the screening length, but also on the valence of the additional ions.

According to Ref. [32], one may introduce a dimensionless scaling variable f_0, accounting for the fraction of counterions relative to the amount of all ions in the system,

$$f_0 := \frac{N_0}{\sum_i z_i^2 N_i}\,, \tag{2.101}$$

where N_i is the total number of ions of species i. Note that in this formulation N_0 denotes only the number of counterions, compensating the surface charge of the channel walls $N_0 = -V\sigma/z_0 d$, while additional ionic species are treated

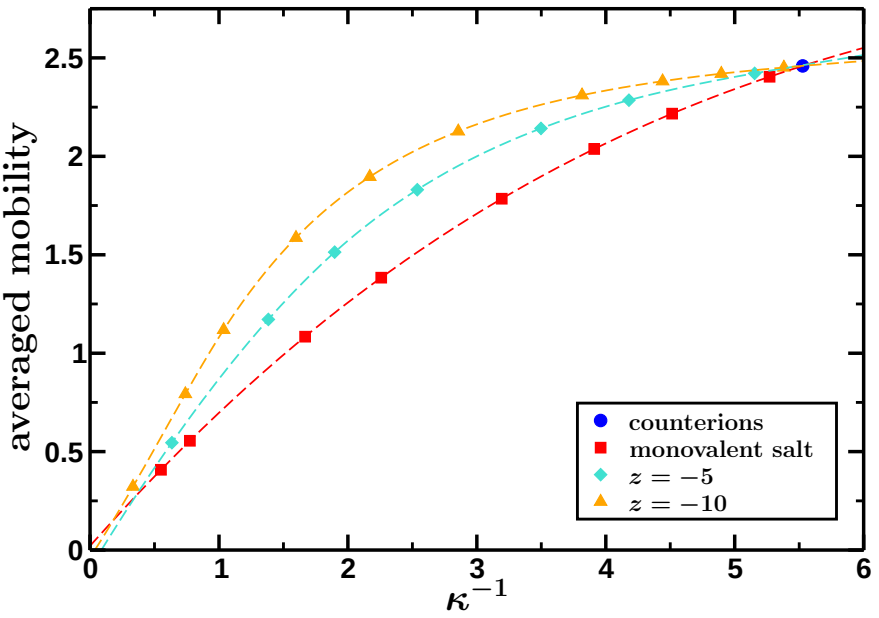

Figure 2.22.: Averaged mobility as function of the screening length κ^{-1} for different mechanisms of screening.

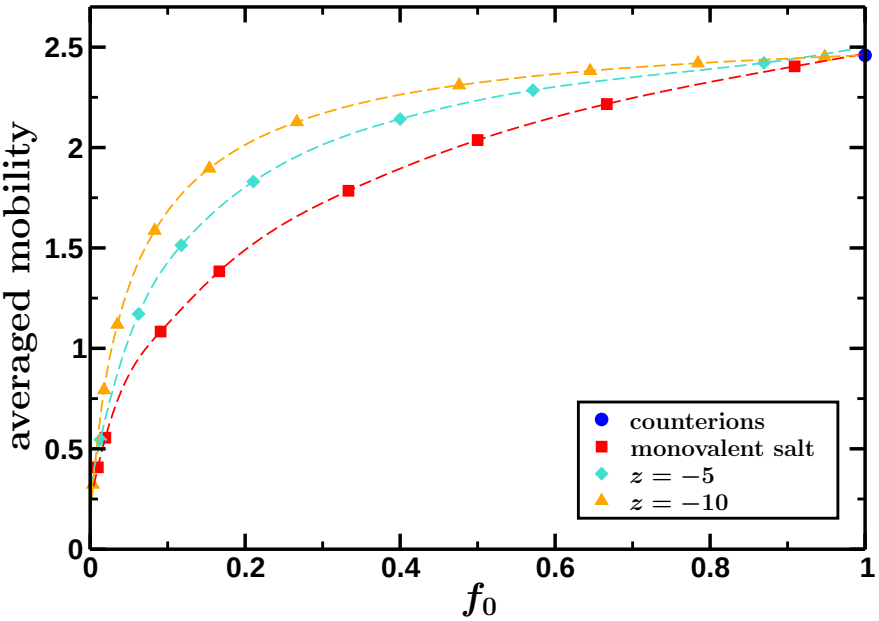

Figure 2.23.: Averaged mobility as function of the counterion fraction f_0 for different mechanisms of screening.

as unsymmetric salt ($-5:1$, $-10:1$). The results are presented in Fig. 2.23. The electro–osmotic mobility depends strongly on the fraction of counterions and differs for different valences of the additional ionic species.

3. Solving the Convection-Diffusion Equation on a Lattice

The Nernst–Planck equation, Eq. (1.13), is the equation of motion of the ion concentration fields. On the one hand, the motion of ions is subject to a deterministic driving field, i. e. electric forces and the convective velocity field. Furthermore, they undergo a diffusive process. Hence, the Nernst–Planck equation is a *convection–diffusion* equation (CDE). In its linear formulation, Eq. (1.62a)[1], some terms are independent of the first order concentration field, but rather depend on the zeroth order. Those terms represent a source or sink term of the CDE. The goal of this chapter is the investigation of a lattice algorithm for convection–diffusion equations of the general form

$$\left(\frac{\partial}{\partial t} + \nabla \cdot \boldsymbol{v}(\boldsymbol{r},t)\right) P(\boldsymbol{r},t) = D\nabla^2 P(\boldsymbol{r},t) + S(\boldsymbol{r},t)\,, \tag{3.1}$$

where D is the diffusion constant and $\boldsymbol{v}$ is the convective current. P denotes a density, e.g. the concentration of a chemical species or a probability density, and S is a source term. In the absence of a source term Eq. (3.1) describes a conservation law for the density P,

$$\int d\boldsymbol{r} P(\boldsymbol{r},t) = const.\,, \tag{3.2}$$

and we demand that the inclusion of sinks and sources should keep this conservation law valid. For concentration fields, this means that the total particle production must be zero,

$$\int d\boldsymbol{r} S(\boldsymbol{r},t) = 0\,. \tag{3.3}$$

The convective current is given by an external velocity field $\boldsymbol{v}$, which depends on the spatial position $\boldsymbol{r}$ and on the time t, and must *not* necessarily satisfy the incompressibility condition. Note that here $\boldsymbol{v}$ is *not* the convective velocity field from electrokinetics $\boldsymbol{v}^{(1)}$, rather $\boldsymbol{v}$ is the zeroth order electric driving field $-D_i z_i \nabla \psi^{(0)}$. In the linearized electrokinetic equations the flow velocity field $\boldsymbol{v}^{(1)}$ is part of the source term since it couples only with the zeroth order concentration fields.

[1] In the non–stationary formulation the left hand side is replaced by the time derivative of the first order concentration field.

3.1. The Source–Free Case

First, the source–free case of Eq. (3.1) is discussed and later source terms are added.

3.1.1. Discretization and Scaling Principles

Our first aim is to investigate a *lattice* algorithm to solve Eq. (3.1). The computational domain is a cubic parallelepiped with periodic boundary conditions. We spatially discretize it by a regular lattice with lattice spacing a and a finite time step h for the time domain.
Transport must always occur such that density is moved from one lattice site to another one. Hence, we introduce grid velocities $\boldsymbol{c}_i$, defined by the condition that $\boldsymbol{r} + h\boldsymbol{c}_i$ is a lattice site, if $\boldsymbol{r}$ is a lattice site. The smallest set of grid velocities depends on the dynamics and the desired accuracy of the algorithm. We will show that a second–order algorithm can be achieved, using a set of velocities only corresponding to the nearest neighbors. To obtain a fourth–order algorithm, the next nearest neighbor shell must be included. This is consistent with the observations of Chubynsky and Slater [74], who recently developed a new highly accurate Lattice Monte Carlo method for diffusion processes. Furthermore, we avoid assumptions about the set of grid velocities at an early stage, and keep the analysis rather general as long as possible.

For dimensional reasons we expect that the diffusion constant will behave like

$$D \propto \frac{a^2}{h}\,. \tag{3.4}$$

The most natural choice for a velocity on a regular lattice is

$$c_s \propto \frac{a}{h}\,, \tag{3.5}$$

since the grid–velocity vectors connect two lattice sites. We will call it "speed of sound" c_s , similar to the *lattice Boltzmann* nomenclature[2]. From this we find

$$h \propto \frac{D}{c_s^2}\,, \tag{3.6a}$$

$$a \propto \frac{D}{c_s}\,, \tag{3.6b}$$

[2]We will see later that our analysis is very similar to the Chapman–Enskog expansion for the lattice Boltzmann method, and hence it is very helpful to use LB nomenclature and concepts.

Thus, one has to make the parameter c_s large in order to reach the continuum limit $a \to 0, h \to 0$. Hence, we define a small scaling parameter

$$\epsilon \propto \frac{1}{c_s}\,, \tag{3.7}$$

and write

$$\begin{aligned} a &= \epsilon a_0\,, && \text{(3.8a)}\\ h &= \epsilon^2 h_0\,, && \text{(3.8b)}\\ \boldsymbol{c}_i &= \frac{a}{h}\hat{\boldsymbol{c}}_i = \epsilon^{-1}\frac{a_0}{h_0}\hat{\boldsymbol{c}}_i = \epsilon^{-1}\boldsymbol{c}_{i0}\,, && \text{(3.8c)}\\ \boldsymbol{c}_i h &= \epsilon^{-1}\boldsymbol{c}_{i0}\epsilon^2 h_0 = \epsilon h_0 \boldsymbol{c}_{i0}\,. && \text{(3.8d)} \end{aligned}$$

This means that we impose *diffusive scaling* from the outset.

3.1.2. The Corresponding Master Equation

In principle, standard methods for solving linear partial differential equations using finite–difference or finite–element schemes can be used to solve Eq. (3.1). On the other hand, special care must be taken not to violate conservation laws. Hence, it is desirable to design the algorithm such that the discrete analogue of the conservation law (3.2) is intrinsically satisfied.
It is well known that a symmetric random walk describes the behavior of a simple diffusion equation. Since a particle is moved from one lattice site to another, mass conservation is intrinsically satisfied. The idea is now to construct an algorithm in form of an asymmetric random walk procedure in order to take convective contributions into account. However, we are only interested in the density, and hence we can get rid of the stochastic character of a random walk and go towards a deterministic algorithm working directly on the level of densities.
We start with the Master equation

$$P(\boldsymbol{r}, t) = \sum_i T_i(\boldsymbol{r} - \boldsymbol{c}_i h, t - h) P(\boldsymbol{r} - \boldsymbol{c}_i h, t - h)\,. \tag{3.9}$$

The rationale behind this ansatz is a splitting–up of the density $P(\boldsymbol{r}-\boldsymbol{c}_i h, t-h)$ into sub–densities $T_i(\boldsymbol{r} - \boldsymbol{c}_i h, t - h)P(\boldsymbol{r} - \boldsymbol{c}_i h, t - h)$, which are transported to the neighbor shells along the corresponding velocities $\mathbf{c}_i$. The parameters T_i are called *transfer coefficients* and must satisfy the normalization condition

$$\sum_i T_i(\boldsymbol{r}, t) = 1 \tag{3.10}$$

at each site $\boldsymbol{r}$ and every time t, in order to fulfill the discretized conservation law for the density P

$$\sum_{\boldsymbol{r}} P(\boldsymbol{r}, t) = const\,. \tag{3.11}$$

We now derive transfer coefficients T_i such that the continuum limit of Eq. (3.9) is the desired convection-diffusion equation (3.1).
A brief description of this kind of equation and its connection to the convection-diffusion equation can be found in Refs. [75, 76]. The analysis presented there is a Taylor expansion of the Master equation with respect to lattice spacing and time step. However, it is not obvious how to extend the solution to higher accuracy. Furthermore, time dependency of the convective current or the inclusion of sources is not discussed.
In the following, an alternative way of expanding the Master equation is presented. Time dependency of the convection velocity is taken into account and the extension to higher orders in lattice spacing and time step and therefore to higher accuracy is presented.

3.1.3. Leading Order Expansion

From Eq. (3.8) the Master equation becomes

$$P(\boldsymbol{r},t) = \sum_i T_i(\boldsymbol{r} - \epsilon h_0 \boldsymbol{c}_{i0}, t - \epsilon^2 h_0) P(\boldsymbol{r} - \epsilon h_0 \boldsymbol{c}_{i0}, t - \epsilon^2 h_0)\,, \tag{3.12}$$

which can be written in the more compact form

$$P(\boldsymbol{r},t) = \sum_i \exp(-D_i) T_i(\boldsymbol{r},t) P(\boldsymbol{r},t)\,, \tag{3.13}$$

with the differential operator

$$D_i = \epsilon h_0 \boldsymbol{c}_{i0} \cdot \nabla + \epsilon^2 h_0 \frac{\partial}{\partial t} = \epsilon h_0 \left(\partial_\alpha c_{i0\alpha} + \epsilon \frac{\partial}{\partial t} \right)\,, \tag{3.14}$$

where α and β are Cartesian indices for which the Einstein summation convention is applied and $\partial_\alpha \equiv \partial / \partial r_\alpha$. Since the transfer coefficients satisfy Eq. (3.10), we can rewrite Eq. (3.13),

$$\sum_i (1 - \exp(-D_i)) T_i(\boldsymbol{r},t) P(\boldsymbol{r},t) = 0. \tag{3.15}$$

For the leading-order behavior up to order ϵ^2, we make use of the operator expansion

$$\begin{aligned} & 1 - \exp(-D_i) \qquad (3.16)\\ = \;& D_i - \frac{1}{2} D_i^2 + O(\epsilon^3) \\ = \;& \epsilon h_0 \left(\partial_\alpha c_{i0\alpha} + \epsilon \frac{\partial}{\partial t} \right) - \frac{1}{2} \epsilon^2 h_0^2 \partial_\alpha \partial_\beta c_{i0\alpha} c_{i0\beta} + \mathcal{O}(\epsilon^3)\,. \end{aligned}$$

By inserting of this expansion and summation, different moments of transfer coefficients occur which we abbreviate by

$$\sum_i T_i c_{i0\alpha} = u_\alpha, \tag{3.17a}$$

$$\sum_i T_i c_{i0\alpha} c_{i0\beta} = q_{\alpha\beta}. \tag{3.17b}$$

The zeroth moment is given by the normalization condition, Eq. (3.10), and thus one obtains

$$\left(\frac{\partial}{\partial t} + \epsilon^{-1}\partial_\alpha u_\alpha\right) P = \frac{h_0}{2}\partial_\alpha\partial_\beta q_{\alpha\beta} P + \mathcal{O}(\epsilon)\,. \tag{3.18}$$

The transfer coefficients T_i depend on the input velocity $\boldsymbol{v}$, or, for dimensional reasons, on the ratio v/c_s. Since $c_s^{-1} \propto \epsilon$, they should have a regular expansion

$$T_i = T_i^{(0)} + \epsilon T_i^{(1)} + \mathcal{O}(\epsilon^2)\,, \tag{3.19}$$

resulting in related expansions

$$u_\alpha = u_\alpha^{(0)} + \epsilon u_\alpha^{(1)} + \mathcal{O}(\epsilon^2)\,, \tag{3.20a}$$

$$q_{\alpha\beta} = q_{\alpha\beta}^{(0)} + \epsilon q_{\alpha\beta}^{(1)} + \mathcal{O}(\epsilon^2)\,. \tag{3.20b}$$

Furthermore the solution P has an expansion

$$P = P^{(0)} + \epsilon P^{(1)} + O(\epsilon^2)\,. \tag{3.21}$$

Inserting these expansions and collecting terms according to their powers of ϵ, we find at order ϵ^{-1}

$$\partial_\alpha u_\alpha^{(0)} P^{(0)} = 0 \tag{3.22}$$

and at order ϵ^0

$$\left(\frac{\partial}{\partial t} + \partial_\alpha u_\alpha^{(1)}\right) P^{(0)} + \partial_\alpha u_\alpha^{(0)} P^{(1)} = \frac{h_0}{2}\partial_\alpha\partial_\beta q_{\alpha\beta}^{(0)} P^{(0)}. \tag{3.23}$$

In order to recover the convection–diffusion equation, we finally have to adjust T_i such that

$$\boldsymbol{u}^{(0)} = 0\,, \tag{3.24a}$$

$$\boldsymbol{u}^{(1)} = \boldsymbol{v}\,, \tag{3.24b}$$

$$\frac{h_0}{2} q_{\alpha\beta}^{(0)} = D\delta_{\alpha\beta}\,. \tag{3.24c}$$

Furthermore, cubic symmetry contributes to the concrete form of the transfer coefficients. Hence, in analogy to lattice Boltzmann algorithms, we choose a

set of neighbor shells on the lattice and their corresponding velocities. Each velocity is assigned a weight w_i to account for the different lengths of velocities corresponding to different shells. From normalization and cubic symmetry, a general relation for the lattice sums is given by

$$\begin{aligned}
\sum_i w_i &= 1, && \text{(3.25a)}\\
\sum_i w_i c_{i\alpha} &= 0, && \text{(3.25b)}\\
\sum_i w_i c_{i\alpha} c_{i\beta} &= \sigma_2 \delta_{\alpha\beta} = \epsilon^{-2} \sigma_{20} \delta_{\alpha\beta}, && \text{(3.25c)}\\
\sum_i w_i c_{i\alpha} c_{i\beta} c_{i\gamma} &= 0, && \text{(3.25d)}\\
\sum_i w_i c_{i\alpha} c_{i\beta} c_{i\gamma} c_{i\delta} &= \kappa_4 \delta_{\alpha\beta\gamma\delta} + \sigma_4 \left(\delta_{\alpha\beta}\delta_{\gamma\delta} + \delta_{\alpha\gamma}\delta_{\beta\delta} + \delta_{\alpha\delta}\delta_{\beta\gamma}\right) && \text{(3.25e)}\\
&= \epsilon^{-4}\kappa_{40} \delta_{\alpha\beta\gamma\delta} + \epsilon^{-4}\sigma_{40} \left(\delta_{\alpha\beta}\delta_{\gamma\delta} + \delta_{\alpha\gamma}\delta_{\beta\delta} + \delta_{\alpha\delta}\delta_{\beta\gamma}\right).
\end{aligned}$$

Here $\delta_{\alpha\beta\gamma\delta}$ is 1 if $\alpha = \beta = \gamma = \delta$ and vanishes elsewise. We choose the ansatz

$$\begin{aligned}
T_i &= w_i \left(1 + \frac{1}{\sigma_2} \boldsymbol{v} \cdot \boldsymbol{c}_i\right) && \text{(3.26)}\\
&= w_i \left(1 + \frac{\epsilon}{\sigma_{20}} \boldsymbol{v} \cdot \boldsymbol{c}_{i0}\right),
\end{aligned}$$

that results in the moments

$$\begin{aligned}
\sum_i T_i &= 1, && \text{(3.27)}\\
\boldsymbol{u} = \sum_i T_i \boldsymbol{c}_{i0} &= \epsilon \boldsymbol{v}, && \text{(3.28)}\\
q_{\alpha\beta} = \sum_i T_i c_{i0\alpha} c_{i0\beta} &= \sigma_{20} \delta_{\alpha\beta}. && \text{(3.29)}
\end{aligned}$$

Conditions (3.24a) and (3.24b) are thus satisfied, while condition (3.24c) yields the value for the diffusion constant

$$D = \frac{h_0}{2}\sigma_{20} = \frac{\epsilon^{-2}h}{2}\epsilon^2\sigma_2 = \frac{h}{2}\sigma_2, \qquad \text{(3.30)}$$

and the transfer coefficients are

$$T_i = w_i \left(1 + \frac{\epsilon h_0}{2D} \boldsymbol{v} \cdot \boldsymbol{c}_{i0}\right) = w_i \left(1 + \frac{h}{2D} \boldsymbol{v} \cdot \boldsymbol{c}_i\right). \qquad \text{(3.31)}$$

For a d-dimensional cubic lattice, one may choose the set of $2d$ velocities that connect to the nearest neighbors. Thus the weights are given by $w_i = 1/(2d)$ and by applying the lattice sums one obtains $\sigma_{20} = (1/d)(a_0^2/h_0^2)$, or

$$D = \frac{1}{2d}\frac{a_0^2}{h_0} = \frac{1}{2d}\frac{\epsilon^{-2}a^2}{\epsilon^{-2}h} = \frac{1}{2d}\frac{a^2}{h}. \tag{3.32}$$

3.1.4. Beyond the Leading Order

In this section, a conceptually simple and technically straightforward way to extend the expansion to higher accuracy is presented. It should be noted that, in contrast to Ref. [74], the usage of LB nomenclature allows us to make this expansion in a very clear and easily understandable fashion.
We start again with Eq. (3.15) and abbreviate the moments by

$$\sum_i T_i c_{i0\alpha} = u_\alpha, \tag{3.33a}$$

$$\sum_i T_i c_{i0\alpha} c_{i0\beta} = q_{\alpha\beta}, \tag{3.33b}$$

$$\sum_i T_i c_{i0\alpha} c_{i0\beta} c_{i0\gamma} = p_{\alpha\beta\gamma}, \tag{3.33c}$$

$$\sum_i T_i c_{i0\alpha} c_{i0\beta} c_{i0\gamma} c_{i0\delta} = s_{\alpha\beta\gamma\delta}. \tag{3.33d}$$

From this, we get the following operator identities

$$1 - \exp(-D_i) = D_i - \frac{1}{2}D_i^2 + \frac{1}{6}D_i^3 - \frac{1}{24}D_i^4 + O(\epsilon^5), \tag{3.34a}$$

$$\frac{1}{\epsilon^2 h_0}\sum_i D_i T_i = \epsilon^{-1}\partial_\alpha u_\alpha + \frac{\partial}{\partial t}, \tag{3.34b}$$

$$-\frac{1}{2}\frac{1}{\epsilon^2 h_0}\sum_i D_i^2 T_i = -\frac{h_0}{2}\left(\partial_\alpha\partial_\beta q_{\alpha\beta} + 2\epsilon\frac{\partial}{\partial t}\partial_\alpha u_\alpha + \epsilon^2\frac{\partial^2}{\partial t^2}\right), \tag{3.34c}$$

$$\begin{aligned}\frac{1}{6}\frac{1}{\epsilon^2 h_0}\sum_i D_i^3 T_i &= \frac{1}{6}\epsilon h_0^2\partial_\alpha\partial_\beta\partial_\gamma p_{\alpha\beta\gamma} \\ &+ \frac{1}{2}\epsilon^2 h_0^2\frac{\partial}{\partial t}\partial_\alpha\partial_\beta q_{\alpha\beta} + O(\epsilon^3),\end{aligned} \tag{3.34d}$$

$$-\frac{1}{24}\frac{1}{\epsilon^2 h_0}\sum_i D_i^4 T_i = -\frac{1}{24}\epsilon^2 h_0^3\partial_\alpha\partial_\beta\partial_\gamma\partial_\delta s_{\alpha\beta\gamma\delta} + O(\epsilon^3). \tag{3.34e}$$

As mentioned previously, the first moment expansion starts at order $\mathcal{O}(\epsilon^1)$, while the zeroth and second moments start at order $\mathcal{O}(\epsilon^0)$. Thus all odd moments are assumed to have an odd expansion in ϵ, and the even moments

an even expansion

$$
\begin{aligned}
u_\alpha &= \epsilon u_\alpha^{(1)} + \epsilon^3 u_\alpha^{(3)} + O(\epsilon^5), && \text{(3.35a)}\\
q_{\alpha\beta} &= q_{\alpha\beta}^{(0)} + \epsilon^2 q_{\alpha\beta}^{(2)} + O(\epsilon^4), && \text{(3.35b)}\\
p_{\alpha\beta\gamma} &= \epsilon p_{\alpha\beta\gamma}^{(1)} + O(\epsilon^3), && \text{(3.35c)}\\
s_{\alpha\beta\gamma\delta} &= s_{\alpha\beta\gamma\delta}^{(0)} + O(\epsilon^2). && \text{(3.35d)}
\end{aligned}
$$

Applying Eq. (3.34) and Eq. (3.35) leads to the operator identity

$$
\frac{1}{\epsilon^2 h_0} \sum_i \left(1 - \exp(-D_i)\right) T_i = \mathcal{L}^{(0)} + \epsilon^2 \mathcal{L}^{(2)} + O(\epsilon^3)\,, \tag{3.36}
$$

with

$$
\begin{aligned}
\mathcal{L}^{(0)} &= \frac{\partial}{\partial t} + \partial_\alpha u_\alpha^{(1)} - \frac{h_0}{2}\partial_\alpha\partial_\beta q_{\alpha\beta}^{(0)}, && \text{(3.37a)}\\
\mathcal{L}^{(2)} &= \partial_\alpha u_\alpha^{(3)} - \frac{h_0}{2}\partial_\alpha\partial_\beta q_{\alpha\beta}^{(2)} + \frac{h_0^2}{6}\partial_\alpha\partial_\beta\partial_\gamma p_{\alpha\beta\gamma}^{(1)} - \frac{h_0^3}{24}\partial_\alpha\partial_\beta\partial_\gamma\partial_\delta s_{\alpha\beta\gamma\delta}^{(0)}\\
&- h_0\frac{\partial}{\partial t}\partial_\alpha u_\alpha^{(1)} - \frac{h_0}{2}\frac{\partial^2}{\partial t^2} + \frac{h_0^2}{2}\frac{\partial}{\partial t}\partial_\alpha\partial_\beta q_{\alpha\beta}^{(0)}. && \text{(3.37b)}
\end{aligned}
$$

Therefore P must have an expansion

$$
P = P^{(0)} + \epsilon^2 P^{(2)} + O(\epsilon^3)\,, \tag{3.38}
$$

and the error of the algorithm is actually not *first* order in ϵ, rather *second* order, i. e. linear with respect to the time step and quadratic with respect to the lattice spacing. This is precisely what is observed numerically (see Fig. 3.2). In literature we find that this is called *second–order accuracy* (see for example [77]).

Moreover, if we succeed in adjusting the transfer coefficients in such a way that the next order, i. e. $\mathcal{L}^{(2)}P^{(0)}$, is identically zero, $P^{(2)} = 0$ is the solution of the problem at order ϵ^2. This means that the error is indeed of higher order.
Therefore we first make use of the established asymptotic behavior at the leading order to simplify

$$
\begin{aligned}
\mathcal{L}^{(0)} &= \frac{\partial}{\partial t} + \nabla\cdot\boldsymbol{v} - D\nabla^2, && \text{(3.39)}\\
\mathcal{L}^{(2)} &= \partial_\alpha u_\alpha^{(3)} - \frac{h_0}{2}\partial_\alpha\partial_\beta q_{\alpha\beta}^{(2)} + \frac{h_0^2}{6}\partial_\alpha\partial_\beta\partial_\gamma p_{\alpha\beta\gamma}^{(1)} - \frac{h_0^3}{24}\partial_\alpha\partial_\beta\partial_\gamma\partial_\delta s_{\alpha\beta\gamma\delta}^{(0)}\\
&- h_0\frac{\partial}{\partial t}\nabla\cdot\boldsymbol{v} - \frac{h_0}{2}\frac{\partial^2}{\partial t^2} + h_0\frac{\partial}{\partial t}D\nabla^2. && \text{(3.40)}
\end{aligned}
$$

We insert Eq. (3.39) in the form

$$\frac{\partial}{\partial t} = \mathcal{L}^{(0)} - \nabla \cdot \boldsymbol{v} + D\nabla^2 \tag{3.41}$$

into Eq. (3.40) and apply the commutation rules of operator algebra to systematically pull the spatial derivatives to the very left, and $\mathcal{L}^{(0)}$ to the very right. Furthermore, we systematically symmetrize tensors wherever this is possible. This involves some lengthy but fairly straightforward calculations that finally result in

$$\begin{aligned}
\mathcal{L}^{(2)} &= \partial_\alpha \left\{ u_\alpha^{(3)} - \frac{Dh_0}{2}\left(\partial_\beta^2 v_\alpha\right) - \frac{h_0}{2} v_\beta \left(\partial_\beta v_\alpha\right) - \frac{h_0}{2}\left(\frac{\partial v_\alpha}{\partial t}\right) \right\} \\
&+ \partial_\alpha \partial_\beta \left\{ -\frac{h_0}{2} q_{\alpha\beta}^{(2)} + \frac{Dh_0}{2}\left[(\partial_\alpha v_\beta) + (\partial_\beta v_\alpha)\right] + \frac{h_0}{2} v_\alpha v_\beta \right\} \\
&+ \partial_\alpha \partial_\beta \partial_\gamma \left\{ \frac{h_0^2}{6} p_{\alpha\beta\gamma}^{(1)} - \frac{Dh_0}{3}\left[\delta_{\beta\gamma} v_\alpha + \delta_{\alpha\gamma} v_\beta + \delta_{\alpha\beta} v_\gamma\right] \right\} \\
&+ \partial_\alpha \partial_\beta \partial_\gamma \partial_\delta \left\{ -\frac{h_0^3}{24} s_{\alpha\beta\gamma\delta}^{(0)} + \frac{D^2 h_0}{6}\left[\delta_{\alpha\beta}\delta_{\gamma\delta} + \delta_{\alpha\gamma}\delta_{\beta\delta} + \delta_{\alpha\delta}\delta_{\beta\gamma}\right] \right\} \\
&- \frac{h_0}{2} {\mathcal{L}^{(0)}}^2,
\end{aligned} \tag{3.42}$$

where the braces $(\ldots)$ indicate that the derivative acts only on the term within. A detailed calculation can be found in the appendix. The last term, including ${\mathcal{L}^{(0)}}^2$, does not contribute to the action of $\mathcal{L}^{(2)}$ on $P^{(0)}$. The remaining parts of $\mathcal{L}^{(2)}$ should vanish identically. We therefore require the moment relations

$$s_{\alpha\beta\gamma\delta}^{(0)} = \left(\frac{2D}{h_0}\right)^2 \left[\delta_{\alpha\beta}\delta_{\gamma\delta} + \delta_{\alpha\gamma}\delta_{\beta\delta} + \delta_{\alpha\delta}\delta_{\beta\gamma}\right], \tag{3.43}$$

$$p_{\alpha\beta\gamma}^{(1)} = \frac{2D}{h_0}\left[\delta_{\beta\gamma} v_\alpha + \delta_{\alpha\gamma} v_\beta + \delta_{\alpha\beta} v_\gamma\right], \tag{3.44}$$

$$q_{\alpha\beta}^{(2)} = D\left[\partial_\alpha v_\beta + \partial_\beta v_\alpha\right] + v_\alpha v_\beta, \tag{3.45}$$

$$u_\alpha^{(3)} = \frac{Dh_0}{2}\partial_\beta^2 v_\alpha + \frac{h_0}{2} v_\beta \partial_\beta v_\alpha + \frac{h_0}{2}\frac{\partial v_\alpha}{\partial t}. \tag{3.46}$$

Consistency with the leading order requires

$$T_i^{(0)} = w_i, \tag{3.47}$$

$$T_i^{(1)} = \frac{w_i}{\sigma_{20}} \boldsymbol{v} \cdot \boldsymbol{c}_{i0}, \tag{3.48}$$

where $\sigma_{20} = 2D/h_0$. The higher-order coefficients $T_i^{(2)}$ and $T_i^{(3)}$ do not contribute to the leading order and shall be adjusted such that $\mathcal{L}^{(2)} P^{(0)}$ is exactly

zero. Inserting Eq. (3.47) into Eq. (3.33d) and applying Eq. (3.25e), we first find

$$s^{(0)}_{\alpha\beta\gamma\delta} = \kappa_{40}\delta_{\alpha\beta\gamma\delta} + \sigma_{40}\left(\delta_{\alpha\beta}\delta_{\gamma\delta} + \delta_{\alpha\gamma}\delta_{\beta\delta} + \delta_{\alpha\delta}\delta_{\beta\gamma}\right). \tag{3.49}$$

Comparison with Eq. (3.43) shows that the w_i have to be adjusted such that $\kappa_{40} = 0$, and $\sigma_{40} = (2D/h_0)^2 = \sigma_{20}^2$. This problem is mathematically identical to finding the weights for a standard lattice Boltzmann model. One can therefore use, in three dimensions, the weights known for the D3Q19 model [78], i.e. $w_0 = 1/3$, $w_{1-6} = 1/18$ and $w_{7-18} = 1/36$ for the set of velocities with $|\boldsymbol{c}_0| = 0$, $|\boldsymbol{c}_{1-6}| = a/h$ and $|\boldsymbol{c}_{7-18}| = \sqrt{2}\,a/h$. This makes sure that Eq. (3.43) is indeed satisfied. In this case, we have $\sigma_{20} = (1/3)(a_0/h_0)^2$, or $\sigma_2 = (1/3)(a/h)^2$. Using these weights, we calculate from Eq. (3.48)

$$p^{(1)}_{\alpha\beta\gamma} = \sigma_{20}\left[\delta_{\beta\gamma}v_\alpha + \delta_{\alpha\gamma}v_\beta + \delta_{\alpha\beta}v_\gamma\right] = \frac{2D}{h_0}\left[\delta_{\beta\gamma}v_\alpha + \delta_{\alpha\gamma}v_\beta + \delta_{\alpha\beta}v_\gamma\right], \tag{3.50}$$

showing that Eq. (3.44) is indeed also satisfied. We now choose for the higher–order transfer coefficients

$$T_i^{(2)} = \frac{w_i}{2\sigma_{20}^2}\left(c_{i0\alpha}c_{i0\beta} - \sigma_{20}\delta_{\alpha\beta}\right) q^{(2)}_{\alpha\beta}, \tag{3.51}$$

$$T_i^{(3)} = \frac{w_i}{\sigma_{20}}\boldsymbol{u}^{(3)}\cdot\boldsymbol{c}_{i0}, \tag{3.52}$$

which give rise to the given desired moments $q^{(2)}_{\alpha\beta}$ and $\boldsymbol{u}^{(3)}$, respectively. Choosing these latter moments according to Eqs. (3.45) and (3.46) makes sure that these remaining moment conditions are also satisfied. Collecting the various contributions to the transfer coefficients, and transforming back to "unscaled" units (without occurrence of ϵ) finally yields

$$\begin{aligned}\frac{T_i}{w_i} &= 1 + \frac{\boldsymbol{v}\cdot\boldsymbol{c}_i}{\sigma_2} + \frac{1}{2\sigma_2^2}\left(c_{i\alpha}c_{i\beta} - \sigma_2\delta_{\alpha\beta}\right)\left[v_\alpha v_\beta + D\left(\partial_\alpha v_\beta + \partial_\beta v_\alpha\right)\right] \\ &\quad + \frac{h}{2\sigma_2}c_{i\alpha}\left[v_\beta\partial_\beta v_\alpha + D\partial_\beta^2 v_\alpha + \frac{\partial v_\alpha}{\partial t}\right].\end{aligned} \tag{3.53}$$

3.2. Inclusion of Source Term

In the previous section, we studied the CDE in the absence of sources. However, one may ask if it is possible to extend the Master equation, Eq. (3.9), such that the full CDE (3.1) including a time dependent source term is reproduced. Indeed, we find that only a slight change is sufficient to account for the desired source. First we assume that the transfer coefficients account only for the transport of density, but should not depend on production or annihilation of particles. Hence, we add an additional term to the Master equation

$$P(\vec{r},t) = \sum_i T_i(\vec{r} - \vec{c}_i h)P(\vec{r} - \vec{c}_i h, t-h) + B(\vec{r}, t-h). \tag{3.54}$$

where $B(\vec{r},t)$ corresponds to the source term. Repeating the arguments from the previous section and expanding $B(\vec{r},t)$ with respect to ϵ

$$B \equiv B^{(0)} + \epsilon^2 B^{(2)} + \epsilon^4 B^{(4)} + \mathcal{O}(\epsilon^5), \tag{3.55}$$

we find

$$\begin{aligned} 0 &= B^{(0)}, & (3.56)\\ \mathcal{L}^{(0)} P^{(0)} &= \frac{1}{h_0} B^{(2)}, & (3.57)\\ \mathcal{L}^{(2)} P^{(0)} &= \frac{1}{h_0} B^{(4)} + \frac{\partial}{\partial t} B^{(2)}. & (3.58) \end{aligned}$$

By the choice $B^{(2)} = h_0 S$ Eq. (3.57) reproduces the desired CDE in the leading order. In order to go one order of accuracy further, we have to make sure that the next order is again exactly zero. According to the choice of transfer coefficients, Eq. (3.53), all terms of $\mathcal{L}^{(2)} P^{(0)}$ vanish except the term including $\mathcal{L}^{(0)}$, which now has an action on the density $P^{(0)}$. Inserting the second order operator, Eq. (3.42), into Eq. (3.58), one obtains

$$\begin{aligned} \frac{1}{h_0} B^{(4)} + \frac{\partial}{\partial t} B^{(2)} &= \mathcal{L}^{(2)} P^{(0)} \\ &= -\frac{h_0}{2} {\mathcal{L}^{(0)}}^2 P^{(0)} \\ &= -\frac{h_0}{2} \mathcal{L}^{(0)} S, \end{aligned} \tag{3.59}$$

and therefore

$$B^{(4)} = -\frac{h_0^2}{2} \mathcal{L}^{(0)} S - h_0^2 \frac{\partial}{\partial t} S. \tag{3.60}$$

Collecting all contributions to the source term finally results in

$$B(\vec{r},t) = hS(\vec{r},t) - \frac{h^2}{2} \mathcal{L}^{(0)} S(\vec{r},t) - h^2 \frac{\partial}{\partial t} S(\vec{r},t). \tag{3.61}$$

3.3. Numerical Results

3.3.1. Smoluchowski Equation with Periodic Potential

A simple example for a convection–diffusion equation is the Fokker–Planck equation with periodic, but not time dependent potential in the absence of a source term

$$\left(\frac{\partial}{\partial t} + \frac{\partial}{\partial x}\cos(x)\right) P(x,t) = D\frac{\partial^2}{\partial x^2} P(x,t). \tag{3.62}$$

The well known stationary solution of this equation is given by

$$P(x) = \left[\int_{-\pi}^{\pi} dx \exp\left(\frac{\sin(x)}{D}\right)\right]^{-1} \exp\left(\frac{\sin(x)}{D}\right). \tag{3.63}$$

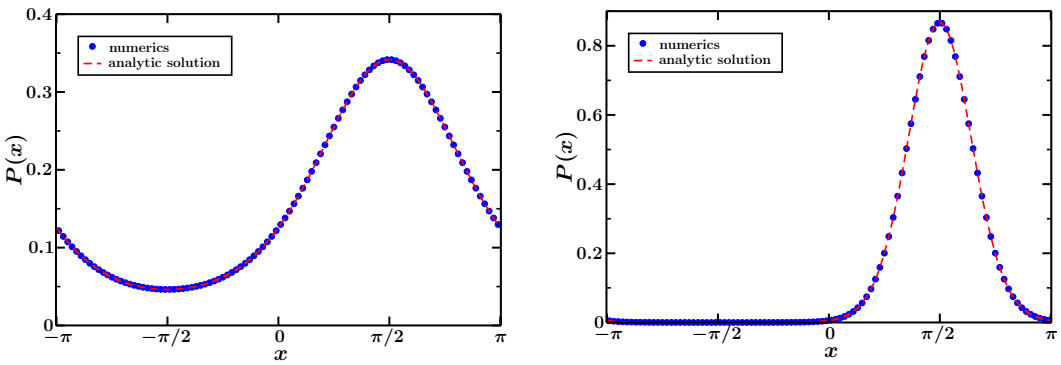

Figure 3.1.: Numerical results and analytical solution for the stationary case of the Fokker–Planck equation (3.62). The lattice constant is $a = 2\pi/200$ and diffusion constant $D = 1$ (left), $D = 0.2$ (right).

This distribution function is shown in Fig. 3.1. The numerical datapoints in this plot were computed with a one dimensional implementation of the 4th order algorithm and a three velocity model. The lattice spacing was set to $a = 2\pi/200$.

Fig. 3.2 shows the averaged error

$$\text{error} = \frac{\sum_i |P_{analytic}(x_i) - P_{numeric}(x_i)|}{\text{number of datapoints}}, \tag{3.64}$$

as function of the lattice spacing a for a one dimensional, two velocity implementation of the second order algorithm and an implementation with fourth

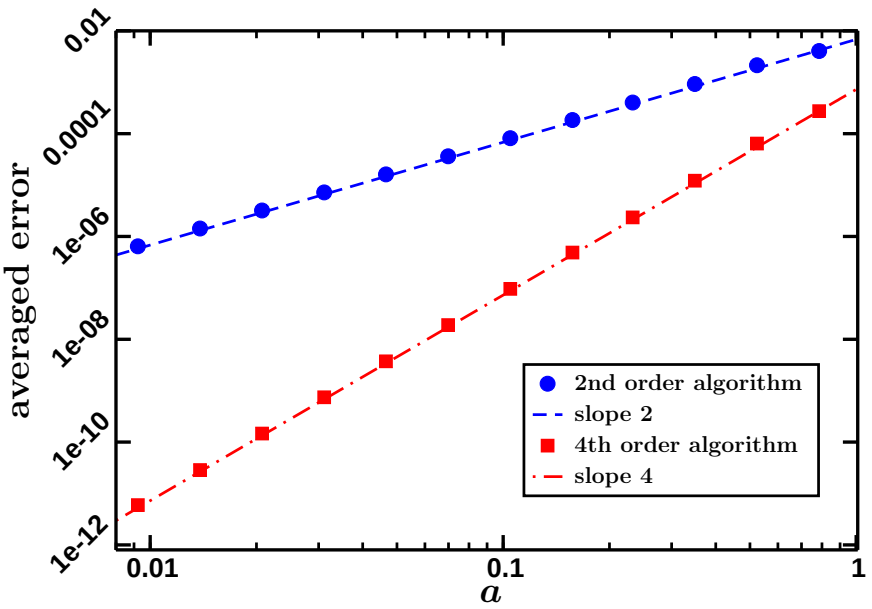

Figure 3.2.: Average error as function of the lattice spacing a for the simple one dimensional, two velocity model and the three grid–velocity model with correction terms. The diffusion constant is set to $D = 1$.

order correction terms and three grid velocities.

A lattice algorithm for the convection–diffusion equation is always limited by the dimensionless grid–Peclet number, defined as

$$\mathrm{Pe} = \frac{va}{D}. \tag{3.65}$$

A kind of singular behavior is observed in the algorithm, in the sense that beyond a critical Peclet number the algorithm does not converge to a stationary limit. This transition from stable to unstable behavior is found to be very sharp and more or less independent of the grid resolution. We found that in terms of the grid–Peclet number the fourth order implementation ($\mathrm{Pe}_{crit} \simeq 5.7$) is roughly twice as stable as the second order version ($\mathrm{Pe}_{crit} \simeq 2.86$). One may counter that the set of grid velocities is not the same in both simulations, and that the higher stability is *only* an effect of the additional shells. Indeed, the stability is increased, if we impose an additional velocity shell to the second order algorithm, i. e. we apply an D1Q3 model on the second order transfer coefficients, Eq. (3.31). The value we observe for this case is $\mathrm{Pe}_{crit} \simeq 4.97$, which is still less stable than the algorithm including the correction terms.

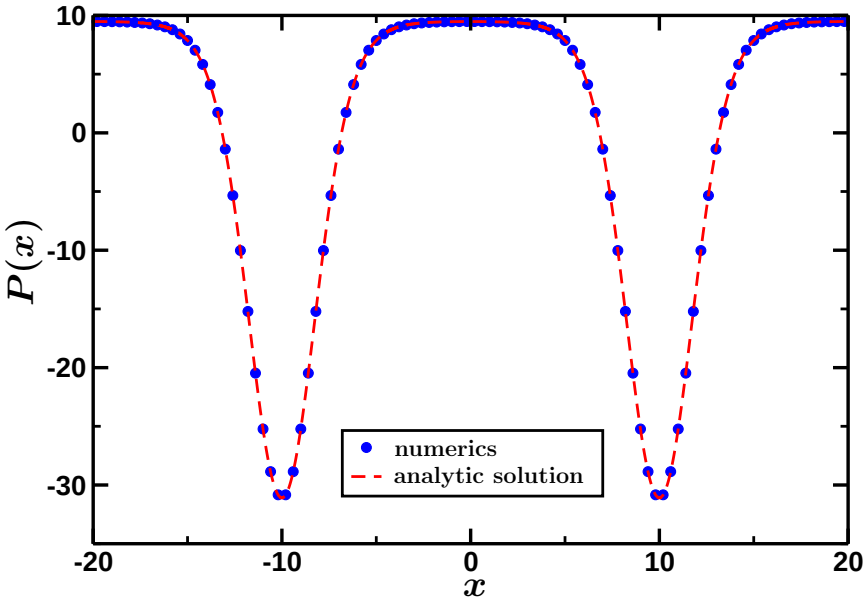

Figure 3.3.: Numerical results and analytical solution for the long time limit of equation (3.66). The resolution is set to 200 datapoints and the parameters are $\alpha = 1$, $\beta = 3$, $k = \frac{2\pi}{L}$ and $L = 20$.

3.3.2. Test Sytem with Source Term

The second test system is a partial differential equation of the form

$$\left(\frac{\partial}{\partial t} + \frac{\partial}{\partial x}\alpha \sin(kx)\right) P(x,t) = \frac{\partial^2}{\partial x^2} P(x,t) + \beta \cos(kx). \tag{3.66}$$

The difference to Eq. (3.62) is essentially given by the time independent source term, which satisfies the condition (3.3), if and only if $k = \frac{n\pi}{L}$, where the simulation box covers the interval $(-L, L)$ and $n \in \mathbb{N}\backslash\{0\}$. The solution for the stationary limit of Eq. (3.66) is given by

$$P(x) = \frac{\beta}{\alpha k} + \gamma \exp\left(-\frac{\alpha}{k}\cos(kx)\right), \tag{3.67}$$

with

$$\gamma = -2\frac{\beta L}{\alpha k}\left[\int_{-L}^{L} dx' \exp\left(-\frac{\alpha}{k}\cos(kx')\right)\right]^{-1}. \tag{3.68}$$

Fig. 3.3 illustrates numerical data and the analytic solution for this problem with $\alpha = 1$, $\beta = 3$, $L = 20$ and $k = \frac{2\pi}{20}$. The averaged error as a function of the lattice spacing, for the same set of parameters, is presented in Fig. 3.4. We also found that the critical grid–Peclet numbers have roughly the same values as in the source–free case.

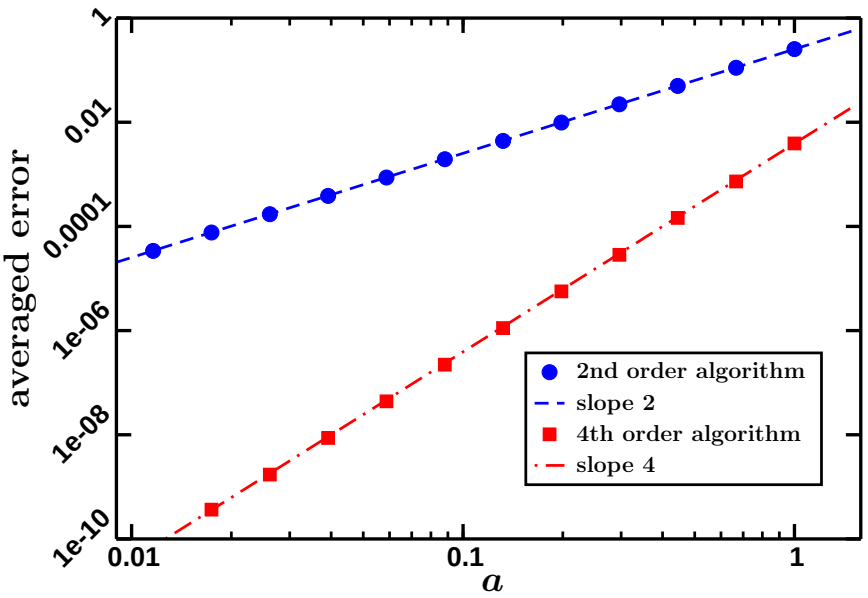

Figure 3.4.: Averaged error as function of the lattice spacing a for the $1d$ simple two velocity model and the three velocity model with correction terms. The coefficients and parameters are the same as in Fig. 3.3

3.4. Diffusive Scaling vs. Multiple Time Scales

In the analysis of the continuum limit of the Master equation in the previous sections, we have seen that this algorithm has a lot in common with lattice Boltzmann algorithms; not least the way of expanding the equations, known as *Chapman–Enskog analysis*. The difference to the standard lattice Boltzmann analysis is that we impose diffusive scaling from the outset. Conversely, one may ask what happens if we introduce a convective and a diffusive time scale separately. In this section we consider the continuum limit $h \to 0$, $a \to 0$, where the ratio a/h is kept constant such that grid velocities $\boldsymbol{c}_i$ remain constant as well. We therefore introduce a small dimensionless parameter ϵ such that $h = \epsilon h_0$, and h_0 keeps constant, and we distinguish between two different time scales $t_0 \equiv t$ and $t_1 \equiv \epsilon t$. This is essentially the Chapman–Enskog expansion as known from kinetic theory. Now we may write the density and the transfer coefficients as function of three arguments. The Master equation then becomes

$$\begin{aligned} P(\boldsymbol{r}, t_0, t_1) &= \sum_i T_i(\boldsymbol{r} - \epsilon \boldsymbol{c}_i h_0, t_0 - \epsilon h_0, t_1 - \epsilon^2 h_0) \\ &\quad \cdot P(\boldsymbol{r} - \epsilon \boldsymbol{c}_i h_0, t_0 - \epsilon h_0, t_1 - \epsilon^2 h_0). \end{aligned} \tag{3.69}$$

We again introduce a differential operator with a slightly different form as in the diffusive–scaling analysis

$$D_i = \epsilon h_0 \left(\frac{\partial}{\partial t_0} + \boldsymbol{c}_i \cdot \nabla \right) + \epsilon^2 h_0 \frac{\partial}{\partial t_1}, \tag{3.70}$$

and repeat the calculations from section 3.1 with the new operator. This means, we again have to expand the equation

$$\sum_i \left(1 - \exp(-D_i)\right) T_i(\boldsymbol{r}, t_0, t_1) P(\boldsymbol{r}, t_0, t_1) \;=\; 0\,. \tag{3.71}$$

We get

$$\begin{aligned} 1 - \exp(-D_i) &= D_i - \frac{1}{2} D_i^2 + O(\epsilon^3) \\ &= \epsilon h_0 \left(\frac{\partial}{\partial t_0} + \boldsymbol{c}_i \cdot \nabla \right) \\ &+ \epsilon^2 h_0 \frac{\partial}{\partial t_1} - \frac{1}{2} \epsilon^2 h_0^2 \left(\frac{\partial}{\partial t_0} + \boldsymbol{c}_i \cdot \nabla \right)^2 + O(\epsilon^3) \end{aligned} \tag{3.72}$$

for the leading–order behavior. Expanding the density P and the transfer coefficients T_i up to linear order and collecting terms according to their powers of ϵ, one obtains in order ϵ

$$\sum_i \left(\frac{\partial}{\partial t_0} + \boldsymbol{c}_i \cdot \nabla \right) T_i^{(0)} P^{(0)} = 0, \tag{3.73}$$

and at order ϵ^2

$$\begin{aligned} &\sum_i \left[\frac{\partial}{\partial t_1} - \frac{h_0}{2} \left(\frac{\partial}{\partial t_0} + \boldsymbol{c}_i \cdot \nabla \right)^2 \right] T_i^{(0)} P^{(0)} \\ + \;&\sum_i \left(\frac{\partial}{\partial t_0} + \boldsymbol{c}_i \cdot \nabla \right) \left(T_i^{(0)} P^{(1)} + T_i^{(1)} P^{(0)} \right) \;=\; 0\,. \end{aligned} \tag{3.74}$$

We abbreviate the moments as before (see Eq. (3.17)) and thus we find at order ϵ

$$\left(\frac{\partial}{\partial t_0} + \nabla \cdot \boldsymbol{u}^{(0)} \right) P^{(0)} \;=\; 0\,, \tag{3.75}$$

and at order ϵ^2

$$\begin{aligned} &\left[\frac{\partial}{\partial t_1} - \frac{h_0}{2} \frac{\partial^2}{\partial t_0^2} - h_0 \frac{\partial}{\partial t_0} \nabla \cdot \boldsymbol{u}^{(0)} - \frac{h_0}{2} \partial_\alpha \partial_\beta q_{\alpha\beta}^{(0)} \right] P^{(0)} \\ + \;&\left(\frac{\partial}{\partial t_0} + \nabla \cdot \boldsymbol{u}^{(0)} \right) P^{(1)} + \nabla \cdot \boldsymbol{u}^{(1)} P^{(0)} \;=\; 0\,. \end{aligned} \tag{3.76}$$

Making use of

$$\left(\frac{\partial}{\partial t_0}+\nabla\cdot\boldsymbol{u}^{(0)}\right)^2=\frac{\partial^2}{\partial t_0^2}+2\frac{\partial}{\partial t_0}\nabla\cdot\boldsymbol{u}^{(0)}+\partial_\alpha u_\alpha^{(0)}\partial_\beta u_\beta^{(0)}-\nabla\cdot\left(\frac{\partial}{\partial t_0}\boldsymbol{u}^{(0)}\right), \quad (3.77)$$

this is rewritten as

$$\begin{aligned}&\left(\frac{\partial}{\partial t_1}+\nabla\cdot\boldsymbol{u}^{(1)}\right)P^{(0)}-\frac{h_0}{2}\left(\frac{\partial}{\partial t_0}+\nabla\cdot\boldsymbol{u}^{(0)}\right)^2P^{(0)} \quad (3.78)\\ +\;&\left(\frac{h_0}{2}\partial_\alpha u_\alpha^{(0)}\partial_\beta u_\beta^{(0)}-\frac{h_0}{2}\partial_\alpha\partial_\beta q_{\alpha\beta}^{(0)}-\frac{h_0}{2}\nabla\cdot\left(\frac{\partial}{\partial t_0}\boldsymbol{u}^{(0)}\right)\right)P^{(0)}\\ +\;&\left(\frac{\partial}{\partial t_0}+\nabla\cdot\boldsymbol{u}^{(0)}\right)P^{(1)}=0.\end{aligned}$$

Applying Eq. (3.75) and the operator identity

$$\partial_\alpha u_\alpha^{(0)}\partial_\beta u_\beta^{(0)}=\partial_\alpha\partial_\beta u_\alpha^{(0)}u_\beta^{(0)}-\partial_\alpha u_\beta^{(0)}(\partial_\beta u_\alpha^{(0)}), \quad (3.79)$$

we further simplify

$$\begin{aligned}&\left(\frac{\partial}{\partial t_1}+\nabla\cdot\boldsymbol{u}^{(1)}\right)P^{(0)}+\left(\frac{\partial}{\partial t_0}+\nabla\cdot\boldsymbol{u}^{(0)}\right)P^{(1)} \quad (3.80)\\ =\;&\frac{h_0}{2}\partial_\alpha\partial_\beta\left(q_{\alpha\beta}^{(0)}-u_\alpha^{(0)}u_\beta^{(0)}\right)P^{(0)}+\frac{h_0}{2}\partial_\alpha\left(u_\beta^{(0)}(\partial_\beta u_\alpha^{(0)})+\left(\frac{\partial}{\partial t_0}u_\alpha^{(0)}\right)\right)P^{(0)}.\end{aligned}$$

Now, imposing the condition that the equations should be conservation laws at each order, we see that the terms involving $P^{(0)}$ would act as source term for $P^{(1)}$, and vice versa, unless they vanish separately. Therefore Eq. (3.80) is splitted up into two equations at order ϵ^2,

$$\left(\frac{\partial}{\partial t_0}+\nabla\cdot\boldsymbol{u}^{(0)}\right)P^{(1)} = 0, \quad (3.81a)$$

$$\begin{aligned}\left(\frac{\partial}{\partial t_1}+\nabla\cdot\boldsymbol{u}^{(1)}\right)P^{(0)} &= \frac{h_0}{2}\partial_\alpha\partial_\beta\left(q_{\alpha\beta}^{(0)}-u_\alpha^{(0)}u_\beta^{(0)}\right)P^{(0)} \quad (3.81b)\\ &+ \frac{h_0}{2}\partial_\alpha\left(u_\beta^{(0)}(\partial_\beta u_\alpha^{(0)})+\left(\frac{\partial}{\partial t_0}u_\alpha^{(0)}\right)\right)P^{(0)}.\end{aligned}$$

Multiplying the latter equation with ϵ and adding to Eq. (3.75), we find

$$\begin{aligned}&\left[\frac{\partial}{\partial t_0}+\epsilon\frac{\partial}{\partial t_1}+\nabla\cdot\left(\boldsymbol{u}^{(0)}+\epsilon\boldsymbol{u}^{(1)}\right)\right]P^{(0)} \quad (3.82)\\ =\;&\frac{h}{2}\partial_\alpha\partial_\beta\left(q_{\alpha\beta}^{(0)}-u_\alpha^{(0)}u_\beta^{(0)}\right)P^{(0)}\\ +\;&\frac{h}{2}\partial_\alpha\left(u_\beta^{(0)}(\partial_\beta u_\alpha^{(0)})+\left(\frac{\partial}{\partial t_0}u_\alpha^{(0)}\right)\right)P^{(0)}.\end{aligned}$$

The full time dependence is given by

$$\frac{\partial}{\partial t} = \frac{\partial t_0}{\partial t}\frac{\partial}{\partial t_0} + \frac{\partial t_1}{\partial t}\frac{\partial}{\partial t_1} = \frac{\partial}{\partial t_0} + \epsilon\frac{\partial}{\partial t_1}\,, \tag{3.83}$$

hence we write

$$\begin{aligned}\left[\frac{\partial}{\partial t} + \nabla\cdot\left(\boldsymbol{u}^{(0)} + \epsilon\boldsymbol{u}^{(1)}\right)\right] P^{(0)} &= \frac{h}{2}\partial_\alpha\partial_\beta\left(q^{(0)}_{\alpha\beta} - u^{(0)}_\alpha u^{(0)}_\beta\right) P^{(0)} \\ &+ \frac{h}{2}\partial_\alpha\left(u^{(0)}_\beta(\partial_\beta u^{(0)}_\alpha) + \left(\frac{\partial}{\partial t_0}u^{(0)}_\alpha\right)\right) P^{(0)}.\end{aligned} \tag{3.84}$$

At this point, there are at least *two* possibilities to make sure that the asymptotic equation for $P^{(0)}$ is indeed the convection–diffusion equation. For the first possibility we set

$$\boldsymbol{u}^{(0)} = 0, \tag{3.85}$$

$$\epsilon\boldsymbol{u}^{(1)} = \boldsymbol{v}, \tag{3.86}$$

$$q^{(0)}_{\alpha\beta} = \frac{2D}{h}\delta_{\alpha\beta}, \tag{3.87}$$

and make sure that these moment conditions are satisfied by the choice of suitable coefficients. Comparison with Eq. (3.24) shows that this is exactly what was achieved for the leading–order in the diffusive-scaling analysis. Therefore we can just copy the transfer coefficients and write

$$T_i = w_i\left(1 + \frac{h}{2D}\boldsymbol{v}\cdot\boldsymbol{c}_i\right). \tag{3.88}$$

We now go back to Eq. (3.84) and discuss the other possibility to obtain the correct asymptotic behavior. This is obtained by requiring

$$\boldsymbol{u}^{(0)} = \boldsymbol{v}\,, \tag{3.89}$$

$$q^{(0)}_{\alpha\beta} = \frac{2D}{h}\delta_{\alpha\beta} + v_\alpha v_\beta\,, \tag{3.90}$$

$$\epsilon u^{(1)}_\alpha = \frac{h}{2}v_\beta\partial_\beta v_\alpha + \frac{h}{2}\frac{\partial}{\partial t_0}v_\alpha\,. \tag{3.91}$$

Choosing the velocity weights w_i in such a way that $\kappa_4 = 0$ and $\sigma_4 = \sigma_2^2$, which means that they have to be chosen like the weights in a standard lattice Boltzmann model, resulting in $\sigma_2 = (1/3)(a/h)^2$, the above conditions can be satisfied by picking

$$\begin{aligned}\frac{T_i}{w_i} &= 1 + \frac{\boldsymbol{v}\cdot\boldsymbol{c}_i}{\sigma_2} + \frac{1}{2\sigma_2^2}\left(c_{i\alpha}c_{i\beta} - \sigma_2\delta_{\alpha\beta}\right)v_\alpha v_\beta \\ &+ \frac{h}{2\sigma_2}c_{i\alpha}v_\beta\partial_\beta v_\alpha + \frac{h}{2\sigma_2}c_{i\alpha}\frac{\partial}{\partial t}v_\alpha\,,\end{aligned} \tag{3.92}$$

again with

$$D = \frac{h}{2}\sigma_2. \tag{3.93}$$

It is extremely interesting that this form is very similar but not identical to Eq. (3.53). We see that here the terms proportional to the diffusion constant do not appear.
Numerical analysis of the two algorithms outlined here shows that the error in *both* cases is $\mathcal{O}(a^2) = \mathcal{O}(h)$. This is, for *both* cases, well understood in terms of the diffusive–scaling analysis. Interestingly enough, however, one finds that the more sophisticated algorithm is also more *stable*: The critical Peclet number $Pe = (va/D)$ at which the results become obviously wrong is, for the second algorithm, again roughly *twice* as large as for the simple implementation.
Fig. 3.5 presents the averaged error as function of the lattice spacing of the numerical results of three dimensional implementations of the fourth order algorithm as discussed in Sec. 3.1.4 and of the algorithm developed by the multi–scale expansion above. Both implementations use the D3Q19 model and are applied to the one dimensional test problem with source (see Sec. 3.3.2). We compare the accuracy to an implementation of a D3Q6 lattice Boltzmann model which was first analyzed by Guo et al. [79, 80] and extended by some correction term in the PhD thesis of J. Lätt [81]. The Chapman–Enskog expansion of this LB model has been performed by the same multi–time scale scheme and up to the same order in ϵ as the analysis above. Indeed we find that in both methods the same expansion yields the same accuracy.

3.5. Boundary Conditions

Defining and analyzing boundary conditions can be one of the most challenging and also one of the most tedious exercises in the method development of lattice algorithms. The goal of this section is to give a conceptually straightforward approximation for *no–flux* boundary conditions in the second order algorithm. In general the CDE is a continuity equation

$$\partial_t P + \nabla \cdot \boldsymbol{j} = 0\,, \tag{3.94}$$

where the flux density $\boldsymbol{j}$ consists of a diffusive and a convective current

$$\boldsymbol{j} = -D\nabla P + \boldsymbol{v}P\,. \tag{3.95}$$

If the spatial domain is confined by solid walls or if a solid object is present, we have to define how the density and the fluxes will interact with a solid interface. At a boundary, we expect that density can only flow parallel to the wall, but never crosses the interface, and thus, the current density perpendicular to the interface must vanish. This can be written in the *no–flux* boundary conditions

$$\boldsymbol{j} \cdot \boldsymbol{n} = 0\,, \tag{3.96}$$

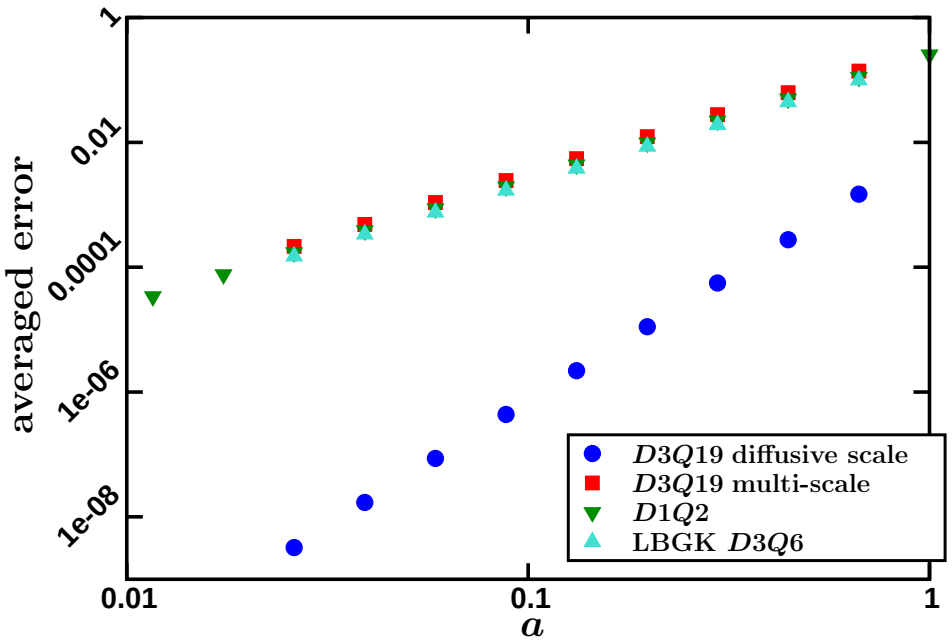

Figure 3.5.: Averaged error as function of the lattice spacing a for 3–dimensional implementations of the fourth order algorithm as discussed in the diffusive scaling section and the algorithm developed by the multi–scale expansion above. This is compared to a (LBGK) lattice Boltzmann implementation, based on the method discussed in [81]. The *LBGK* parameter was set to $\lambda = 1.2$. The coefficients and parameters are the same as in Fig. 3.3. For comparison the data from the $D1Q2$ model of Fig. 3.4 is also plotted.

where $\boldsymbol{n}$ is the normal at the interface, pointing into the fluid.
Since the algorithm is very similar to the lattice Boltzmann method, it turns out that also the boundary conditions can be treated in a very analogous way [82, 83].
We start by decomposing the current density into a part parallel to the surface and one part perpendicular to it,

$$\begin{aligned} \boldsymbol{j} &= (\overleftrightarrow{\boldsymbol{I}} - \boldsymbol{n} \otimes \boldsymbol{n})\boldsymbol{j} + (\boldsymbol{n} \otimes \boldsymbol{n})\boldsymbol{j} \\ &\equiv \boldsymbol{j}^{\parallel} + \boldsymbol{j}^{\perp} . \end{aligned} \tag{3.97}$$

In order to satisfy the no–flux boundary conditions, the perpendicular term must vanish at the surface. This is the case if we succeed in modifying our algorithm such that

$$\boldsymbol{j}(\boldsymbol{r}) = \boldsymbol{j}^{\parallel}(\boldsymbol{r}) , \tag{3.98}$$

where $\boldsymbol{r}$ is a grid node in the boundary. Defining the projection operator

$$\delta^{\parallel}_{\alpha\beta} = \delta_{\alpha\beta} - n_\alpha n_\beta \,, \tag{3.99}$$

one may write the current density

$$\begin{aligned} j^{\parallel}_\alpha &= \delta^{\parallel}_{\alpha\beta} j_\beta \\ &= \delta^{\parallel}_{\alpha\beta}(-D\partial_\beta P + v_\beta P) \\ &= -D\delta^{\parallel}_{\alpha\beta}\partial_\beta P + v^{\parallel}_\alpha P \,, \end{aligned} \tag{3.100}$$

where we abbreviate

$$v^{\parallel}_\alpha = \delta^{\parallel}_{\alpha\beta} v_\beta \,. \tag{3.101}$$

For reasons of simplicity and also of relevance in view of the electrokinetic problem, we restrict ourselves to the case of the leading order algorithm, i. e. the *D3Q6* model, and furthermore, to the case of a convex surface. The goal of this section is to modify the transfer coefficients in such a way that the continuum limit will satisfy the boundary conditions. We start from the ansatz

$$T^{\parallel}_i = w^{\parallel}_i \left(1 + \frac{1}{\sigma_2} \boldsymbol{v} \cdot \boldsymbol{c}^{\parallel}_i\right) \,. \tag{3.102}$$

Here, $\boldsymbol{c}^{\parallel}_i$ is a projected set of grid velocities

$$c^{\parallel}_{i,\alpha} := \delta^{\parallel}_{\alpha\beta} c_{i,\alpha} \,. \tag{3.103}$$

If we choose $\boldsymbol{n}$ to point in a high-symmetry direction of the lattice, then the moments of the weights will satisfy relations analogous to those in the bulk:

$$\sum_i w^{\parallel}_i = 1 \,, \tag{3.104}$$

$$\sum_i w^{\parallel}_i c^{\parallel}_{i,\alpha} = 0 \,, \tag{3.105}$$

$$\sum_i w^{\parallel}_i c^{\parallel}_{i,\alpha} c^{\parallel}_{i,\beta} = \sigma_2 \delta^{\parallel}_{\alpha\beta} \,, \tag{3.106}$$

$$\sum_i w^{\parallel}_i c^{\parallel}_{i,\alpha} c^{\parallel}_{i,\beta} c^{\parallel}_{i,\gamma} = 0 \,, \tag{3.107}$$

resulting in moments of the modified transfer coefficients:

$$\sum_i T_i^{\parallel} = 1\,, \tag{3.108}$$

$$\sum_i T_i^{\parallel} c_{i,\alpha}^{\parallel} = \delta_{\alpha\beta}^{\parallel} v_\beta = v_\beta^{\parallel}\,, \tag{3.109}$$

$$\sum_i T_i^{\parallel} c_{i,\alpha}^{\parallel} c_{i,\beta}^{\parallel} = \sigma_2 \delta_{\alpha\beta}^{\parallel} \equiv \frac{2}{h} D \delta_{\alpha\beta}^{\parallel}\,. \tag{3.110}$$

Hence, the same expansion as done for the bulk case recovers the desired equation in the continuum limit. For consistency reasons we further require

$$\sigma_2 = \frac{1}{d}\frac{a^2}{h^2}\,. \tag{3.111}$$

If this would not be the case, either the timestep or the diffusion constant would differ from the bulk part.
In the three dimensional case with six grid velocities, i. e. the *D3Q6* model, and in the case of a convex interface, we have to distinguish between 3 different classes of *next–to–surface* nodes, concerning to the number of neighboring boundary nodes. The surface normal of the discretized surface is a unit vector, pointing in the direction of the "center of mass" of the remaining links.

Case 1: 1 neighboring boundary node
In the case that moving density is prohibited for only one link, one may classify the weights into three different classes. Obviously, the weight concerning to the forbidden move must be zero,

$$w_0^{\parallel} = 0\,. \tag{3.112}$$

The other two weights pertain to the link aligned with $\boldsymbol{n}$ and pointing into the fluid $w_I^{\parallel}$, and to those four velocities parallel to the surface $w_{II}^{\parallel}$. The projection of the grid velocity perpendicular to the surface vanishes, while the other velocities do not change. Thus we get from the mass conservation condition and from the second moments the conditions

$$w_I^{\parallel} + 4w_{II}^{\parallel} = 1\,, \tag{3.113}$$

$$2w_{II}^{\parallel}\frac{a^2}{h^2} = \sigma_2\,. \tag{3.114}$$

Hence, the weights are given by

$$w_0^{\parallel} = 0\,, \tag{3.115}$$
$$w_I^{\parallel} = \frac{1}{3}\,, \tag{3.116}$$
$$w_{II}^{\parallel} = \frac{1}{6}\,. \tag{3.117}$$

Case 2: 2 neighboring boundary nodes
In the second case, density could be moved along four remaining links. One can classify the links, and thus the weights, into three different classes. For the "forbidden" links, the weights must again vanish. Two links have some portion aligned parallel to the surface and some perpendicular to it. Their weights must be equal for symmetry reasons and we denote this weight by $w_I^{\parallel}$. The remaining two links are strictly aligned tangential to the surface, and are weighted by $w_{II}^{\parallel}$. From the mass conservation condition one obtains

$$2w_I^{\parallel} + 2w_{II}^{\parallel} = 1\,. \tag{3.118}$$

The second moment yields

$$\frac{1}{2}w_I^{\parallel}\frac{a^2}{h^2} = \frac{1}{2}\sigma_2\,, \tag{3.119}$$
$$2w_{II}^{\parallel}\frac{a^2}{h^2} = \sigma_2\,. \tag{3.120}$$

This results in

$$w_0^{\parallel} = 0\,, \tag{3.121}$$
$$w_I^{\parallel} = \frac{1}{3}\,, \tag{3.122}$$
$$w_{II}^{\parallel} = \frac{1}{6}\,. \tag{3.123}$$

Case 3: 3 neighboring boundary nodes
The last case consists in a grid node, surrounded by three "forbidden" and three "movable" links. In this case, no link is strictly aligned parallel or perpendicular to the solid interface, and we get only two classes of connectors. Setting again $w_0^{\parallel} = 0$, we obtain from normalization

$$w_I^{\parallel} = \frac{1}{3}\,. \tag{3.124}$$

This is perfectly consistent with the second moment condition, resulting in

$$w_I^{\parallel}\frac{a^2}{h^2} = \sigma_2\,. \tag{3.125}$$

All together this results in a boundary condition where the weights of the bulk method corresponding to "forbidden" links are added to the weight of the corresponding mirror-image.

4. Solving the Stokes Equation via Surface Integrals

In the previous chapters, numerical methods have been presented for solving the Poisson equation, the Poisson-Boltzmann equation and the convection-diffusion equation. Last but not least, a numerical method to solve the stationary incompressible Stokes equation (1.54b) and (1.54c) is needed. More general, this equation is of the form

$$\nabla \cdot \boldsymbol{v}(\boldsymbol{r}) = 0\,, \tag{4.1a}$$

$$-\nabla p(\boldsymbol{r}) + \eta \nabla^2 \boldsymbol{v}(\boldsymbol{r}) = -\boldsymbol{f}(\boldsymbol{r})\,. \tag{4.1b}$$

Here, $\boldsymbol{f}$ is an external force density and η denotes the viscosity of the fluid. As mentioned before, the computational domain is a rectangular parallelepiped with periodic boundary conditions and the colloids are massive objects located within this spatial domain.
Since we are only interested in the stationary case and vanishing Reynolds number, Eq. (4.1) is of a rather simple form. In this chapter a fast method will be presented, making use of these simplifications.
After the calculation of the corresponding Green's function, a "reaction force density" is defined, accounting for the boundary conditions at the surface of a solid object. This reaction force density can be determined by integrating over the surface of the obstacles.
The idea of using surface integrals for solving the Stokes equation in the presence of solid objects is not new. In 1972, Youngren and Acrivos [84] were the first to publish a numerical method employing surface integrals to solve the Stokes flow past particles of arbitrary shape in unbounded flows. Later, Zick and Homsy [85] also replaced the Stokes problem by equivalent integral equations for systems of periodic arrays of spheres.

4.1. The Stationary Stokes Equation and its Solution in Bulk

If, in a first step, the boundary conditions are neglected, the Green's function of Eq. (4.1) can be calculated analytically. This Green's function is called Oseen tensor and its calculation belongs to the standard methods in hydrodynamics (see for example [86]).

Since in Fourier space the evaluation of differential operators is rather simple, an expansion by Fourier series is applied to p, $\boldsymbol{v}$ and $\boldsymbol{f}$,

$$p(\boldsymbol{r}) = \sum_{\boldsymbol{k}} \hat{p}(\boldsymbol{k}) \exp[-i\boldsymbol{k}\cdot\boldsymbol{r}]\,, \tag{4.2}$$

$$\boldsymbol{v}(\boldsymbol{r}) = \sum_{\boldsymbol{k}} \hat{\boldsymbol{u}}(\boldsymbol{k}) \exp[-i\boldsymbol{k}\cdot\boldsymbol{r}]\,, \tag{4.3}$$

$$\boldsymbol{f}(\boldsymbol{r}) = \sum_{\boldsymbol{k}} \hat{\boldsymbol{f}}(\boldsymbol{k}) \exp[-i\boldsymbol{k}\cdot\boldsymbol{r}]\,. \tag{4.4}$$

In Fourier space, the Stokes equation then has the form

$$0 = -i\boldsymbol{k}\cdot\hat{\boldsymbol{v}}(\boldsymbol{k})\,, \tag{4.5a}$$

$$0 = i\boldsymbol{k}\,\hat{p}(\boldsymbol{k}) - \eta\boldsymbol{k}^2\,\hat{\boldsymbol{v}}(\boldsymbol{k}) + \hat{\boldsymbol{f}}(\boldsymbol{k})\,. \tag{4.5b}$$

Multiplying by $i\boldsymbol{k}$ and making use of the incompressibility condition, one obtains

$$0 = -\boldsymbol{k}^2\,\hat{p}(\boldsymbol{k}) + i\boldsymbol{k}\cdot\hat{\boldsymbol{f}}(\boldsymbol{k})\,. \tag{4.6}$$

Solving this for $\hat{p}$ results in

$$\hat{p}(\boldsymbol{k}) = \frac{i}{\boldsymbol{k}^2}\boldsymbol{k}\cdot\hat{\boldsymbol{f}}(\boldsymbol{k})\,, \tag{4.7}$$

and hence

$$\begin{aligned} i\boldsymbol{k}\,\hat{p}(\boldsymbol{k}) &= -\frac{1}{\boldsymbol{k}^2}\boldsymbol{k}\left(\boldsymbol{k}\cdot\hat{\boldsymbol{f}}(\boldsymbol{k})\right) \\ &= -\frac{\boldsymbol{k}\otimes\boldsymbol{k}}{\boldsymbol{k}^2}\hat{\boldsymbol{f}}(\boldsymbol{k})\,. \end{aligned} \tag{4.8}$$

This means that we adjust the pressure such that the incompressibility is enforced, i. e. the pressure has the function of a Lagrange multiplier related to the constraint of incompressibility. Now, inserting Eq. (4.8) into Eq. (4.5) and solving for $\hat{\boldsymbol{v}}$ finally yields the velocity field in Fourier space

$$\begin{aligned} \hat{\boldsymbol{v}}(\boldsymbol{k}) &= \frac{1}{\eta\boldsymbol{k}^2}\left(\overleftrightarrow{\boldsymbol{I}} - \frac{\boldsymbol{k}\otimes\boldsymbol{k}}{\boldsymbol{k}^2}\right)\hat{\boldsymbol{f}}(\boldsymbol{k}) \\ &\equiv \hat{\overleftrightarrow{\boldsymbol{T}}}(\boldsymbol{k})\hat{\boldsymbol{f}}(\boldsymbol{k})\,. \end{aligned} \tag{4.9}$$

For the back transformation, we first require that the externally given force field does not accelerate the finite system, i. e. the flow is observed in the center-of-mass reference frame. Hence, $\boldsymbol{f}$ has to satisfy the condition

$$\int_V d^3r\,\boldsymbol{f}(\boldsymbol{r}) = 0\,. \tag{4.10}$$

Making use of this requirement, the force density can also be expressed as

$$\boldsymbol{f}(\boldsymbol{r}) = \int_V d^3r' \left(\boldsymbol{f}(\boldsymbol{r}')\delta(\boldsymbol{r}-\boldsymbol{r}') - \frac{1}{V}\boldsymbol{f}(\boldsymbol{r}') \right) , \tag{4.11}$$

where the latter term describes a constant compensating field. Multiplying $\boldsymbol{f}(\boldsymbol{r})$ with $\exp[i\boldsymbol{q}\cdot\boldsymbol{r}]$ and integrating over the finite volume results in

$$\begin{aligned} \int_V d^3r\, \boldsymbol{f}(\boldsymbol{r}) \exp[i\boldsymbol{q}\cdot\boldsymbol{r}] &= \sum_{\boldsymbol{k}} \hat{\boldsymbol{f}}(\boldsymbol{k}) \int_V d^3r\, \exp[-i(\boldsymbol{k}-\boldsymbol{q})\cdot\boldsymbol{r}] \\ &= \sum_{\boldsymbol{k}} \hat{\boldsymbol{f}}(\boldsymbol{k}) V \delta_{\boldsymbol{kq}} \\ &= V\hat{\boldsymbol{f}}(\boldsymbol{q}) \end{aligned} \tag{4.12}$$

or

$$\hat{\boldsymbol{f}}(\boldsymbol{k}) = \frac{1}{V}\int_V d^3r\, \boldsymbol{f}(\boldsymbol{r}) \exp[i\boldsymbol{k}\cdot\boldsymbol{r}] . \tag{4.13}$$

Application of Eq. (4.11) yields

$$\begin{aligned} \hat{\boldsymbol{f}}(\boldsymbol{k}) &= \frac{1}{V}\int_V d^3r \int_V d^3r'\, \boldsymbol{f}(\boldsymbol{r}')\delta(\boldsymbol{r}-\boldsymbol{r}') \exp[i\boldsymbol{k}\cdot\boldsymbol{r}] \\ &\quad -\frac{1}{V^2}\int_V d^3r \int_V d^3r'\, \boldsymbol{f}(\boldsymbol{r}') \exp[i\boldsymbol{k}\cdot\boldsymbol{r}] \\ &= \frac{1}{V}\int_V d^3r'\, \boldsymbol{f}(\boldsymbol{r}') \exp[i\boldsymbol{k}\cdot\boldsymbol{r}'] - \frac{1}{V}\int_V d^3r'\, \boldsymbol{f}(\boldsymbol{r}')\delta_{\boldsymbol{k}0} \\ &= \frac{1}{V}\int_V d^3r'\, \boldsymbol{f}(\boldsymbol{r}') \exp[i\boldsymbol{k}\cdot\boldsymbol{r}'] (1-\delta_{\boldsymbol{k}0}) . \end{aligned} \tag{4.14}$$

Inserting this into Eq. (4.9) and applying Eq. (4.3), finally results in the desired solution for the Stokes equation

$$\begin{aligned} \boldsymbol{v}(\boldsymbol{r}) &= \int_V d^3r' \frac{1}{V\eta} \sum_{\boldsymbol{k}\neq 0} \frac{\exp[-i\boldsymbol{k}\cdot(\boldsymbol{r}-\boldsymbol{r}')]}{\boldsymbol{k}^2} \left(\overleftrightarrow{\boldsymbol{I}} - \frac{\boldsymbol{k}\otimes\boldsymbol{k}}{\boldsymbol{k}^2} \right) \boldsymbol{f}(\boldsymbol{r}') \\ &= \int d^3r'\, \overleftrightarrow{\boldsymbol{T}}\,(\boldsymbol{r}-\boldsymbol{r}')\boldsymbol{f}(\boldsymbol{r}') . \end{aligned} \tag{4.15}$$

The tensor

$$\overleftrightarrow{\boldsymbol{T}}\,(\boldsymbol{r}) = \frac{1}{V\eta} \sum_{\boldsymbol{k}\neq 0} \frac{\exp[-i\boldsymbol{k}\cdot\boldsymbol{r}]}{\boldsymbol{k}^2} \left(\overleftrightarrow{\boldsymbol{I}} - \frac{\boldsymbol{k}\otimes\boldsymbol{k}}{\boldsymbol{k}^2} \right) \tag{4.16}$$

is the famous Oseen tensor in a finite size corrected formulation.

4.2. Boundary Conditions and Induced Force Density

Eq. (4.16) is the bulk solution of the Stokes equation, i. e. only periodic boundary conditions occur. Now consider a solid object with surface Ω dissolved in an ambient fluid with an externally applied force field $\boldsymbol{f}_{ext}(\boldsymbol{r})$ with $\int_V d^3r\, \boldsymbol{f}_{ext}(\boldsymbol{r}) = 0$. This object will move with a constant velocity through the fluid, which implies a boundary condition of $\boldsymbol{v}(\boldsymbol{r}_\Omega) = const.$ on the surface of the solid obstacle.
This problem is strongly related to solving the Poisson equation when a constant field is acting on a metallic sphere. In both cases, the Green's function is known and similarly to the problem above, the boundary condition for the metallic sphere is given by a constant potential $\psi(\boldsymbol{r}) = const.$ on the surface. In the electrostatic case, it is well known that a charge density is induced on the surface to compensate the effect of an external field and thus it satisfies the boundary condition.
In the hydrodynamic case, this picture is very helpful for finding a solution for the Stokes equation. We introduce, in analogy to the induced charge density, a *reaction force density* $\boldsymbol{f}_{reac}$, which accounts for the boundary conditions. This reaction force is only acting on the surface of the particle

$$\boldsymbol{f}_{reac}(\boldsymbol{r}) = 0, \quad \text{if } \boldsymbol{r} \notin \Omega\,. \tag{4.17}$$

The solution of the Stokes equation then reads as

$$\begin{aligned} \boldsymbol{v}(\boldsymbol{r}) &= \int_V d^3r'\ \overleftrightarrow{\boldsymbol{T}}\,(\boldsymbol{r}-\boldsymbol{r}')\left\{\boldsymbol{f}_{ext}(\boldsymbol{r}') + \boldsymbol{f}_{reac}(\boldsymbol{r}')\right\} \\ &\equiv \int_V d^3r'\ \overleftrightarrow{\boldsymbol{T}}\,(\boldsymbol{r}-\boldsymbol{r}')\,\boldsymbol{f}_{tot}(\boldsymbol{r}')\,. \end{aligned} \tag{4.18}$$

Thus, one may decompose the velocity field into a bulk part plus some reaction part $\boldsymbol{v} \equiv \boldsymbol{v}^{(1)} + \boldsymbol{v}^{(2)}$, with

$$\boldsymbol{v}^{(1)}(\boldsymbol{r}) = \int_V d^3r'\ \overleftrightarrow{\boldsymbol{T}}\,(\boldsymbol{r}-\boldsymbol{r}')\,\boldsymbol{f}_{ext}(\boldsymbol{r}')\,, \tag{4.19}$$

$$\boldsymbol{v}^{(2)}(\boldsymbol{r}) = \int_V d^3r'\ \overleftrightarrow{\boldsymbol{T}}\,(\boldsymbol{r}-\boldsymbol{r}')\,\boldsymbol{f}_{reac}(\boldsymbol{r}')\,. \tag{4.20}$$

The reaction force has to be adjusted such that the boundary conditions are satisfied. Although the constant value of the Dirichlet boundary condition is a priori not known, it can be replaced by a "difference" condition in the discrete case

$$\boldsymbol{v}(\boldsymbol{r}_{ref}) - \boldsymbol{v}(\boldsymbol{r}_\Omega) = 0\,. \tag{4.21}$$

Here, $\boldsymbol{r}_{ref} \in \Omega$ is an arbitrary but fixed reference point on the surface of the solid object. Making use of Eq. (4.18), this condition can equivalently be written as

$$\int_V d^3r' \overleftrightarrow{\boldsymbol{T}}(\boldsymbol{r}_{ref} - \boldsymbol{r}')\boldsymbol{f}_{tot}(\boldsymbol{r}') - \int_V d^3r' \overleftrightarrow{\boldsymbol{T}}(\boldsymbol{r}_{\Omega} - \boldsymbol{r}')\boldsymbol{f}_{tot}(\boldsymbol{r}') = 0\,, \tag{4.22}$$

and since reaction forces only occur on the surface of the object, the volume integral can be replaced by surface integrals

$$\begin{aligned} &\int d\Omega' \overleftrightarrow{\boldsymbol{T}}(\boldsymbol{r}_{ref} - \boldsymbol{r}')\boldsymbol{f}_{reac}(\boldsymbol{r}') - \int d\Omega' \overleftrightarrow{\boldsymbol{T}}(\boldsymbol{r}_{\Omega} - \boldsymbol{r}')\boldsymbol{f}_{reac}(\boldsymbol{r}') \\ = \;& \boldsymbol{v}^{(1)}(\boldsymbol{r}_{\Omega}) - \boldsymbol{v}^{(1)}(\boldsymbol{r}_{ref})\,. \end{aligned} \tag{4.23}$$

Since the system is studied in the center-of-mass reference frame, it is required that the total reaction force must vanish

$$\int d\Omega' f_{reac}(\boldsymbol{r}') = 0. \tag{4.24}$$

On a regular cubic lattice, these conditions are replaced by a linear set of equations

$$\sum_{\Omega'} \left(\overleftrightarrow{\boldsymbol{T}}(\boldsymbol{r}_{ref} - \boldsymbol{r}_{\Omega'}) - \overleftrightarrow{\boldsymbol{T}}(\boldsymbol{r}_{\Omega} - \boldsymbol{r}_{\Omega'}) \right) \boldsymbol{f}_{reac}(\boldsymbol{r}_{\Omega'}) = \boldsymbol{v}^{(1)}(\boldsymbol{r}_{\Omega}) - \boldsymbol{v}^{(1)}(\boldsymbol{r}_{ref})\,, \tag{4.25}$$

and

$$\sum_{\Omega'} \boldsymbol{f}_{reac}(\boldsymbol{r}_{\Omega'}) = 0\,. \tag{4.26}$$

For consistency reasons we use a discrete formulation of the Oseen tensor, analogous to the lattice–Green's function of the Poisson equation (see Eq. (1.75)). The derivation of the discretized Oseen tensor is presented in appendix A.4. Eq. (4.25) is trivially satisfied if $\boldsymbol{r}_{\Omega} = \boldsymbol{r}_{ref}$. Hence, Eq. (4.25) results in $M - 1$ independent equations for M surface nodes. Together with Eq. (4.26), we have a linear set of M linearly independent equations for M unknown reaction forces.

It should be noted that this formulation of the Stokes solver neglects possible rotations of the obstacles. However, since we are only interested in highly symmetric objects, i. e. spheres, rotations should not occur. Due to the requirement that we are searching for a stationary solution, a further limitation of this method consists in the fact that, if more than one particle should be observed, these objects will move collectively, i. e. no relative velocities occur. In the case of colloidal crystals this means that all colloids are connected via rigid bonds.

4.3. Algorithm

Combining the way of solving the Stokes equation in the bulk with the method of calculating reaction forces in order to satisfy the Dirichlet boundary conditions results in a computational algorithm consisting of only a few steps. These steps follow the principle that a Fourier transformation can be computed much more efficiently than a convolution, since highly optimized libraries like the *FFTW3* project are readily available [87].

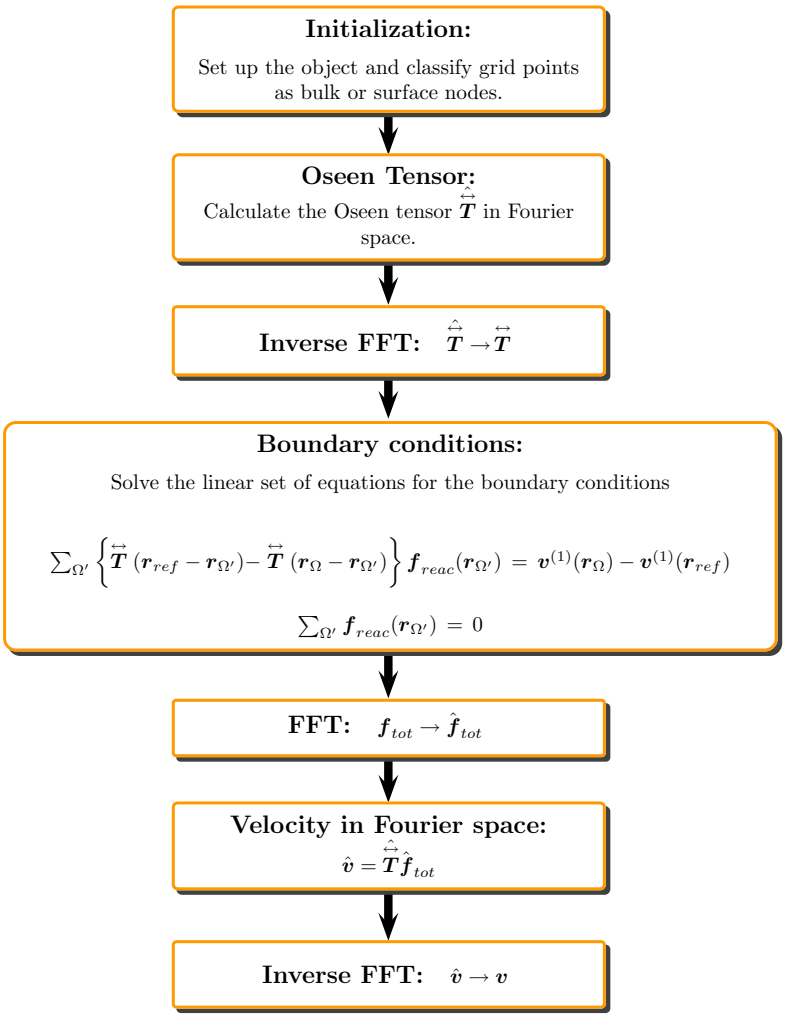

Figure 4.1.: Illustration of the Stokes equation solver.

In a first step, the system has to be initialized. This means that each lattice site has to be marked as a 'bulk' or 'surface' node to define the boundary of the

obstacles. Then, the Oseen tensor in Fourier space can be easily calculated and transformed back to real space. At this point, everything for the calculation of the total force density is known, including the external and the reaction forces. A linear set of equations of the following form has to be solved

$$\overleftrightarrow{\boldsymbol{A}}\, \boldsymbol{f}_{tot} = \boldsymbol{b}\,, \tag{4.27}$$

where $\overleftrightarrow{\boldsymbol{A}}$ includes Eq. (4.25) and Eq. (4.26). After calculating the total force in real space, we again apply a fast Fourier transformation $\boldsymbol{f}_{tot} \rightarrow \hat{\boldsymbol{f}}_{tot}$ to calculate the flow velocity field in Fourier space

$$\hat{\boldsymbol{v}} = \hat{\overleftrightarrow{\boldsymbol{T}}}\hat{\boldsymbol{f}}_{tot}\,. \tag{4.28}$$

A backtransformation $\hat{\boldsymbol{v}} \rightarrow \boldsymbol{v}$ then results in the desired solution of Stokes equation. The algorithm is briefly illustrated in Fig. 4.1.

The computationally most expensive part is to solve Eq. (4.27). The matrix $\overleftrightarrow{\boldsymbol{A}}$ has M^2 values and is dense. Eq. (4.27) thus can either be solved by direct methods or by an iterative method. Although M is in general small compared to the number of all lattice sites, it can easily be of the order of 10^3 grid points. Since direct methods have usually a runtime complexity of order $\mathcal{O}(M^3)$, an iterative method should be the method of choice. From computational comparison, a variant of the conjugate gradient algorithm, namely the *BiCGStab* algorithm[88, 89], turns out to be much faster than a direct routine for a matrix of this size. Table 4.1 shows performance results for the Stokes solver using the BiCGStab method compared to an implementation where the linear set of equations is solved via a LU-decomposition routine from the *gsl* library [90]. The runs were performed on an Intel Core 2 Duo E6600 FSB 1066 2x2.4 GHz with 4GB RAM. The systems used for the performance tests are discussed in the next section (Sec. 4.4).

lattice structure	grid spacing	# surface nodes	BiCGStab $6\pi\eta\mu$	time [s]	gsl $6\pi\eta\mu$	time[s]
sc	0.5	674	0.2206	3	0.2207	13
sc	0.4	1034	0.2063	7	0.2064	46
bcc	0.5	1348	0.1968	14	0.1970	101
bcc	0.4	2068	0.1773	32	0.1775	361
fcc	0.5	2696	0.1699	51	0.1703	797
fcc	0.45	3368	0.1586	74	0.1589	1542
fcc	0.4	4136	0.1453	133	0.1456	2853

Table 4.1.: Comparison of the computational time needed to solve the Stokes equation via the BiCGStab method compared to a gsl routine. The radius of spheres is set to $R = 3$ and every data point is taken for 64^3 lattice sites.

4.4. Numerical Results

The test system we study is the flow around three types of cubic arrays of spheres with radius R, dragged by a constant external force F_{ext}. The constant force is acting in the x-direction and the different kinds of lattices are given by simple cubic (sc), body–centered cubic (bcc) and face-centered cubic (fcc) crystal structures. The Stokes equation is only solved for one primitive unit cell of the crystal, while the structure is given by the periodic images. Thus the lattice constant d coincides with the linear box size L of the computational domain. This means that the sc structure consists of one single sphere in the center of a cubic box with periodic boundary conditions. The bcc lattice has two spheres per unit cell. The basis is usually described by

$$\boldsymbol{e}_{bcc}^{(1)} = \frac{d}{2}(1,1,-1), \tag{4.29}$$

$$\boldsymbol{e}_{bcc}^{(2)} = \frac{d}{2}(-1,1,1), \tag{4.30}$$

$$\boldsymbol{e}_{bcc}^{(3)} = \frac{d}{2}(1,-1,1). \tag{4.31}$$

The first sphere is set up at $\boldsymbol{s}_{bcc,1} = \frac{L}{4}(1,1,1)$ and the second at $\boldsymbol{s}_{bcc,2} = \boldsymbol{s}_{bcc,2} + \boldsymbol{e}_{bcc}^{(1)} + \boldsymbol{e}_{bcc}^{(2)} + \boldsymbol{e}_{bcc}^{(3)} = \frac{3}{4}L(1,1,1)$.

In the case of the fcc lattice structure, one finds four spheres per unit cell. The

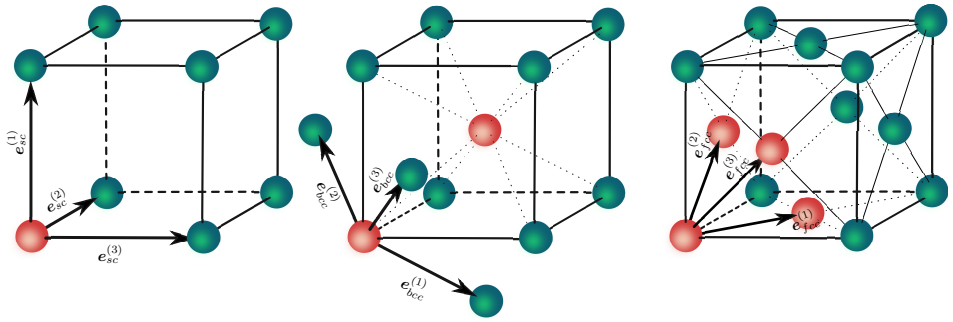

Figure 4.2.: Crystal structures of the observed arrays of spheres. The red spheres are set into one unit cell.

basis is given by

$$\boldsymbol{e}_{fcc}^{(1)} = \frac{d}{2}(1,1,0), \tag{4.32}$$

$$\boldsymbol{e}_{fcc}^{(2)} = \frac{d}{2}(0,1,1), \tag{4.33}$$

$$\boldsymbol{e}_{fcc}^{(3)} = \frac{d}{2}(1,0,1). \tag{4.34}$$

In the computational domain, we choose the location for the first sphere again as $\boldsymbol{s}_{fcc,1} = \frac{L}{4}(1,1,1)$. The other three particles are then located at $\boldsymbol{s}_{fcc,2} = \boldsymbol{s}_{fcc,1} + \boldsymbol{e}_{fcc}^{(1)}$, $\boldsymbol{s}_{fcc,3} = \boldsymbol{s}_{fcc,1} + \boldsymbol{e}_{fcc}^{(2)}$ and $\boldsymbol{s}_{fcc,4} = \boldsymbol{s}_{fcc,1} + \boldsymbol{e}_{fcc}^{(3)}$.
Fig. 4.6 and 4.7 show two dimensional cuts in the x-y-plane of the calculated flow profile in the center-of-mass frame (com frame) and, by subtraction of the particle velocity, also in the rest frame of the spheres.

The quanitity we measure is the mobility $\mu = v_x(\boldsymbol{r}_\Omega)/F_{ext}$. In the case of an isolated single sphere in an infinite large domain, the analytic expression for this mobility is well known and is given by the Stokes formula

$$\mu = \frac{1}{6\pi\eta R}\,. \tag{4.35}$$

If periodic arrays of spheres are studied, packing effects will occur. Eq. (4.35) then is modified to

$$\mu = \frac{1}{6\pi\eta}\left(\frac{1}{R} - \frac{\alpha}{L} + \mathcal{O}(L^{-3})\right). \tag{4.36}$$

The constant α depends on the given lattice structure. For the sc, bcc and fcc structure, these constants have first been calculated by Hasimoto [91] and are

found to be

$$\alpha_{sc} = 2.837, \tag{4.37}$$
$$\alpha_{bcc} = 3.639, \tag{4.38}$$
$$\alpha_{fcc} = 4.584. \tag{4.39}$$

In Fig. 4.3 the mobility $6\pi\eta\mu$ is plotted as function of the lattice spacing a of

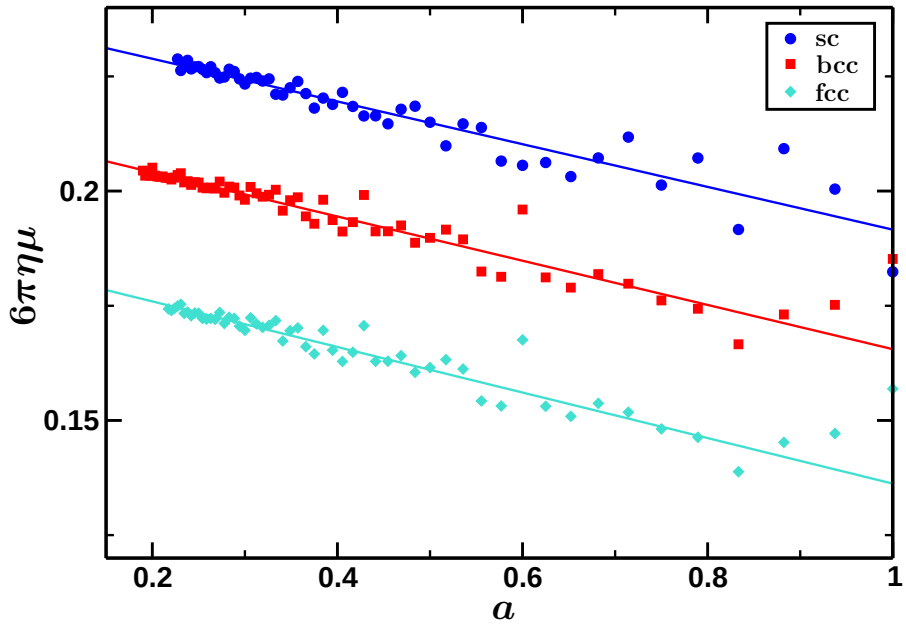

Figure 4.3.: Mobility $6\pi\eta\mu$ as function of lattice spacing a for sc, bcc and fcc lattice structure. The solid lines are linear fits.

the computational grid. The box size was fixed as $L = 30\lambda_0$ and the radius of the spheres was set to $R = 3\lambda_0$. The solid lines are linear fits

$$f(x) = c_1 + c_2 a. \tag{4.40}$$

Using Eq. (4.36) and extrapolating the fit to the continuum limit $a \to 0$, we should be able to reproduce the sphere radius

$$R_{fit} = \frac{1}{c_1 + \alpha L^{-1}}. \tag{4.41}$$

Indeed, we find that this agrees reasonably well,

$$R_{fit}^{sc} = 3.005\,\lambda_0, \tag{4.42}$$
$$R_{fit}^{sc} = 2.985\,\lambda_0, \tag{4.43}$$
$$R_{fit}^{sc} = 2.953\,\lambda_0. \tag{4.44}$$

In this plot, one could also observe that for a finite lattice spacing, $a > 0$. the "effective" radius of the sphere is systematically increased. This is an effect of the discretization scheme, which marks all points as surface nodes which are closest to any point on the particle surface.

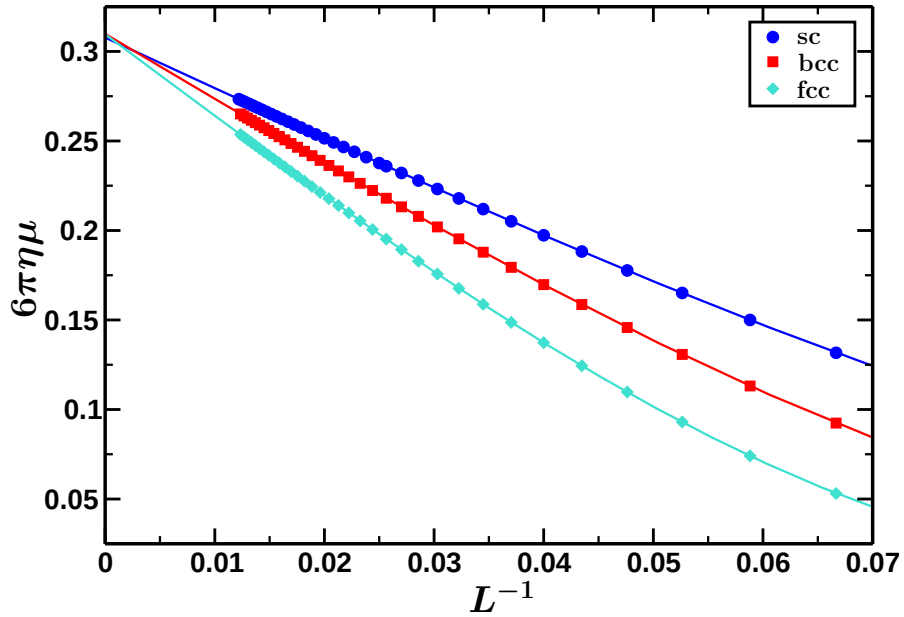

Figure 4.4.: Mobility $6\pi\eta\mu$ as function of inverse box size L^{-1}.

The data in Fig. 4.4 were taken for a fixed lattice spacing $a = 0.5\lambda_0$ and again a sphere radius of $R = 3\lambda_0$. We varied the box size L and plotted $6\pi\eta\mu$ as function of the inverse box size L^{-1}. The solid lines are fits as

$$g(x) = \frac{1}{R_{eff}} - \frac{\alpha}{L} + \frac{\beta}{L^3}. \tag{4.45}$$

The resulting fit parameters are reported in Tab. 4.2. We see that the linear prefactors α agree quite well with the values given by Hasimoto and it is not surprising that the effective radii are about half a lattice spacing larger than the input parameter. In the paper of Hasimoto, one further finds a figure with the so–called drag coefficient $(6\pi\eta R\mu)^{-1}$ plotted as function of the cubic root of the volume fraction $\Phi^{\frac{1}{3}}$. Since Hasimoto's formulations are only valid for low volume fractions, we compared the results of our program with the values given in the paper of Zick and Homsy [85] (see Fig. 4.5). The simulation curves are re-parametrized using the effective radii from Tab. 4.2. It is surprising that in the observed range of volume fractions the drag coefficients of the bcc and fcc crystals are nearly identical while the curve for the sc structure deviates

	R_{eff}	α	β
sc	3.249	2.830	42.6
bcc	3.227	3.637	84.7
fcc	3.230	4.567	162.3

Table 4.2.: Fit parameters pertaining to Fig. 4.4.

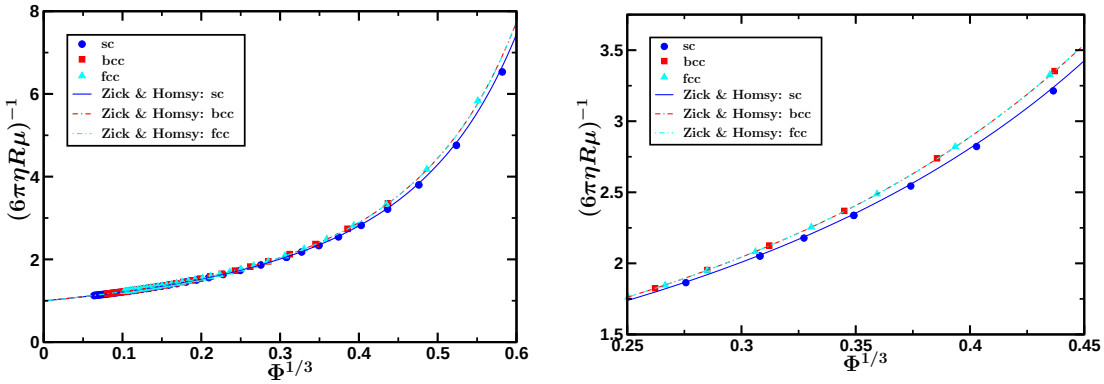

Figure 4.5.: Drag coefficient $(6\pi\eta R\mu)^{-1}$ as function of the cubic root of the volume fraction for sc, bcc and fcc lattice structure. The lines are results from Ref. [85].

by some percentage.

Since the packing effect of the Stokes flow is related to the determination of the Madelung constant as mentioned by Hasimoto [91], one would expect to find this effect also in the values of the Madelung constant, which indeed is the case. In a metal with a simple crystal structure, the electrostatic energy per ion is written in the form $V = -Z^2e^2\alpha_M/2r_0$. Here, r_0 is the atomic Wigner-Seitz radius and α_M is the dimensionless constant characteristic of the lattice structure [92, 93], namely the equivalent of the Madelung constant of ionic crystals. Moreover, the first order packing effect in hydrodynamics α is directly proportional to this Madelung constant,

$$\alpha_M = \alpha \left(\frac{3}{4\pi}\frac{1}{n}\right)^{\frac{1}{3}}, \tag{4.46}$$

where n is the number of spheres in a unit cell (see Ref. [91][1]).

[1]The first column of Table 1 in the paper of Hasimoto presents values of α and the quantity presented in the second column is identical to the Madelung constant α_M. From here, some basic algebra results in Eq. (4.46)

Tab. 4.3 presents the values of the Madelung constant for three different lattice structures. Indeed we see that α_M is nearly identical for the bcc and fcc crystal,

	sc	bcc	fcc
α_M	1.760	1.79186	1.79172

Table 4.3.: Madelung constants as reported in Ref.[94].

and differs slightly for the sc structure.

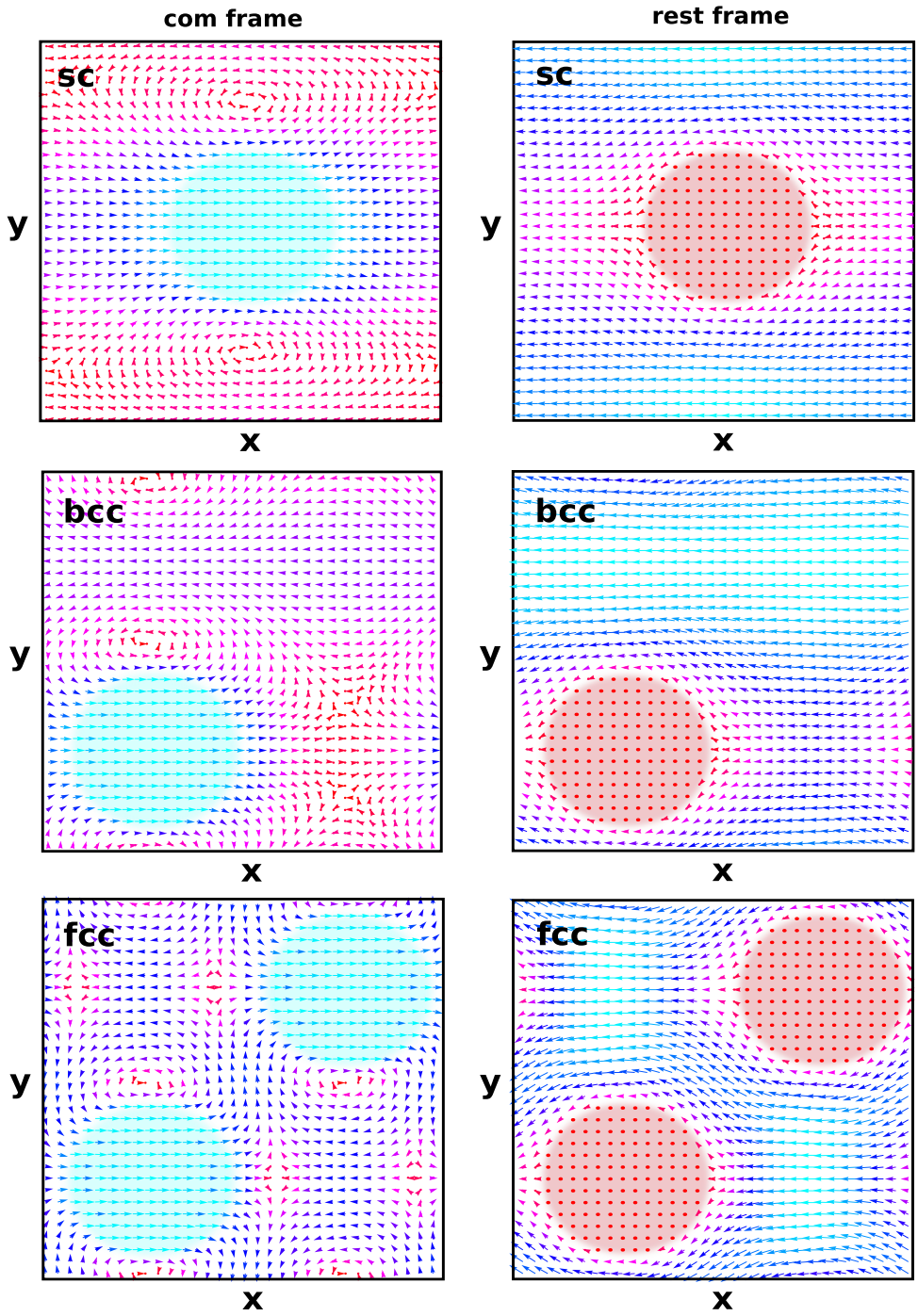

Figure 4.6.: 2 dimensional cuts of the flow profile for cubic arrays of spheres, dragged by a constant force in the x-direction. For the sc lattice, the cut was taken at $z = 0.5L_z$ and for the bcc and fcc structure at $z = 0.25L_z$.

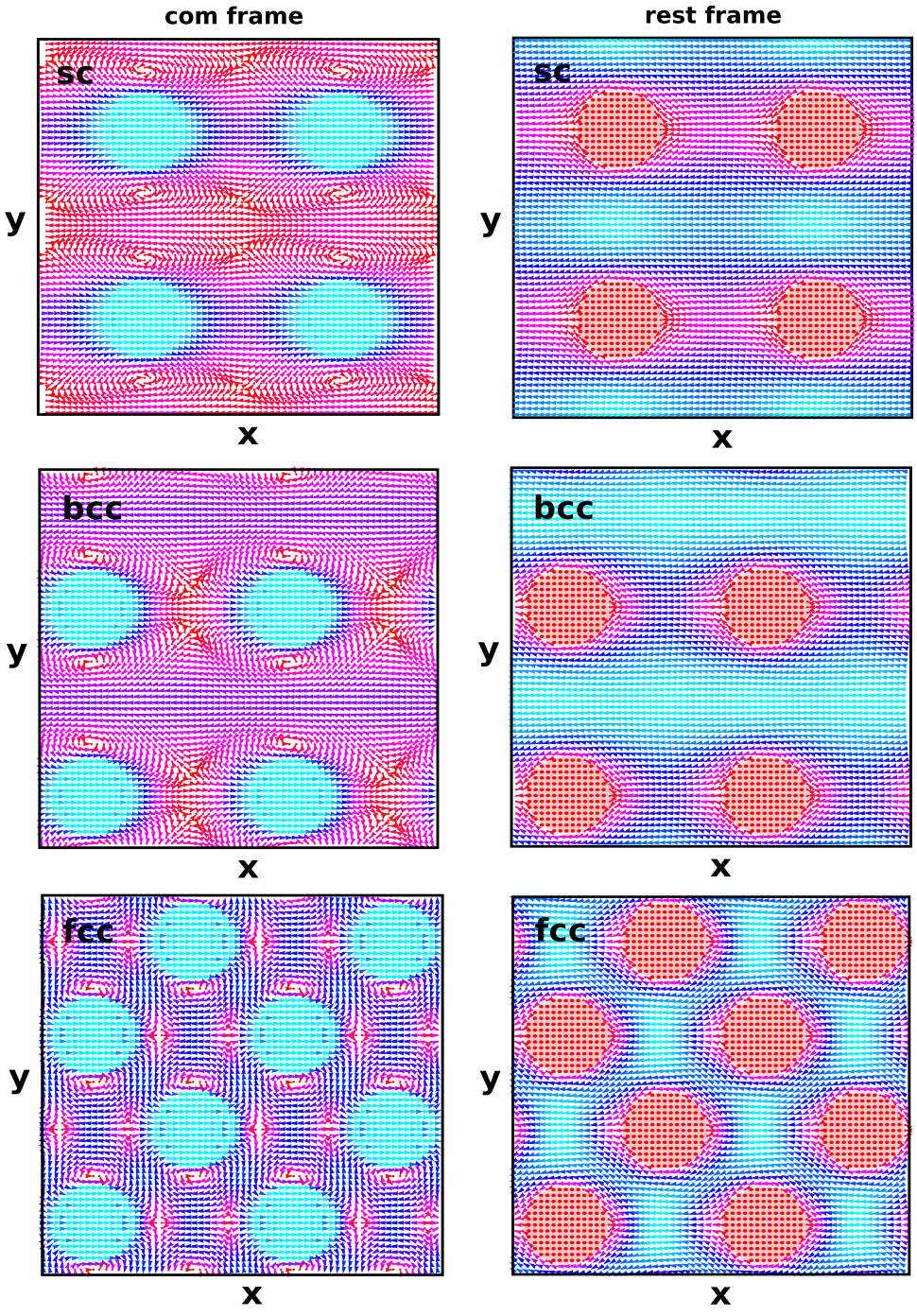

Figure 4.7.: Same as Fig. 4.6 with periodic images.

5. Numerical Solutions of the Electrokinetic Equations

The aim of this chapter is the presentation of numerical results for the electrokinetic problem, using the computational method described in the previous chapters.

Since the electrophoretic mobility μ_{red} is a dimensionless quantity, it can only depend on dimensionless parameters as well. B. Dünweg et al. [32] printed out that, in a finite system with added salt ions and where all ion types have the same properties, i. e. all ions are monovalent and have all the same friction coefficient, these parameters are given by the reduced charge $\hat{Z} = Z\,l_B/R$, the rescaled colloid radius $\tilde{R} = \kappa R$, the diffusion constant of the ions $\tilde{D}$ or l_B/a, with a an effective radius of the ions, and a dimensionless quantity f_0 which specifies the fraction of counterions relative to the salt ions. Note that the reduced charge is not identical to $\tilde{Z} = 4\pi l_B \kappa Z$, occurring in our original rescaling scheme of the electrokinetic equations of Sec. 1.1 (see Tab. 1.1).

In general f_i is the fraction of the ionic species i relative to all ions in the system

$$f_i = \frac{N_i}{\sum_j z_j^2 N_j}\,. \tag{5.1}$$

In former studies the meaning of *volume* V in the definition of ionic concentrations is not clear, in the sense that it is not specified if V denotes the full volume of the system or only the free volume with the regions occupied by colloidal spheres excluded. Here, we adopt the convention that we always use the free volume as basis, i. e. $V = L^3 - 4\pi N R^3/3$, which is the correct way to define κ, as one sees from the finite-volume version of linearized Poisson-Boltzmann theory. Note that N is the number of colloids and Z is their charge, while N_0 and z_0 are the number and valence of counterions, respectively. Therefore the relation between volume fraction Φ and f_0 differs from the expression in Ref. [32] by a small correction factor. The volume fraction is given by

$$\Phi = \frac{\frac{4N}{3}\pi R^3}{V + \frac{4N}{3}\pi R^3}\,. \tag{5.2}$$

Hence, one may write

$$\Phi^{-1} = 1 + \frac{3}{4N\pi}\frac{V}{R^3} \tag{5.3}$$

$$\Rightarrow \frac{3}{4N\pi}\frac{V}{R^3} = \frac{1-\Phi}{\Phi} \tag{5.4}$$

$$\Rightarrow V = \frac{4N\pi}{3}R^3\frac{1-\Phi}{\Phi}\,. \tag{5.5}$$

Applying this to the definition of κ^2, Eq. (1.48), we obtain a relation between f_0 and the volume fraction

$$\begin{aligned}
\tilde{R}^2 &= \kappa^2 R^2 \qquad (5.6)\\
&= 4\pi l_B \sum_i z_i^2 \frac{N_i}{V} R^2\\
&= 4\pi \frac{3}{4N\pi}\frac{l_B}{R}\frac{\Phi}{1-\Phi}\sum_i z_i^2 N_i\\
&= -3\frac{Z}{z_0 N_0}\frac{l_B}{R}\frac{\Phi}{1-\Phi}\sum_i z_i^2 N_i\\
&= -3\frac{\hat{Z}}{z_0}\frac{\Phi}{1-\Phi}\frac{\sum_i z_i^2 N_i}{N_0}\\
&= -3\frac{\hat{Z}}{z_0 f_0}\frac{\Phi}{1-\Phi}
\end{aligned}$$

or

$$\frac{\Phi}{1-\Phi} = -\frac{z_0 f_0}{3\hat{Z}}\tilde{R}^2\,. \tag{5.7}$$

Within this chapter we use these dimensionless quantities for the characterization of a system. However, $\tilde{Z}$ and the initial salt concentrations are well defined by these parameters. One verifies easily that

$$\tilde{Z} = 4\pi\tilde{R}\hat{Z}\,. \tag{5.8}$$

If the initial salt concentration in physical units is denoted by $c_{i,0} = N_i/V$, one obtains in reduced units

$$\begin{aligned}
\tilde{c}_{i,0} &= \frac{4\pi l_B}{\kappa^2} c_{i,0} \qquad (5.9)\\
&= \frac{4\pi l_B}{4\pi l_B \sum_j z_j^2 N_j/V} c_{i,0}\\
&= \frac{N_i}{\sum_j z_j^2 N_j}\\
&= f_i\,.
\end{aligned}$$

Making use of Eq. (5.1), we can write

$$\sum_i z_i^2 f_i = 1\,, \tag{5.10}$$

and if only monovalent ions and only one salt species are assumed, this results in

$$\tilde{c}_{i,0} \;=\; \frac{1}{2}(1 - f_0)\,,\;\; i = 1, 2\,. \tag{5.11}$$

Furthermore, a *dimensionless resolution* d is defined such that for given d a sphere is always discretized by the same number of lattice sites. Thus, the resolution is expressed by

$$d := \frac{\tilde{\Delta x}}{\tilde{R}}\,, \tag{5.12}$$

where $\tilde{\Delta x}$ denotes the lattice spacing and $\tilde{R}$ is the radius of the particle.

We implemented the iterative method as described by Fig. 1.1. The code is split into two independent programs, written in *C*. The first one is the "Maggs–type" Poisson–Boltzmann solver as discussed in Chap. 2. The second program reads the output files of the PB solver and computes the solution of the first order equations iteratively, using the FFT-based Poisson solver, the surface integration method of Chap. 4 for the solution of the Stokes equation and the second order *D3Q6* method of Chap. 3 for the relaxation of the concentration fields. The program was run until the relative residual,

$$\varepsilon \;:=\; \left| \frac{\mu_{red}^{(i)} - \mu_{red}^{(i-1)}}{\mu_{red}^{(i)}} \right|\,, \tag{5.13}$$

with i the iteration step, reached the limit of $\varepsilon \leq 10^{-5}$. Indeed we found that the iterative method converges nicely (see Fig. 5.1). Note that the convergence of the method can be improved using not the full new velocity field for the next iteration of calculating the concentration fields, but rather a linear combination of the previous iteration and the result of the Stokes solver $\tilde{\boldsymbol{v}}^*$:

$$\tilde{\boldsymbol{v}}_i^{(1)} = \omega\tilde{\boldsymbol{v}}^* + (1 - \omega)\tilde{\boldsymbol{v}}_{i-1}^{(1)}\,, \quad 0 < \omega \leq 1\,. \tag{5.14}$$

In practice we used $\omega = 1/2$.

Nevertheless, there are some limitations to the possible parameters due to the discrete character of the algorithm. For example, we often find plots in the literature showing some theoretical functions for the dependence of μ_{red} on $\tilde{R}$ and interpolating from the Hückel ($\tilde{R} \to 0$) to the Smulochowski limit ($\tilde{R} \to \infty$) (see e. g. Fig. 3.16 in Ref. [6]). The discretized formulation is only valid in an intermediate range of $\tilde{R}$. d is always finite and decreasing its value

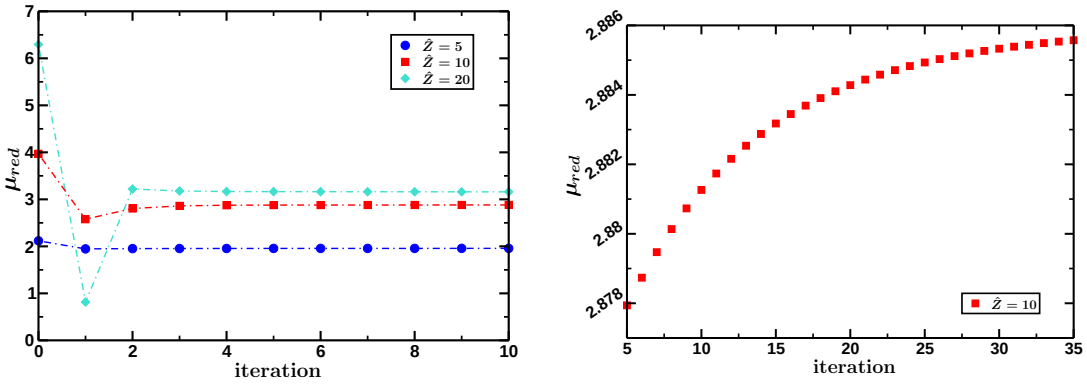

Figure 5.1.: Convergence of the iterative procedure for three systems with $f_0 \simeq 0.3$, $\tilde{R} = 1$, $\tilde{E} = 10^{-2}$, $d = 0.07$ and reduced charges as indicated by the legend.

increases the amount of memory and the computational time needed. Thus, keeping d fixed and increasing the value of $\tilde{R}$, also the lattice spacing $\tilde{\Delta x}$ is increased. Obviously, large values of $\tilde{\Delta x}$ result in inaccurate calculations or in numerical instabilities. Since $\tilde{\Delta x} \ll 1$ is required, reliable results will only be obtained for resolutions d which are small compared to $\tilde{R}^{-1}$. Therefore we are far away from getting close to the Smulochowski limit. On the other hand, the numerical calculations take always place in a finite sized box with a finite volume fraction and with a finite amount of salt ions and counterions, while the earlier studies usually used one single charged sphere in infinite space, and therefore counterions do not occur. Keeping the resolution fixed, the volume fraction is independent of the radius of the macro–ions, rather depends only on the number of lattice sites M^3. Furthermore, the salt concentration must be positive and due to Eq. (5.11), this restricts $f_0 < 1$. For a given volume fraction and colloid charge, this ends up in a lower bound for $\tilde{R}$,

$$\tilde{R}^2 > -\frac{3\hat{Z}}{z_0}\frac{\Phi}{1-\Phi}\,. \tag{5.15}$$

Thus, underlying practical limitations to the value of the volume fraction restrain the calculations of reaching the Hückel limit. Fig. 5.2 shows the reduced mobility as function of $\tilde{R}$ for $d = 0.07$ and $\Phi \simeq 7.07 \cdot 10^{-3}$ ($M = 120$) for four different colloid charges as indicated by the legend. For this value of the volume fraction we get from Eq. (5.15) that the minimum sphere radius is of the order $\tilde{R} > 0.21$ for $\hat{Z} = 2$ and $\tilde{R} > 0.46$ for $\hat{Z} = 10$. In the given range we could observe a reduction of the mobility with increasing $\tilde{R}$. Note that the present representation is given for constant $\hat{Z}$, which differs from the classical calculations [19–23] keeping the ζ-potential fixed, i. e. the electrostatic potential at the colloidal surface.

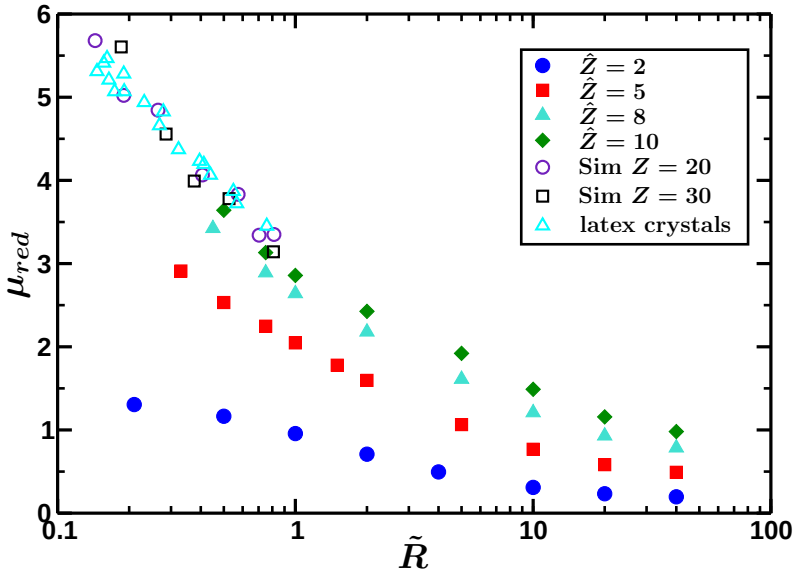

Figure 5.2.: Reduced mobility as function of $\tilde{R}$. The open symbols are experimental results from Ref. [14] and from Ref. [31].

The numerical results are compared to results from Lobaskin et al. [31] (see open symbols in Fig. 5.2). The circles and squares are simulation results using the *MD/LB* raspberry model [41]. In the simulations a single colloid of charge $Z = 20$ ($Z = 30$) and radius $R_C = 3$ ($R_C = 5$) is surrounded by counterions. Both systems were calculated with a Bjerrum length of $l_B = 1.3$, resulting in a reduced charge of $\hat{Z} = 8.5$. The triangles are experimental results for latex crystals in bcc structure with a particle size of $R = 34nm$ in a deionized aqueous suspension. The effective charge is quoted as $Z^*_\sigma \simeq 450$ determined from conductivity measurements [95] and resulting in a reduced charge of the order $\hat{Z}^* \simeq 10$. In all cases of the reference the colloidal charge and the particle size were fixed and salt ions were absent (up to the self-dissociation of water). The screening length was varied via changing the volume fraction. This is qualitatively different from our numerical calculations, where the volume fraction is kept fixed and the screening length is varied via adding salt to the system. Nevertheless, the numerical results seem to agree reasonably well with the results from the literature. The small discrepancies are not surprising since the MD/LB simulations use a different charge and also the diffusion constant of the counterions differs from the numerical parameter. While our calculations are performed using a diffusion constant of $\tilde{D} = 1.5$, we find for the simulation $\tilde{D} \simeq l_B/a = 1.3/0.5 = 2.6$, with a the radius of the microions. Even worse in the case of experiments. Here, the effective charge

is not a well defined quantity and it is not clear how to map an effective charge from a real physical system to the bare charge in the Mean-Field calculations. Furthermore the diffusion constant of the ions in the experiment is even larger. If we consider for example sodium ions of radius $a \simeq 0.1nm$ in aqueous solution with $l_B \simeq 0.7nm$, this results in diffusion constants of the order $\tilde{D} \simeq 7$. We will see later that the resulting mobility is increased by increasing the diffusion constant.

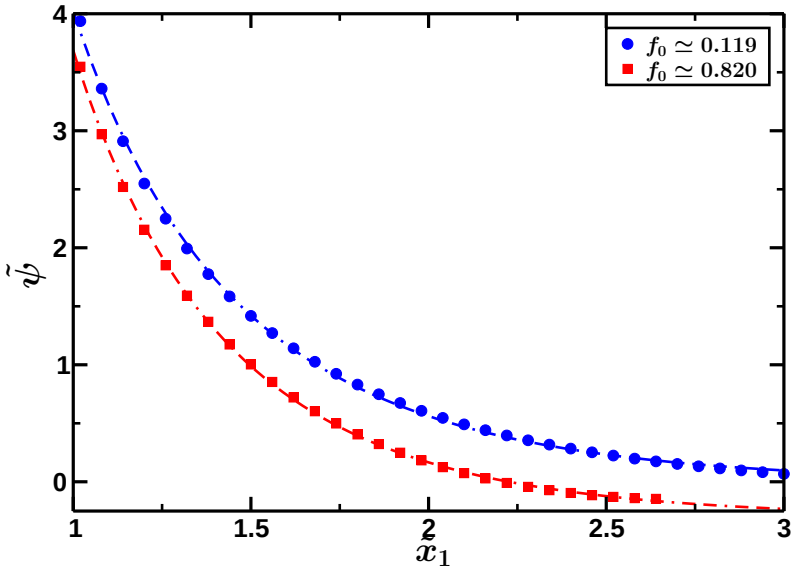

Figure 5.3.: Electrostatic potential in $\tilde{x}_1$–direction for a salt dominated system with $\hat{Z} = 10$, $\tilde{R} = 1$ and $f_0 \simeq 0.119$ and for a counterion dominated system with $f_0 \simeq 0.820$. The symbols are numerical data from the iterative Poisson–Boltzmann solver with a lattice resolution of $d = 0.06$. The lines are fits via an exponential decay function.

A second limitation occurs for highly charged spheres. For a salt-free system we mentioned in Chap. 2 that the lattice spacing should be at most of the order of the Gouy–Chapman length. In reduced units, the Gouy–Chapman length is given by Eq. (2.77). Using Eq. (5.8), the reduced surface charge density can be written as

$$\tilde{\sigma} = \frac{\hat{Z}}{\tilde{R}}, \tag{5.16}$$

and hence

$$\tilde{\lambda}_{GC} = -\frac{2\tilde{R}}{z_0 \hat{Z}}. \tag{5.17}$$

For monovalent ions, the restriction of the lattice spacing then yields

$$\frac{\tilde{\Delta x}}{\tilde{\lambda}_{GC}} = \frac{d}{2}|\hat{Z}| \lesssim 1\,, \tag{5.18}$$

or

$$|\hat{Z}| \lesssim \frac{2}{d}\,. \tag{5.19}$$

Since adding some amount of salt to the system, the shape of the ion concentrations is less sharp compared to the salt-free system, we suppose that this limit is only a rough approximation for a reliable range of possible colloid charges. The claim that this limit is less strict in the high salt regime can also be confirmed by the observation that the decay of the electrostatic potential is faster in counterion screened systems than in salt-screened systems, even though the screening parameter κ is identical. For example, the electrostatic potential along the x_1–axis for a colloidal sphere in the high salt regime ($f_0 \simeq 0.119$) and in counterion dominated screening ($f_0 \simeq 0.820$) is shown in Fig. 5.3. The symbols are numerical data from the iterative PB solver and the dash–dotted lines are fits via a screened potential of the form

$$\tilde{\psi}(\tilde{x}_1) := \frac{A}{\tilde{x}_1} \exp\left(-\frac{\tilde{x}_1}{\lambda}\right) - \psi_\infty\,. \tag{5.20}$$

The decay length in the counterion screened system $\lambda = 0.69 \pm 0.01$ is smaller than in the salt dominated system $\lambda = 0.80 \pm 0.02$ [1], which indicates that the numerical restrictions are less strict when the amount of salt in the system is increased.

In Fig. 5.4 three different curves are presented showing results for the reduced mobility as function of the reduced charge. The three curves are computed for systems with $\tilde{R} = 1$, $\tilde{R} = 3$, both with $f_0 \simeq 0.3$ and the last curve corresponds to $\tilde{R} = 8$ with $f_0 \simeq 0.01$. Each data point was generated for a resolution of $d = 0.07$, and hence data points with $\hat{Z} \gtrsim 28.6$ should be regarded with suspicion. In the famous publication of O'Brien and White [23], the data curves start with a linear behavior in the Hückel limit $\tilde{R} = 0$ and then bend over to smaller slopes until $\tilde{R} \simeq 3$, and then increase again (see Sec. 1.5). This effect can also be achieved here. For the data of Fig. 5.4 we calculated the ζ-potential from the solution of the Poisson–Boltzmann equation. The result of this rescaling is presented in Fig. 5.5. It should be noticed that the data of Fig. 5.5 was calculated for a diffusion constant of $\tilde{D} = 1.5$. Although O'Brien and White do not quote a value for the drag coefficient, $\tilde{D} = 1$ seems to be more reasonable. In Fig. 5.6 numerical data generated with our iterative lattice method for a system with $d = 0.07$, $\tilde{R} = 8$, $f_0 \simeq 0.01$ (strongly salt dominated) and various ζ–potentials and with diffusion constants $\tilde{D} = 1.5$ and $\tilde{D} = 1$ are compared to the results of O'Brien and White. While the data

[1] For comparison, the Gouy–Chapman length for this system is $\tilde{\lambda}_{GC} = 0.2$.

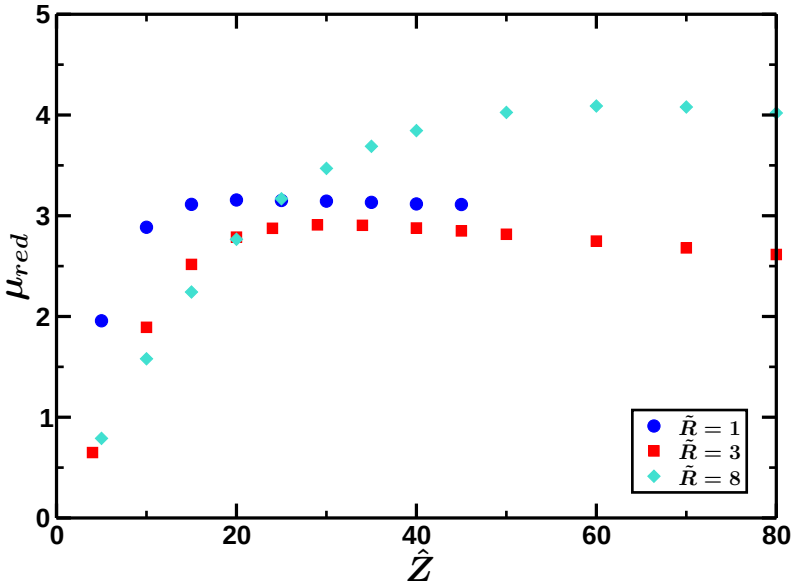

Figure 5.4.: Reduced mobility as function of $\hat{Z}$ for $\tilde{R} = 1$, $\tilde{R} = 3$ and $\tilde{R} = 8$.

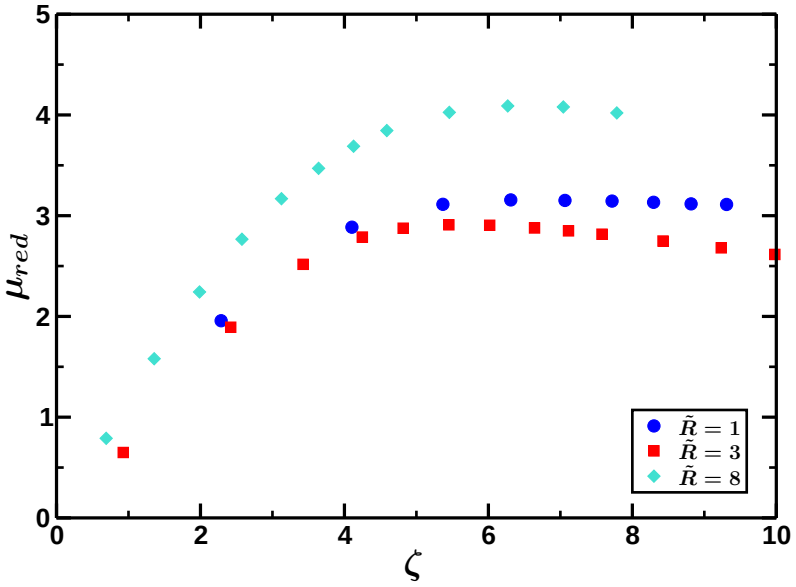

Figure 5.5.: Reduced mobility as function of the dimensionless ζ-potential for $\tilde{R} = 1$, $\tilde{R} = 3$ and $\tilde{R} = 8$.

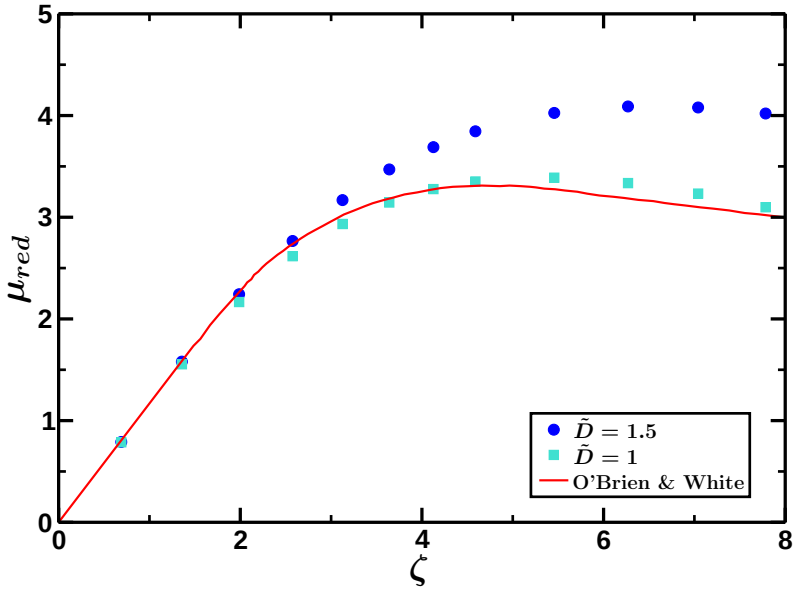

Figure 5.6.: Reduced mobility as function of the dimensionless ζ-potential for $\tilde{R} = 8$, $d = 0.07$ and $\tilde{D} = 1.5$ and $\tilde{D} = 1$. The red line are results from Ref. [23].

for $\tilde{D} = 1.5$ are significantly too high, the data with $\tilde{D} = 1$ agrees quite well with the curve digitized from Ref. [23]. We also attempted an extrapolation of this data curve to the continuum limit, $d \to 0$. Unfortunately the feasibility of running the calculations for much higher resolutions is strongly restricted for the current single processor code due to computer time requirements and demand on memory. On the other hand, the resolution should be not too low to get reliable results. Furthermore, both, the data on the x–axis (ζ–potential) and on the y–axis (μ_{red}), are functions of the colloidal charge, and hence the extrapolation must be applied to both dimensions. It turned out that by use of the current implementation the attempted extrapolation is subject to substantial numerical errors, such that no improvement of the quality of the data is obtained. Nevertheless, the good agreement in Fig. 5.6 is an impressive indication for the reliability of our numerical method.

Regardless of the limitations of the numerical method, the lattice algorithm offers the opportunity of systematic studies for the electrophoretic problem in finite geometries in an adequate computational time, and this was not possible with direct simulation methods or commercial finite-element packages before. Moreover, the present computational method offers the possibility of controlling the parameters of a system independently. Within the following subsec-

tions we present some applications, which, for the best of our knowledge, have not been studied before.

5.1. Salt Screening vs. Counterion Screening

As mentioned previously, the scaling parameter f_0 distinguishes between counterion dominated systems and salt screened systems. The common view within the community is that the exact mechanism of ion screening is not important for the value of the reduced electrophoretic mobility. Although previous studies showed that within the given accuracy the effect of f_0 on the mobility is at least weak [31], there is no stringent reason, why the mobility must be independent of f_0. With the current implementation of the iterative solver a system can be chosen such that $\tilde{R}$, $\hat{Z}$ and $\tilde{D}$ are remaining constant, while changing the box size affects the screening mechanism. Low volume fractions correspond to low values of f_0 and high salt concentration; higher values of Φ cause high values of f_0, and hence lead to counterion screened systems. Fig. 5.7 shows 2-dimensional cuts in the $x-y$–plane of the first-order concentration profiles and charge distribution for a single sphere of charge $\hat{Z} = 10$ in an external field of $\tilde{E} = 10^{-2}$. The value of f_0 in the system is intermediate ($f_0 \simeq 0.469$). The concentration profiles show that ions, both negative and positive, accumulate behind the colloid which is moving in positive x-direction. This is consistent with results which can be found in the literature [29, 30].

We study three different lattice structures, as already described in Chap. 4, and vary the scaling parameter f_0. The computational resolution is fixed as constant. Thus, the systematic discretization effect should be the same for each data point and leads to a smooth behavior of the measured data curves. The results of this analysis are presented in Fig. 5.8. Here, we calculated the reduced mobility for three different lattice structures with the same parameters chosen as $\tilde{R} = 1$, $\hat{Z} = 10$, $\tilde{D} = 1.5$ and $d = 0.08$. The plot nicely shows a nontrivial dependency of the reduced mobility on the screening effect for all three types of lattice structures. However, the effect is only of the order of 5 to 10%, and hence was not observable previously.

A second interesting observation is that the data curves in the counterion screened domain differ from bcc and fcc structures to the sc lattice by roughly 3%, while the bcc and fcc curve are almost identical. This effect could also be observed in the case of the simple Stokes problem of Chap. 4 and the Madelung constant (see Fig. 4.5 and Tab. 4.3).

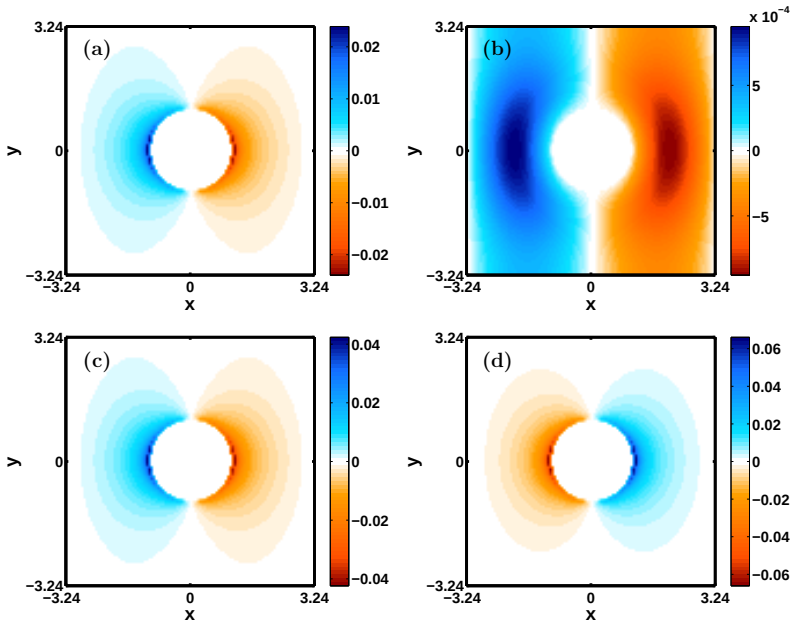

Figure 5.7.: 2 dimensional cuts of the first order concentration fields at $z = 0$ for a system of one single charged sphere in a periodic box with parameters $\tilde{R} = 1$, $\hat{Z} = 10$, $f_0 \simeq 0.469$, $d = 0.06$, $\tilde{D} = 3/2$ and $\tilde{E} = 10^{-2}$. The four plots present the first order concentrations of (a) the negative salt ions, (b) the positive salt ions, (c) the counterions and (d) the first order charge density.

For the sc lattice several data points were generated for the same set of parameters. The resolution was varied between $d = 0.06$ to $d = 0.09$ and the values of f_0 were varied from the salt dominated regime to counterion screened systems. The data were interpolated via cubic spline functions. Using linear regression, the continuum limit $d \to 0$ was calculated (see e. g. Fig. 5.9). The result of this extrapolation, namely the reduced mobility as function of the scaling parameter f_0 in the limit $d \to 0$, is presented in Fig. 5.10. Note that the extrapolated data should be regarded with some suspicion due to the small range of resolutions used for the extrapolation. Nevertheless, we see that the dependency of μ_{red} on f_0 seems not to be an effect of the discretization.

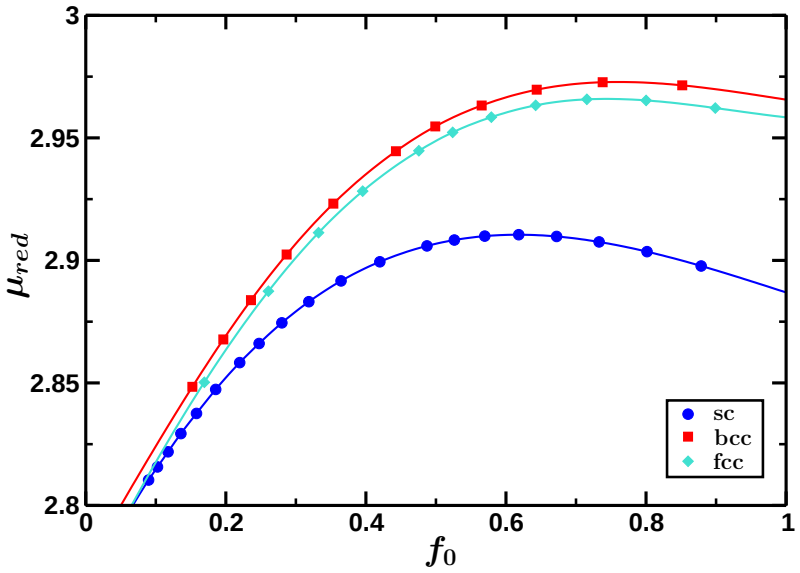

Figure 5.8.: Mobility as function of f_0 for constant $\tilde{R} = 1$ and three types of lattice structure as indicated by the legend. Every sphere carries a reduced charge of $\hat{Z} = 10$ and the computational resolution is $d = 0.08$.

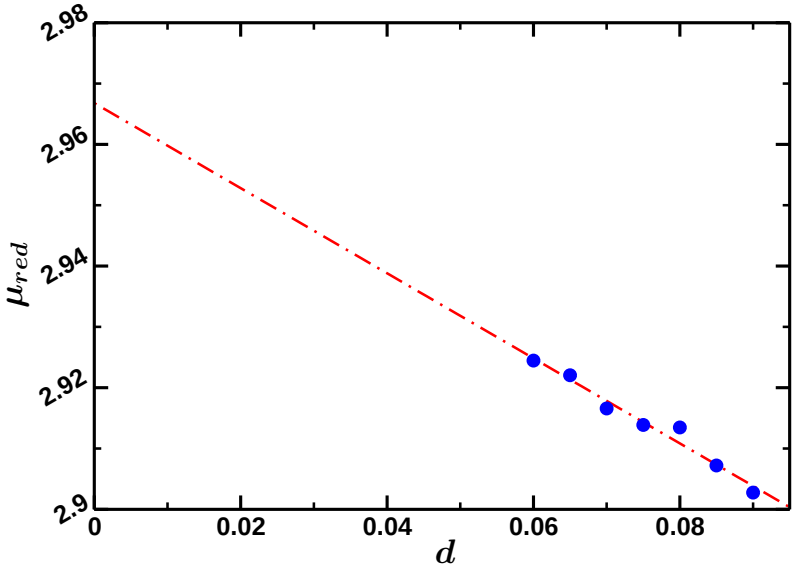

Figure 5.9.: Reduced electrophoretic mobility as function of the sphere resolution d for a constant value of $f_0 = 0.5$. The red line shows a linear fit to the numerical data.

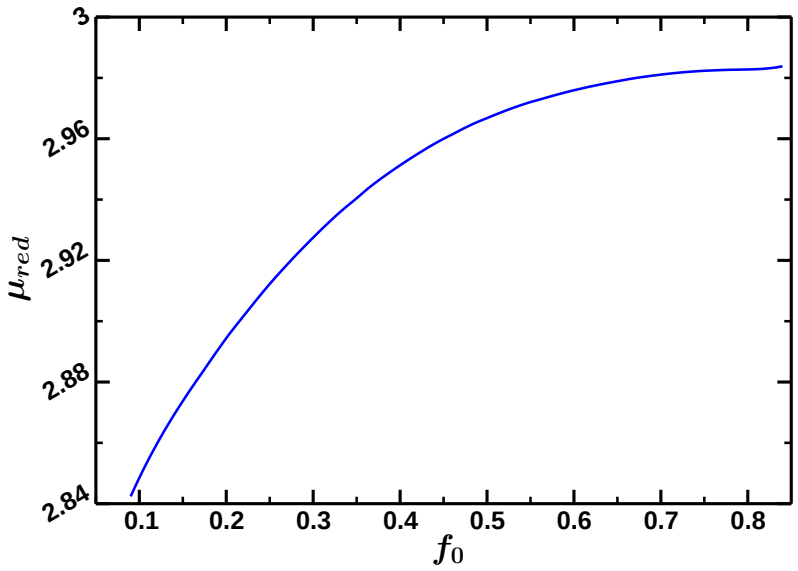

Figure 5.10.: Reduced electrophoretic mobility as function of f_0 in the continuum limit $d \to 0$.

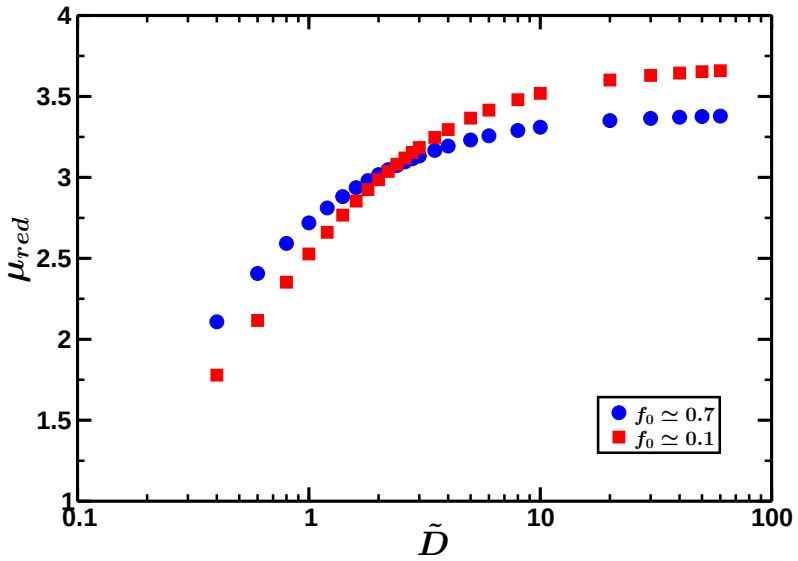

Figure 5.11.: Reduced electrophoretic mobility as function of the diffusion constant. Both curves are generated for a system with $\tilde{R} = 1$, $\hat{Z} = 10$, $d = 0.07$ and various values of f_0 as indicated by the legend.

5.2. Influence of the Diffusion Constant

All data within the previous section were calculated for a diffusion constant of $\tilde{D} = 1.5$. However, the electrophoretic mobility should be affected by changes in the diffusion constant of the microions, as already observed from Fig. 5.6. While the Poisson–Boltzmann equation does not depend on the diffusion constant, the first order equations, Eq. (1.62a), do. In the limit of $\tilde{D} \to 0$, all terms of the Nernst–Planck equation vanish, except the term containing the convective flow velocity. This leads to

$$\tilde{\boldsymbol{v}}^{(1)} \cdot \tilde{\nabla} \tilde{c}_i^{(0)} = 0\,, \tag{5.21}$$

and since the zeroth order concentration fields have a nonzero gradient, $\tilde{\boldsymbol{v}}^{(1)}$ and therefore μ_{red} must vanish. On the other hand, if $\tilde{D} \gg 1$, one could neglect the convective term in the Nernst–Planck equation since $\tilde{\boldsymbol{v}}^{(1)} \cdot \tilde{\nabla} \tilde{c}_i^{(0)} / \tilde{D}$ is small. Hence, the equations get independent of the diffusion constant and the

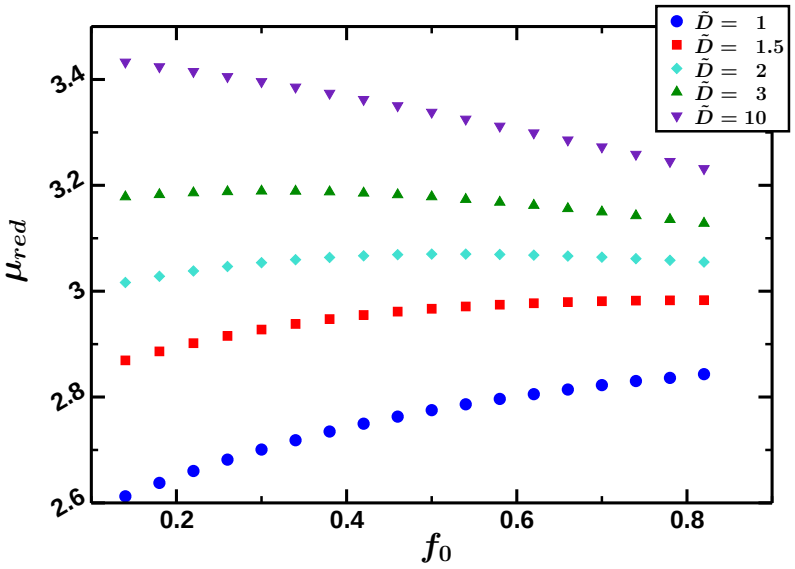

Figure 5.12.: Mobility as function of f_0 for one single sphere in a periodic box (sc lattice) and the same parameters as in Fig. 5.8 for different diffusion constants as indicated by the legend. This plot shows extrapolated values to $d \to 0$.

electrophoretic mobility is expected to reach a finite plateau value. Indeed this is the case as one can see in Fig. 5.11. The data shown there were calculated for $\tilde{R} = 1$, $\hat{Z} = 10$ and $d = 0.07$, but for different screening mechanisms. The blue circles were produced for a data set of a counterion dominated system

with $f_0 \simeq 0.733$ and the red squares represent data for the salt screening case with $f_0 \simeq 0.093$. From this plot, we assume that the effect of f_0 on μ_{red} could change for different values of the diffusion constant. This is indeed the case as observed from Fig. 5.12. Finally, one may conclude that indeed the mechanism of screening has an effect on the electrophoretic mobility, and moreover, this effect depends on the diffusion coefficient of the surrounding ion species.

5.3. Reversal of the Concentration Profile in Weakly Charged Systems

Consider an uncharged spherical obstacle in a solution of negatively and positively charged ions. Applying a constant external electric field, electro–osmotic flow is generated by electric forces acting on the salt ions; positive charges move with the field direction, negative charged ions against it. Since the ions can not penetrate the solid sphere, the ion fluxes will be deflected by the particle. Thus, negative salt ions accumulate at one side of the sphere, while positive ions are depleted in that region. Since no electric forces act on the uncharged particle, the accumulation of positive ions at one side and negative ions at the opposite side must be symmetric. This accumulation effect leads to a polarization of the system. Note that the induced dipole moment points in the "wrong" direction, i. e. anti–parallel to the driving field.

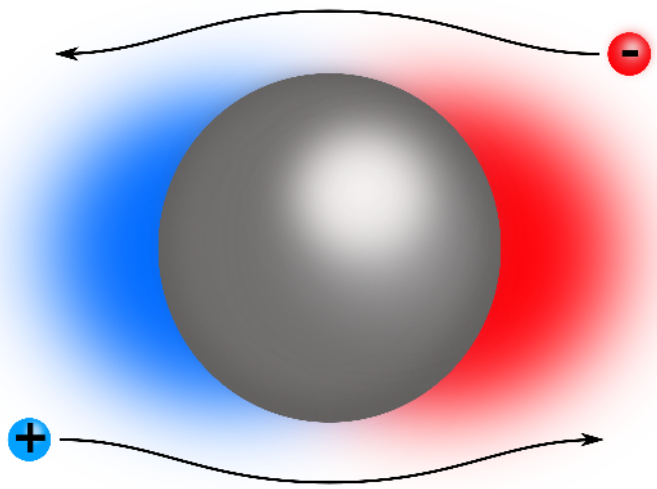

Figure 5.13.: Illustration of the charge accumulation for a neutral sphere in an external field.

This is interesting, because it is in contrast to the usual observation that if the

sphere carries charges itself, both, positive and negative ions accumulate behind the sphere, resulting in dipole moment that points in the "right" direction, parallel to the external field.
Recently, K. Kang and J. K. G. Dhont presented an analytic calculation for the anomalous dipole moment in the case of a single uncharged colloidal sphere in a salt solution in the presence of a slowly varying external electric field [4]. This calculation can be easily repeated, and simplified, for the case that only a constant electric field is acting on the monovalent salt ions.
In the dimensionless formulation (see Tab. 1.1), where we omit all tildes or hats with the understanding that all quantities are given in reduced units[2], and in the case of an uncharged colloidal sphere, i. e. in the absence of counterions, the Nernst–Planck equation has the form

$$\frac{\partial c_\pm}{\partial t} = D\nabla\cdot(\nabla c_\pm \pm c_\pm\nabla\psi) + \nabla\cdot(\boldsymbol{v}c_\pm)\,, \tag{5.22}$$

where the electrostatic potential ψ can be decomposed such that

$$\nabla\psi = \nabla\psi' - \boldsymbol{E}\,. \tag{5.23}$$

Here, $\boldsymbol{E}$ is the external electric field, and ψ' is the solution of the Poisson equation

$$\nabla^2\psi' = -\rho\,, \tag{5.24}$$

with the charge density

$$\rho = c_+ - c_-\,. \tag{5.25}$$

The subscript $\pm$ denotes the charge of the ionic species.
Linearization with respect to the external field, results in the non–stationary version of Eq. (1.54a),

$$\frac{\partial c_\pm^{(1)}}{\partial t} = D\nabla\cdot\left(\nabla c_\pm^{(1)} \pm c_\pm^{(0)}\nabla\psi^{(1)}\right) + \nabla\cdot\left(\boldsymbol{v}^{(1)}c_{(\pm)}^{(0)}\right)\,. \tag{5.26}$$

Since the colloid is uncharged, the zeroth order equations are simply solved by

$$\psi^{(0)} = const.\,, \tag{5.27}$$
$$c_\pm^{(0)} = const.\,. \tag{5.28}$$

The latter constant in reduced units is easily verified to be

$$c_\pm^{(0)} = \frac{1}{2}\,. \tag{5.29}$$

Applying this and the incompressibility condition

$$\nabla\cdot\boldsymbol{v} = 0\,, \tag{5.30}$$

[2]Note that this means that later the charge Z has to be understood as $\hat{Z}$, and not as $\tilde{Z}$.

the convective term of first order vanishes. Hence, the Nernst–Planck equation reduces to

$$\begin{aligned}\frac{1}{D}\frac{\partial}{\partial t}(\epsilon c_+^{(1)} - \epsilon c_-^{(1)}) &= \nabla\cdot\Big(\nabla(\epsilon c_+^{(1)} - \epsilon c_-^{(1)}) \\ &+ (c_+^{(0)} + c_-^{(0)})\nabla\epsilon\psi^{(1)}\Big) + \mathcal{O}(\epsilon^2)\,, \end{aligned} \tag{5.31}$$

and together with the Poisson equation, Eq. (5.31) can be written as

$$\frac{1}{D}\frac{\partial\rho}{\partial t} \simeq (\nabla^2 - 1)\rho\,. \tag{5.32}$$

The electrostatic potential must be continuous and differentiable at the surface of the colloidal sphere. This results in two boundary conditions for the potential

$$\psi'^{(in)}\big|_{r=R} = \psi'^{(out)}\big|_{r=R}\,, \tag{5.33}$$

$$\frac{\partial}{\partial r}\psi'^{(in)}\big|_{r=R} = \frac{\partial}{\partial r}\psi'^{(out)}\big|_{r=R}\,. \tag{5.34}$$

Here, R is the radius of the particle and the superscripts distinguish between the solution inside the sphere $\psi'^{(in)}$ or in the ambient fluid $\psi'^{(out)}$. A third boundary condition results from the requirement that no ionic concentration is allowed to flow inside the particle. This yields a no–flux boundary condition of the form

$$\begin{aligned}&\boldsymbol{n}\cdot\boldsymbol{j}_\pm\big|_{r=R} \\ =\;& \boldsymbol{n}\cdot\big(-D\nabla c_\pm^{(1)} \mp D(\nabla\psi'^{(1)} - \boldsymbol{E}^{(1)})c_\pm^{(0)}\big)\Big|_{r=R} \\ =\;& 0\,, \end{aligned} \tag{5.35}$$

where $\boldsymbol{n}$ is a unit vector perpendicular to the surface and pointing into the fluid, and $\boldsymbol{j}_\pm\big|_{r=R}$ denotes the current density of the corresponding ionic concentration at the particle–fluid interface. Taking the difference of the no–flux boundary conditions for the two ionic species and making use of Eq. (5.29), one obtains

$$\boldsymbol{n}\cdot\big(\nabla\rho^{(1)} + \nabla\psi'^{(1)} - \boldsymbol{E}^{(1)}\big)\Big|_{r=R} = 0\,. \tag{5.36}$$

In spherical coordinates, the normal vector always points in direction of the radial vector, and hence one may write

$$\left(\frac{\partial}{\partial r}\rho^{(1)} + \frac{\partial}{\partial r}\psi'^{(1)} - E_r^{(1)}\right)\Big|_{r=R} = 0\,, \tag{5.37}$$

where $E_r^{(1)}$ is the radial component $E_r^{(1)} = \hat{\boldsymbol{e}}_r \cdot \boldsymbol{E}^{(1)}$.
We make the following ansatz for the charge distribution and for the electrostatic potential: A charge distribution of the form

$$\rho(\boldsymbol{r}) \;=\; \rho_0 \boldsymbol{E}^{(1)} \cdot \nabla \frac{e^{-r}}{r}\,, \tag{5.38}$$

satisfies the stationary version of Eq. (5.32). The potential in the region of the fluid is assumed to have a screened part and a long–range term

$$\psi'^{(out)}(\boldsymbol{r}) \;=\; \rho_0 \boldsymbol{E}^{(1)} \cdot \nabla \left(-\frac{e^{-r}}{r} + V_0 \frac{1}{r} \right)\,, \tag{5.39}$$

and in the region occupied by the particle the potential is assumed to be

$$\psi'^{(in)}(\boldsymbol{r}) \;=\; -W_0 \boldsymbol{E}^{(1)} \cdot \boldsymbol{r}\,. \tag{5.40}$$

The constants ρ_0, V_0 and W_0 can be calculated from the boundary conditions. Inserting Eq. (5.39) and Eq. (5.40) into the boundary conditions Eq. (5.33) and Eq. (5.34), one obtains

$$\left(\frac{e^{-r}}{r} + \frac{e^{-r}}{r^2} - V_0 \frac{1}{r^2} \right) \Bigg|_{r=R} \;=\; -\frac{W_0}{\rho_0} R\,, \tag{5.41}$$

$$\left(-\frac{e^{-r}}{r} - 2\frac{e^{-r}}{r^2} - 2\frac{e^{-r}}{r^3} + V_0 \frac{1}{r^3} \right) \Bigg|_{r=R} \;=\; -\frac{W_0}{\rho_0}\,. \tag{5.42}$$

Thus we get

$$V_0 \;=\; \left(1 + R + \frac{1}{3}R^2 \right) e^{-R}\,, \tag{5.43}$$

$$W_0 \;=\; \frac{\rho_0}{3R} e^{-R}\,. \tag{5.44}$$

Inserting the ansatz Eq. (5.38) into the no–flux boundary condition, Eq. (5.37), one obtains

$$\rho_0 \left(\frac{\partial^2}{\partial r^2} \frac{e^{-r}}{r} - \frac{\partial^2}{\partial r^2} \frac{e^{-r}}{r} + V_0 \frac{\partial^2}{\partial r^2} \frac{1}{r} \right) \Bigg|_{r=R} = 1\,, \tag{5.45}$$

and applying the expression for V_0 results in

$$\rho_0 \;=\; \frac{R^3}{2} \frac{1}{V_0} \;=\; \frac{R^3 e^R}{2\left(1 + R + \frac{1}{3}R^2\right)}\,. \tag{5.46}$$

Knowing the prefactor ρ_0, the dipole moment can be calculated via

$$\boldsymbol{p} \;=\; \int_{r>R} d^3r\, \boldsymbol{r} \rho^{(1)}(\boldsymbol{r})\,. \tag{5.47}$$

Making use of spherical coordinates, this becomes

$$\begin{aligned}
\boldsymbol{p} &= \rho_0 \int_R^\infty \int_0^\pi \int_{-\pi}^\pi dr d\vartheta d\varphi \, r^3 \sin\vartheta \, \hat{\boldsymbol{e}}_r (\boldsymbol{E}^{(1)} \cdot \hat{\boldsymbol{e}}_r) \frac{\partial}{\partial r} \frac{e^{-r}}{r} \\
&= \rho_0 \int_R^\infty dr \, r^3 \frac{\partial}{\partial r} \frac{e^{-r}}{r} \cdot \int_0^\pi \int_{-\pi}^\pi d\vartheta d\varphi \, \sin\vartheta \, (\hat{\boldsymbol{e}}_r \otimes \hat{\boldsymbol{e}}_r) \, \boldsymbol{E}^{(1)} \\
&= -\rho_0 \, 3 \left(1 + R + \frac{1}{3} R^2 \right) e^{-R} \, \frac{4\pi}{3} \overleftrightarrow{\boldsymbol{I}} \, \boldsymbol{E}^{(1)} \\
&= -2\pi R^3 \boldsymbol{E}^{(1)} \, . \qquad (5.48)
\end{aligned}$$

This is exactly what is obtained from the result in Ref. [4] in the limit of vanishing frequency of the external field.

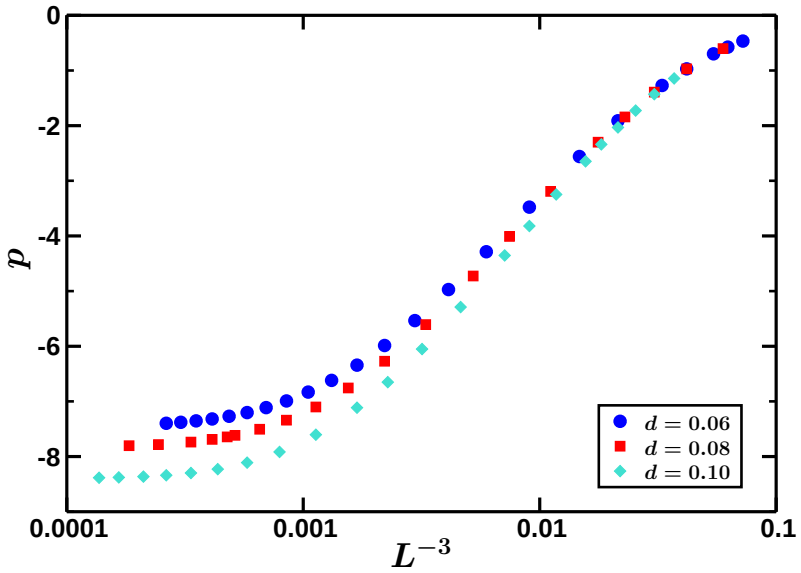

Figure 5.14.: Dipole moment as function of the inverse box size for three different resolutions.

First, we applied our numerical method to the problem of an uncharged sphere. The radius of the sphere was $R = 1$ and the electric field was set to $E = 1$. For these parameters we expect from Eq. (5.48) a dipole moment of $p = -2\pi$. Since the numerical method operates on a system of one sphere in the center of a periodic box, finite size effects are expected to be strong, due to dipole–dipole interactions of the periodic images. To compare the numerical results with the analytic expression, we first have to extrapolate our computational data to the limit of an infinitely extended box. Furthermore, Eq. (5.48) shows that

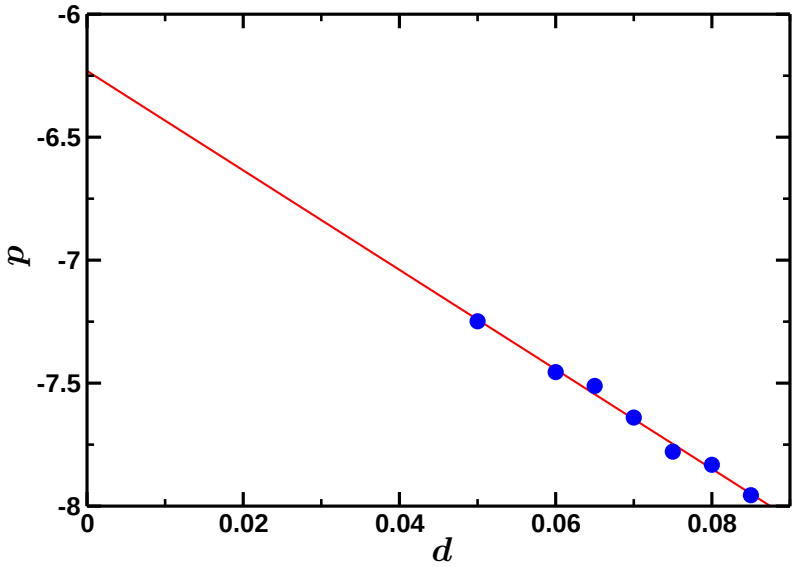

Figure 5.15.: Dipole moment as function of the lattice spacing $d \equiv \Delta x/R$. The blue data points are extrapolated to the limit of infinite box size. The red line is a linear fit to obtain the continuum limit $d \to 0$.

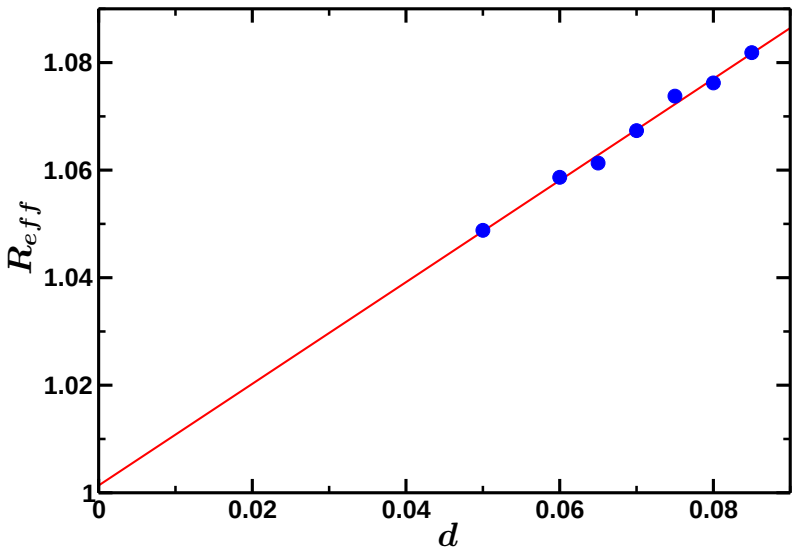

Figure 5.16.: The data of Fig. 5.15 have been rescaled to an effective radius $R_{eff} = (-p/2\pi E)^{1/3}$. The red line is a linear fit. We expect $R = 1$ in the continuum limit.

the dipole moment is proportional to the cube of the particle radius. Thus, the numerical results depend strongly on discretization effects and we should extrapolate our numerical data to the continuum limit.
The results of this analysis are presented in Fig. 5.14, 5.15 and 5.16. In Fig. 5.14 the computed dipole moment is plotted as function of the inverse box size L^{-3} for three different grid resolutions $d \equiv \Delta x/R$. Indeed, the anomalous dipole moment can be observed, and furthermore the results are subject to rather strong finite size effects. Several of such curves with different grid resolutions have been extrapolated to the limit $L^{-3} \to 0$. In Fig. 5.15 the results of the extrapolation are presented. We obtain the continuum limit of the dipole moment by a linear fit (red line), resulting in

$$p(d \to 0) \simeq -6.23\,, \tag{5.49}$$

which deviates less than 1% from the expected value of -2π.
Since the particle is assumed to be systematically too large (due to the discretization), we rescaled the extrapolated values of the dipole moment such that we obtain effective radii for the discretized spheres,

$$R_{eff} = \left(-\frac{p}{2\pi E}\right)^{1/3}\,. \tag{5.50}$$

The effective particle radius is presented in Fig. 5.16 as function of the resolution. A linear fit recovers the expected value of $R = 1$ quite well in the continuum limit, $R_{eff}(d \to 0) \simeq 1.0014$.

Starting from there, the *reduced charge* of the colloidal sphere was increased by small steps and the hydrodynamic equations and the convective velocity field were taken into account. Three different curves for the dipole moment as function of the particle charge are presented in Fig. 5.17. The reduced colloid radius was set to $R = 1$ and the electric field was set to $E = 1$ acting in x direction. The curves presented were computed for a resolution of $d = 0.07$ and a volume fraction of $\Phi \simeq 12.21 \cdot 10^{-3}$ (blue circles) and $\Phi \simeq 8.24 \cdot 10^{-3}$ (red squares) and for a resolution of $d = 0.08$ with $\Phi \simeq 8.18 \cdot 10^{-3}$ (turquoise diamonds). Indeed the dipole moment increases with increasing charge. For a reduced charge of about $Z = 2$, depending on the volume fraction, the sign of the dipole moment changes. In Fig. 5.18, 5.19 and 5.20 two dimensional cuts in the x-y–plane are presented for the first order concentration of the negative salt ions (Fig. 5.18), the positive salt ions (Fig. 5.19) and the first order charge density (Fig. 5.20). All images were produced for systems characterized by $d = 0.08$, $\Phi \simeq 8.18 \cdot 10^{-3}$, $R = 1$ and $E = 1$. The corresponding charges and measured dipole moments are $Z = 0$ with $p \simeq -6.44$, $Z = 1.8$ with $p \simeq 0.087$ and $Z = 3$ with $p \simeq 11.16$. Fig. 5.20 (b), showing the first order charge distribution for the system with $d = 0.08$, $R = 1$, $E = 1$ and

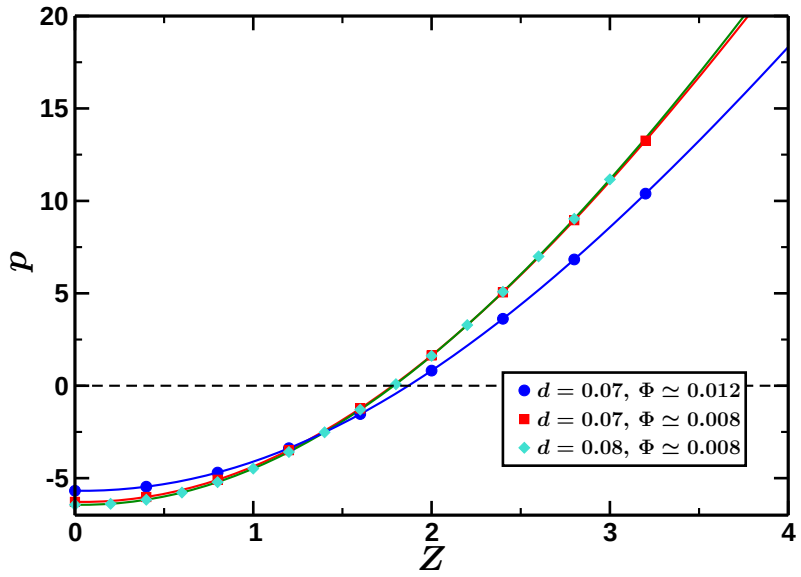

Figure 5.17.: Dipole moment as function of the reduced particle charge, for $R = 1$, $d = 0.07$ with $\Phi \simeq 12.21 \cdot 10^{-3}$ (blue), $\Phi \simeq 8.24 \cdot 10^{-3}$ (red) and $d = 0.08$ with $\Phi \simeq 8.18 \cdot 10^{-3}$ (turquoise). The solid lines are just guides to the eye.

$\Phi \simeq 8.18 \cdot 10^{-3}$, seems to have still an anomalous dipole moment $p < 0$. However, the measured dipole moment is $p \simeq 0.0873$. In Fig. 5.21 the same data are presented, but with a rescaled colormap. In this representation, we see that far from the colloid surface the ion cloud begins to reverse. The corresponding velocity field of this system is shown in Fig. 5.22.

Furthermore, several runs were performed for $d = 0.07$, $R = 1$, $E = 1$ and some different volume fractions and colloid charges in the vicinity of the critical value, i. e. the charge of the colloidal sphere, at which the dipole moment switches its sign. The value of the critical charge was obtained from splines. The results of these runs are shown in Fig. 5.23. We plotted the roots of the splines versus the inverse box size L^{-1} and observed a linear dependency. A linear regression and extrapolation to zero volume fraction results in a critical charge of

$$Z_{crit}(\Phi \to 0) \;=\; 1.11 \pm 0.02\,. \tag{5.51}$$

We also reproduced the curves of Fig. 5.17 for different field strengths in the range of $E = 0.01 \ldots 10$, and compared the values of p/E, and indeed, they match perfectly, as expected from the linearization of the underlying equations.

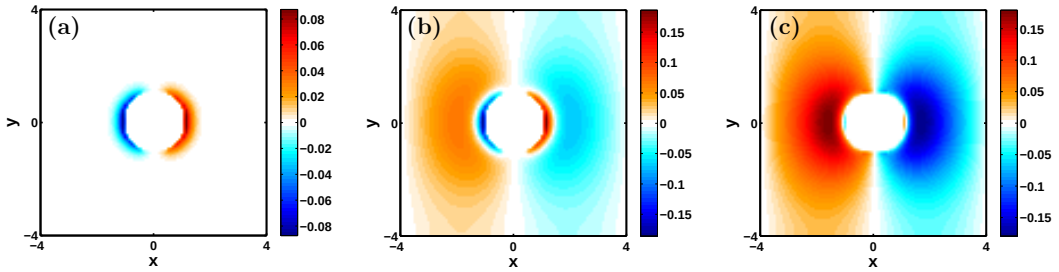

Figure 5.18.: 2–dimensional cuts of the first order concentration profile of the negative salt ions $c_{-}^{(1)}$, for the parameters $d = 0.08$, $R = 1$, $\Phi \simeq 8.18 \cdot 10^{-3}$ and an electric field of $E = 1$ acting in the x direction. The reduced charges of the sphere and the dipole moments of the system are (a) $Z = 0.0$, $p = -6.44$, (b) $Z = 1.8$, $p = 0.087$ and (c) $Z = 3.0$, $p = 11.16$.

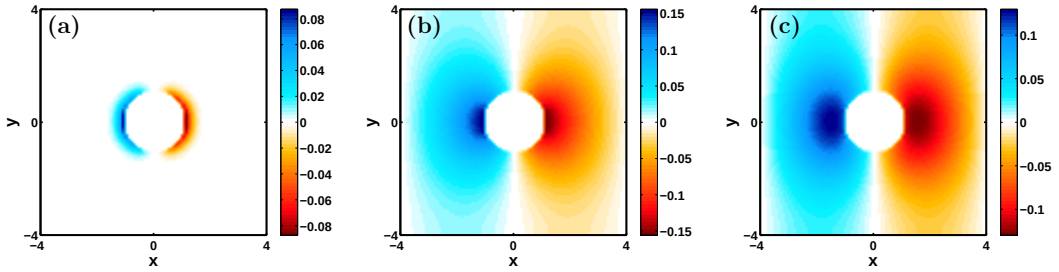

Figure 5.19.: 2–dimensional cuts of the positively charged salt concentration $c_{+}^{(1)}$, for the same sets of parameters as in Fig. 5.18.

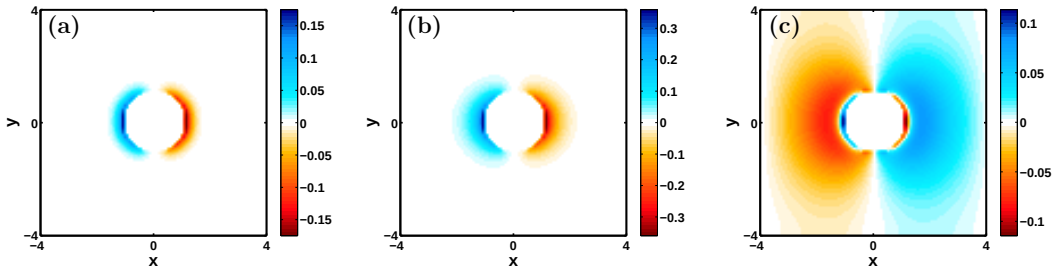

Figure 5.20.: 2–dimensional cuts of the first order charge density $\rho^{(1)}$. The parameters are the same as in the previous images (see Fig. 5.18).

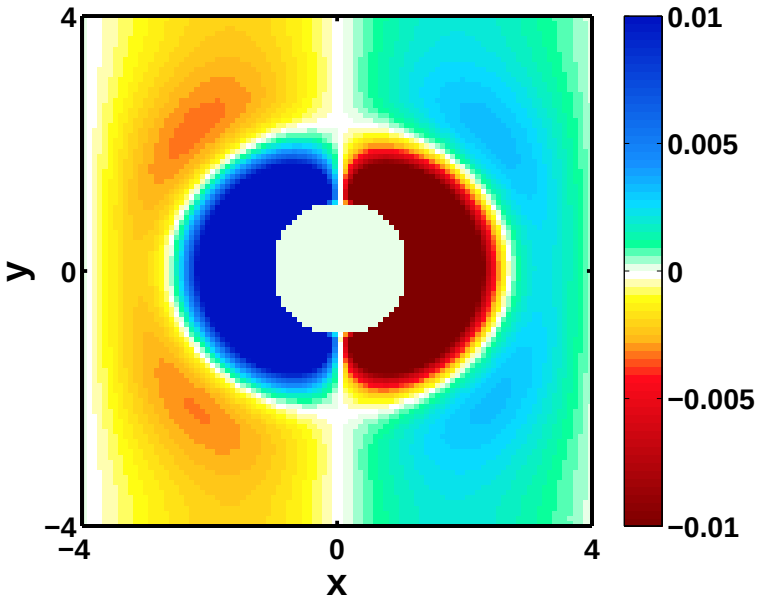

Figure 5.21.: 2–dimensional cut of $\rho^{(1)}$ for $d = 0.08$, $\Phi \simeq 8.18 \cdot 10^{-3}$, $R = 1.0.$, $E = 1$, $Z = 1.8$ and $p = 0.087$. Same data as in Fig. 5.20(b) but with rescaled colormap.

Common electrokinetic studies usually treat the problem of highly charged colloidal particles, thus, Kang and Dhont are the first addressing the problem of uncharged colloids. They emphasize that structural changes may be induced by an external field not only in charged systems where the salt ions interact with the electric field generated by the surface charges of the macroions, but even for uncharged systems where ion fluxes are deflected at the cores of the colloids. Our method offers the opportunity to study both cases, i. e. uncharged and charged colloids, and increase the particle charge slowly and systematically.

Finally, we investigate the speculation that the difference in the dipole moment between both cases could be an effect of convection. The convective term only occurs in the linearized electrokinetic equations for the charged spheres, but is absent in the neutral case. Since we study the problem in the rest frame of the macro–particles the convective flow could carry ions and therefore charges of both polarities around the sphere. An advantage of the Mean-Field equations is that we can test this hypothesis by just omitting the velocity field in the

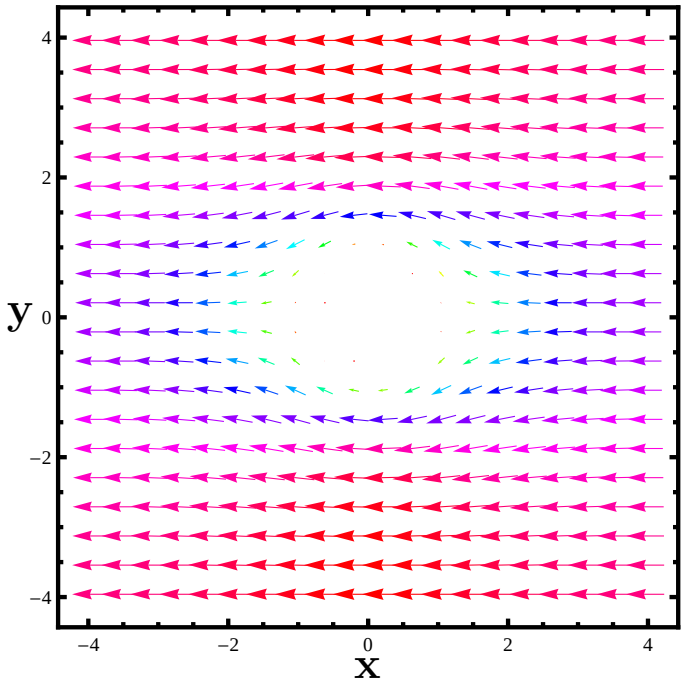

Figure 5.22.: Illustration of the convective velocity field. The parameters are the same as in Fig. 5.21.

convection-diffusion equation and run the program again for a charged sphere.[3] We applied this "experiment" to some data for colloidal systems with $R = 1$, $E = 1$, $d = 0.08$ and $\Phi \simeq 8.18 \cdot 10^{-3}$ and for several charges. We find that the convective velocity field is not the only effect responsible for the reversal of the dipole moment. Nevertheless, it intensifies the effect strongly as shown in Fig. 5.24.

[3]Note that this is equivalent with the limit of an infinite diffusion constant of the surrounding ions.

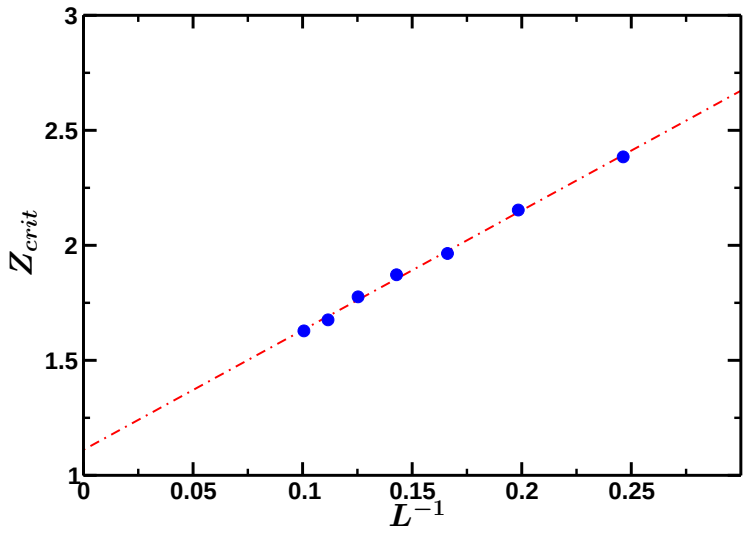

Figure 5.23.: Critical charge as function of the inverse box length L^{-1} as obtained from the roots of spline functions. The line is a linear fit to the data points.

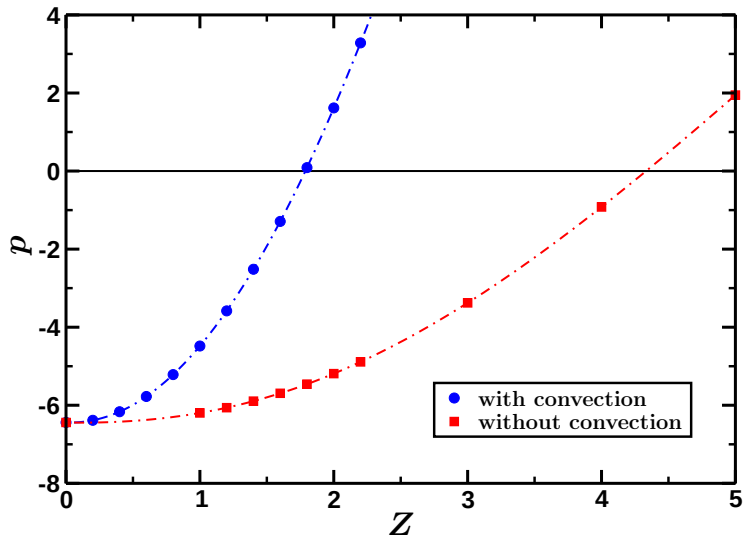

Figure 5.24.: Dipole moment as function of the reduced charge for the same parameters as in Fig. 5.17. Here, we choose $d = 0.08$ and $\Phi \simeq 8.18 \cdot 10^{-3}$. The blue circles are the same data as before. For the red squares the convection velocity was set to $\boldsymbol{v}^{(1)} \equiv 0$. The dash–dotted lines are cubic splines.

6. Hydrodynamics Near Surfaces

In chapter 3 a lattice method for the solution of the convection–diffusion equation was introduced. The lattice version of the algorithm operates directly on the desired density/concentration and thus does not require concrete simulation of a certain number of particles. On the other hand, in continuous space a particle-based stochastic algorithm can also be used for solving the CDE numerically [96, 97].
In this chapter a new application for such a particle based stochastic CDE solver is presented, namely the quantitative analysis of experimental data from a new surface sensitive method for the study of hydrodynamic effects close to solid–fluid interfaces, known as *Fluorescence Cross–Correlation Spectroscopy in Total Internal Reflection* (TIR-FCCS).
This project was done in collaboration with Stoyan Yordanov and Kaloian Koynov (AK Butt, MPIP Mainz), who designed and performed the experiments.

The assumption of *stick* boundary conditions, i. e. zero flow velocity at the solid–fluid interface, is very convenient, when fluid flow is studied in macrochannels. Nevertheless, on small length scales a liquid possibly slips over the solid surface of the channel. Thus the assumption of stick boundary conditions is not always sufficient when channels of micrometer or even nanometer size are considered [98]. The effect of fluid slippage is usually described by *slip* boundary conditions, which are typically characterized by the ratio of the dynamic viscosity and the finite friction coefficient per unit area of the fluid at the solid surface. Since the ratio has the dimension of a length, it is known as *slip length* l_s. Measuring the slip length by experiments is very challenging, since high resolution techniques are necessary to gain information close to interfaces. Therefore the existence and the extent of a slip length in real physical systems and its dependence on surface properties is a highly debated topic in the community.

In order to address this problem, S. Yordanov et al. recently introduced a new optical experimental method, called TIR-FCCS [5], which is based on a method known as two-beam FCCS [99]. Here, fluorescent tracer particles in the fluid are used to analyze the flow. They are excited by laser light focused to two observation volumes, and the signal of the emitted light of the tracer particles in the two observation volumes is convoluted to a time

cross–correlation function. For a quantitative data analysis an analytical model for the form of the correlation functions is needed. In some special cases, such analytical functions can be calculated. For example, in the case of single focus TIR-FCS and if only free diffusion is assumed, an expression for the auto–correlation function is known [100, 101], or in the bulk case, i. e. far away from interfaces, analytical solutions can also be derived if diffusion plus a constant or linear flow profile is assumed [99, 102–104]. However, in the present case, i. e. diffusion and a non–trivial fluid flow close to an interface, it is difficult, or even impossible, to derive an analytic expression for the auto– and cross–correlation functions.

In the following we introduce a new numerical method for the problem and apply it to experimental results in the case of fluid flow through a microchannel with hydrophilic walls.

6.1. Experimental Setup

Since the aim of this chapter is the development of the computational method for the generation of correlation curves and the discussion of a statistical method for the comparison of experimental and numerical data, this section is devoted to a brief introduction into the experimental method and the basic ideas and quantities. Further explanations on the experimental setup can be found in the publication of S. Yordanov et al. [5].
The experimental setup is based on a commercial confocal FCS device (Carl Zeiss, Jena, Germany). A parallel laser beam enters a rectangular flow channel through its bottom wall. By increasing the angle of incidence over a critical value total internal reflection occurs producing an evanescent wave. The intensity distribution $I(\boldsymbol{r})$ of this wave has approximately a Gaussian shape in the x-y-plane, i. e. parallel to the interface, and decays exponentially in the z-direction with a decay length d_p. This decay length is called *penetration depth* and depends on the laser wavelength and the indexes of refraction of both media. It can be varied by changing the incident angle. Tracer molecules are dissolved in the fluid and emit fluorescence light when excited by the laser beam. This fluorescence light is then collected by an objective and is equally split up by passing through a neutral 50:50 beam splitter to enter two independent detection channels. In each channel the fluorescent light passes through an emission filter and a confocal pinhole to finally reach the detector. Each of the two confocal pinholes defines its own observation volume. The space dependent molecular detection efficiencies (MDE) of the two volume elements depend on the excitation intensity profile $I(\boldsymbol{r})$, on the quantum efficiency of the fluorescent tracer molecules and the detector and on the space–dependent collection efficiency of the setup. The lateral shape of the MDEs is generally

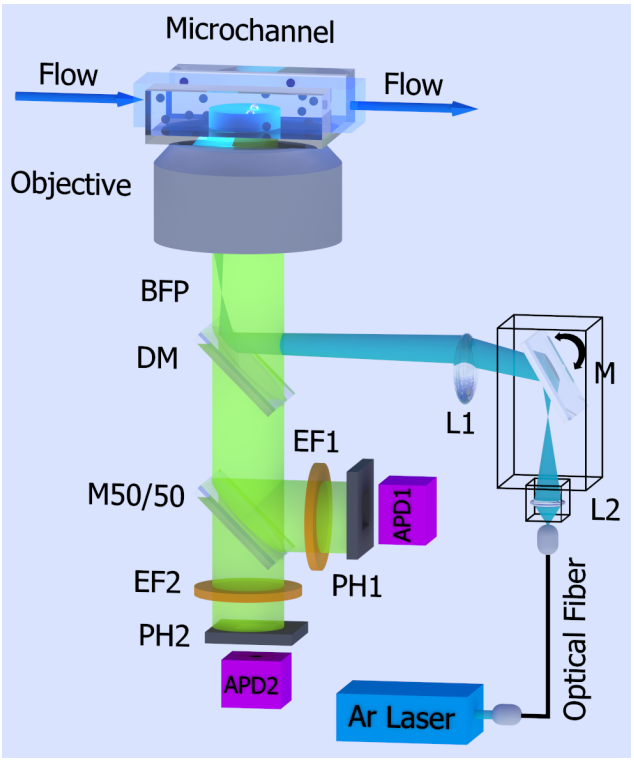

Figure 6.1.: Illustration of the experimental TIR-FCCS setup. BFP - back focal plane of the objective; DM - dichroic mirror; M50/50 - neutral 50% beam splitter; EF1, EF2 - emission filters; PH1, PH2 - pinholes; APD1, APD2 - avalanche photodiodes; L1 - tube lens; L2 - collimator lens; M - collimator's prism based mirror. Note that the two spatially separated observation volumes are created by shifting the pinholes PH1/PH2 in x-y-plane. The cyan color indicates the excitation wavelength and the yellow-green color the fluorescence light, respectively. (This image was created by S. Yordanov and is presented here with his kind permission.)

given by the point-spread function (PSF) of the objective, convoluted with the image of the pinhole (see for example Ref. [105]). Furthermore the MDEs decay exponentially along the optical axis due to the evanescent wave. Thus, we can define the MDEs of the two pinholes as

$$W_1(\boldsymbol{r}) \propto \int_{|\boldsymbol{r}_{0,xy}|<R} d^2\boldsymbol{r}_{0,xy} \left(\frac{2J_1(kNA|\boldsymbol{r}_{xy} - \boldsymbol{r}_{0,xy}|)}{kNA|\boldsymbol{r}_{xy} - \boldsymbol{r}_{0,xy}|} \right)^2 \exp\left[-\frac{z}{d_p} \right], \qquad (6.1a)$$

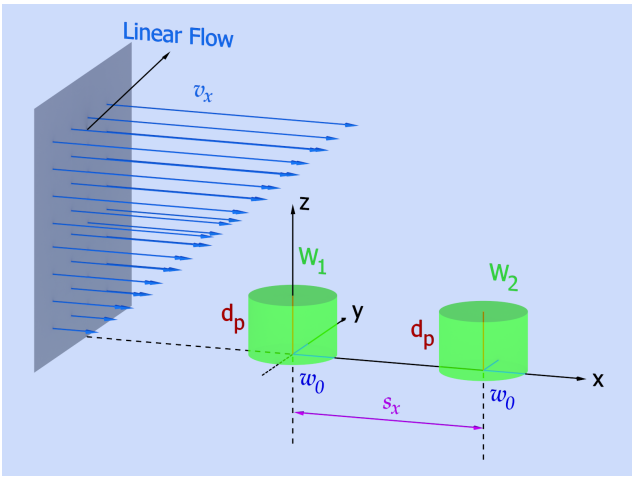

Figure 6.2.: The coordinate system and the linear flow field employed in the TIR-FCCS experiment. W_1 and W_2 denote the shape and location of the observation volumes as seen by pinhole PH1 and pinhole PH2, respectively; d_p is the penetration depth, which define the axial extend of the observation volume; w_0 is the $1/e^2$ radius in x-y-plane of the observation volumes; s_x indicates the observation volumes separation, center to center distance; v_x is the velocity field in positive x direction, which depends linearly on z and with other velocity components equal $v_{y,z} = 0$, respectively. (This image was created by S. Yordanov and is presented here with his kind permission.)

$$W_2(\boldsymbol{r}) \propto \int_{|\boldsymbol{r}_{0,xy}|<R} d^2\boldsymbol{r}_{0,xy} \left(\frac{2J_1(kNA|\boldsymbol{r}_{xy} - s_x\hat{\boldsymbol{e}}_x - \boldsymbol{r}_{0,xy}|)}{kNA|\boldsymbol{r}_{xy} - s_x\hat{\boldsymbol{e}}_x - \boldsymbol{r}_{0,xy}|} \right)^2 \times \exp\left[-\frac{z}{d_p} \right]. \tag{6.1b}$$

Here, J_1 is the first *Bessel function*, k is the wave number of the fluorescent light, NA denotes the numerical aparture of the objective, $\boldsymbol{r}_{xy}$ is a two-dimensional vector in the x-y-plane and R denotes the radius of the pinhole in the image plane. s_x is the separation of the centers of the two detection volumes along the flow axis. The factor kNA has the dimension of an inverse length and defines the "width" of the pinhole convoluted point-spread function (PCPSF). Later we will introduce this factor as fitting parameter in the form $\lambda := (kNA)^{-1}$. In accordance with the existing literature and the common approximations, we first approximate the MDEs by Gaussian functions, such

that the observation volumes can be written as

$$W_1(\boldsymbol{r}) \;\propto\; \exp\left[-2\frac{x^2+y^2}{w_0^2}\right]\exp\left[-\frac{z}{d_p}\right], \tag{6.2a}$$

$$W_2(\boldsymbol{r}) \;\propto\; \exp\left[-2\frac{(x-s_x)^2+y^2}{w_0^2}\right]\exp\left[-\frac{z}{d_p}\right]. \tag{6.2b}$$

The lateral size of the focus is given by w_0. The experimental setup is sketched in Figs. 6.1 and 6.2.

6.2. Correlation Functions

The tracer particles move due to diffusion and the flow field and pass consecutively through the two observation volumes. This results in two time–resolved fluorescence intensities $I_1(t)$ and $I_2(t)$. From the fluctuations of this quantity the time dependent auto– and cross–correlation functions can be calculated as

$$G_{ij}(t) \;=\; \frac{\langle \delta I_i(0)\delta I_j(t)\rangle}{\langle I_i\rangle\langle I_j\rangle}, \quad (i,j=1,2)\,, \tag{6.3}$$

where $\langle\cdot\rangle$ denotes the time average or, when ergodicity is assumed, an ensemble average. As described in Refs. [99, 102, 106], a theoretical expression for this correlation function can be obtained from

$$G_{ij}(t) \propto \int\int d^3r d^3r' W_i(\boldsymbol{r}) W_j(\boldsymbol{r}')\Phi(\boldsymbol{r},\boldsymbol{r}',t), \tag{6.4}$$

where $\boldsymbol{r}$, $\boldsymbol{r}'$ are spatial positions, and $\Phi(\boldsymbol{r},\boldsymbol{r}',\tau)$ is called concentration fluctuation function. It contains the dynamics of the system and is given by

$$\Phi(\boldsymbol{r},\boldsymbol{r}',t) = \langle \delta C(\boldsymbol{r},t)\delta C(\boldsymbol{r}',0)\rangle\,, \tag{6.5}$$

where $\delta C(\boldsymbol{r},t) = C(\boldsymbol{r},t) - \langle C\rangle$ is the fluctuation in the concentration $C(\boldsymbol{r},\tau)$ of the fluorescent tracers. The tracer particles undergo a diffusion process and move in an externally driven flow field $\boldsymbol{v}$. Hence, the concentration–fluctuation function is described by a convection–diffusion equation (CDE) of the form

$$\partial_\tau \Phi(\boldsymbol{r},\boldsymbol{r}',t) = D\nabla^2_{\boldsymbol{r}}\Phi(\boldsymbol{r},\boldsymbol{r}',t) - \boldsymbol{v}(\boldsymbol{r})\cdot\nabla_{\boldsymbol{r}}\Phi(\boldsymbol{r},\boldsymbol{r}',t), \tag{6.6}$$

with the initial condition $\Phi(\boldsymbol{r},\boldsymbol{r}',0) = \langle C\rangle\delta(\boldsymbol{r}-\boldsymbol{r}')$, and the *no–flux* boundary condition $j_z|_{z=0} = 0$, where j_z is the particle current density perpendicular to the channel wall, and hence the desired solution of the CDE is only defined in the positive half space, $z > 0$. Note that the initial condition states that the equilibrium concentration fluctuations are spatially uncorrelated.

For simplicity reasons, the hydrodynamic interactions with the surface are neglected, and hence the diffusive term is described by an isotropic diffusion constant D.
Since in the experiment the exponential decay length of the spatial detection volume normal to the surface is in the range of $100nm$, while the channel size is a few orders of magnitude larger, it is justified to assume the flow field to be approximately linear in the vicinity of the interface. Although it is possible to obtain an analytic solution for the CDE with a linear flow profile in bulk [103, 104], it is difficult, or even impossible, to find such a solution if a wall breaks spatial symmetry.

Note that Eq. (6.4) is only rigorously true, if and only if W_1 and W_2 are the true observation volumes detected in each detector. In the standard two beam FCCS case, it is known that this is not the case, but both detectors would detect a small amount of particles illuminated by the second laser spot. This phenomenon is called *cross-talk* [99] and causes an additional auto-correlation like behavior of the cross-correlation function, known as *pseudo-cross-correlation function*. In the FCS community it is commonly accepted that the subtraction of this pseudo-cross correlation curve, basically measured by the backward-cross correlation G_{21}, leads to the pure cross-correlation curve as expected from the two MDEs. However, the error done by this procedure is indeed small, if both the overlap of W_1 and W_2 and the cross-talk are small. If this is the case, one may introduce two extended MDEs as

$$\mathcal{M}_1 := W_1 + \kappa W_2 \,, \tag{6.7a}$$
$$\mathcal{M}_2 := W_2 + \kappa W_1 \,, \tag{6.7b}$$

where the fraction κ is known as *overlapping factor*. Using these observation volumes and defining the asymmetric bilinear form

$$\langle A|B\rangle := \int\int d^3r d^3r' B(\boldsymbol{r}) A(\boldsymbol{r}') \Phi(\boldsymbol{r}, \boldsymbol{r}', t) \,, \tag{6.8}$$

Eq. (6.4) is replaced by

$$G_{ij}(t) \propto \langle \mathcal{M}_i | \mathcal{M}_j \rangle \,. \tag{6.9}$$

For the forward-cross correlation this results in

$$\begin{aligned} G_{12}(t) &\propto \langle \mathcal{M}_1 | \mathcal{M}_2 \rangle \\ &= \langle W_1 + \kappa W_2 | W_2 + \kappa W_1 \rangle \\ &= \langle W_1 | W_2 \rangle + \kappa(\langle W_1 | W_1 \rangle + \langle W_2 | W_2 \rangle) + \kappa^2 \langle W_2 | W_1 \rangle \,, \end{aligned} \tag{6.10}$$

and analogously for G_{21}. Subtraction of the backward-cross correlation then yields

$$G_{12}(t) - G_{21}(t) \propto (1 - \kappa^2)(\langle W_1 | W_2 \rangle - \langle W_2 | W_1 \rangle) \,. \tag{6.11}$$

Now, assuming κ is small (usually of the order of 1%), one may set the prefactor as unity. Note that for similar reasons we have also ignored the κ-dependence of the proportionality factor between the double integral and G_{ij}.
However, in the present experimental setup there are not two independent illumination spots, rather the two observation volumes are defined by the pinholes, and thus this kind of cross-talk is experimentally not expected. Nevertheless, the cross-correlation data also show an auto-correlation like behavior (see Fig. 6.5), which cannot be explained by the pure overlap of W_1 and W_2. This is perhaps an effect of reflections in the optical setup (e.g. reflections within the dichroic 50% beam splitter), interference effects, non-perfect angles in the optical setup, resulting in distortions of the observation volumes, or other non-idealities of the optical setup. Since the source of this effect is at present not known and is also not easy to track in experiment, we assume in a first step that the same corrections which are usually done for the standard two beam FCCS measurements provide a reasonable cross-correlation curve plus some small corrections

$$G_{12} - G_{21} \simeq c_c(\langle W_1|W_2\rangle - \langle W_2|W_1\rangle)\,, \tag{6.12}$$

where c_c is a scaling constant, which can be treated as a fitting parameter (see Sec. 6.6). If a flow field is applied in the direction from W_1 towards W_2, the last term in this equation is generally given by the overlap of the observation volumes at time $t = 0$. If Gaussian shaped MDEs are assumed, this term can be neglected for the parameters in the given experiments. The numerical method itself, which is presented in the following, does, in its applicability, not depend on the shape of the observation volumes at all. Results for fitting the difference curve are discussed in Sec. 6.7. In this section results for Gaussian observation volumes are presented first. In the end, some results are shown for simulations where the Gaussian shaped MDEs are replaced by PCPSFs.

6.3. Sampling Algorithm

As already discussed in Chap. 3, the convection-diffusion equation for concentration fields has the same form as a Fokker-Planck equation for Brownian particles. This equivalence allows us to use a stochastic method, i. e. a Brownian Dynamics (BD) algorithm, to solve the CDE [96, 97, 107]. The idea is to simulate a random walk and to follow the trajectory of a single Brownian particle taking into account the velocity field, then repeat the procedure until we acquire enough statistics, which samples the solution of Eq. (6.6) by means of a large number of such trajectories. In the first step we re–interpret some parameters in terms of stochastic variables. The concentration fluctuation function can be interpreted as a propagator and hence $\Phi(\boldsymbol{r}, \boldsymbol{r}', t)$ is replaced by $P(\boldsymbol{r}', t'|\boldsymbol{r}, t)$, which is the propagator of a Brownian particle from the spatial

position $\boldsymbol{r}$ at time t to position $\boldsymbol{r}'$ at time t'. Furthermore, W_1 can be considered as a kind of detection probability, which acts as a production probability density for a Brownian particle and W_2 is just an observable at time $t > 0$. In other words, we generate particles according the probability distribution W_1 and observe them in the intensity field described by W_2. This ansatz has all advantages of an importance sampling algorithm [68] and reduces the noise in the final results.
The isomorphism between the Fokker–Planck picture and the Langevin picture [108–110] allows to describe the convection–diffusion process in terms of an overdamped Langevin equation. Thus an equivalent stochastic differential equation for the spatial position of the particle $\boldsymbol{r}(t)$ reads

$$\dot{\boldsymbol{r}}(t) = \boldsymbol{v}(\boldsymbol{r}(t)) + \boldsymbol{\eta}(t). \tag{6.13}$$

Here $\dot{\boldsymbol{r}}(t)$ is the tracer velocity, $\boldsymbol{v}$ is the deterministic (external) velocity and $\boldsymbol{\eta}$ is a stochastic noise term (due to the diffusion) with mean 0 and its second moment is defined by the fluctuation–dissipation theorem,

$$\langle \eta_\alpha(t) \rangle = 0, \tag{6.14a}$$
$$\langle \eta_\alpha(t') \eta_\beta(t) \rangle = 2D\delta_{\alpha\beta}\delta(t'-t), \tag{6.14b}$$

where $\alpha, \beta = x, y, z$ are Cartesian indices and $\delta_{\alpha\beta}$ is the Kronecker delta. In the case of constant shear flow in the x-z-plane with slip length l_s, the deterministic part has the form

$$\boldsymbol{v}(\boldsymbol{r}(t)) = \dot{\gamma} \overleftrightarrow{\boldsymbol{\varepsilon}} \, (\boldsymbol{r}(t) + l_s \hat{\boldsymbol{e}}_z), \tag{6.15}$$

where $\dot{\gamma} = \partial v_x / \partial z$ is the constant shear rate, $\hat{\boldsymbol{e}}_z$ denotes the unit vector in z-direction and $\overleftrightarrow{\boldsymbol{\varepsilon}}$ is the dimensionless rate-of-strain tensor,

$$\overleftrightarrow{\boldsymbol{\varepsilon}} = \begin{pmatrix} 0 & 0 & 1 \\ 0 & 0 & 0 \\ 0 & 0 & 0 \end{pmatrix}. \tag{6.16}$$

The propagation by a small time step is performed by a formal integration of Eq. (6.13),

$$\begin{aligned} \boldsymbol{r}(t+\Delta t) &= \boldsymbol{r}(t) + \int_t^{t+\Delta t} dt' \boldsymbol{v} + \int_t^{t+\Delta t} dt' \boldsymbol{\eta} \\ &\simeq \boldsymbol{r}(t) + \Delta t \dot{\gamma} \overleftrightarrow{\varepsilon} \, (\boldsymbol{r}(t) + l_s \hat{\boldsymbol{e}}_z) + \Delta \boldsymbol{r}^{sto}. \end{aligned} \tag{6.17}$$

According to Eq. (6.14), the stochastic displacements $\Delta \boldsymbol{r}^{sto}$ have to satisfy the moment conditions

$$\langle \Delta r_\alpha^{sto} \rangle = 0 \tag{6.18a}$$
$$\begin{aligned} \langle \Delta r_\alpha^{sto} \Delta r_\beta^{sto} \rangle &= \int_t^{t+\Delta t} dt' \int_t^{t+\Delta t} dt'' \langle \eta_\alpha(t') \eta_\beta(t'') \rangle \\ &= 2D \, \Delta t \, \delta_{\alpha\beta}. \end{aligned} \tag{6.18b}$$

Thus, we write

$$\boldsymbol{r}(t+\Delta t) = \boldsymbol{r}(t) + \Delta t\dot{\gamma}\overleftrightarrow{\varepsilon}\,(\boldsymbol{r}(t) + l_s\hat{\boldsymbol{e}}_z) + \sqrt{2D\Delta t}\boldsymbol{\chi}, \tag{6.19}$$

where $\boldsymbol{\chi}$ is a vector of Gaussian random numbers with mean 0 and variance 1. Eq. (6.19) is the well known first order Euler update and the simplest Brownian Dynamics (BD) algorithm. Thus the algorithm consists of the production of a particle with initial position $\boldsymbol{r}'$ at time $t_1 = 0$ with probability $W_1(\boldsymbol{r}')$ and the propagation for n time steps via $P(\boldsymbol{r}, t|\boldsymbol{r}', 0)$, $t = n\Delta t$. The probability density to find a particle at position $\boldsymbol{r}$ after a time t is

$$Q(\boldsymbol{r}, t) = \int d^3r' P(\boldsymbol{r}, t|\boldsymbol{r}', 0) W_1(\boldsymbol{r}'). \tag{6.20}$$

Then, for each point $\boldsymbol{r}(t)$, the particle is observed in the intensity field $W_2(\boldsymbol{r})$, for the cross–correlation, and $W_1(\boldsymbol{r})$, for the auto–correlation, respectively. This allows the correlation function to be expressed as the mean value of the functions W_1, W_2 at a certain time $t = n\Delta t$ over different and statistical independent trajectories. Averaging an arbitrary observable A, one obtains

$$\begin{aligned} \langle A\rangle(n\Delta t) &= \int d^3r A(\boldsymbol{r}) Q(\boldsymbol{r}, n\Delta t) \\ &= \int d^3r' \int d^3r A(\boldsymbol{r}) P(\boldsymbol{r}, n\Delta t|\boldsymbol{r}', 0) W_1(\boldsymbol{r}')\,. \end{aligned} \tag{6.21}$$

Thus the desired cross-correlation function is computed by the substitution $A(\boldsymbol{r}) = W_2(\boldsymbol{r})$, which up to a constant prefactor yields

$$\begin{aligned} G_{12}^{(\mathrm{s})}(t) &\propto \langle W_2\rangle(t) \\ &= \int d^3r' \int d^3r W_2(\boldsymbol{r}) P(\boldsymbol{r}, t|\boldsymbol{r}', 0) W_1(\boldsymbol{r}'). \end{aligned} \tag{6.22}$$

$G^{(\mathrm{s})}$ denotes the simulated correlation curve. Analogously the auto-correlation function is produced by setting $A(\boldsymbol{r}) = W_1(\boldsymbol{r})$.
The boundary condition at the wall is taken into account via reflection of the particles at position $z = 0$, i. e. the z component in the random walk is replaced by its absolute value $z(t) \equiv |z(t)|$ to assure that the solution is only sampled in the positive half space, $z > 0$.

6.4. Parameter Space and Dimensionless Units

For the purpose of numerical calculations, one may rewrite the problem in dimensionless units. Therefore we should first identify the whole parameter space.
The observation volume of the system is defined by Gaussians or PCPSFs in the x-y-plane with width $w_0/2$ (or λ) and a penetration depth d_p for the exponential decay perpendicular to the surface. Furthermore, the centers of observation volumes are separated by a length s_x along the x-axis, i. e. in flow direction. For the flow and the dynamics of the particles three additional intrinsic parameters occur, namely the diffusion constant D, the shear rate $\dot{\gamma}$ and the slip length l_s. For the discretization in the time domain, we further have to choose a time step Δt.
The height of auto- and cross-correlation functions also depends on the averaged concentration of tracer particles. Since the simulation method carries no information about this concentration, three additional unknowns have to be taken into account, which are the prefactors of the double integral of Eq. (6.22), c_1, c_2 accounting for the auto–correlation functions, and c_c adjusting the height of the cross–correlation function.
To re-formulate the problem in terms of dimensionless units, one should identify some intrinsic time and length scale. The most natural time scale of a diffusive system, independent of any flow velocity, is the diffusion constant divided by the square of a typical length scale. Choosing the penetration depth as intrinsic length scale, all time and space parameters are transformed via

$$\tilde{r} = \frac{r}{d_p}, \tag{6.23a}$$

$$\tilde{t} = t\frac{D}{d_p^2}. \tag{6.23b}$$

Hence, we have to replace $w_0 = \tilde{w}_0\, d_p$ ($\lambda = \tilde{\lambda}\, d_p$), $\dot{\gamma} = \tilde{\dot{\gamma}}\, D/d_p^2$, $l_s = \tilde{l}_s\, d_p$, $s_x = \tilde{s}_x\, d_p$ and $\Delta t = \tilde{\Delta t}\, d_p^2/D$. Introducing this dimensionless formulation, one may write the Euler update, Eq. (6.19), in the form

$$\tilde{\boldsymbol{r}}(\tilde{t}+\tilde{\Delta t}) = \tilde{\boldsymbol{r}}(\tilde{t}) + \tilde{\Delta t}\tilde{\dot{\gamma}}\, \overleftrightarrow{\boldsymbol{\varepsilon}}\, (\tilde{\boldsymbol{r}}(\tilde{t}) + \tilde{l}_s\hat{\boldsymbol{e}}_z) + \sqrt{2\tilde{\Delta t}}\boldsymbol{\chi}, \tag{6.24}$$

and the MDEs can be written as

$$W_1 \propto \exp\left(-2\frac{\tilde{x}^2+\tilde{y}^2}{\tilde{w}_0^2}\right)\exp(-\tilde{z}), \tag{6.25a}$$

$$W_2 \propto \exp\left(-2\frac{(\tilde{x}-\tilde{s}_x)^2+\tilde{y}^2}{\tilde{w}_0^2}\right)\exp(-\tilde{z}), \tag{6.25b}$$

or, if the observation volumes are modeled as diffraction patterns, as

$$W_1(\tilde{\boldsymbol{r}}) \propto \int_{|\tilde{\boldsymbol{r}}_{0,xy}|<\tilde{R}} d^2\tilde{\boldsymbol{r}}_{0,xy} \left(\frac{2J_1(\tilde{\lambda}^{-1}|\tilde{\boldsymbol{r}}_{xy} - \tilde{\boldsymbol{r}}_{0,xy}|)}{\tilde{\lambda}^{-1}|\tilde{\boldsymbol{r}}_{xy} - \tilde{\boldsymbol{r}}_{0,xy}|} \right)^2 \exp(-\tilde{z}), \quad (6.26a)$$

$$W_2(\tilde{\boldsymbol{r}}) \propto \int_{|\tilde{\boldsymbol{r}}_{0,xy}|<\tilde{R}} d^2\tilde{\boldsymbol{r}}_{0,xy} \left(\frac{2J_1(\tilde{\lambda}^{-1}|\tilde{\boldsymbol{r}}_{xy} - \tilde{s}_x\hat{\boldsymbol{e}}_x - \tilde{\boldsymbol{r}}_{0,xy}|)}{\tilde{\lambda}^{-1}|\tilde{\boldsymbol{r}}_{xy} - \tilde{s}_x\hat{\boldsymbol{e}}_x - \tilde{\boldsymbol{r}}_{0,xy}|} \right)^2 \times \exp(-\tilde{z}). \quad (6.26b)$$

Thus the simulation is completely defined by the parameters $\tilde{w}_0$ ($\tilde{\lambda}$), $\tilde{\dot{\gamma}}$, $\tilde{l}_s$, $\tilde{s}_x$ and $\tilde{\Delta}t$. The prefactors c_i can be seen as scaling parameters and have no direct influence on the results of the simulation. Similarly d_p and D define the spatial and time units, but do not occur in the equations for the computational method.

6.5. Numerical Test

As a simple test case, we used our algorithm to calculate the auto-correlation function for vanishing flow and a Gaussian MDE, where an analytical solution of the CDE and the double integral over observation volumes of the form Eq. (6.25) is known [100, 101]. In our dimensionless units, it is, up to constant prefactors, given by

$$G^{(\mathrm{a})}(\tilde{t}) = \frac{1}{1+\frac{4\tilde{t}}{\tilde{w}_0^2}} \left\{ \left(1-2\tilde{t}\right) \exp\left[\tilde{t}\right] \operatorname{erfc}\left[\sqrt{\tilde{t}}\right] + \sqrt{\frac{4}{\pi}\tilde{t}} \right\}. \quad (6.27)$$

The superscript (a) denotes for the analytic solution. Since the Langevin and the Fokker–Planck picture are rigorously equivalent, the simulated curve must coincide *exactly* with this analytic expression. Indeed we find that this is the case. Fig. 6.3 shows the analytic auto-correlation function with $\tilde{w}_0 = 2$ and its simulated counterpart, averaged over 10^3 independent trajectories, where a small time step of $\tilde{\Delta}t = 10^{-3}$ was used. In Fig. 6.4 the deviation of simulated data ($G^{(s)}$) from the analytic expression is shown,

$$\mathrm{error}(\tilde{t}) = G^{(\mathrm{s})}(\tilde{t}) - G^{(\mathrm{a})}(\tilde{t}). \quad (6.28)$$

Clearly, the numerical solution converges to the analytical result when the number of trajectories is increased, as it should be.

6.6. Statistical Data Analysis

Fitting experimental results via an analytic function for determining parameters and their error bars is a well known standard tool in science, and a huge

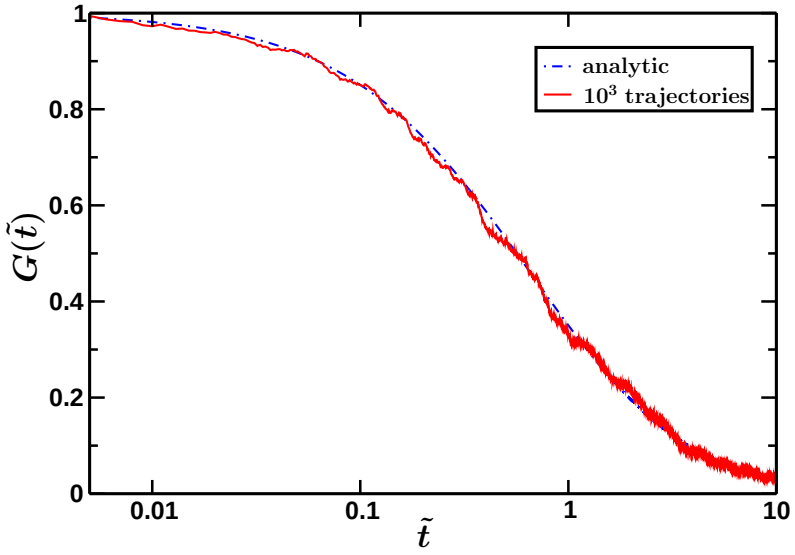

Figure 6.3.: Analytical solution and simulated data for the average over 10^3 trajectories.

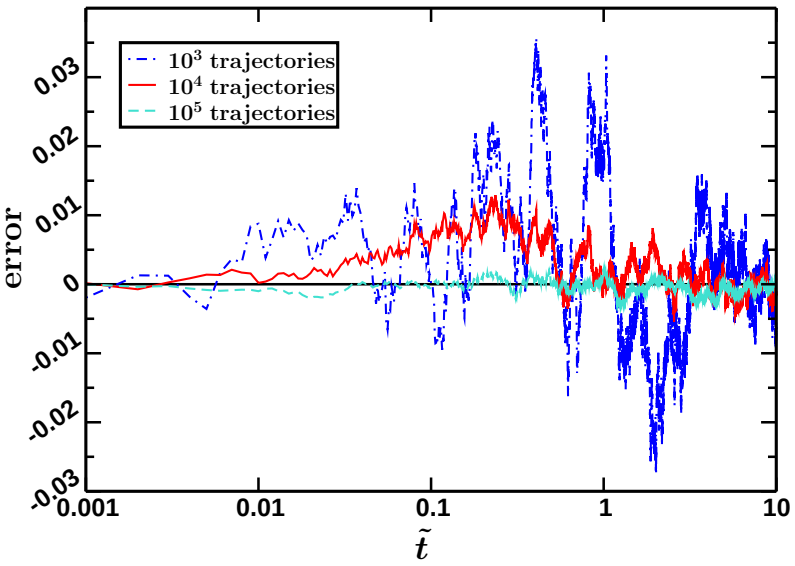

Figure 6.4.: Deviation from the analytic curve for 10^3,10^4 and 10^5 trajectories.

number of programs for this purpose is available. However, we do not have an analytic expression, but rather a second set of data points generated by a "computer experiment". These data points are means of random variables,

and hence tainted with statistical errors. In the following, a way of comparing these simulated results with experimental data points is presented. In a second step, we introduce a Monte Carlo (MC) method to determine the most probable values of the parameters and their statistical errors.

6.6.1. Comparing Experimental Data with Simulation Results

Here, each simulated data point is a mean value X_i, averaged over $m_x \simeq 2.5{\cdot}10^5$ independent trajectories and each experimental data point Y_i is the mean of $m_y = 40$ independent measurements. The index $i = 1, \ldots, M$ counts the number of data points, according to the time scale and to the three different curves (two auto– and one cross–correlation curve). From the statistical point of view, both, m_x as well as m_y, can be viewed as a large number such that X_i and Y_i are assumed to be Gaussian distributed around $\langle X_i \rangle$, $\langle Y_i \rangle$ with variance $(\sigma_i^{x,y})^2 = (s_i^{x,y})^2/m_{x,y}$. Here, $(s_i^{x,y})^2$ is the spread of the independent data

$$(s_i^x)^2 := \frac{1}{m_x - 1} \sum_{j=1}^{m_x} (X_i^j - X_i)^2, \tag{6.29}$$

$$(s_i^y)^2 := \frac{1}{m_y - 1} \sum_{j=1}^{m_y} (Y_i^j - Y_i)^2. \tag{6.30}$$

To measure the "goodness" of simulation, we define the weighted deviation between the experimental and the simulated data points

$$\alpha_i := \frac{X_i - Y_i}{\sqrt{(\sigma_i^x)^2 + (\sigma_i^y)^2}}\,. \tag{6.31}$$

Due to the statistical independence of experiment and simulation and the Gaussian distribution of the data points, α_i is also distributed normally;

$$\begin{aligned} P(\alpha) &= \int_{-\infty}^{\infty} dX \int_{-\infty}^{\infty} dY\, P(X) P(Y) \\ &\quad \cdot\delta\left(\alpha - \frac{X - Y}{\sqrt{(\sigma^x)^2 + (\sigma^y)^2}}\right) \\ &= \int_{-\infty}^{\infty} dX \int_{-\infty}^{\infty} dY\, P(X) P(Y) \\ &\quad \cdot\frac{1}{2\pi} \int_{-\infty}^{\infty} dk\, \exp\left[-ik\left(\alpha - \frac{X - Y}{\sqrt{(\sigma^x)^2 + (\sigma^y)^2}}\right)\right], \end{aligned} \tag{6.32}$$

and with

$$P(X) = \frac{1}{\sqrt{2\pi(\sigma^x)^2}} \exp\left[-\frac{(X-\langle X\rangle)^2}{2(\sigma^x)^2}\right], \tag{6.33}$$

$$P(Y) = \frac{1}{\sqrt{2\pi(\sigma^y)^2}} \exp\left[-\frac{(Y-\langle Y\rangle)^2}{2(\sigma^y)^2}\right], \tag{6.34}$$

integration yields

$$P(\alpha) = \frac{1}{\sqrt{2\pi}} \exp\left[-\frac{1}{2}\left(\alpha - \frac{\langle X\rangle - \langle Y\rangle}{\sqrt{(\sigma^x)^2+(\sigma^y)^2}}\right)^2\right]. \tag{6.35}$$

Since the simulation should match the experimental results, we aim for

$$\langle X\rangle - \langle Y\rangle = 0\,, \tag{6.36}$$

and hence

$$P(\alpha) = \frac{1}{\sqrt{2\pi}} \exp\left[-\frac{1}{2}\alpha^2\right]. \tag{6.37}$$

Furthermore, we define the *goodness of simulation* as the mean square weighted distance of simulation to the experimental data curves

$$\xi := \frac{1}{M}\sum_{i=1}^{M} \alpha_i^2\,. \tag{6.38}$$

Making use of Eq. (6.37), one obtains for a perfect match of both data curves

$$\begin{aligned}\langle\xi\rangle &= \frac{1}{M}\sum_{i=1}^{M}\langle\alpha_i^2\rangle \\ &= \langle\alpha^2\rangle \\ &= \frac{1}{\sqrt{2\pi}}\int_{-\infty}^{\infty} d\alpha\,\alpha^2\,\exp\left[-\frac{\alpha^2}{2}\right] \\ &= 1\,.\end{aligned} \tag{6.39}$$

It should be noted that if m_y is small, $(Y-\langle Y\rangle)/\sigma^y$ is not distributed normally any more, but rather follows a χ^2 distribution [111]. Even worse, if also m_x is not large, one has to think about the (yet unsolved) problem of comparing two random variables with different variances. However, the latter problem can be approximately treated by a variant of Student's t test, published by Welch in 1938 [112], who pointed out that α_i is approximately distributed via Student's t distribution with an estimated number of degrees of freedom

$$f_i = \frac{(\sigma_i^x+\sigma_i^y)^2}{\frac{(\sigma_i^x)^2}{m_x}+\frac{(\sigma_i^y)^2}{m_y}}\,. \tag{6.40}$$

The distribution of α_i then reads

$$T(\alpha, f) = \frac{\Gamma\left(\frac{f+1}{2}\right)}{\sqrt{f\pi}\,\Gamma\left(\frac{f}{2}\right)} \left(1 + \frac{\alpha^2}{f}\right)^{-\frac{f+1}{2}} . \tag{6.41}$$

Assuming this distribution, we also can calculate the expectation value of the goodness of simulation

$$\begin{aligned} \langle \xi \rangle &= \int_{-\infty}^{\infty} d\alpha\, \alpha^2\, T(\alpha, f) \\ &= \frac{f}{f-2} . \end{aligned} \tag{6.42}$$

As mentioned previously, $m_x \simeq 2.5 \cdot 10^5$ is much larger than the number of experiments $m_y = 40$, and hence we assume that the error of the simulated data is negligible compared to the experimental error and f becomes of the order of m_y. In this limit, we get $\langle \xi \rangle \simeq 1.05$, which agrees very well with the idealized case of normal distributed values. Moreover, in the limit $f \to \infty$, the Student's function indeed converges to the Gaussian distribution,

$$\lim_{f\to\infty} T(\alpha, f) = \frac{1}{\sqrt{2\pi}} e^{-\frac{\alpha^2}{2}} . \tag{6.43}$$

In the present case, i. e. $f \simeq 40$, an integrated deviation between $T(\alpha, f)$ and the Gaussian distribution, achieved via

$$\text{error}(f) := \int_{-\infty}^{\infty} d\alpha |P(\alpha) - T(\alpha, f)| , \tag{6.44}$$

is evaluated as $\text{error}(40) \simeq 0.016$. This, however, is quite accurate. (For comparison, the expected goodness for a small set of experimental data with $f \simeq 4$ would be $\langle \xi \rangle \simeq 2$ and the integrated deviation to a normal distribution is $\text{error}(4) \simeq 0.151$.) Thus we conclude that the treatment via Gaussians is indeed a reliable method for the purpose of a quantitative data analysis via stochastic methods.

6.6.2. Good Parameters and their Statistical Errors

A very elegant method for determining the input parameters, resulting in the best possible agreement between simulation and experiment, and in addition, for the calculation of their statistical errors, is the use of the distribution of α to construct a Monte Carlo (MC) importance sampling algorithm.

We define a vector in the input–parameter space[1]

$$\mathbf{\Pi} = (c_1, c_2, c_c, d_p, w_0, s_x, D, \dot{\gamma}, l_s) \tag{6.45}$$

and restrict the MC sampling to a rectangular box in this 9–dimensional space $\Omega_{\mathbf{\Pi}}$. The algorithm starts from a random point $\mathbf{\Pi}^{(0)}$ in $\Omega_{\mathbf{\Pi}}$ and generates subsequently new configurations from the previous points via

$$\Pi_\alpha^{(n+1)} \;=\; \Pi_\alpha^{(n)} \;+\; \Delta\Pi_\alpha r_\alpha \,, \tag{6.46}$$

where the index α pertains to the parameters and the superscript n counts the MC step. $\Delta\Pi_\alpha$ is the MC step width and r_α a uniform random number in the range $[-1, 1]$. Note that summation convention is *not* applied. If $\mathbf{\Pi}^{(n+1)} \in \Omega_{\mathbf{\Pi}}$, $\alpha_i^{(n+1)}$ is calculated for every data point. Conversely, if $\mathbf{\Pi}^{(n+1)} \notin \Omega_{\mathbf{\Pi}}$, this configuration is rejected and a new point is generated. The α_i are assumed to be statistically independent, and hence one can calculate

$$P(\sum_i \alpha_i^{(n+1)}) = \prod_i P(\alpha_i^{(n+1)}). \tag{6.47}$$

Then a standard Metropolis step is applied [68], such that $\Pi^{(n+1)}$ is accepted if a random number $\rho \in [0, 1)$ satisfies the condition

$$\rho < \frac{\prod_i P(\alpha_i^{(n+1)})}{\prod_j P(\alpha_j^{(n)})} \,. \tag{6.48}$$

In the nomenclature of statistical mechanics, $\mathbf{\Pi}$ is a point in the phase space and $\frac{\mathcal{H}}{k_B T} := \frac{1}{2}\sum_i \alpha_i^2$ is a Hamiltonian giving rise to a Boltzmann distribution.

For practical reasons, one should notice that α must be a function of the input parameters $\mathbf{\Pi}$, but not of the random numbers used for the BD algorithm,

$$\alpha_i \equiv \alpha_i(\mathbf{\Pi}) \,. \tag{6.49}$$

Thus, one should use the same sequence of random numbers for every MC step. Although we perform the BD simulation using several hundred thousands of trajectories, the results still depend somewhat on the set of random numbers which have been used in the BD. Therefore in order to allow a smooth MC sampling of parameters (analogously finding a smooth free energy minimum in parameter space) we kept the sequence of random numbers strictly fixed when performing an MC move from one set of parameters to another one. This

[1] Note that here $\mathbf{\Pi}$ is a point in the parameter space, if Gaussian observation volumes are used. However, the method is rather general, and therefore it is also valid in the case of PCPSF.

however implies that the final results will depend somewhat on the sequence of random numbers that have been used ("sample-to-sample fluctuations"). The effect of these fluctuations on our statistical error bars will be investigated though not systematically in Sec. 6.7.2.
Finally, averaging over all MC sweeps should end up in proper values for the desired parameters and the second moments yield estimators for the statistical errors of these quantities.

6.6.3. Scale Invariance and Averaging

From the convection-diffusion equation one can observe that the parameters are subject to a scale invariance in space. Starting with the convection-diffusion equation

$$\frac{\partial}{\partial t}P(\boldsymbol{r},t|\boldsymbol{r}',0) = D\nabla_r^2 P(\boldsymbol{r},t|\boldsymbol{r}',0) - \nabla_r \cdot \boldsymbol{v}P(\boldsymbol{r},t|\boldsymbol{r}',0)\,, \tag{6.50}$$

with

$$\boldsymbol{v}(\boldsymbol{r}) = \dot{\gamma}\overleftrightarrow{\varepsilon}\cdot(\boldsymbol{r} + l_s\hat{\boldsymbol{e}}_z)\,, \tag{6.51}$$

one may rescale the spatial coordinates such that we get

$$\boldsymbol{r} \equiv a\boldsymbol{s}\,, \tag{6.52}$$

and

$$\frac{\partial}{\partial \boldsymbol{r}} = \frac{\partial}{\partial(a\boldsymbol{s})} = \frac{1}{a}\frac{\partial}{\partial \boldsymbol{s}}\,. \tag{6.53}$$

The propagator can then be modified such that

$$P(\boldsymbol{r},t|\boldsymbol{r}',0)d^3\boldsymbol{r} = \Psi(\boldsymbol{s},t|\boldsymbol{s}',0)d^3\boldsymbol{s}\,, \tag{6.54}$$

and thus we get

$$\Psi = a^3 P\,. \tag{6.55}$$

Inserting this into the convection-diffusion equation, one obtains

$$\frac{\partial}{\partial t}\Psi = \frac{D}{a^2}\nabla_s^2\Psi - \nabla_s \cdot \dot{\gamma}\overleftrightarrow{\varepsilon}\cdot(\boldsymbol{s} + \frac{l_s}{a}\hat{\boldsymbol{e}}_z)\Psi\,. \tag{6.56}$$

Furthermore the observation volumes also depend on spatial parameters

$$W_i \equiv W_i(\boldsymbol{r},\{\sigma_i\})\,, \tag{6.57}$$

with $\{\sigma_i\}$ the lengths characterizing the geometry. Note that we may interprete W_i as production or detection probability density, and thus we can define a rescaled MDE

$$\Omega_i = a^3 W_i\,, \tag{6.58}$$

such that

$$W_i d^3\boldsymbol{r} = \Omega_i d^3\boldsymbol{s}\,. \tag{6.59}$$

The correlation functions can then be rewritten as

$$\begin{aligned} G_{ij}(t) &= \frac{1}{\langle C\rangle}\int d^3\boldsymbol{r}\int d^3\boldsymbol{r}' W_j(\boldsymbol{r})P(\boldsymbol{r},t|\boldsymbol{r}',0)W_i(\boldsymbol{r}') \\ &= \frac{1}{a^3}\frac{1}{\langle C\rangle}\int d^3\boldsymbol{s}\int d^3\boldsymbol{s}'\Omega_j(\boldsymbol{s})\Psi(\boldsymbol{s},t|\boldsymbol{s}',0)\Omega_i(\boldsymbol{s}')\,, \end{aligned} \tag{6.60}$$

where we took into account that the normalization constant is the effective averaged concentration $\langle C\rangle$ of the tracer molecules and that the MDEs are normalized to 1. This leads to

$$G_{ij}(t,\langle C\rangle, D, \dot\gamma, l_s, \{\sigma_i\}) = G_{ij}\left(t, a^3\langle C\rangle, \frac{D}{a^2}, \dot\gamma, \frac{l_s}{a}, \left\{\frac{\sigma_i}{a}\right\}\right)\,. \tag{6.61}$$

Now it should be noted that there is no spatial parameter with vanishing or very small experimental error bar. Thus the results of our data analysis can never be more accurate than the most accurate of our input lengths. The MC runs in the following section seem to be not long enough to observe this scale invariance explicitly in the data. However, to take the effect into account we do not only average over the single MC steps, but rather over all "iso-lines" pertaining to every data point. Assuming that the most accurate parameters are the penetration depth $d_p = 100 \pm 10nm$, the diffusion constant $D = 36 \pm 5\mu m^2/s$ and the separation distance $s_x = 800 \pm 80nm$, we calculate for every data point a minimum and a maximum scaling factor a, such that we get $d_p^{(min)} < a^{-1}d_p < d_p^{(max)}$, $s_x^{(min)} < a^{-1}s_x < s_x^{(max)}$ and $D^{(min)} < a^{-2}D < D^{(max)}$, $\forall a \in (a_{min}, a_{max})$. Then we generate an iso-line for every data point of the MC simulation and average over all these iso-lines, excluding the data of the first 5×10^4 MC sweeps.

6.7. Results and Discussion

6.7.1. Results for Gaussian Shaped Observation Volumes

In this section we discuss results from an implementation of the BD algorithm and the MC based data analysis. We first use the common model in the FCS community, where the lateral extension of the observation volumes is described by a Gaussian shape, i. e. we use observation volumes of the form Eq. (6.25). For the experiments, carboxylate-modified quantum dots (Qdot585 ITK Carboxyl, Molecular Probes, Inc.) with a hydrodynamic radius $R_H \simeq 7nm$ were used as tracer particles, suspended in aqueous solution of

potassium phosphate (K_2HPO_4) buffer ($pH \simeq 8$). The experiments have been performed in a rectangular microchannel of $L_y \simeq 4mm$ width, $L_z \simeq 100\mu m$ height and $L_x \simeq 50mm$ length, where the solution of Qdot585 flows and induces Poiseuille flow. The penetration depth of the evanescent wave was fixed to $d_p \simeq 100nm$. The lateral size of the observation volumes was about $w_0 \simeq 260nm$ and their center-to-center separation was set to $s_x \simeq 800nm$. From dynamic light scattering experiments the diffusion constant of the tracer particles is known to be roughly $D \simeq 36\mu m^2/s$. Correlation curves were

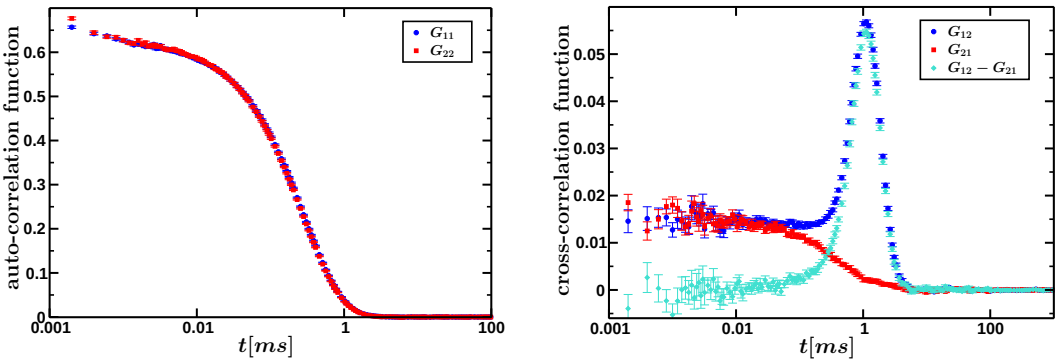

Figure 6.5.: Experimental auto- and cross-correlation functions measured for a hydrophilic surface.

measured for a hydrophilic wall surface. Fig. 6.5 shows experimentally measured auto- and cross-correlation data. For the cross-correlation we plotted the forward- (G_{12}), the backward- (G_{21}), and the difference-cross-correlation function ($G_{12} - G_{21}$). Indeed, the cross-correlation curve has some auto-correlation like fraction, which we could not explain by the small overlap of W_1 and W_2 as mentioned previously.
Within this section every simulated data point is an average over 123×2^{11} independent trajectories[2]. Figs. 6.6 and 6.7 present the experimental TIR-FCCS data compared to simulated auto- and cross-correlation curves, and in Fig. 6.8 the distribution of α_i^2 is shown. This distribution is compared with the distribution functions for α^2 according to Student's t function

$$T'(\alpha^2, f) = \frac{\Gamma\left(\frac{f+1}{2}\right)}{\sqrt{f\pi}\,\Gamma\left(\frac{f}{2}\right)} \frac{1}{\sqrt{\alpha^2}} \left[1 + \frac{\alpha^2}{f}\right]^{-\frac{f+1}{2}}, \tag{6.62}$$

and the normal distribution

$$P'(\alpha^2) = \frac{1}{\sqrt{2\pi\alpha^2}}\, e^{-\frac{\alpha^2}{2}}. \tag{6.63}$$

[2]We used 2048 parallel processes, each computing 123 BD trajectories, for the MC analysis.

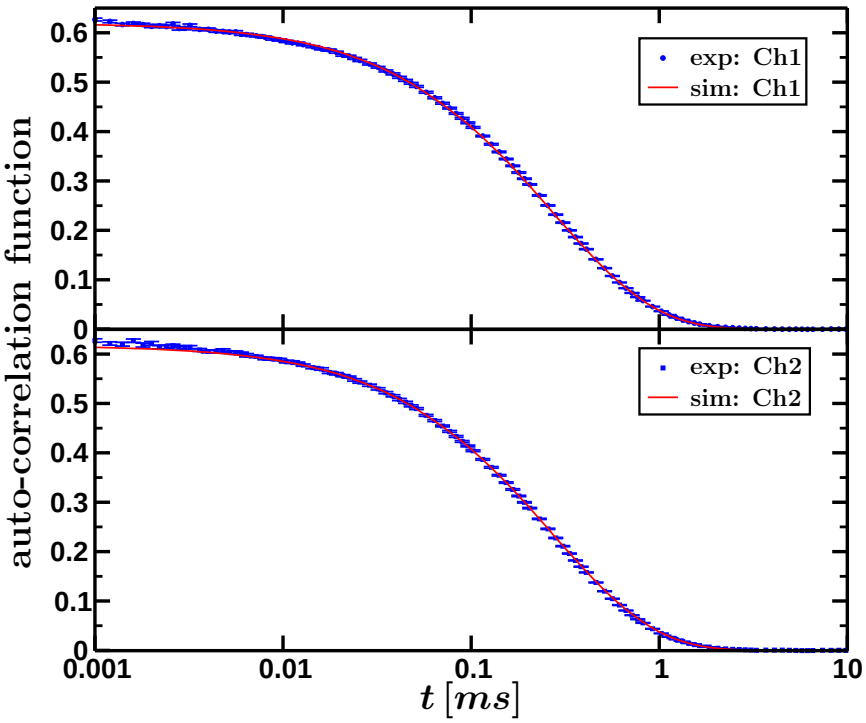

Figure 6.6.: Auto-correlation functions for $c_1' = 0.619$, $c_2' = 0.616$, $c_c' = 0.0554$, $w_0 = 245.71nm$, $d_p = 98.05nm$, $D = 36.38\,\mu m^2/s$, $s_x = 753.34nm$, $\dot{\gamma} = 3800\,s^{-1}$ and $l_s = 6.26nm$. The goodness of simulation was calculated to be $\xi \simeq 2.5$.

In a first run, all input parameters were kept fixed, except the shear rate and the slip length, and the landscape of ξ was computed (see Fig. 6.9). We see that varying the slip length and the shear rate is not independent in terms of auto– and cross–correlation curves. Increasing l_s has the same effect on the shape of these curves as decreasing $\dot{\gamma}$, and one would never get results for these two parameters independently by TIR–FCCS measurements within the given model. However, using double-focus FCCS or single-focus FCS measurements in bulk, one can obtain an independent value for the shear rate [102, 113] measuring the flow profile throughout the microchannel and afterwards deriving it via Poiseuille fit. Here, single focus confocal FCS was used. Fig. 6.10 presents such a flow velocity profile, measured under the same conditions as the TIR–FCCS measurements. Since the ratio between width and height of the channel is large and the slip length is supposed to be small compared to the channel dimensions, it is valid to use a simple one dimensional Poiseuille profile to fit the experimental data. More details on

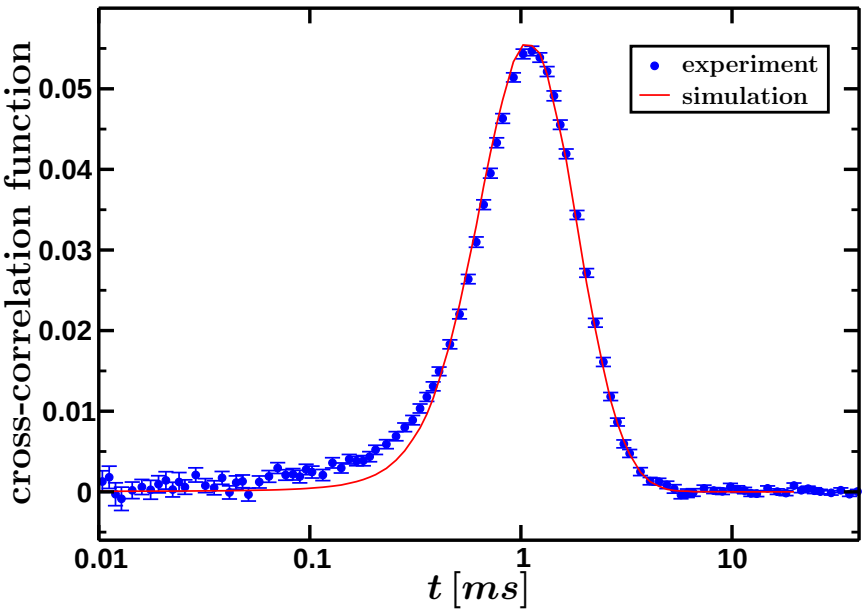

Figure 6.7.: Difference-Cross-correlation function for the same set of parameters as in Fig. 6.6.

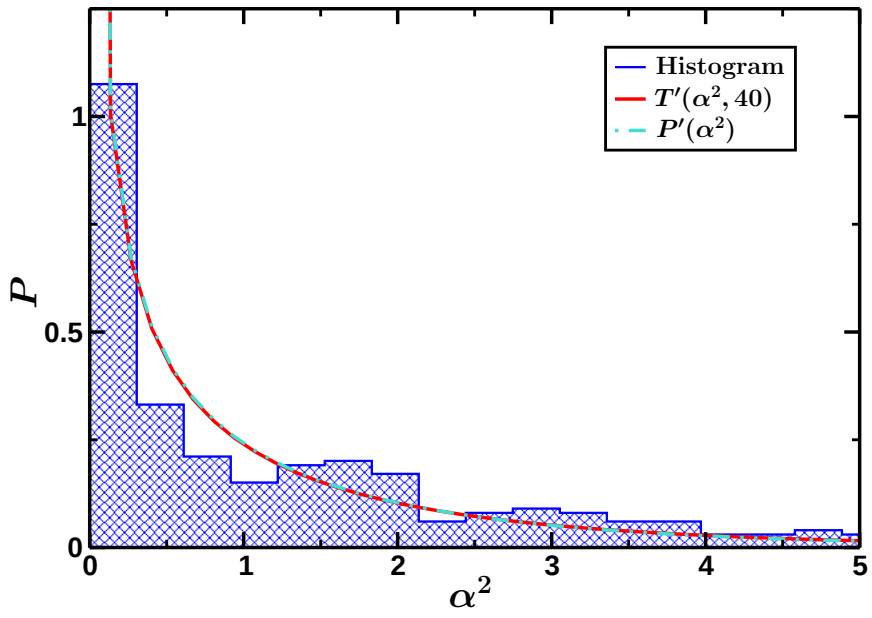

Figure 6.8.: Distribution of α_i^2 for the same set of input parameters as in Fig. 6.6.

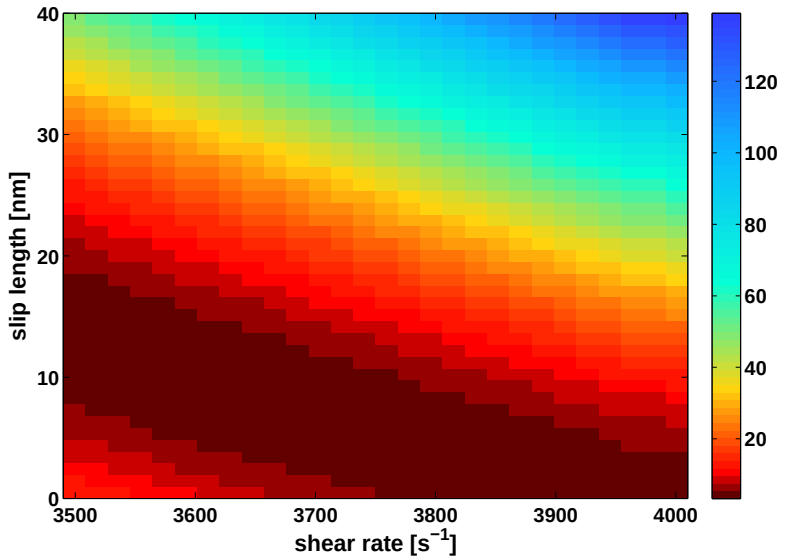

Figure 6.9.: ξ as function of slip length and shear rate. The other parameters are the same as in Fig. 6.6.

this issue and some theoretical background are presented in appendix B.1. From the Poiseuille fit, one can obtain the shear rate at the hydrophilic wall, which is determined to be $\dot{\gamma} = 3854 \pm 32\, s^{-1}$. Note that the quoted error is obtained from the fitting routine (gnuplot), but is not the real physical error from the experimental inaccuracy.

Several Monte Carlo runs have been performed for various, but fixed, values of the shear rate in the range of $3500 s^{-1}$ to $4000 s^{-1}$. The MC runs were computed on 512 nodes (2048 processes) on the *IBM Blue Gene–P* in the *Rechenzentrum Garching*. We adjusted $\Delta\Pi$ in order to obtain a reasonable acceptance rate of roughly 77%. Each sampling has been run for more than $5 \cdot 10^5$ MC sweeps. The mean values of the parameters and their standard deviations were calculated, excluding the first $5 \cdot 10^4$ configurations, and averaging over iso-lines as described previously. The results are presented in Tab. 6.1[3].

The convergence behavior of the method is shown in Fig. 6.12, where we plot ξ as function of the number of Monte Carlo iterations. Fig. 6.11 presents data

[3]Note that here the simulation results have been rescaled such that the maximum values of the correlation curves are set to 1. The parameters c_i' then are adjusted to match the heights of the experimental data curves.

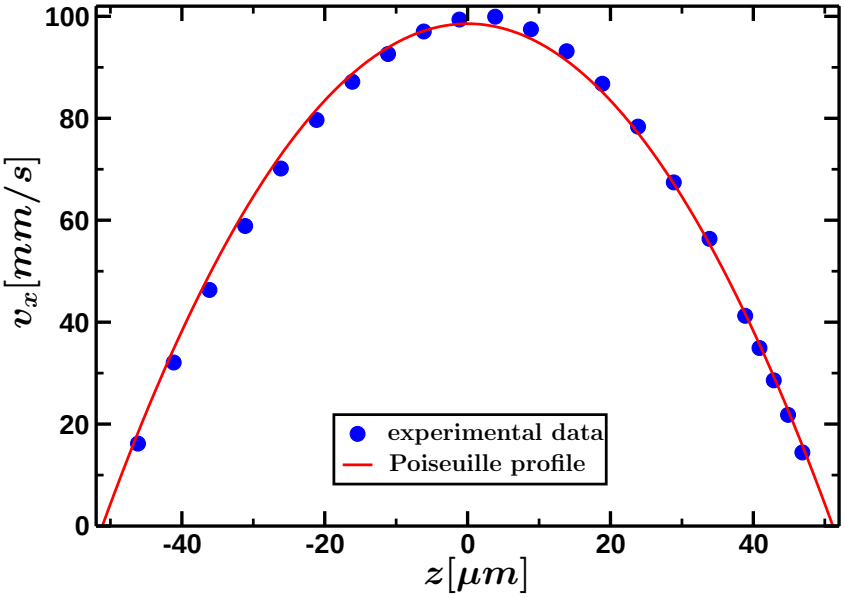

Figure 6.10.: Flow profile and Poiseuille fit along z-direction (surface of measurement is located at $z \simeq 50\mu m$).

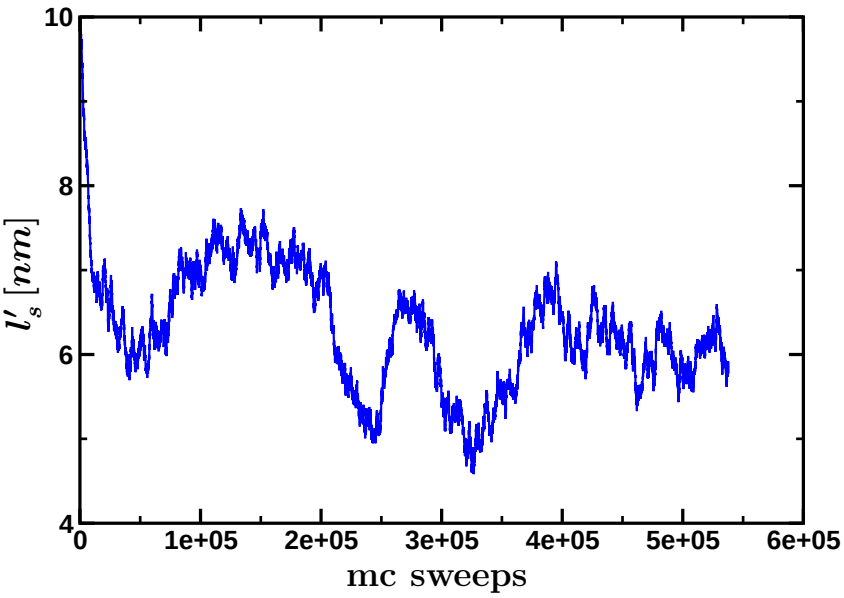

Figure 6.11.: Slip length as function of the number of MC steps for $\dot{\gamma} = 3800\,s^{-1}$.

on the evolution of l_s during the Monte Carlo process for $\dot{\gamma} = 3800s^{-1}$. Calculating the means and the statistical errors, we are able to obtain a relation between the shear rate and the slip length (see Fig. 6.13). From the independent measurement of the experimental shear rate, we can conclude within the given model that the slip length at the hydrophilic surface should not exceed the value of $l_s \lesssim 10nm$. It is interesting that the given model, i. e. the linear profile and the exponential decay along the optical axis, allows us to map the measured slip length of the point particle to a slip length where steric interactions with the wall are taken into account. The reflection at the wall at $z = 0$ must be replaced by a reflection at $z = R$, with R the radius of the tracer particles. This implies a coordinate transformation

$$z' = z - R\,, \tag{6.64}$$

or

$$z = z' + R\,, \tag{6.65}$$

where z denotes the real distance from the wall, while z' is the coordinate used in the algorithm. For the exponential decay of the MDEs we therefore get

$$\exp\left(-\frac{z}{d_p}\right) = \exp\left(-\frac{R}{d_p}\right)\exp\left(-\frac{z'}{d_p}\right)\,, \tag{6.66}$$

in other words, the MDEs have the same form except for an unimportant prefactor. Furthermore, one has to transform the flow velocity as

$$\begin{aligned} v_x(z) &= \dot{\gamma}(z + l_s) \\ &= \dot{\gamma}(z' + (l_s + R)) \\ &\equiv \dot{\gamma}(z' + l_s')\,. \end{aligned} \tag{6.67}$$

From this we see that exactly the same method can be used for tracer particles with finite size, only the interpretations of the spatial position and of the slip length change. Since l_s' is the number produced by the algorithm, the real slip length is $l_s = l_s' - R$, where steric interactions have been taken into account. Note that the figures in the text always show data for l_s', i. e. where steric interactions have not been taken into account. Assuming that the particle radius is $R \simeq 7nm$, this observation allows us to conclude that the real slip length at a hydrophilic surface is indeed very close or identical to zero.

$\dot{\gamma}[s^{-1}]$	3500		3600		3700	
	av	σ	av	σ	av	σ
c_1'	0.6187	0.0005	0.6188	0.0005	0.6188	0.0005
c_2'	0.6160	0.0006	0.6161	0.0006	0.6161	0.0006
c_c'	0.0554	0.0002	0.0554	0.0002	0.0554	0.0002
$d_p[nm]$	100.78	2.96	100.11	3.08	99.72	3.16
$w_0[nm]$	247.57	6.74	247.67	7.06	247.49	7.33
$s_x[nm]$	754.64	20.25	756.37	21.23	757.93	22.15
$D[\mu m^2/s]$	37.47	2.01	37.32	2.09	37.18	2.17
$l_s'[nm]$	14.33	0.72	11.50	0.71	8.71	0.66
ξ	2.637	0.012	2.677	0.012	2.717	0.011
acceptance rate	77.2%		77.4%		77.6%	
# data points	491000		490500		910100	
$\dot{\gamma}[s^{-1}]$	3800		3900		4000	
	av	σ	av	σ	av	σ
c_1'	0.6189	0.0006	0.6189	0.0006	0.6190	0.0007
c_2'	0.6162	0.0006	0.6163	0.0006	0.6163	0.0007
c_c'	0.0554	0.0002	0.0554	0.0002	0.0554	0.0002
$d_p[nm]$	98.89	3.31	98.87	3.51	98.05	3.69
$w_0[nm]$	247.77	7.69	247.56	8.02	247.60	8.38
$s_x[nm]$	759.74	23.19	761.42	24.16	763.35	25.14
$D[\mu m^2/s]$	37.03	2.26	36.88	2.34	36.74	2.42
$l_s'[nm]$	6.31	0.66	3.84	0.77	1.64	0.79
ξ	2.757	0.011	2.797	0.011	2.837	0.012
acceptance rate	77.9%		78.0%		78.1%	
# data points	487900		494400		495000	

Table 6.1.: Averaged values (av) and standard deviations (σ) calculated from the MC simulations for Gaussian shaped observation volumes.

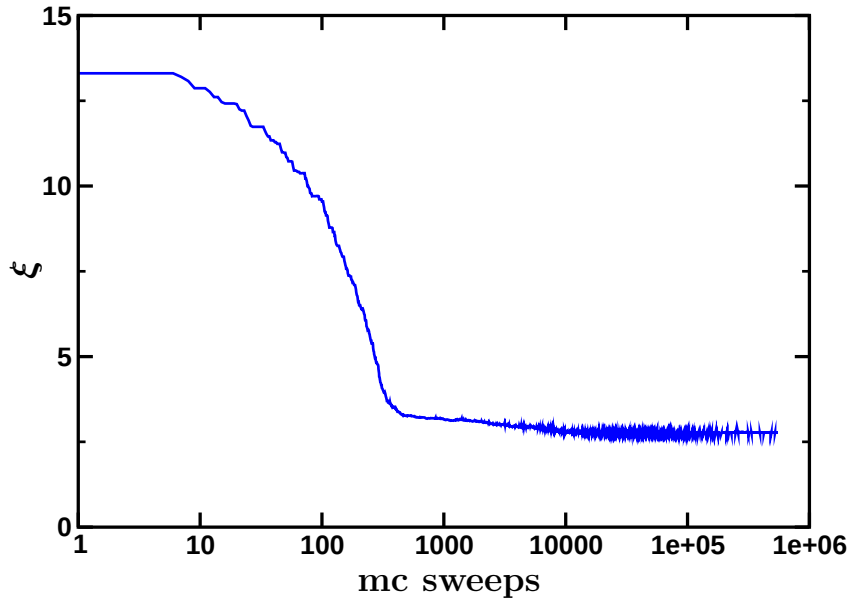

Figure 6.12.: Goodness of simulation ξ as function of the number of MC steps for $\dot{\gamma} = 3800\,s^{-1}$.

6.7.2. The Influence of Diffraction Patterns

Although the ξ landscape is rather sharp, resulting in small fluctuations in ξ during the MC procedure, the best fits only reached values beyond $\xi \gtrsim 2.5$, i. e. larger than the expected value for a perfect matching of experiment and simulation. This indicates that some systematic errors occur. Indeed we find that although the auto–correlation curves match very well (see Fig. 6.6), and the cross–correlation curves matches over a wide range, there is still a small gap between experimentally measured and simulated cross–correlation curves (see the left shoulder in Fig. 6.7).

Since the overlap of the observation volumes is very small for a reasonable width and separation distance, this is not an effect of neglecting the backward-cross correlation in the simulation results, $\langle W_2|W_1\rangle$. However, in the limit of strongly overlapping observation volumes the corrected experimental curve differs significantly from the simulation: While the simulated data runs into the limit of auto–correlation, the experimental curve disappears. For testing, we included this effect in the numerical method by subtraction of the average over $W_2((-x, y, |z|))$. We observed that in the relevant range of parameters the effect of this correction is negligible. Furthermore, one could expect that a possible lateral shift of the observation volumes, i. e. orthogonal to the

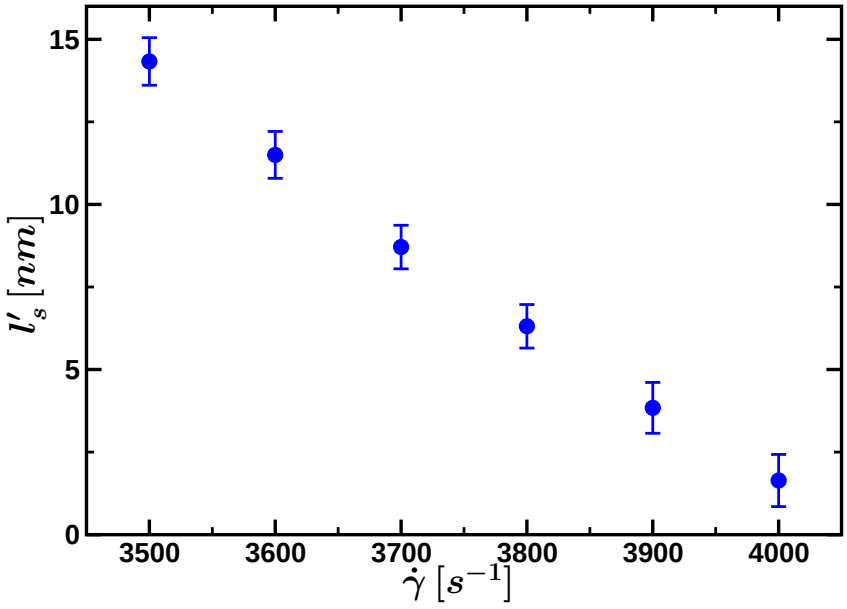

Figure 6.13.: Averaged slip length as function of the shear rate, calculated from the MC results.

flow direction, could affect the shape of the cross–correlation curve. The experimentalists estimated this error to be smaller than $s_y \lesssim 20nm$. In a simple numerical test we fixed all parameters except s_y and calculated the cross–correlation curve. It turned out that s_y must be about one order of magnitude larger than the estimated error range to observe significant changes in the cross–correlation curve, and hence this effect indeed seems to be negligible.

In our physical model we used the common approximations of the general FCS community, i. e. the lateral shape of observation volumes is approximated by Gaussians. However, we know that the Gaussian shape is only a rough approximation for the true intensity profile. For this subsection we replaced the Gaussian shaped MDEs, Eqs. (6.2), by PCPSFs as given by Eqs. (6.1).

Finding an analytical solution for the convolution of the point-spread function with the image of the pinhole is complicated, and hence we decided to solve this integral numerically. We first rewrite the integral as

$$\begin{aligned} W_{xy}(\boldsymbol{r}_{xy}) &\propto \int_{|\boldsymbol{r}_{0,xy}|<R} d^2\boldsymbol{r}_{0,xy} \left[\frac{2J_1(kNA|\boldsymbol{r}_{xy}-\boldsymbol{r}_{0,xy}|)}{kNA|\boldsymbol{r}_{xy}-\boldsymbol{r}_{0,xy}|}\right]^2 \\ &\propto \int_{|\boldsymbol{\rho}_0|<R'} d^2\boldsymbol{\rho}_0 \left[\frac{2J_1(|\boldsymbol{\rho}-\boldsymbol{\rho}_0|)}{|\boldsymbol{\rho}-\boldsymbol{\rho}_0|}\right]^2 \equiv W_{xy}(\boldsymbol{\rho})\,, \end{aligned} \tag{6.68}$$

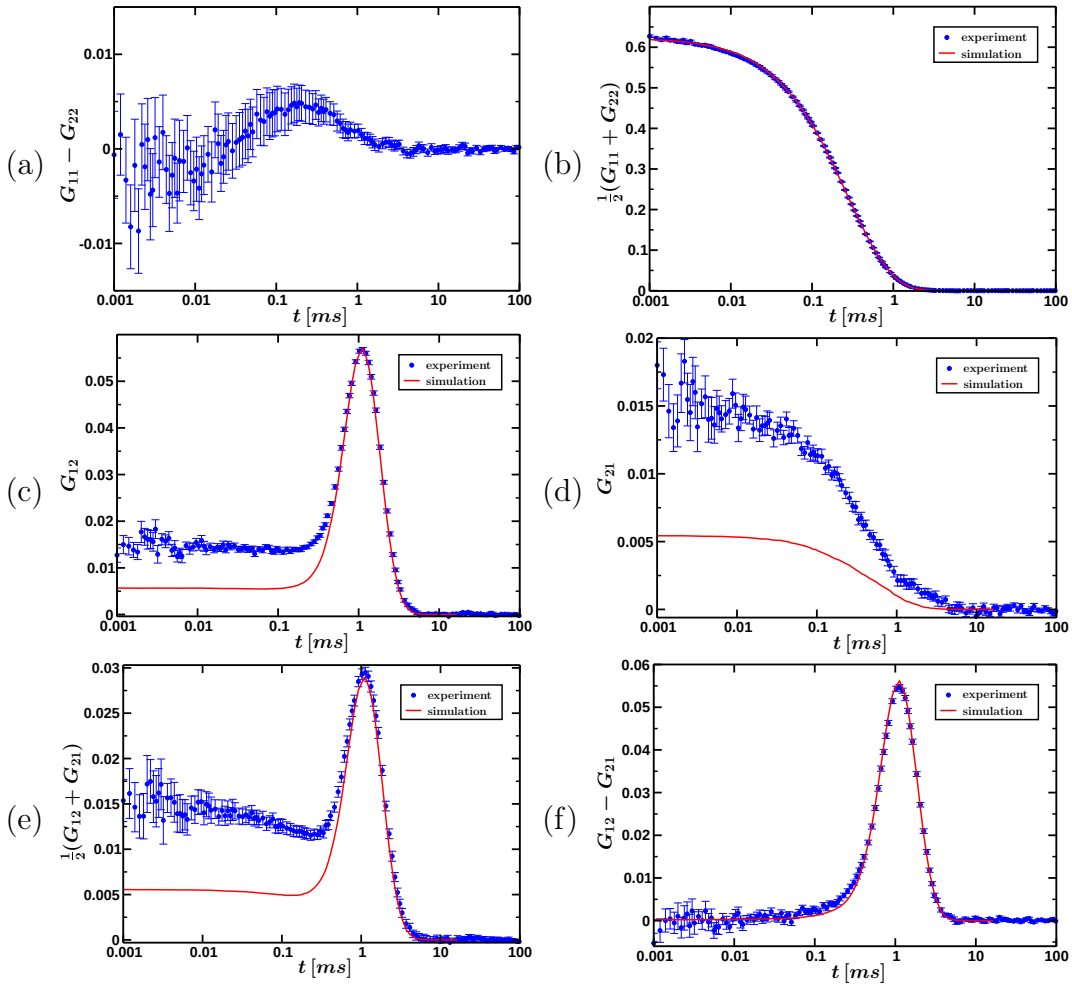

Figure 6.14.: Correlation functions G_{ij} as defined in the text, and linear combinations thereof, comparing the experimental data (with error bars) with the numerical fit functions (without) for an optimized parameter set. The statistical error of the numerical data is smaller than the line width. The images have been obtained by modeling the observation volumes by Eq. 6.1. The goodness of simulation was found to be $\xi = 1.36$.

with

$$\boldsymbol{\rho} := kNA\,\boldsymbol{r}_{xy}\,, \tag{6.69a}$$
$$\boldsymbol{\rho}_0 := kNA\,\boldsymbol{r}_{0,xy}\,, \tag{6.69b}$$
$$R' := kNA\,R\,, \tag{6.69c}$$

and

$$W(\boldsymbol{r}) \equiv W_{xy}(\boldsymbol{r}_{xy})\,W_z(z) \propto W_{xy}(\boldsymbol{r}_{xy})\,\exp\left(-\frac{z}{d_p}\right). \tag{6.70}$$

$\boldsymbol{\rho}$ and $\boldsymbol{\rho}_0$ are two-dimensional vectors. Since the function $W(\boldsymbol{\rho})$ depends only on the absolute value $|\boldsymbol{\rho}|$, one may restrict the calculation to one specific direction, i. e. the integration is only performed along the x-axis,

$$\boldsymbol{\rho} = (x,0)^T\,, \tag{6.71a}$$
$$\boldsymbol{\rho}_0 = (x_0,y_0)^T\,. \tag{6.71b}$$

For every point $x \in (-R',R')$ we then perform a Monte-Carlo integration as follows: To get a vector with $|\boldsymbol{\rho}_0| < R'$ we generate a pair of uniformly distributed random numbers in the range $u,v \in (-1/2,1/2)$. All pairs for which $u^2+v^2 > 1/4$ are discarded and the remaining ones are transformed via

$$x_0 = 2R'\,u\,, \tag{6.72a}$$
$$y_0 = 2R'\,v\,. \tag{6.72b}$$

Finally, averaging the function

$$\mathcal{A}(\boldsymbol{\rho},\boldsymbol{\rho}_0) = \left[\frac{2J_1(|\boldsymbol{\rho}-\boldsymbol{\rho}_0|)}{|\boldsymbol{\rho}-\boldsymbol{\rho}_0|}\right]^2 \tag{6.73}$$

using a large number of $\boldsymbol{\rho}_0$ results in the desired PCPSF. In contrast to the convolution Eq. (6.68), the normalization constant can be calculated analytically, since the order of integration over $\boldsymbol{\rho}_0$ and $\boldsymbol{\rho}$ can be exchanged. Using a table of integrals [114] the normalization constant is calculated to be $(4\pi)^{-1}$. Initial positions of Brownian particles (in the x-y-plane) are chosen by uniformly distributed angles ϑ and by generating uniformly distributed random numbers $\zeta \in (0,1)$ and comparison with the integral

$$\zeta = 2\pi \int_0^\rho d\rho'\rho' W_{xy}(\rho')\,, \tag{6.74}$$

such that $\boldsymbol{\rho} \equiv \rho(\sin(\vartheta),\cos(\vartheta))^T$ is distributed via PCPSF. It should be noted, that the convolution solely depends on kNA in combination with the radius of the pinhole $R' = kNA\,R$. We use the "width" of the PCPSF as fitting parameter $\lambda := (kNA)^{-1}$ such that we can write

$$\boldsymbol{r}_{xy} = \lambda\boldsymbol{\rho}\,, \tag{6.75}$$

and thus we should calculate the convolution in every MC step. However, since the numerical evaluation is computationally expensive, we only vary the parameter λ, while keeping R' constant. This assumption has the advantage that we only have to calculate the integral once. In practice, this has been done using a self-contained program written by B. Dünweg. The resulting tabulated observation volume was written to the hard disk and read in when starting the BD/MC simulation.

Indeed, using the PCPSF a substantial improvement of the match of simulation with the experimental data is observable. Above, we have seen that the experimental auto-correlation curves are nearly identical. Thus we replace the two auto-correlation curves by their average $G_{auto} := \frac{1}{2}(G_{11} + G_{22})$ and calculate the goodness of simulation in the following with respect to G_{auto} and the difference-cross-correlation curve $G_{12} - G_{21}$. We again performed several Monte Carlo runs in the space of $(\langle C\rangle_a, \langle C\rangle_c, d_p, \lambda, s_x, D, l_s)$. $\langle C\rangle_a$ and $\langle C\rangle_c$ denote the effective averaged concentrations of the tracer particles for the averaged auto- and the difference-cross-correlation curves. The width of the Gaussian observation volumes w_0 is replaced by the parameter λ, accounting for the extension of the PCPSFs. The shear rate $\dot{\gamma}$ was fixed again and we performed MC runs for $\dot{\gamma} = 3500s^{-1}, \ldots, 4000s^{-1}$. The Monte Carlo algorithm was run for more than $6.5 \cdot 10^5$ steps, and again the first $5 \cdot 10^4$ configurations were discarded for the calculation of average values and standard deviations via "iso-line averaging". The acceptance rate in each run was roughly 82%.
Figs. 6.14 show correlation functions G_{ij}, comparing experimental data with the simulation results for an optimized parameter set, i. e. a snapshot of an MC run. The goodness of simulation is $\xi = 1.36$, and thus we observe a much better match of simulation and experiment as in the case of Gaussian observation volumes. The non-vanishing back-correlation in Fig. 6.14d indicates now a substantial overlap of the two observation volumes. Although the uncorrected curves still do not match the experiment, the difference-curve fits almost perfectly. From comparison of Fig. 6.7 with Fig. 6.14f we see that the gap between experimental and numerical data decreases substantially. As mentioned before, we performed a few MC runs for the same shear rate, but different sequences of random numbers for the BD. The results quoted in Tab. 6.2 show that some "sample-to-sample fluctuations" occur, and thus the real statistical errors of the slip lengths are indeed somewhat larger than calculated from the single MC run. In Tab. 6.3 the results of the Monte Carlo runs are quoted, and Fig. 6.15 illustrates the averaged slip length as function of the shear rate. We see that the values of the slip length slightly increase compared to the results for the Gaussian shaped observation volumes. Nevertheless, taking steric interactions into account the results show that the slip length at the hydrophilic surface should not exceed a few nanometers.
The results demonstrate impressively that the method of TIR–FCCS in com-

seed	42		4711		2409	
	av	σ	av	σ	av	σ
$\langle C\rangle_A[\mu m^{-3}]$	17.83	1.92	17.81	1.96	17.94	1.94
$\langle C\rangle_C[\mu m^{-3}]$	16.53	1.80	16.45	1.82	16.83	1.83
$d_p[nm]$	95.81	3.50	96.02	3.58	95.78	3.52
$\lambda[nm]$	68.70	2.60	68.58	2.61	69.81	2.69
$s_x[nm]$	781.94	27.70	779.54	28.28	793.22	28.24
$D[\mu m^2/s]$	36.59	2.56	36.47	2.62	36.63	2.57
$l'_s[nm]$	12.80	1.10	11.62	0.90	15.14	1.21
ξ	1.441	0.018	1.277	0.016	1.718	0.017
acceptance rate	82.0%		82.0%		82.2%	
# data points	609410		609590		610510	

Table 6.2.: Averaged values (av) and standard deviations (σ) calculated from MC simulations with fixed $\dot{\gamma} = 3800s^{-1}$, but different seeds for the random number generator.

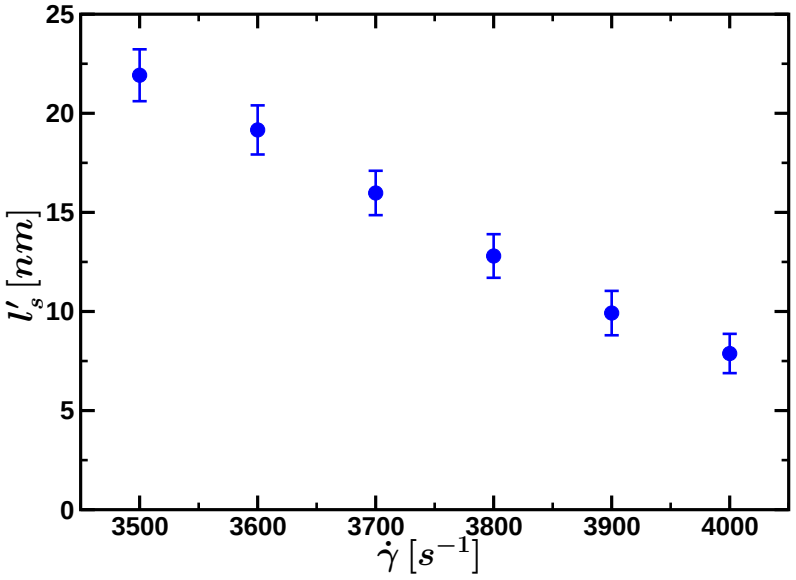

Figure 6.15.: Averaged slip length as function of the shear rate as observed from MC simulations. Here the lateral shape of the observation volumes was set as PCPSFs.

$\dot{\gamma}[s^{-1}]$	3500		3600		3700	
	av	σ	av	σ	av	σ
$\langle C\rangle_A[\mu m^{-3}]$	17.82	1.90	17.91	1.88	17.93	1.89
$\langle C\rangle_C[\mu m^{-3}]$	19.94	1.82	17.00	1.80	16.82	1.78
$d_p[nm]$	95.83	3.46	95.66	3.42	95.64	3.44
$\lambda[nm]$	68.84	2.53	69.10	2.55	69.01	2.56
$s_x[nm]$	774.39	26.59	777.98	26.63	780.53	26.97
$D[\mu m^2/s]$	36.71	2.49	36.76	2.48	36.72	2.51
$l'_s[nm]$	21.92	1.31	19.16	1.24	15.98	1.12
ξ	1.377	0.016	1.40	0.016	1.420	0.017
acceptance rate	82.1%		82.1%		82.1%	
# data points	608090		611290		610160	

$\dot{\gamma}[s^{-1}]$	3800		3900		4000	
	av	σ	av	σ	av	σ
$\langle C\rangle_A[\mu m^{-3}]$	17.83	1.92	17.67	2.00	17.96	1.89
$\langle C\rangle_C[\mu m^{-3}]$	16.53	1.80	16.21	1.86	16.41	1.74
$d_p[nm]$	95.81	3.50	96.14	3.70	95.58	3.41
$\lambda[nm]$	68.70	2.60	68.42	2.71	69.01	2.56
$s_x[nm]$	781.94	27.70	783.75	28.76	789.77	27.35
$D[\mu m^2/s]$	36.59	2.56	36.46	2.64	36.71	2.51
$l'_s[nm]$	12.80	1.10	9.92	1.12	7.88	0.99
ξ	1.441	0.018	1.464	0.019	1.477	0.016
acceptance rate	82.0%		81.9%		82.0%	
# data points	609410		610330		610440	

Table 6.3.: Averaged values (av) and standard deviations (σ) calculated from MC simulations with seed = 42, and various shear rates.

bination with the presented BD and MC based data analysis is a powerful tool for the prediction of hydrodynamic effects near solid–liquid interfaces. Already within the presented model, we can conclude an upper bound for the slip length at a hydrophilic surface of $l_s \lesssim 10nm$. Even if one would succeed in finding an analytic solution of the CDE, Eq. (6.6), in the case of shear flow close a solid wall, the computational method has the advantage to be easily extensible to include more complex effects. For example, the hydrodynamic interactions of the particles with the wall would cause an anisotropy and a z dependence in the diffusion tensor [115], electrostatic interactions would give rise for an additional force term in the Fokker-Planck equation, and furthermore, polydispersity could be investigated by randomizing the diffusion constant and the particle size with a given distribution [116]. While these contributions are expected to yield a further substantial improvement of the method, this was not attempted here, and is rather mentioned as a suggestion for a following research project. However, a big bottleneck seems to be the poor physical understanding of the existing "cross-talk" or overlap effects at short times.
We believe that, in the future, the new combination of surface sensitive experimental methods and stochastic simulations provides a new powerful technique for quantitative data analysis and could contribute to the discussion about possible differences in the effect of slippage over hydrophilic and hydrophobic surfaces.

Concluding Remarks

The topic of this thesis has been method development for the purpose of the computational treatment of colloidal systems. We investigated two new numerical approaches for rather different problems.

In the major part containing chapter 1 to 5, we focused on the theoretical treatment of a charge–stabilized colloidal dispersion in an external electric field. Charged colloidal spheres in a solution of negatively and positively charged ions are surrounded by a cloud of ions of opposite polarity, while the ions of the same polarity are depleted in the direct vicinity of the colloidal sphere. In a finite geometry counterions assure the charge neutrality condition. If a constant external electric field is applied, the ion clouds are distorted and the macro-ions move with constant velocity due to the balance of electric forces and friction. This effect is known as *electrophoresis* and the pertaining transport coefficient in the linear response regime, i. e. for weak fields, is the famous *electrophoretic mobility*. On a Mean–Field level, the system is described in terms of concentrations, electrostatic potential, velocity and pressure fields, and the equations of motion are given by the Stokes equation, the Poisson equation and the Nernst–Planck equation, resulting in a set of non-linear coupled partial differential equations. The aim of this work was the development of a lattice algorithm in order to solve these Mean–Field equations in a rectangular domain in the stationary limit. The colloidal sphere is treated as fixed boundary condition. Linearizing the equations with respect to the external field, the nonlinearity is shifted to the zeroth order, i. e. the equilibrium equations where the electric driving field is absent, while the first order equations are linear. In chapter 1 an overview of the system of equations, its structure and linearization is given and its dimensionless formulation is discussed. Furthermore, the main strategy for an iterative and modular solver is investigated. The idea is to divide the equations into a set of subproblems and solve them via specialized algorithms. Finally, those solvers are connected in a global loop to an iterative procedure. In the subsequent chapters 2 to 4, specialized algorithms are presented for the treatment of the independent subproblems.

The zeroth order is given by the fully non-linear Poisson–Boltzmann equation. A new iterative approach is presented in chapter 2, based on a constrained variational formulation of the Poisson–Boltzmann equation. The distinction

to earlier functional methods is the formulation in terms of the electric field instead of the electrostatic potential. This results in a free energy landscape, where the solution of the Poisson–Boltzmann equation is a true minimum, while in the potential formulation the solution is a saddle point. Starting with an initial setup, which satisfies all constraints of the system, optimal local updates in the ion concentrations and the electric fields decrease the functional value in every iterative step and the algorithm runs ultimately into the one and only minimum. As a consequence, one may conclude that this procedure ends up with an unconditionally stable algorithm. In addition to the solution of the Poisson–Boltzmann equation for a single charged colloidal sphere in a cubic box two possible applications of this methods have been discussed, namely the numerical treatment of *electro–osmotic* flow through a slit channel and the opportunity of calculating radial distribution functions of colloidal systems with fully non-linear Poisson–Boltzmann interaction. For the first application we studied the effect of different screening effects on the electro–osmotic flow profile, which, for the best of our knowledge, was not addressed before. The latter application was only tested fairly inaccurately for a rather small system. However, the results seemed to match reasonably well some results from Molecular–Dynamic simulations for screened potentials using effective charges gained from the isotropic Poisson–Boltzmann cell model. These results are very interesting, since they confirm the concept of *effective charges*, and further research in this direction seems to be worthwhile.

The Nernst–Planck equation is a convection–diffusion equation. In chapter 3, a solver for a rather general form of the convection–diffusion equation, including a *space* and *time* dependent convective term and an additional source term, is presented. The lattice method is based on the observation that a convection–diffusion equation describing the evolution of a concentration field is equivalent to the Fokker–Planck equation for the propagator of a Brownian particle. It is known that the Fokker–Planck equation can be transformed to a Master equation on a regular lattice by means of a Taylor expansion. However, we imposed a carefully performed analysis in terms of an asymptotic expansion with respect to a small scaling parameter, analogous to the Chapman–Enskog expansion known from kinetic theory. While earlier studies on this topic focused mainly on the leading order expansions and a rather limited formulation of the equation, we presented a straightforward way of expanding the equations to fourth order accuracy and beyond, and do this for a rather broad class of convection–diffusion equations. Furthermore, we developed a simple way for the treatment of *no–flux boundary conditions* in the case of the leading order algorithm.

The incompressible and stationary Stokes equation can be easily formulated and solved in Fourier space by means of the Oseen tensor. The pressure is

seen as Lagrange multiplier accounting for the constraint of incompressibility and is easily eliminated in Fourier space. In chapter 4 a numerical solver for the Stokes equation around a solid particle in a finite geometry is presented, which is based on the finite-size corrected Oseen tensor. Dirichlet boundary conditions are imposed at the surface of the solid particle. The velocity of the colloidal sphere must be constant everywhere on its surface. However, the value of this constant is a priori not known. Thus, the Dirichlet boundary conditions are replaced by a set of difference conditions plus one condition for the conservation of the center of mass motion. Analogous to an induced charge density accounting for the constant-potential condition on the surface of a conducting sphere in an external electric field, we introduced an induced *reaction force density*. This reaction force density can be calculated by means of surface integrals over the surface of the colloidal particle. The efficiency of the resulting algorithm depends almost only on the efficiency of the method used for solving a linear set of equations in order to calculate the reaction force.
We tested the algorithm exhaustively for the well-known problem of cubic arrays of spheres dragged by a constant external force. The method was applied to three different lattice structures, namely sc, bcc and fcc lattices, and the results were compared successfully to results known from the literature.

The combination of all these methods in an iterative algorithm was implemented and numerical results were presented in chapter 5. In the beginning of the chapter some practical limitations due to the discrete character of the method are discussed, e. g. the choice of the volume fraction or the colloid charge are limited due to the finite lattice spacing. While the demand on memory for the bulk method increases linearly with the number of grid nodes, the surface integral solver for the Stokes equation requires a dense matrix connecting all surface nodes of the colloidal particles. Thus, the amount of memory needed for the storage of this matrix increases rapidly with the resolution of the sphere. Therefore this method is very efficient up to a certain value of the resolution; beyond alternative solutions must be developed. However, the iterative method has the advantage that it is designed as a modular solver and every module can be replaced via an alternative algorithm. One possible approach for going to higher resolutions is to replace the Stokes solver by a bulk method. For example, the time step of a lattice Boltzmann method can be adjusted such that it is the same as the time step of the convection–diffusion solver. Thus, the iterative method could be modified in a way that the Nernst–Planck and the Stokes equation are solved simultaneously. Furthermore, the lattice Boltzmann method would have the same degree of locality as the convection–diffusion equation solver, and hence parallelization using a domain decomposition would be easily implemented. However, this was not attempted here and is mentioned as a suggestion for a

prospective project.
Nevertheless, the current single processor implementation is quite efficient and reliable for a rather satisfactory range of parameters. The numerical results agree reasonably well with some experimental results from the literature and comparing the numerical data with the famous results of O'Brien and White shows a quite good agreement. Furthermore, all parameters in the method are controlled independently, which offers e. g. the opportunity of studying the dependency of the electrophoretic mobility on the diffusion coefficient of the surrounding ions. One of the most interesting results of this thesis is the conclusion that the screening mechanism has got an effect on the electrophoretic mobility, i. e. the mobility varies by some per cent if the amount of salt is increased in the solution, while the screening length is kept constant. Up to date, the common opinion was that the mobility is only affected by the screening length, but *not* by the exact mechanism. This perception is applicable up to a certain accuracy, however, we showed that if the accuracy reaches a limit of about 5%, special care must be taken for the exact screening mechanism. Moreover, we showed that this dependency is affected by the diffusion coefficient.
Another very interesting application is the examination of weakly charged colloidal systems. If an electric field is acting on a system of an uncharged colloidal sphere in salt solution, ions move and are reflected at the surface of the solid particle, resulting in an anomalous dipole moment anti–parallel to the driving field. This anomalous dipole moment was recently addressed by K. Kang and J.K.G. Dhont via analytic calculations. We were able to reproduce the analytical value using our numerical method up to 1% difference. Furthermore, the numerical method is certainly less restricted than the analytic predictions. We recognized that the dipole moment for systems of charged spheres is oriented parallel to the external field. Increasing the colloid charge, we observed a *critical value* at which the direction of the dipole moment changes and also the ion cloud surrounding the colloidal sphere reverses.

In chapter 6 we returned to the mathematical problem of solving a convection–diffusion equation. However, we left the field of electrokinetics and developed a new method for the quantitative data analysis of a new surface sensitive experimental method, known as Fluorescence Cross–Correlation Spectroscopy in Total Internal Reflection (TIR–FCCS). In this experimental approach fluorescent colloidal particles are used to trace the flow profile through a micro channel. A laser beam is focused to one channel wall in total internal reflection such that only tracer particles in the proximity of the wall, i. e. in the region of the evanescent wave, are illuminated. The fluorescent light of two spatially shifted observation volumes is collected and auto– and cross–correlation functions are generated by a convolution of the detector signals.

The concentration fluctuations of the tracer particles are described by a convection–diffusion equation and the correlation function is a double integral over the solution of this equation and the two observation volumes. Since an analytical solution for this problem is certainly out of reach for most problems, we developed a computational approach for the treatment of the correlation functions in the case that the velocity profile is linearly approximated near the solid–fluid interface and the presence of a solid wall. The combination of *Brownian Dynamics* methods accounting for the convection–diffusion equation and an *importance sampling* approach for the evaluation of the double integral over the two observation volumes ends up in a rather simple, efficient and reliable algorithm. A single particle is generated in compliance with a probability function equivalent to the first observation volume and propagated via Brownian Dynamics simulations. Evaluating the position of the particle for every time step with the second observation volume and averaging over a large number of such particles, finally yields the desired correlation functions. This method is easy to implement and highly parallelizable, since every trajectory is independent. The comparison with the experiments shows a quite good agreement, both qualitatively and also quantitatively.
In order to evaluate the experimental results by means of simulations, we combined the Brownian Dynamics simulation with a Monte–Carlo technique, sampling the space of input parameters for the simulations. The first and second moments of the parameters then allows us to quote the most probable values of the parameters and their statistical errors. This data analysis was applied to experimental results measured for a hydrophilic glass–water interface. The question we addressed was, if it is possible to measure the effect of slippage of the fluid over the surface in the form of a slip length. Indeed we found that the slip length for that system is less than $10nm$, taking steric interactions into account. Although we made use of rather crude approximations, our results seem to be much more accurate than all previous experimental results measured with optical methods. Furthermore the computational method is easily extensible to more complex systems, for example polydispersity, hydrodynamic and electrostatic interaction with the wall. Some discrepancies between experiment and simulation were shortly adressed and could be traced back to an imperfectness in the form of the observation volumes. The nature of this imperfectness is not known yet and efforts to deal with this problem must be done in the future.
All together, we developed a powerful tool for the quantitative data analysis of TIR–FCCS measurements and hope that we could contribute to future research in the question of the difference of the slippage over hydrophilic and hydrophobic surfaces.

A. Appendix: Electrokinetics

A.1. The PB Cell Model

In Fig. 2.9 of Sec. 2.4.2 we compared the results of our iterative Poisson–Boltzmann solver for a single sphere in a periodic box with the solution, generated by the isotropic cell model. In this appendix, a detailed presentation of the routine used to calculate the isotropic solution is given.
In reduced units (see Tab. 1.1) the Poisson–Boltzmann equation is given by

$$\nabla^2\psi \,+\, \sum_i z_i A_i \exp(-z_i\psi) \,=\, 0\,, \tag{A.1}$$

with

$$N_i = A_i \int_V dV \,\exp(-z_i\psi)\,. \tag{A.2}$$

In the isotropic case we have $\psi \equiv \psi(r)$, and the second derivative yields

$$\begin{aligned} \nabla^2\psi &= \frac{1}{r^2}\frac{\partial}{\partial r}\left(r^2\frac{\partial\psi}{\partial r}\right) \\ &= \frac{\partial^2\psi}{\partial r^2} + \frac{2}{r}\frac{\partial\psi}{\partial r}\,. \end{aligned} \tag{A.3}$$

The Poisson–Boltzmann equation therefore reads

$$-\frac{\partial^2\psi}{\partial r^2} \,-\, \frac{2}{r}\frac{\partial\psi}{\partial r} \,=\, \sum_i z_i A_i \exp(-z_i\psi)\,. \tag{A.4}$$

Introducing the electric field, this becomes

$$\frac{\partial\psi}{\partial r} \;=\; -E\,, \tag{A.5}$$

$$\frac{\partial E}{\partial r} \;=\; -\frac{2E}{r} + \sum_i z_i A_i \exp(-z_i\psi)\,, \tag{A.6}$$

or, for only one ionic species (counterions with $z = -1$), one may write

$$\frac{\partial\psi}{\partial r} \;=\; -E\,, \tag{A.7}$$

$$\frac{\partial E}{\partial r} \;=\; -\frac{2E}{r} \,-\, A\exp(\psi)\,. \tag{A.8}$$

This is somewhat reminiscent of Hamilton's equations of motion, however with a force which depends on "velocity" and also explicitly on "time". Nevertheless, we employ the same strategy for its numerical solution, i. e. the velocity Verlet algorithm known from Molecular Dynamics [117]. The idea is to view the integration constant A as input parameter, which is *finally* adjusted such that integration results in the correct value of N. The equations are integrated from the inner $r^{(i)}$ to the outer radius $r^{(o)}$ of the spherical cell.
At the inner radius, we choose $\psi(r^{(i)}) = 0$ and the value of the field is a direct consequence from Gauss' law at the colloid surface,

$$E(r^{(i)}) \;=\; \frac{N}{4\pi(r^{(i)})^2}\,. \tag{A.9}$$

For the correct solution the electric field must vanish at the outer radius, $E(r^{(o)}) = 0$. Thus, E is positive everywhere, and hence we see from Eq. (A.7) that the potential must be negative, $\psi(r) < 0$. Therefore the estimate $A = N/V$ is a *lower bound* to the correct value of A. Using the definition of κ^2, Eq. (1.48), one can easily show that in our reduced units that value is simply unity. We hence start with $A = 1$ and search from there by doubling combined with bisection. The algorithm is sketched by Fig. A.1.

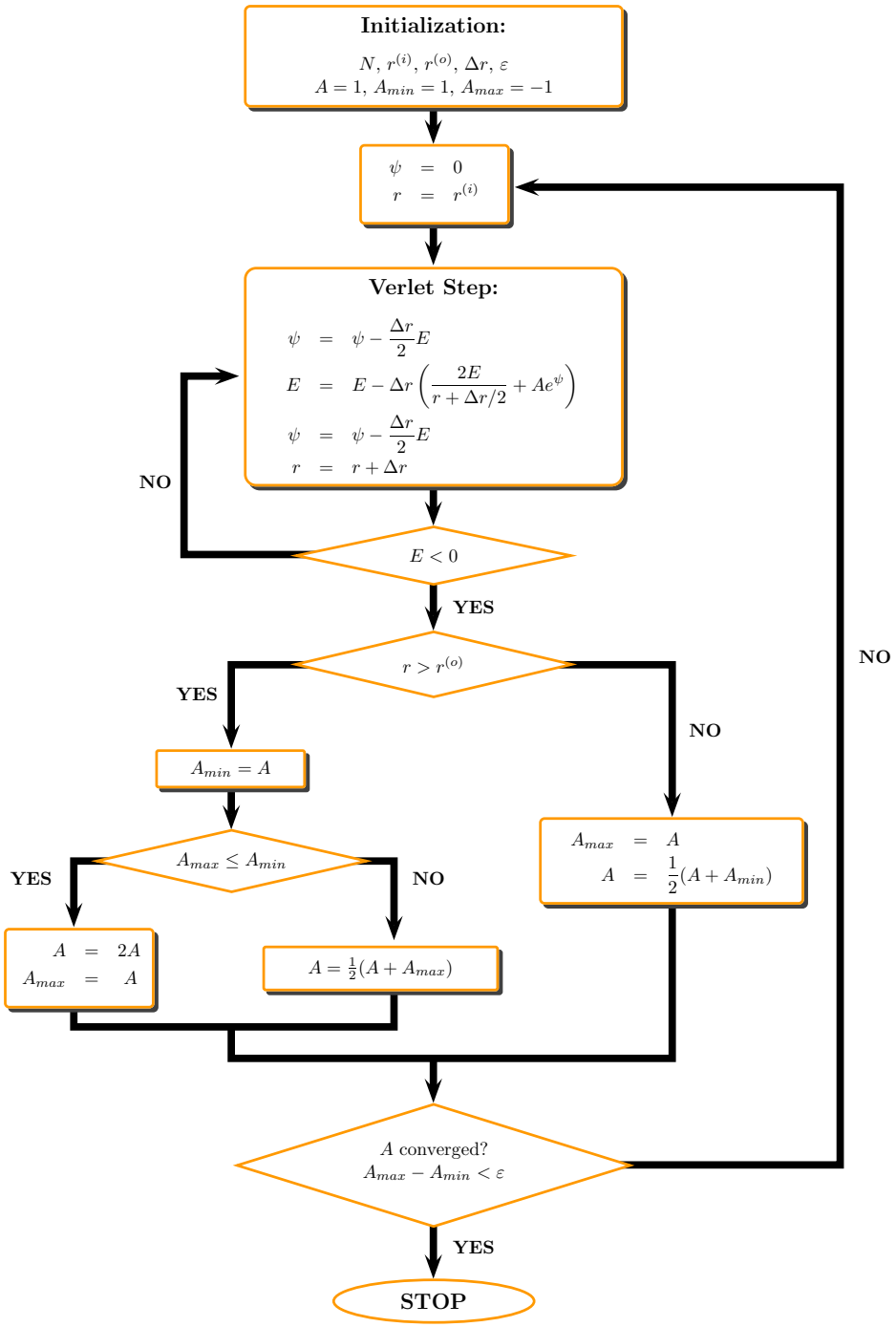

Figure A.1.: Illustration of the numerical solver for the isotropic Poisson–Boltzmann cell model.

A.2. The Gouy–Chapman Solution

In section 2.4.2 we quoted the solution for the counterion-concentration field of a single infinite charged plane, Eq. (2.76), with surface charge density σ. Here, we show that Eq. (2.76) indeed solves the Poisson-Boltzmann equation within this simple geometry. We start from the one-dimensional Poisson-Boltzmann equation in reduced units for only one ionic species, given by

$$\frac{\partial^2}{\partial x^2}\psi + zA\exp(-z\psi) = 0\,. \tag{A.10}$$

The counterion concentration is related to the electrostatic potential via

$$c = A\exp(-z\psi)\,, \tag{A.11}$$

or equivalently

$$\psi = -\frac{1}{z}(\ln c - \ln A)\,. \tag{A.12}$$

Making the ansatz

$$c(x) = \frac{B}{(x+\lambda_{GC})^2}\,, \tag{A.13}$$

where B is a constant factor and λ_{GC} is the so called Gouy-Chapman length. Derivating the potential twice and making use of Eq. (A.12), one obtains

$$\begin{aligned}
\frac{\partial^2}{\partial x^2}\psi &= -\frac{1}{z}\frac{\partial^2}{\partial x^2}\ln c \\
&= \frac{2}{z}\frac{\partial^2}{\partial x^2}\ln(x+\lambda_{GC}) \\
&= -\frac{2}{z}\frac{1}{(x+\lambda_{GC})^2} \\
&= -\frac{2}{z}\frac{1}{B}c \\
&= -\frac{2}{z}\frac{A}{B}\exp(-z\psi)\,.
\end{aligned} \tag{A.14}$$

Comparing with Eq. (A.10) yields the prefactor

$$B = \frac{2}{z^2}\,, \tag{A.15}$$

and one may write the concentration field as

$$c(x) = \frac{2}{z^2(x+\lambda_{GC})^2}\,. \tag{A.16}$$

The Gouy-Chapman length can then be calculated from the boundary condition

$$-\left.\frac{\partial\psi}{\partial x}\right|_{x=0} = \sigma\,. \tag{A.17}$$

Making use of Eq. (A.12) and Eq. (A.16), one obtains

$$\begin{aligned} \left.\frac{\partial\psi}{\partial x}\right|_{x=0} &= \left.-\frac{1}{z}\frac{\partial}{\partial x}\ln c\right|_{x=0} \\ &= \left.\frac{2}{z}\frac{\partial}{\partial x}\ln(x+\lambda_{GC})\right|_{x=0} \\ &= \left.\frac{2}{z}\frac{1}{x+\lambda_{GC}}\right|_{x=0} \\ &= \frac{2}{z\lambda_{GC}}\,. \end{aligned} \tag{A.18}$$

Hence, the Gouy-Chapman length in our reduced units is given by

$$\lambda_{GC} = -\frac{2}{\sigma z}\,. \tag{A.19}$$

A.3. Derivation of Eq. (3.42)

In Sec. 3.1.4 we omitted the exact derivation of the second order operator, Eq. (3.42). This calculation is shown in detail in the following.
We start with Eq. (3.40) and abbreviate

$$\mathcal{Q} \equiv \partial_\alpha u_\alpha^{(3)} - \frac{h_0}{2}\partial_\alpha\partial_\beta q_{\alpha\beta}^{(2)} + \frac{h_0^2}{6}\partial_\alpha\partial_\beta\partial_\gamma p_{\alpha\beta\gamma}^{(1)} - \frac{h_0^3}{24}\partial_\alpha\partial_\beta\partial_\gamma\partial_\delta s_{\alpha\beta\gamma\delta}^{(0)}\,. \tag{A.20}$$

Insertion of Eq. (3.41) results in

$$\begin{aligned} \mathcal{L}^{(2)} &= \mathcal{Q} - \frac{h_0}{2}\frac{\partial}{\partial t}[\mathcal{L}^{(0)} - \partial_\alpha v_\alpha + D\partial_\alpha\partial_\alpha] \\ &- h_0\frac{\partial}{\partial t}\partial_\alpha v_\alpha + h_0\frac{\partial}{\partial t}D\partial_\alpha\partial_\alpha \\ &= \mathcal{Q} - \frac{h_0}{2}\frac{\partial}{\partial t}\mathcal{L}^{(0)} - \frac{h_0}{2}\frac{\partial}{\partial t}[\partial_\alpha v_\alpha - D\partial_\alpha\partial_\alpha] \\ &= \mathcal{Q} - \frac{h_0}{2}\frac{\partial}{\partial t}\mathcal{L}^{(0)} - \frac{h_0}{2}[\partial_\alpha v_\alpha - D\partial_\alpha\partial_\alpha]\frac{\partial}{\partial t} - \frac{h_0}{2}\partial_\alpha\left(\frac{\partial}{\partial t}v_\alpha\right) \\ &= \mathcal{Q} - \frac{h_0}{2}[\mathcal{L}^{(0)} - \partial_\alpha v_\alpha + D\partial_\alpha\partial_\alpha]\mathcal{L}^{(0)} \\ &- \frac{h_0}{2}[\partial_\alpha v_\alpha - D\partial_\alpha\partial_\alpha][\mathcal{L}^{(0)} - \partial_\alpha v_\alpha + D\partial_\alpha\partial_\alpha] - \frac{h_0}{2}\partial_\alpha\left(\frac{\partial}{\partial t}v_\alpha\right) \\ &= \mathcal{Q} - \frac{h_0}{2}\mathcal{L}^{(0)^2} + \frac{h_0}{2}[\partial_\alpha v_\alpha - D\partial_\alpha\partial_\alpha]^2 - \frac{h_0}{2}\partial_\alpha\left(\frac{\partial}{\partial t}v_\alpha\right)\,. \end{aligned} \tag{A.21}$$

Making use of the operator identities

$$\partial_\alpha v_\alpha\partial_\beta v_\beta = \partial_\alpha\partial_\beta v_\alpha v_\beta - \partial_\alpha v_\beta(\partial_\beta v_\alpha)\,, \tag{A.22}$$

$$\partial_\alpha\partial_\alpha\partial_\beta v_\beta = \frac{1}{3}\partial_\alpha\partial_\beta\partial_\gamma[\delta_{\beta\gamma}v_\alpha + \delta_{\alpha\gamma}v_\beta + \delta_{\alpha\beta}v_\gamma]\,, \tag{A.23}$$

$$\begin{aligned}\partial_\alpha v_\alpha\partial_\beta\partial_\beta &= \frac{1}{3}\partial_\alpha\partial_\beta\partial_\gamma[\delta_{\beta\gamma}v_\alpha + \delta_{\alpha\gamma}v_\beta + \delta_{\alpha\beta}v_\gamma] \\ &- \partial_\alpha\partial\beta[(\partial_\alpha v_\beta) + (\partial_\beta v_\alpha)] + \partial_\alpha(\partial_\beta^2 v_\alpha)\,,\end{aligned} \tag{A.24}$$

and

$$\partial_\alpha\partial_\alpha\partial_\beta\partial_\beta = \frac{1}{3}\partial_\alpha\partial_\beta\partial_\gamma\partial_\delta[\delta_{\alpha\beta}\delta_{\gamma\delta} + \delta_{\alpha\gamma}\delta_{\beta\delta} + \delta_{\alpha\delta}\delta_{\beta\gamma}]\,, \tag{A.25}$$

and sorting with respect to the derivatives finally results in Eq. (3.42),

$$\begin{aligned}\mathcal{L}^{(2)} &= \partial_\alpha\left\{u_\alpha^{(3)} - \frac{Dh_0}{2}\left(\partial_\beta^2 v_\alpha\right) - \frac{h_0}{2}v_\beta\left(\partial_\beta v_\alpha\right) - \frac{h_0}{2}\left(\frac{\partial v_\alpha}{\partial t}\right)\right\} \\ &+ \partial_\alpha\partial_\beta\left\{-\frac{h_0}{2}q_{\alpha\beta}^{(2)} + \frac{Dh_0}{2}\left[(\partial_\alpha v_\beta) + (\partial_\beta v_\alpha)\right] + \frac{h_0}{2}v_\alpha v_\beta\right\} \\ &+ \partial_\alpha\partial_\beta\partial_\gamma\left\{\frac{h_0^2}{6}p_{\alpha\beta\gamma}^{(1)} - \frac{Dh_0}{3}\left[\delta_{\beta\gamma}v_\alpha + \delta_{\alpha\gamma}v_\beta + \delta_{\alpha\beta}v_\gamma\right]\right\} \\ &+ \partial_\alpha\partial_\beta\partial_\gamma\partial_\delta\left\{-\frac{h_0^3}{24}s_{\alpha\beta\gamma\delta}^{(0)} + \frac{D^2h_0}{6}\left[\delta_{\alpha\beta}\delta_{\gamma\delta} + \delta_{\alpha\gamma}\delta_{\beta\delta} + \delta_{\alpha\delta}\delta_{\beta\gamma}\right]\right\} \\ &- \frac{h_0}{2}{\mathcal{L}^{(0)}}^2.\end{aligned} \tag{A.26}$$

A.4. Discrete Formulation of the Oseen Tensor in Fourier Space

In chapter 1.4 the discretized Green's function of the Poisson equation in Fourier space was presented (see Eq. (1.75)). The idea was to use a 6-point stencil finite–difference scheme on a regular lattice and transform this stencil to a Fourier series. Within this appendix, we show an analogous way for deriving a lattice-Green's function for the Stokes equation. In other words, we present the discretized version of the Oseen tensor we used in the reaction force algorithm of chapter 4.3.

From Eq. (1.74) we already know the discretized version of the Fourier transformed Laplacian. Analogous to the factor $-\boldsymbol{k}^2$ of the continuous version, we abbreviate for convenience

$$-\xi_{k,l,m}^2 := \frac{2}{a^2}\left\{\cos\left(2\pi\frac{k}{N_x}\right) + \cos\left(2\pi\frac{l}{N_y}\right) + \cos\left(2\pi\frac{m}{N_z}\right) - 3\right\}\,, \tag{A.27}$$

where a is again the lattice spacing, N_x is the number of lattice sites in x-direction and N_y , N_z are the numbers of grid points in the other directions,

respectively. Thus, one may write the second derivative of a periodic function $g(n_x, n_y, n_z)$ in the form

$$\nabla^2 g \simeq -\sum_{k=0}^{N_x-1}\sum_{l=0}^{N_y-1}\sum_{m=0}^{N_z-1} \xi^2_{k,l,m}\hat{g}(k,l,m)e^{-2\pi i\left(\frac{kn_x}{N_x}+\frac{ln_y}{N_y}+\frac{mn_z}{N_z}\right)}. \tag{A.28}$$

Here, n_α addresses the lattice site in the corresponding direction.

Conversely, on the discrete lattice the Laplacian is not necessarily the divergence of a gradient. Thus we also have to apply the discrete 6-point stencil to the gradient of a scalar field and the divergence of a vector field.

The gradient is approximated via

$$\begin{aligned}\nabla g(n_x,n_y,n_z) \simeq \frac{1}{2a}\big\{&(g(n_x+1,n_y,n_z)-g(n_x-1,n_y,n_z))\hat{\boldsymbol{e}}_x \\ &+(g(n_x,n_y+1,n_z)-g(n_x,n_y-1,n_z))\hat{\boldsymbol{e}}_y \\ &+(g(n_x,n_y,n_z+1)-g(n_x,n_y,n_z-1))\hat{\boldsymbol{e}}_z\big\}\end{aligned} \tag{A.29}$$

and hence the Fourier transformation results in

$$\begin{aligned}\nabla g(n_x,n_y,n_z) \simeq &\sum_{k=0}^{N_x-1}\sum_{l=0}^{N_y-1}\sum_{m=0}^{N_z-1}\frac{1}{2a}\,\hat{g}(k,l,m) \\ &\cdot\Big\{(e^{-2\pi i\frac{k}{N_x}}-e^{+2\pi i\frac{k}{N_x}})\hat{\boldsymbol{e}}_x+(e^{-2\pi i\frac{l}{N_y}}-e^{+2\pi i\frac{l}{N_y}})\hat{\boldsymbol{e}}_y \\ &+(e^{-2\pi i\frac{m}{N_z}}-e^{+2\pi i\frac{m}{N_z}})\hat{\boldsymbol{e}}_z\Big\}e^{-2\pi i\left(\frac{kn_x}{N_x}+\frac{ln_y}{N_y}+\frac{mn_z}{N_z}\right)} \\ = &-i\sum_{k=0}^{N_x-1}\sum_{l=0}^{N_y-1}\sum_{m=0}^{N_z-1}\frac{1}{a}\,\hat{g}(k,l,m) \\ &\cdot\Big\{\sin\left(2\pi\frac{k}{N_x}\right)\hat{\boldsymbol{e}}_x+\sin\left(2\pi\frac{l}{N_y}\right)\hat{\boldsymbol{e}}_y \\ &+\sin\left(2\pi\frac{m}{N_z}\right)\hat{\boldsymbol{e}}_z\Big\}e^{-2\pi i\left(\frac{kn_x}{N_x}+\frac{ln_y}{N_y}+\frac{mn_z}{N_z}\right)},\end{aligned} \tag{A.30}$$

where $\hat{e}_\alpha$ are the Cartesian basis vectors. Analogously, one may write the

divergence of a discretized vector field $\boldsymbol{h}(n_x, n_y, n_z)$[1] as

$$\begin{aligned} \nabla \cdot \boldsymbol{h} \;\simeq\; & -i \sum_{k=0}^{N_x-1} \sum_{l=0}^{N_y-1} \sum_{m=0}^{N_z-1} \frac{1}{a}\, \hat{\boldsymbol{h}}(k,l,m) \\ & \cdot \Bigg\{ \sin\left(2\pi \frac{k}{N_x}\right) \hat{\boldsymbol{e}}_x + \sin\left(2\pi \frac{l}{N_y}\right) \hat{\boldsymbol{e}}_y \\ & + \sin\left(2\pi \frac{m}{N_z}\right) \hat{\boldsymbol{e}}_z \Bigg\} e^{-2\pi i \left(\frac{kn_x}{N_x} + \frac{ln_y}{N_y} + \frac{mn_z}{N_z}\right)} . \end{aligned} \tag{A.31}$$

Defining

$$\begin{aligned} \boldsymbol{q}_{k,l,m} \;:=\; & \frac{1}{a} \sin\left(2\pi \frac{k}{N_x}\right) \hat{\boldsymbol{e}}_x \\ + \; & \frac{1}{a} \sin\left(2\pi \frac{l}{N_y}\right) \hat{\boldsymbol{e}}_y \\ + \; & \frac{1}{a} \sin\left(2\pi \frac{m}{N_z}\right) \hat{\boldsymbol{e}}_z , \end{aligned} \tag{A.32}$$

the Stokes equation becomes in the discretized Fourier space

$$0 \;=\; -i \boldsymbol{q}_{k,l,m} \cdot \hat{\boldsymbol{v}}(k,l,m) , \tag{A.33a}$$

$$0 \;=\; i \boldsymbol{q}_{k,l,m} \hat{p}(k,l,m) - \eta \xi^2_{k,l,m} \hat{\boldsymbol{v}}(k,l,m) + \hat{\boldsymbol{f}}(k,l,m) . \tag{A.33b}$$

From here, the calculation is analogous to the calculation of the Oseen tensor in the continuous Fourier space (see chapter 4.1). Multiplication with $i\boldsymbol{q}$ and using the incompressibility results in

$$0 \;=\; -\boldsymbol{q}^2 \hat{p} + i \boldsymbol{q} \hat{\boldsymbol{f}} , \tag{A.34}$$

and hence

$$\hat{p} = \frac{i}{\boldsymbol{q}^2} \boldsymbol{q} \cdot \hat{\boldsymbol{f}} . \tag{A.35}$$

Inserting this into the Stokes equation, one obtains

$$\begin{aligned} 0 \;&=\; -\frac{1}{\boldsymbol{q}^2} \boldsymbol{q} (\boldsymbol{q} \cdot \hat{\boldsymbol{f}}) - \eta \xi^2 \hat{\boldsymbol{v}} + \hat{\boldsymbol{f}} \\ &=\; \left(\overleftrightarrow{\boldsymbol{I}} - \frac{\boldsymbol{q} \otimes \boldsymbol{q}}{\boldsymbol{q}^2} \right) \hat{\boldsymbol{f}} - \eta \xi^2 \hat{\boldsymbol{v}} . \end{aligned} \tag{A.36}$$

Solving this for the velocity field, we get

$$\hat{\boldsymbol{v}} \;=\; \frac{1}{\eta \xi^2} \left(\overleftrightarrow{\boldsymbol{I}} - \frac{\boldsymbol{q} \otimes \boldsymbol{q}}{\boldsymbol{q}^2} \right) \hat{\boldsymbol{f}} . \tag{A.37}$$

[1] Note that we do not impose the Yee discretization scheme [62]. For simplicity reasons all fields are located on the lattice sites.

Thus, the desired discretized version of the Oseen tensor in Fourier space, is expressed as

$$\hat{\overleftrightarrow{\boldsymbol{T}}}(k,l,m) \;=\; \frac{1}{\eta\xi^2_{k,l,m}}\left(\overleftrightarrow{\boldsymbol{I}} - \frac{\boldsymbol{q}_{k,l,m}\otimes\boldsymbol{q}_{k,l,m}}{\boldsymbol{q}^2_{k,l,m}}\right). \tag{A.38}$$

The discretized Tensor in real space is then obtained from a fast Fourier transformation.

A.5. Constrained Variational Formulation of the Stokes Equation

After the great success of the variational approach for the Poisson–Boltzmann equation, our first suggestion was to treat the Stokes equation in a similar way. So we asked, if it is possible to formulate the stationary Stokes equation

$$\eta\nabla^2\boldsymbol{v} - \nabla p + \boldsymbol{f} \;=\; 0\,, \tag{A.39}$$
$$\nabla\cdot v \;=\; 0\,, \tag{A.40}$$

in a constrained variational formulation. And indeed it is.
The Euler–Lagrange equations of a functional of the form

$$\begin{aligned}\Phi \;&:=\; \int d^3r\mathcal{L} \\ &\equiv\; \int d^3r\left[A(\nabla\times\boldsymbol{v})^2 + B\boldsymbol{f}\cdot\boldsymbol{v} + Cp(\nabla\cdot\boldsymbol{v})\right]\end{aligned} \tag{A.41}$$

recover the incompressible Stokes equation in the center of mass frame of the system for an appropriate choice of the prefactors A, B and C. Defining

$$\mathcal{L}_0 \;:=\; A(\nabla\times\boldsymbol{v})^2\,, \tag{A.42}$$
$$\mathcal{L}_1 \;:=\; Cp(\nabla\cdot\boldsymbol{v})\,, \tag{A.43}$$

and making use of the identity

$$\begin{aligned}(\nabla\times\boldsymbol{v})^2 \;&=\; \varepsilon_{\alpha\beta\gamma}(\partial_\beta v_\gamma)\varepsilon_{\alpha\mu\nu}(\partial_\mu v_\nu) \\ &=\; (\delta_{\beta\mu}\delta_{\gamma\nu} - \delta_{\beta\nu}\delta_{\gamma\mu})(\partial_\beta v_\gamma)(\partial_\mu v_\nu) \\ &=\; (\partial_\beta v_\gamma)(\partial_\beta v_\gamma) - (\partial_\beta v_\gamma)(\partial_\gamma v_\beta)\,,\end{aligned} \tag{A.44}$$

where the greek subscripts are Cartesian indices, $\varepsilon_{\alpha\beta\gamma}$ is the asymmetric Levi–

Civita tensor and we abbreviate $\partial_\alpha = \partial/\partial x_\alpha$, we get

$$\partial_\beta \frac{\partial \mathcal{L}_0}{\partial(\partial_\beta v_\gamma)} = 2A\left[\partial_\beta\partial_\beta v_\gamma - \partial_\gamma\partial_\beta v_\beta\right], \tag{A.45}$$

$$\frac{\partial \mathcal{L}}{\partial v_\gamma} = Bf_\gamma, \tag{A.46}$$

$$\frac{\partial \mathcal{L}}{\partial p} = C\nabla\cdot\boldsymbol{v}, \tag{A.47}$$

$$\partial_\beta \frac{\partial \mathcal{L}_1}{\partial(\partial_\beta v_\gamma)} = C\partial_\gamma p. \tag{A.48}$$

Taking all together, the Euler–Lagrange equations result in

$$2A\left[\nabla^2\boldsymbol{v} - \nabla(\nabla\cdot\boldsymbol{v})\right] + C\nabla p = B\boldsymbol{f}, \tag{A.49}$$

$$\nabla\cdot\boldsymbol{v} = 0. \tag{A.50}$$

Choosing $2A = \eta$, $C = -1$ and $B = -1$, this recovers the incompressible Stokes equation, Eq. (A.39) and Eq. (A.40), and the functional becomes

$$\Phi = \int d^3r \left[\frac{\eta}{2}(\nabla\times\boldsymbol{v})^2 - \boldsymbol{f}\cdot\boldsymbol{v} - p(\nabla\cdot\boldsymbol{v})\right]. \tag{A.51}$$

In this formulation, the role of the pressure as Lagrange multiplier for the incompressibility condition is nicely obvious.

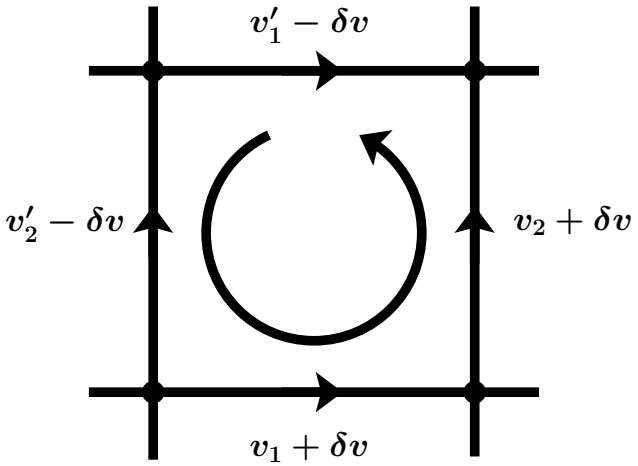

Figure A.2.: Rotational move for the velocity field on a plaquette.

As in the original Maggs algorithm, the system is initially set up at an arbitrary point of the constraint surface, i. e. the initial configuration should be located

in the center of mass frame and satisfy the incompressibility condition

$$\int d^3r \boldsymbol{v} = 0\,, \tag{A.52}$$

$$\nabla \cdot \boldsymbol{v} = 0\,. \tag{A.53}$$

Minimizing the functional via rotational moves, analogous to the Maggs approach for the electric field, conserves the constraints, and since we stay strictly on the constraint surface, we may neglect the Lagrange–multiplier term. Furthermore, such an algorithm would run ultimately in a true minimum (not into a saddle point). This can be observed by decomposing the velocity field into the solution $\boldsymbol{v}_0$ plus some small perturbation

$$\boldsymbol{v} = \boldsymbol{v}_0 + \boldsymbol{v}'\,. \tag{A.54}$$

The square of the curl then results in

$$(\nabla \times \boldsymbol{v})^2 = (\nabla \times \boldsymbol{v}_0)^2 + (\nabla \times \boldsymbol{v}')^2 + 2(\nabla \times \boldsymbol{v}_0) \cdot (\nabla \times \boldsymbol{v}')\,. \tag{A.55}$$

Thus, also Φ can be written as the solution plus a small deviation

$$\Phi \equiv \Phi[\boldsymbol{v}_0] + \Phi'\,. \tag{A.56}$$

Since the functional derivative is zero for $\boldsymbol{v}_0$ by construction, $\delta\Phi/\delta\boldsymbol{v}\big|_{\boldsymbol{v}_0} = 0$, all terms linear in $\boldsymbol{v}'$ do not contribute to Φ', and hence the deviation is essentially given by

$$\Phi' = \frac{\eta}{2} \int d^3r\, (\nabla \times \boldsymbol{v}')^2\,, \tag{A.57}$$

which is positive definite, and thus, the solution $\Phi[\boldsymbol{v}_0]$ is a true minimum of the landscape.

The rotational moves in $\boldsymbol{v}$ are performed similar to the rotational moves of $\boldsymbol{E}$ in the Poisson–Boltzmann solver. Consider for example a loop with a sequence of velocities v_1, v_2, v_1' and v_2' as sketched by Fig. A.2. The updates then are given by

$$v_1 \rightarrow v_1 + \delta v\,, \tag{A.58}$$

$$v_2 \rightarrow v_2 + \delta v\,, \tag{A.59}$$

$$v_1' \rightarrow v_1' - \delta v\,, \tag{A.60}$$

$$v_2' \rightarrow v_2' - \delta v\,. \tag{A.61}$$

Since the functional Φ depends explicitly on the curl of the velocity field, the calculation of the change in the functional value becomes less local as it is the case in the Poisson–Boltzmann formalism. Rather all plaquettes in

the vicinity of the updated links must be taken into account, and thus the change in the functional depends on 13 plaquettes. Therefore the calculation of this change is somewhat lengthy and tedious. Nevertheless, it is possible. The result is a quadratic function in δv, which can be easily minimized to determine the optimal value. A first implementation of this method showed that the algorithm indeed works and converges, but unfortunately only very slowly. This was the reason for replacing the variational approach by the surface integral method of Chap. 4.

B. Appendix: TIR–FCCS

B.1. The Stokes Equation in a Rectangular Channel

Experiments have been performed to measure the flow profile perpendicular to the surface over the whole channel diameter to get an independent estimator for the shear rate. From experimental studies it is known that the influence of a non vanishing slip length on the flow profile is only weak, and therefore hard to obtain by direct measurements [113, 118]. However, from the theoretical point of view, it is yet unclear how a possible slip length influences the flow profile in a microchannel, and furthermore, the shear rate at the surface. In the following we will show that a one dimensional Poiseuille flow with neglecting any possible slip length, is sufficient for a proper estimation of the shear rate. The problem we solve in this section is the solution of the Stokes equation

$$\left(\frac{\partial^2}{\partial y^2} + \frac{\partial^2}{\partial z^2}\right) v_x(y,z) \;=\; -\frac{f}{\eta}\,, \tag{B.1}$$

in a rectangular channel with the dimensions $[-\frac{L_y}{2}, \frac{L_y}{2}] \times [-\frac{L_z}{2}, \frac{L_z}{2}]$ in the $y-z$-plane, as it is given in the experimental setup. Here, η is the viscosity of the fluid and f is the driving force density or pressure gradient acting on the fluid in x-direction.
The solution for this problem, which can be found in the textbook of Spurk and Aksel [119], has the disadvantage that it shows no invariance under exchanging the y and z coordinate, and more important, this solution is only valid in the case of no slip boundary conditions and it is not clear how to modify the formula given there, if slip boundary conditions are applied.
In the following we will show an alternative solution for Eq. (B.1), first with stick boundary conditions and then discussing the influence of applying slip boundary conditions. From this solution the effect of non zero-slip length on the overall flow profile and the shear rate close to a boundary is studied.

B.1.1. No-Slip Boundary Conditions

In a first step one may write Eq. (B.1) in Dirac's BraKet notation

$$\mathcal{H}|v\rangle = -|q\rangle\,, \tag{B.2}$$

with $q = f/\eta$ and $\mathcal{H} = \frac{\partial^2}{\partial y^2} + \frac{\partial^2}{\partial z^2}$. For solving this problem a standard method can be used, well known from quantum mechanical calculations, namely expanding the function $|v\rangle$ in terms of eigenfunctions of $\mathcal{H}$,

$$\mathcal{H}|\psi_{mn}\rangle = \lambda_{mn}|\psi_{mn}\rangle. \tag{B.3}$$

Suppose $|\psi_{mn}\rangle$ is an *orthonormal* basis of Hilbert space, such that

$$\sum_{mn} |\psi_{mn}\rangle\langle\psi_{mn}| \;=\; 1, \tag{B.4a}$$

$$\langle\psi_{mn}|\psi_{mn}\rangle \;=\; 1. \tag{B.4b}$$

Solving this problem is a standard calculation in quantum mechanical textbooks, since the operator $\mathcal{H} = \frac{\partial^2}{\partial y^2} + \frac{\partial^2}{\partial z^2}$ is the Hamilton operator for a free particle in two dimensions, and hence the problem reduces to the solution of the Schrödinger equation of a free quantum mechanical particle in a two dimensional box (see e. g. Ref. [120]). Knowing that $|\psi_{mn}\rangle$ is an eigenfunction of the Hamiltonian, its spectral form is given by

$$\mathcal{H} \;=\; \sum_{mn} \lambda_{mn}|\psi_{mn}\rangle\langle\psi_{mn}|, \tag{B.5}$$

and hence also its inverse is known. Together with Eq. (B.2), one obtains

$$\langle\psi_{mn}|v\rangle = -\frac{1}{\lambda_{mn}}\langle\psi_{mn}|q\rangle, \tag{B.6}$$

and expanding $|v\rangle$ with respect to the eigenfunctions, yields

$$|v\rangle \;=\; -\sum_{mn} \frac{1}{\lambda_{mn}}\langle\psi_{mn}|q\rangle|\psi_{mn}\rangle. \tag{B.7}$$

At this point, we reduced the problem to the calculation of eigenvalues and eigenfunctions of $\mathcal{H}$.
Making the product ansatz

$$\psi(y,z) \equiv A(y)B(z)\,, \tag{B.8}$$

and inserting this into Eq. (B.2), one can write down two independent equations for A and B

$$\frac{\partial^2}{\partial y^2}A(y) \;=\; -\lambda_y^2 A(y), \tag{B.9a}$$

$$\frac{\partial^2}{\partial z^2}B(z) \;=\; -\lambda_z^2 B(z), \tag{B.9b}$$

and

$$\lambda \equiv -(\lambda_y^2 + \lambda_z^2). \tag{B.10}$$

This is a well known wave equation and can be solved making the ansatz

$$A(y) = a_1 e^{i\lambda_y y} + a_2 e^{-i\lambda_y y}. \tag{B.11}$$

Symmetry $A(y) = A(-y)$ dictates that only the even parts survive, while the odd contributions vanish, and therefore

$$a \equiv a_1 = a_2, \tag{B.12}$$

and

$$A(y) = 2a\cos(\lambda_y y). \tag{B.13}$$

The λ's are defined by the boundary conditions. As mentioned before and since the effect of the slip length is supposed to be small, we first introduce *stick* boundary conditions, i. e. the flow velocity should be zero at the walls and hence

$$A(\frac{L_y}{2}) = 2a\cos(\frac{\lambda_y}{2}L_y) = 0. \tag{B.14}$$

From this we find

$$\lambda_{y,n} = \frac{2n+1}{L_y}\pi, \tag{B.15}$$

with $n = 0, 1, 2, \ldots$. The prefactor a can be determined from the normalization condition

$$\begin{aligned} 1 &= \int_{-\frac{L_y}{2}}^{\frac{L_y}{2}} A^2(y)dy \\ &= 2L_y\, a^2, \end{aligned} \tag{B.16}$$

and therefore

$$a = \frac{1}{\sqrt{2L_y}}. \tag{B.17}$$

Obviously, $B(z)$ can be calculated in the same way.

Taking all together results in

$$\begin{aligned} \langle\psi_{mn}| &= |\psi_{mn}\rangle \\ &= \frac{2}{\sqrt{L_y L_z}}\cos\left(\frac{2n+1}{L_y}\pi y\right)\cos\left(\frac{2m+1}{L_z}\pi z\right), \end{aligned} \tag{B.18}$$

$$\begin{aligned} \lambda_{mn} &= -(\lambda_{y,n}^2 + \lambda_{z,m}^2) \\ &= -\pi^2\left(\frac{(2n+1)^2}{L_y^2} + \frac{(2m+1)^2}{L_z^2}\right). \end{aligned} \tag{B.19}$$

The scalar product of ψ with q is then given by

$$\begin{aligned}
&\langle\psi_{mn}|q\rangle \\
= \;& \frac{f}{\eta}\frac{2}{\sqrt{L_y L_z}}\int_{-\frac{L_y}{2}}^{\frac{L_y}{2}} dy \cos\left(\frac{2n+1}{L_y}\pi y\right) \\
& \cdot \int_{-\frac{L_z}{2}}^{\frac{L_z}{2}} dz \cos\left(\frac{2m+1}{L_z}\pi z\right) \\
= \;& \frac{f}{\eta}(-1)^{m+n}\frac{8}{(2n+1)(2m+1)}\frac{\sqrt{L_y L_z}}{\pi^2}.
\end{aligned} \tag{B.20}$$

Inserting Eq. (B.18), (B.19) and Eq. (B.20) into Eq. (B.7), one finally obtains

$$v_x(y,z) = \frac{f}{\eta}\sum_{mn}\Lambda_{mn}\cos\left(\frac{2n+1}{L_y}\pi y\right)\cos\left(\frac{2m+1}{L_z}\pi z\right), \tag{B.21}$$

with

$$\Lambda_{mn} = \frac{16}{\pi^4}(-1)^{m+n}\cdot\frac{1}{\frac{(2n+1)^2}{L_y^2}+\frac{(2m+1)^2}{L_z^2}}\cdot\frac{1}{(2n+1)(2m+1)}. \tag{B.22}$$

This solution has the advantage that it has the correct spatial invariance in y and z-direction and *slip* boundary conditions can easily be applied by replacing Eq. (B.14). In order to obtain the famous one dimensional Poiseuille profile from Eq. (B.21) by taking the limit $L_y \to \infty$, one first cuts the channel at $y = 0$, resulting in

$$\begin{aligned}
\lim_{L_y\to\infty} v_x(0,z) \;=\; & \frac{16}{\pi^4}\frac{f}{\eta}L_z^2\left(\sum_n \frac{(-1)^n}{2n+1}\right) \\
& \cdot\left(\sum_m \frac{(-1)^m}{(2m+1)^3}\cos\left(\frac{2m+1}{L_z}\pi z\right)\right).
\end{aligned} \tag{B.23}$$

The sum over n is known as *Leibniz* series and has the limit value (see Ref. [114])

$$\sum_{n=0}^{\infty}\frac{(-1)^n}{2n+1} = \frac{\pi}{4}. \tag{B.24}$$

Evaluation of the sum over m by expansion of the cosine up to quadratic order

results in

$$\begin{aligned}
&\sum_m \frac{(-1)^m}{(2m+1)^3} \cos\left(\frac{2m+1}{L_z}\pi z\right) \\
&= \sum_m \frac{(-1)^m}{(2m+1)^3}\left(1 - \frac{\pi^2}{2}(2m+1)^2\frac{z^2}{L_z^2}\right) + \mathcal{R} \\
&= \frac{\pi^3}{32} - \frac{\pi^2}{2}\frac{z^2}{L_z^2}\sum_m \frac{(-1)^m}{2m+1} + \mathcal{R} \\
&= \frac{\pi^3}{32} - \frac{\pi^3}{8}\frac{z^2}{L_z^2} + \mathcal{R}. \qquad \text{(B.25)}
\end{aligned}$$

Inserting this into Eq. (B.23) reproduces the Poiseuille solution plus some correction terms,

$$\lim_{L_y\to\infty} v_x(0,z) = \frac{1}{2}\frac{f}{\eta}L_z^2\left(\frac{1}{4} - \frac{z^2}{L_z^2}\right) + \mathcal{R}'\,. \qquad \text{(B.26)}$$

from the known solution of the Poiseuille problem in a one-dimensional channel, we know that $\mathcal{R}'$ must vanish identically, but we have not been able to show this directly from the series representation. Numerically, however, $\mathcal{R}' = 0$ can be shown without any doubt. As shown in Fig. B.1, the flow profile in

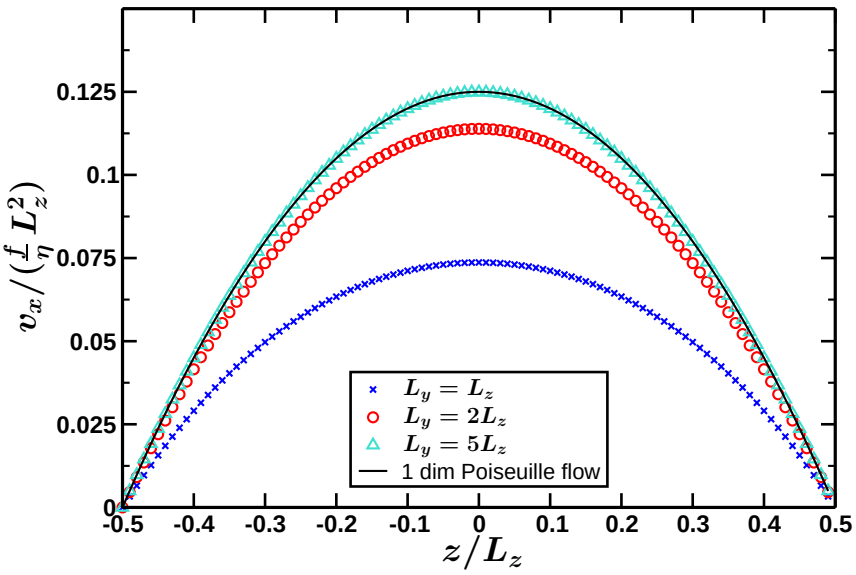

Figure B.1.: 1–dimensional cut of the flow profile at $y = 0$ for no slip boundary conditions and several values of L_y.

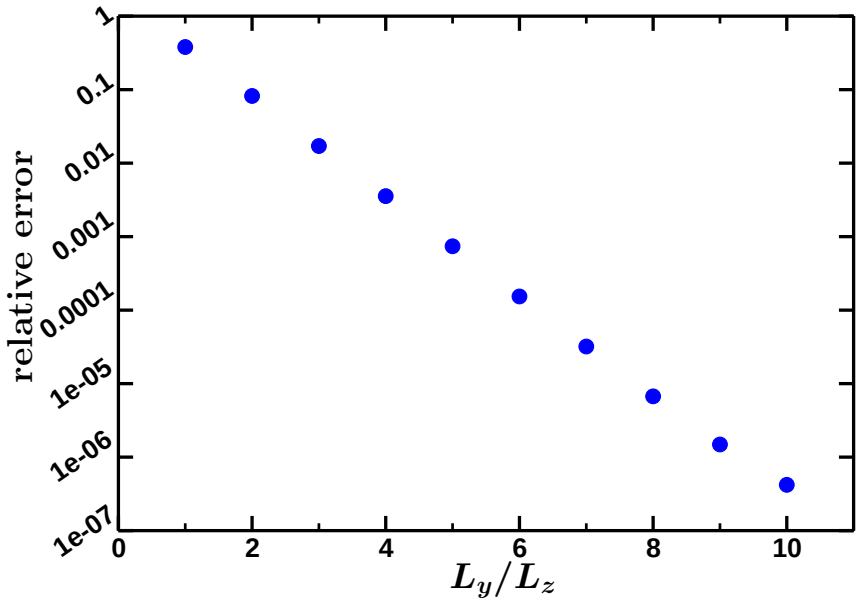

Figure B.2.: Averaged deviation of a one dimensional cut at $y = 0$ of Eq. (B.21) and the Poiseuille solution as function of the width-height ratio of the channel.

z-direction converges to the ideal Poiseuille solution for increasing width-to-height ratios L_y/L_z of the channel, as it should be. The averaged deviation from the Poiseuille profile

$$\text{relative error} = \frac{1}{N}\sum_{i=1}^{N}\left|\frac{v_x(0,z_i) - v_{\mathrm{P}}(z_i)}{v_{\mathrm{P}}(z_i)}\right|, \tag{B.27}$$

is presented as function of L_y/L_z. Here, N is the number of calculated data-points.

B.1.2. Slip Boundary Conditions

If the friction ζ of the fluid at the surface has got a finite value, *slip* boundary conditions occur and have the form

$$\mp l_s \frac{\partial v_x}{\partial z}(0, \pm\frac{L_z}{2}) \;=\; v_x(0, \pm\frac{L_z}{2}), \tag{B.28}$$

and analogous in y-direction. Here, $l_s = \eta/\zeta$ is the so called *slip length*. Since Eq. (B.13) is independent of the concrete form of the eigenvalues, one may write

$$l_s\lambda_z \sin\left(\lambda_z\frac{L_z}{2}\right) \;=\; \cos\left(\lambda_z\frac{L_z}{2}\right). \tag{B.29}$$

Introducing dimensionless parameters,

$$\tilde{\lambda}_z := l_s \lambda_z, \tag{B.30a}$$

$$\tilde{L}_z := \frac{L_z}{l_s}, \tag{B.30b}$$

Eq. (B.29) can be written as

$$\tilde{\lambda}_z = \cot\left(\tilde{\lambda}_z \frac{\tilde{L}_z}{2}\right). \tag{B.31}$$

This has one unique solutions per interval

$$\tilde{\lambda}_{z,n} \in \left(n\frac{2\pi}{\tilde{L}_z}, (n+1)\frac{2\pi}{\tilde{L}_z}\right), \quad n = 0, 1, 2, \ldots, \tag{B.32}$$

which must be evaluated numerically. The normalization condition again yields the constant a,

$$a = \frac{1}{2\sqrt{l_s}} \cdot \frac{1}{\sqrt{\frac{\tilde{L}_z}{2} + \sin^2(\tilde{\lambda}_z \tilde{L}_z/2)}}. \tag{B.33}$$

From this we get

$$\begin{aligned} \psi_{mn} &= \frac{1}{l_s \sqrt{\frac{\tilde{L}_y}{2} + \sin^2(\tilde{\lambda}_{y,n}\frac{\tilde{L}_y}{2})}\sqrt{\frac{\tilde{L}_z}{2} + \sin^2(\tilde{\lambda}_{z,m}\frac{\tilde{L}_z}{2})}} \\ &\quad \cdot \cos\left(\tilde{\lambda}_{y,n}\frac{y}{l_s}\right)\cos\left(\tilde{\lambda}_{z,m}\frac{z}{l_s}\right), \end{aligned} \tag{B.34}$$

$$\lambda_{mn} = -\frac{1}{l_s^2}(\tilde{\lambda}_{y,n}^2 + \tilde{\lambda}_{z,m}^2), \tag{B.35}$$

and furthermore

$$\begin{aligned} &\langle \psi_{mn} | q \rangle \\ &= \frac{f}{\eta} \cdot \frac{4 l_s \sin(\tilde{\lambda}_{y,n}\frac{\tilde{L}_y}{2}) \sin(\tilde{\lambda}_{z,m}\frac{\tilde{L}_z}{2})}{\tilde{\lambda}_{y,n}\tilde{\lambda}_{z,m}\sqrt{\frac{\tilde{L}_y}{2} + \sin^2(\tilde{\lambda}_{y,n}\frac{\tilde{L}_y}{2})}\sqrt{\frac{\tilde{L}_z}{2} + \sin^2(\tilde{\lambda}_{z,m}\frac{\tilde{L}_z}{2})}}. \end{aligned} \tag{B.36}$$

Finally the velocity profile for non zero slip is found to be

$$\begin{aligned} &v_x(y,z) \\ &= \frac{f}{\eta}\sum_{mn} \frac{l_s^2}{\tilde{\lambda}_{y,n}^2 + \tilde{\lambda}_{z,m}^2} \frac{1}{\tilde{\lambda}_{y,n}\tilde{\lambda}_{z,m}} \\ &\quad \cdot \frac{4\sin(\tilde{\lambda}_{y,n}\frac{\tilde{L}_y}{2}) \sin(\tilde{\lambda}_{z,m}\frac{\tilde{L}_z}{2})}{\left(\frac{\tilde{L}_y}{2} + \sin^2(\tilde{\lambda}_{y,n}\frac{\tilde{L}_y}{2})\right)\left(\frac{\tilde{L}_z}{2} + \sin^2(\tilde{\lambda}_{z,m}\frac{\tilde{L}_z}{2})\right)} \\ &\quad \cdot \cos\left(\tilde{\lambda}_{y,n}\frac{y}{l_s}\right)\cos\left(\tilde{\lambda}_{z,m}\frac{z}{l_s}\right). \end{aligned} \tag{B.37}$$

The dimensions of the channel in the experiment are about $L_y \simeq 4\,mm$ width and $L_z \simeq 100\,\mu m$ height, so that we get a ratio of about $L_y/L_z \simeq 40$. Using this ratio numerical tests show that the slip length has no influence on the shear rate. Only if the ratio of channel dimensions is of the order of $L_y/L_z \simeq 1$ a dependency on the slip length is observable. From Fig. B.2 we know that a ratio of 40 is large enough to assume ideal Poiseuille flow behavior. The one dimensional Poiseuille profile with slip boundary conditions reads

$$v^{(p)}(z) = \frac{1}{2}\frac{f}{\eta}L_z^2\left(\frac{l_s}{L_z} + \frac{1}{4} - \frac{z^2}{L_z^2}\right) . \tag{B.38}$$

Thus it is not surprising that the shear rate does not depend on the slip length, since the one dimensional solution is only shifted by a non vanishing slip length, but the shape of the flow profile remains the same (see Ref. [102]).

B.1.3. Estimation of the Shear Rate via Throughput Rate

We have already seen that with the dimensions of the channel given in the experiment, a one dimensional Poiseuille profile fits the flow field almost perfectly. Neglecting a possible slip length, the shear rate is the slope of the flow profile at the channel wall, and therefore given by

$$\dot{\gamma} = \frac{f}{\eta}\frac{L_z}{2} . \tag{B.39}$$

Knowing the height of the channel L_z, one may ask, if the parameter f/η can be observed easily in the experiment. In principle, this is indeed possible. Integration of the flow profile over the cross section area of the channel would deliver the amount of liquid flowing through the cross section per time unit, known as throughput rate Q. Since f/η is the only unknown for the entire velocity profile, the integration results in a linear relation between throughput rate and f/η. Starting with Eq. (B.21) and integrating over y and z, one

obtains

$$\begin{aligned} Q &= \int_{-\frac{L_y}{2}}^{\frac{L_y}{2}} dy \int_{-\frac{L_z}{2}}^{\frac{L_z}{2}} dz\, v_x(y,z) \qquad \text{(B.40)} \\ &= \frac{f}{\eta}\sum_{mn}\Lambda_{mn}\int_{-\frac{L_y}{2}}^{\frac{L_y}{2}} dy\, \cos\left(\frac{2n+1}{L_y}\pi y\right)\int_{-\frac{L_z}{2}}^{\frac{L_z}{2}} dz\, \cos\left(\frac{2m+1}{L_z}\pi z\right) \\ &= \frac{f}{\eta}\sum_{mn}\Lambda_{mn}(-1)^{m+n}\frac{4L_yL_z}{(2n+1)(2m+1)}\frac{1}{\pi^2} \\ &= \frac{f}{\eta}\frac{64}{\pi^6}\sum_{mn}\frac{1}{\frac{(2n+1)^2}{L_y^2}+\frac{(2m+1)^2}{L_z^2}}\cdot\frac{L_yL_z}{(2n+1)^2(2m+1)^2}\,. \end{aligned}$$

Applying the assumption $L_y \gg L_z$, the first term in the denominator is negligible, and hence an asymptotic solution for the throughput rate is given by

$$\begin{aligned} Q(L_y \gg L_z) &\simeq \frac{f}{\eta}\frac{64}{\pi^6}\sum_{mn}\frac{1}{\frac{(2m+1)^2}{L_z^2}}\cdot\frac{L_yL_z}{(2n+1)^2(2m+1)^2} \qquad \text{(B.41)} \\ &= \frac{f}{\eta}\frac{64}{\pi^6}L_yL_z^3\sum_{mn}\frac{1}{(2m+1)^4}\,\frac{1}{(2n+1)^2} \\ &= \frac{f}{\eta}\frac{64}{\pi^6}L_yL_z^3\cdot\frac{\pi^6}{768} \\ &= \frac{f}{\eta}\frac{L_yL_z^3}{12}\,. \end{aligned}$$

Solving this for f/η and inserting into Eq. (B.39), one finally obtains

$$\dot\gamma = \frac{6}{L_yL_z^2}\cdot Q\,. \qquad \text{(B.42)}$$

If the shear rate is measured in this way, a small error occurs since the profile is slightly shifted due to the effect of slippage. However, if the slip length is small compared to the channel dimensions, this effect should be negligible. Fig. B.3 shows numerical results for the dependency of the throughput rate on the slip length. As mentioned in the previous section, the slip length is assumed not to exceed $l_s/L_z \lesssim 10^{-3}$, and thus the numerical results indeed indicate that the error is less than 1%. Therefore one may conclude that the throughput rate is certainly well described by the approximation, Eq. (B.41).

The advantage of this consideration is quite obvious: If it is possible to measure the throughput rate at the same time as the experiment is performed, the shear rate can be measured simultaneously, and thus, the measurement of the flow profile gets unnecessary. Unfortunately, this was not the case in the current experimental setup. However, this is mentioned as a suggestion for experimentalists and manufacturers of FCS devices.

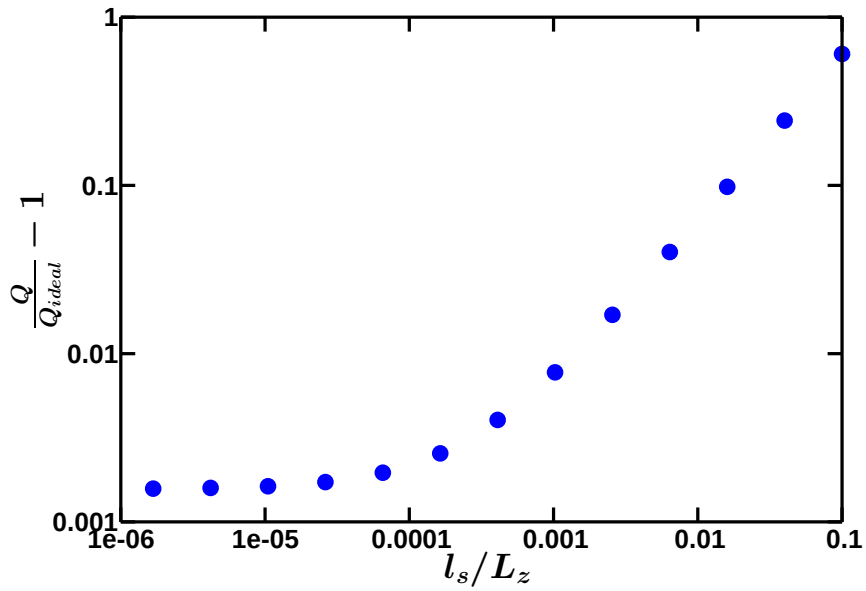

Figure B.3.: Relative deviation of the throughput rate from the idealized value, Eq. (B.41), as function of the slip length ($L_y/L_z = 100$).

C. Attachment: CD with Source Codes

A compact disc with the source codes we implemented is attached to the printed version of this thesis. The codes are all written in C and should be compiled on a Linux system. The CD contains the following folders and routines:

Electrokinetics

- **Poisson_Boltzmann**
  - **Cell_Model**
    This folder contains only one source file named *one_dim_pb.c*. This is the routine written by B. Dünweg using the Verlet algorithm to solve the isotropic PB cell model (see App. A.1). The output is given in reduced units.
  - **Double_Plane**
    Here the source code for the effectively one dimensional test problem discussed in Sec. 2.4.1 can be found. The main program is the file *pb_dp.c*. The code is parallelized using MPI, and therefore requires the library *mpi.h*. Furthermore the Poisson equation is solved using the Fourier transformation, and thus the *fftw3* library must be installed. The makefile uses the *mpicc* compiler. Note that the number of lattice sites in the x_3-direction must be a multiple of the number of parallel processes.
  - **PBp_Ion**
    This program is almost identical with the code for the "double plane" problem and requires the same libraries. The main program is the file *PBp_ion.c* and computes the solution of the PB equation around a solid charged sphere in a rectangular box. The parameters in the input file (*Input.dat*) are given in reduced units. The output of this program is required to run the first order solver.
  - **Electro_Osmosis**
    In this folder two programs can be found, which are nearly identical. The only differences are the units of the output. One program computes the solution of the electro-osmotic flow problem in a slit

channel (see Sec. 2.5) in LJ units, while the results of the second version are transformed to SI units (temperature: $T = 300K$, aqueous solution $\varepsilon_r = 80.1$).

  - **statMC**
    Here, the test code for the combination of the iterative PB solver with a force biased MC algorithm is given. The code should only be seen as a first attempt; it is not parallelized yet and further optimization is required. The *fftw3* library must be installed in order to solve the Poisson equation.

- **Convection_Diffusion**
  This folder contains the test sources for the convection-diffusion equation solver developed in Chap. 3. Here, test versions in one and three dimensions are given.

  - **1d_cde**
    Source codes for the two test problems of Sec. 3.3.1 (*test_1*) and 3.3.2 (*test_2*) can be found in this subfolder. As default the 4th order algorithm is applied in both cases. The 2nd order versions of both diffusive- and multiple time scale analysis are implemented, but commented out.

  - **3d_cde**
    A three dimensional code for the test problem including a source term (Sec. 3.3.2) is implemented, containing a *D3Q19* version of the fourth order algorithm, a *D3Q6* implementation of the second order algorithm from the diffusive scaling analysis, a *D3Q19* model for the multi-time scale version and a *D3Q6* LBGK model.

- **Stokes_ReactionForce**
  The routine *srf.c* computes the Stokes flow field for a cubic array of spheres as discussed in Chap. 4. With this code sc, bcc and fcc lattice structures can be studied. The *fftw3* library must be installed.

- **First_Order_Equations**
  Within this folder the source code for the iterative solver for the first order electrokinetic equations can be found. The main procedure is in the file *cds_sc.c*. Here, only the version for the sc lattice structure, i. e. one sphere in the center of the box, is implemented, but the source can easily be modified by changing the expression for f_0 (see comments in the source code). Further changes are not necessary in order to run the code in the case of bcc or fcc structures, since the classification of the grid nodes is adopted from the PB solution. Thus, the input file only specifies the diffusion constant and the strength of the

external field, which are not necessary for the zeroth order, and in addition the location of the PB results, which should be used as input fields and the desired location of the output data. The *fftw3* library is required.

TIRFCCS

- **Code_BDMC_Gauss**
  This folder contains the program for the data analysis of TIR–FCCS measurements as discussed in Chap. 6. The implementation is the code we used on the *Blue Gene P* (*Rechenzentrum Garching* (RZG)). Here, not only the auto- and cross-correlation curves are computed, but also the MC based data analysis is set on top. The lateral shape of the observation volumes is approximated by a Gaussian. The experimental data we analyzed can be found in the folder *Input/hphil*.
  Since the code is parallelized using MPI, this library is required. The folder contains three different makefiles: *Makefile* compiles the program via *mpicc* on a simple Linux machine, while *Makefile_pwr6* uses *mpcc_r* for compilation on the *Power6* machine at the RZG and *Makefile_bgp* is written for compilation of the source on the *Blue Gene P* using the *mpixlc_r* compiler.

- **Code_BDMC_PCPSF**
  The files within this folder are essentialy equivalent to those in *Code_BDMC_Gauss*.
  However, the program *FCSBDMC_rzg_PCPSF.c* computes the BD/MC algorithm for the data analysis of the TIR-FCCS experiments. The observation volumes are extended to PCPSFs and the program requires the tabulated observation volumes as input file. The goodness of fit is calculated with respect to the averaged auto-correlation curve and the difference-cross-correlation data.

- **Create_PCPSF**
  This folder only contains only the small program *pcpsf.c*, written by B. Dünweg and performing the Monte-Carlo integration discussed in Chap. 6.7.2.

- **Rectangular_Stokes**
  The file *RecStokes.c* is a C–written code for the numerical tests used in appendix B.1. The Stokes equation is solved in a rectangular channel. The double sum is performed up to n_{max} terms in each direction and the eigenvalues in the slip boundary case are numerically calculated using a combination of bisection and Newton method in order to solve Eq.

(B.32). The program offers the opportunity to generate flow profiles in one and two dimensions, and compares the solutions with slip and stick boundary condition and the one dimensional Poiseuille profile, to calculate the shear rate or the throughput rate as function of the slip length, and tests the value of the crest $v_x(0,0)$ as function of n_{max}.

Bibliography

[1] see http://www.britannica.com/EBchecked/topic/125898/colloid.

[2] T. Graham, *Philosophical Transactions of the Royal Society of London* **151**, 183 (1861).

[3] W. B. Russel, D. A. Saville and W. Schowalter, *Colloidal Dispersions*, Cambridge University Press, Cambridge, 1989.

[4] J. K. G. Dhont and K. Kang, *Eur. Phys. J. E* **33**, 51 (2010).

[5] S. Yordanov, A. Best, H. J. Butt and K. Koynov, *Optics Express* **17**, 21149 (2009).

[6] R. J. Hunter, *Zeta–Potential in Colloid Science*, Academic Press, London, 1981.

[7] O. M. Stuetzer, *J. Appl. Phys.* **31**, 136 (1960).

[8] A. Richter, A. Plettner, K. A. Hofmann and H. Sandmaier, *Sensors and Actuators A* **29**, 159 (1991).

[9] J. Yang, F. Lu, L. W. Kostiuk and D. Y. Kwok, *J. Micromech. Microeng.* **13**, 963 (2003).

[10] R. Westermeier, *Electrophoresis in Practice*, Wiley, Weinheim, 2005.

[11] M. Evers, N. Garbow, D. Hessinger and T. Palberg, *Phys. Rev. E* **57**, 6774 (1998).

[12] M. Medebach and T. Palberg, *J. Chem. Phys.* **119**, 3360 (2003).

[13] M. Medebach and T. Palberg, *J. Phys. Condens. Matter* **16**, 5653 (2004).

[14] N. Garbow, M. Evers, T. Palberg and T. Okubo, *J. Phys. Condens. Matter* **16**, 3835 (2004).

[15] T. Palberg, M. Medebach, N. Garbow, M. Evers, A. B. Fontecha, H. Reiber and E. Bartsch, *J. Phys. Condens. Matter* **16**, S4039 (2004).

[16] M. v. Smoluchowski, *Z. phys. Chem.* **92**, 129 (1917).

[17] E. Hückel, *Phys. Z.* **25**, 204 (1924).

[18] D. C. Henry, *Proc. R. Soc. A* **133**, 106 (1931).

[19] J. T. G. Overbeek, *Kolloidchem. Beihefte* **54**, 287 (1943).

[20] F. Booth, *Proc. R. Soc. A* **203**, 514 (1950).

[21] P. H. Wiersema, A. L. Loeb and J. T. G. Overbeek, *J. Colloid Interface Sci.* **22**, 70 (1966).

[22] H. Ohshima, T. W. Healy and L. R. White, *J. Chem. Soc., Faraday Trans. 2* **79**, 1613 (1983).

[23] R. W. O'Brien and L. R. White, *J. Chem. Soc., Faraday Trans. 2* **74**, 1607 (1978).

[24] C. S. Mangelsdorf and L. R. White, *J. Chem. Soc., Faraday Trans.* **88**, 3567 (1992).

[25] H. Ohshima, *J. Colloid Interface Sci.* **228**, 190 (2000).

[26] N. A. Mishchuk and S. S. Dukhin, *Electrophoresis* **23**, 2012 (2002).

[27] I. Pasichnyk and B. Dünweg, *J. Phys. Cond. Matt.* **16**, S3999 (2004).

[28] F. Capuani, I. Pagonabarraga and D. Frenkel, *J. Chem. Phys.* **121**, 973 (2004).

[29] K. Kim, Y. Nakayama and R. Yamamoto, *Phys. Rev. Lett.* **96**, 208302 (2006).

[30] V. Lobaskin, B. Dünweg and C. Holm, *J. Phys. Cond. Matt.* **16**, S4063 (2004).

[31] V. Lobaskin, B. Dünweg, M. Medebach, T. Palberg and C. Holm, *Phys. Rev. Lett.* **98**, 176105 (2007).

[32] B. Dünweg, V. Lobaskin, , K. Seethalakshmy-Hariharan and C. Holm, *J. Phys. Cond. Matt.* **20**, 404214 (2008).

[33] S. Allison, H. Wu, U. Twahir and H. Pei, *J. Colloid Interface Sci.* **352**, 1 (2010).

[34] A. Malevanets and R. Kapral, *J. Chem. Phys.* **110**, 8605 (1999).

[35] M. Ripoll, K. Mussawisade, R. G. Winkler and G. Gompper, *Phys. Rev. E* **72**, 016701 (2005).

[36] G. Gompper, T. Ihle, D. M. Kroll and R. G. Winkler, *Adv. Polym. Sci.* **221**, 1 (2009).

[37] M. W. Heemels, M. H. J. Hagen and C. P. Lowe, *J. Comp. Phys.* **164**, 48 (2000).

[38] J. Horbach and D. Frenkel, *Phys. Rev. E* **64**, 061507 (2001).

[39] A. J. C. Ladd and R. Verberg, *J. Stat. Phys.* **104** (2001).

[40] R. Z. Wan, H. P. Fang, Z. Lin and S. Chen, *Phys. Rev. E* **68**, 011401 (2003).

[41] V. Lobaskin and B. Dünweg, *New J. Phys.* **6**, 54 (2004).

[42] W. H. Press, S. A. Teukolsky, W. T. Vetterling and B. P. Flannery, *Numerical Recipes in C*, Cambridge University Press, 2nd edition, 1992.

[43] W. Rocchia, E. Alexov and B. Honig, *J. Phys. Chem. B* **105**, 6507 (2001).

[44] M. Holst, N. Baker and F. Wang, *J. Comp. Chem.* **21**, 1319 (2000).

[45] A. C. Maggs and V. Rossetto, *Phys. Rev. Lett.* **88**, 196402 (2002).

[46] A. C. Maggs, *J. Chem. Phys.* **117**, 1975 (2002).

[47] L. Levrel, F. Alet, J. Rottler and A. C. Maggs, *Pramana* **64**, 1001 (2005).

[48] J. Rottler and A. C. Maggs, *J. Chem. Phys.* **120**, 3119 (2004).

[49] J. Rottler and A. C. Maggs, *Phys. Rev. Lett.* **93**, 170201 (2004).

[50] M. Baptista, R. Schmitz and B. Dünweg, *Phys. Rev. E* **80**, 016705 (2009).

[51] S. Zhao, Z. Wang and B. Li, *accepted in Phys. Rev. E* (2011).

[52] S. L. Brenner and D. A. McQuarrie, *J. Theor. Biol.* **39**, 343 (1973).

[53] S. L. Brenner and R. E. Roberts, *J. Phys. Chem* **77**, 2367 (1973).

[54] E. S. Reiner and C. J. Radke, *J. Chem. Soc. Faraday Trans.* **86**, 3901 (1990).

[55] K. A. Sharp and B. Honig, *J. Phys. Chem.* **94**, 7684 (1990).

[56] V. Kralj-Iglic and A. Iglic, *J. Phys. II France* **6**, 477 (1996).

[57] F. Fogolari and J. M. Briggs, *Chem. Phys. Lett.* **281**, 135 (1997).

[58] J. Che, J. Dzubiella, B. Li and J. A. McCammon, *J. Phys. Chem. B* **112**, 3058 (2008).

[59] M. J. Holst, The Poisson–Boltzmann Equation, see http://ccom.ucsd.edu/~mholst/pubs/dist/Hols94d.pdf.

[60] R. Duan, T. Yang and C. Zhu, *J. Math. Anal. Appl.* **327**, 425 (2007).

[61] B. Li, *Nonlinearity* **22**, 811 (2009).

[62] K. Yee, *IEEE Trans. Antennas and Propagation* **14**, 302 (1966).

[63] S. Engstrom and H. Wennerstrom, *J. Phys. Chem.* **82**, 2711 (1978).

[64] see the eke project, http://code.google.com/p/eke/.

[65] A. Y. Grosberg, T. T. Nguyen and B. I. Shklovskii, *Rev. Mod. Phys.* **74**, 329 (2002).

[66] E. J. W. Verwey and J. T. G. Overbeek, *Theory of the Stability of Lyophobic Colloids*, Elsevier, Amsterdam, 1948.

[67] L. Belloni, *J. Chem. Phys.* **85**, 519 (1986).

[68] D. P. Landau and K. Binder, *A Guide to Monte Carlo Simulations in Statistical Physics*, Cambridge Univ. Press, Cambridge, 2000.

[69] L. Belloni, *Colloids Surf. A* **140**, 227 (1998).

[70] M. Deserno, C. Holm and S. May, *Macromolecules* **33**, 199 (2000).

[71] J. Zhao, *Kolloide in externen elektrischen und magnetischen Feldern*, PhD thesis, Universität Siegen, Siegen, 2010.

[72] J. Smiatek, M. Sega, C. Holm, U. D. Schiller and F. Schmid, *J. Chem. Phys.* **130**, 244702 (2009).

[73] J. Smiatek, *Mesoscopic simulations of electrohydrodynamic phenomena*, PhD thesis, Universität Bielefeld, Bielefeld, 2009.

[74] M. V. Chubynsky and G. W. Slater, *arXiv:1008.3558v1 [cond-mat.stat-mech]* .

[75] G. H. Weiss, *Aspects and Applications of the Random Walk*, North-Holland, Amsterdam, 1994.

[76] R. Metzler, *Eur. Phys. J. B* **19**, 249 (2001).

[77] J. C. Strikwerda, *Finite Difference Schemes and Partial Differential Equations*, Siam, Philadelphia, 2. edition, 2004.

[78] B. Dünweg and A. J. C. Ladd, *Adv. Polym. Sci.* **221**, 89 (2009).

[79] Z. Guo, B. Shi and C. Zheng, *Internat. J. Numer. Methods Fluids* **39**, 325 (2002).

[80] Z. Guo, C. Zheng and B. Shi, *Phys. Rev. E* **65**, 046308 (2002).

[81] J. Lätt, *Hydrodynamic Limit of Lattice Boltzmann Equations*, PhD thesis, Université de Genève, Genève, 2007.

[82] U. D. Schiller, *Thermal fluctuations and boundary conditions in the lattice Boltzmann method*, PhD thesis, Johannes Gutenberg-Universität, Mainz, 2008.

[83] U. D. Schiller and B. Dünweg, in preparation.

[84] G. K. Youngren and A. Acrivos, *J. Fluid Mech.* **69**, 377 (1972).

[85] A. A. Zick and G. M. Homsy, *J. Fluid Mech.* **115**, 13 (1982).

[86] L. D. Landau and E. M. Lifschitz, *Lehrbuch der Theoretischen Physik VI - Hydrodynamik*, Akademie Verlag, Berlin, 5 edition, 1991.

[87] M. Frigo and S. G. Johnson, *Proceedings of the IEEE* **93**, 216 (2005).

[88] J. Dongarra, A. Lumsdaine, R. Pozo and K. A. Remington, *IML++ v. 1.2, Reference Guide*, 1996.

[89] A. Meister, *Numerik linearer Gleichungssysteme*, Friedr. Vieweg & Sohn, Braunschweig/Wiesbaden, 1999.

[90] GNU Scientific Library, see http://savannah.gnu.org/projects/gsl.

[91] H. Hasimoto, *J. Fluid Mech.* **5**, 317 (1959).

[92] W. A. Harrison, *Electronic Structure and the Properties of Solids*, Freeman, San Francisco, 1980.

[93] H. L. Skriver, *Phys. Rev. B* **31**, 1909 (1984).

[94] W. J. Carr, *Phys. Rev.* **122**, 1437 (1961).

[95] P. Wette, H. J. Schöpe and T. Palberg, *J. Chem. Phys.* **116**, 10981 (2002).

[96] P. Szymczak and A. J. Ladd, *Phys. Rev. E* **68**, 036704 (2003).

[97] P. Szymczak and A. J. Ladd, *Phys. Rev. E* **69**, 036704 (2004).

[98] C. Neto, D. R. Evans, E. Bonaccurso, H.-J. Butt and V. S. J. Craig, *Rep. Prog. Phys.* **68**, 2859 (2005).

[99] M. Brinkmeier, K. Dörre, J. Stephan and M. Eigen, *Analytical Chemistry* **71**, 609 (1999).

[100] K. Hassler, T. Anhut, R. Rigler, M. Gösch and T. Lasser, *Biophysical Journal* **88**, L01 (2005).

[101] J. Ries, E. P. Petrov and P. Schwille, *Biophysical Journal* **95**, 390 (2008).

[102] D. Lumma, A. Best, A. Gansen, F. Feuillebois, J. O. Rädler and O. I. Vinogradova.

[103] D. E. Elrick, *Aust. J. Phys.* **15**, 283 (1962).

[104] R. T. Foister and T. G. M. Van De Ven, *J. Fluid Mech.* **96**, 105 (1980).

[105] B. Zhang, J. Zerubia and J. Olivo-Marin, *Applied Optics* **46**, 1819 (2007).

[106] P. S. Dittrich and P. Schwille, *Analytical Chemistry* **74**, 4472 (2002).

[107] H. C. Öttinger, *Stochastic Processes in Polymeric Fluids*, Springer, Berlin, 1996.

[108] H. Risken, *The Fokker–Planck Equation*, Springer, Berlin Heidelberg New York, 2 edition, 1996.

[109] R. M. Mazo, *Brownian Motion*, Clarendon Press, Oxford, 1 edition, 2002.

[110] J. Honerkamp, *Stochastic dynamical systems*, VCH, New York, 1994.

[111] R. J. Barlow, *Statistics*, Wiley, Chichester, 1989.

[112] B. L. Welch, *Biometrika* **29**, 350 (1938).

[113] O. I. Vinogradova, K. Koynov, A. Best and F. Feuillebois, *Phys. Rev. Lett.* **102**, 118302 (2009).

[114] I. S. Gradshteyn and I. M. Ryzhik, *Table of Integrals, Series, and Products*, Academic Press, Orlando, 1980.

[115] P. Holmqvist, J. K. G. Dhont and P. R. Lang, *J. Chem. Phys.* **126**, 044707 (2007).

[116] W. Schaertl and H. Sillescu, *J. Stat. Phys.* **77**, 1007 (1994).

[117] M. P. Allen and D. J. Tildesley, *Computer Simulation of Liquids*, Oxford University Press, Oxford, 1989.

[118] P. Joseph and P. Tabeling, *Phys. Rev. E* **71**, 035303 (2005).

[119] J. H. Spurk and N. Aksel, *Strömungslehre*, Springer, Berlin Heidelberg New York, 6 edition, 2006.

[120] C. Cohen-Tannoudji, B. Diu and F. Laloë, *Quantum Mechanics 1*, Wiley, New York, 1977.